Dipl.-Ing. Stefan Manfred Spann

Accelerated Arterial Spin Labeling - Quantification of Brain Perfusion

DOCTORAL THESIS

to achieve the university degree of
Doktor der technischen Wissenschaften

submitted to

Graz University of Technology

Supervisor

Univ.-Prof. Dipl-Ing. Dr.techn. Rudolf Stollberger
Institute of Medical Engineering

Graz, Austria, 2020

Abstract

Arterial spin labeling (ASL) is a very promising non-invasive magnetic resonance imaging (MRI) method for determining perfusion in various organs. Because of its non-invasivity and the possibility of absolute quantification of cerebral blood flow (CBF), the method has been in the focus of research since its invention in 1992, but has not yet found broad clinical application. Various studies show the great potential for ASL in the detection of cerebrovascular diseases such as stroke, arteriovenous malformations, sickle cell anemia, and in the diagnosis of tumors as well as in functional brain examinations. However, there are still essential challenges for application in clinical routine. ASL has an inherently low signal-to-noise ratio (SNR), which is accompanied by a low resolution and partial volume effects (PVE) as well as long acquisition times. Hemodynamic variations can affect the ASL-signal and the method is susceptible to motion artifacts.

The aim of this work is to address these major limitations and to bring ASL close to clinical routine. For noise suppression, variational methods for static and dynamic ASL data were developed, which consider the whole measurement data set at once. These techniques improve the SNR, increase the reliability of the perfusion signal, and allow a significant reduction of the acquisition time from 45 minutes to 5 minutes for high resolution 2D measurements. Subsequently, a pipeline for real-time imaging, signal monitoring, artifact detection, and neurofeedback presentation was implemented. Finally, the problem of motion sensitivity in segmented 3D coding was addressed. For this purpose, a single-shot acquisition method was developed, which combines parallel imaging and image reconstruction with a novel spatio-temporal regularization function and hence needs only a fraction of the normally required measurement data. With the developed technique, high-resolution, motion-robust whole brain perfusion images can be acquired in a clinically compatible acquisition time of less than 3 minutes. Furthermore, the efficient signal encoding offers the possibility to investigate neuronal activation and to measure dynamic ASL data.

Keywords: Arterial Spin Labeling, Variational Methods, Magnetic Resonance Imaging, Image Enhancement

Kurzfassung

Arterial Spin Labeling (ASL) ist eine sehr vielversprechende nicht-invasive MR-Methode zur Bestimmung der Perfusion in verschiedenen Organen. Wegen ihrer Nicht-Invasivität und der Möglichkeit der absoluten Quantifizierung des zerebralen Blutflusses ist die Methode seit ihrer Erfindung im Jahr 1992 im Fokus der Forschung, ist aber bisher nicht in eine breite klinische Anwendung gekommen. Verschiedene Studien zeigen das große Potenzial für ASL bei der Erkennung von zerebrovaskulären Erkrankungen wie Schlaganfall, arteriovenöse Missbildungen, Sichelzellanämie und bei der Tumordiagnose sowie bei der funktionellen Untersuchung des Gehirns. Es gibt jedoch noch essentielle Herausforderungen für eine klinische Routineanwendung. ASL hat ein inhärent niedriges Signal-Rausch-Verhältnis (SNR), begleitet von einer niedrigen Auflösung und Partialvolumeneffekten (PVE) sowie langen Aufnahmezeiten. Hämodynamische Variationen können das ASL-Signal beeinflussen und die Methode ist anfällig für Bewegungsartefakte.

Das Ziel dieser Arbeit ist es die zuvor beschriebene wesentlichen Problem zu adressieren und ASL in Richtung klinischen Alltag zu bringen. Dazu wurden zur Rauschunterdrückung variationelle Verfahren für statische und dynamische ASL-Daten entwickelt, die den gesamten Messdatensatz auf einmal betrachten. Diese Techniken verbessern das SNR, erhöhen die Zuverlässigkeit des Perfusionssignals und ermöglichen eine wesentliche Reduzierung der Aufnahmezeit von 45 Minuten auf 5 Minuten für hochaufgelöste 2D Messungen. In weiter Folge wurde eine Pipeline für Echtzeit-Bildgebung, Signalüberwachung, Artefakterkennung und Neurofeedback-Präsentation implementiert. Abschließend wurde das Problem der Bewegungssensitivität bei segmentierter 3D-Kodierung behandelt. Zu diesem Zweck wurde eine single-shot Aufnahmemethode entwickelt, die durch Kombination von paralleler Bildgebung und Bildrekonstruktion mit einem neuartigen räumlich-zeitlichen

Regularisierungsfunktional mit einem Bruchteil der normalerweise notwendigen Messdaten auskommt. Mit der hier entwickelten Technik können hochauflösende, bewegungsstabile Perfusionsbilder vom gesamten Gehirn in einer klinisch vertretbaren Aufnahmezeit von weniger als 3 Minuten aufgenommen werden. Darüber hinaus bietet die effiziente Signalkodierung die Möglichkeit, die neuronale Aktivierung zu untersuchen und dynamische ASL Daten zu messen.

Schlagwörter: Arterial Spin Labeling, Variationsmethoden, Magnetresonanz-Bildgebung, Bildverbesserung

Affidavit

I declare that I have authored this thesis independently, that I have not used other than the declared sources/resources, and that I have explicitly indicated all material which has been quoted either literally or by content from the sources used.

Date

Signature

Eidesstattliche Erklärung

Ich erkläre an Eides statt, dass ich die vorliegende Arbeit selbstständig verfasst, andere als die angegebenen Quellen/Hilfsmittel nicht benutzt, und die den benutzten Quellen wörtlich und inhaltlich entnommene Stellen als solche kenntlich gemacht habe.

Ort

Datum

Unterschrift

Acknowledgments

During my time as a PhD student I had the pleasure of working with many talented, motivated and inspiring people. Now it is time to say thank you to all who supported me during this time.

First of all I would like to thank my supervisor Prof. Stollberger for introducing me to the exciting field of MRI and ASL. For his continuous support, exciting discussions and scientific guidance, and for giving me the opportunity to visiting various international conferences. Thank you to Prof. Bredies and Prof. Kazimierski form the Institute of Mathematics and Scientific Computing for giving me insights into the complex world of numerical optimization and supporting me throughout my PhD. Special thanks to Prof. Wang and Dr. Shao from the University of Southern California for the fruitful cooperation. A big part of my thesis would not be possible without your support, and thanks for the opportunity to come to LA to meet and discuss with many compete people form your research group. Thanks to Dr. Pfeuffer for providing advanced ASL sequences and for his valuable comments and support during projects.

I would like to thank all my colleagues and cooperation partners from the Institute of Medical Engineering, from the Department of Neurology (Medical University of Graz), from the Ludwig Boltzman Institute, from the Institute of Psychology, and from the Institute of Mathematics and Scientific Computing (University of Graz). It was a pleasure to work with you and thanks for numerous discussions and the pleasant working atmosphere.

Special thanks go to all proofreaders, especially M. Söllradl, whose comments greatly helped me to finish this thesis.

I would express my immense gratitude to all my friends who accompany me in my life and are always here for me. Thanks to Christina for your love and adventures beside the work. Thanks for listening to my presentation, improving my pronunciation, and for spending time in the MRI so that I could test new sequences and algorithm.

Finally, I am deeply grateful for my family, my parents, Gabriele and Helmut, and my sisters, Claudia and Julia, for their continuous support throughout my life and for their endless love.

Contents

List of Figures

List of Tables

1

Introduction and Outline

Contents

1.1 Introduction

Perfusion delivers essential nutritions and oxygen to the tissue, assuring a proper function of cells and for tissue growing. Even a short interruption can lead to permanent cell death with irreversible tissue damage. For a long time, measurement of perfusion has been used as an important physiological parameter for the assessment of organ health and functionality. [120, 143] In the daily clinical routine perfusion measurements are often used for the diagnosis of various brain diseases, especially those associated with the cerebrovascular system such as vascular stenosis or stroke. According to the World Health Organization (WHO) 15 million people suffer from stroke every year worldwide and approximately 20.000 alone in Austria. Stroke is the second leading cause of death and the third leading cause of immobility.

The current gold standard for measuring perfusion is Oxygen-15 positron emission tomography (PET). This technique uses a radioactive tracer with short half-live period. Consequently, an on-site cyclotron is required for creating the tracer [301]. An alternative imaging modality for perfusion measurements is magnetic resonance imaging (MRI), which uses typically gadolinium compounds as an exogenous tracer. The search for an alternative to contrast agent based perfusion imaging methods is of great importance, because contrast agents can generally lead to side effects and are contraindicated for patients with renal insufficiency, pregnants, pediatric populations or for monitoring disease progression [128]. In addition, perfusion measurements are of major interest for multiple applications in research which require a complete non-invasive and non-harmful technique. Perfusion provides information of neuronal activity, functional connectivity, neurodegenerative diseases and provides insights into changes of the brain system due to drug administration [128, 151, 303].

A very promising technique for the non-invasive measurement of brain perfusion is MRI-based arterial spin labeling (ASL) [66]. This method uses magnetically labeled arterial blood instead of an exogenous contrast agent. ASL has distinct advantages compared to other perfusion measurement techniques. It is non-invasive, non-harmful, provides the possibility of absolute quantification and can be repeated multiple times. Therefore, ASL opens a broad range of applications in the clinical routine and scientific research. Since its original invention [66], ASL has gained increased popularity in the scientific community leading to remarkably improvements in labeling techniques, data sampling strategies and sophisticated post-processing methods. The great interest and potential of ASL in clinical and scientific applications is underlined by the recently published consensus paper [8].
Beside all these advantages, several challenges remain for robust perfusion measurements with ASL. The main drawback of this method is that the signal effect is very low and typically in the range of noise. In order to obtain clinically usable images with sufficient signal-to-noise ratio (SNR), repeated measurements have to be performed. This leads to clinically unacceptable acquisition times with an increased risk of motion artifacts, which can lead to clinically non interpretable perfusion images. The motion sensitivity is especially a problem for scanning patients with specific diseases like stroke which limits the applicability of ASL for such important patient groups. To bring ASL imaging towards clinical practice, robust methods which improves the SNR, motion-insensitivity, quantification accuracy and reliability of the cerebral blood flow (CBF)-maps are very important. This thesis describes the development and validation of modern variational models to address some of these challenges in ASL imaging.

1.2 Outline of the Thesis

This PhD thesis compromises 8 chapters. Chapter 2 is a basic background chapter that provides a general introduction to perfusion in the brain and the main principles of ASL imaging. An overview of different labeling approaches, readout schemes and quantification models are presented as well as a short overview of advanced ASL techniques is given. In addition to the basic principles, the challenges and limitations are discussed as a motivation for the subsequent chapters.

Chapter 3 deals with one of the major drawback of ASL imaging, the low SNR. This chapter starts with a short introduction to variational image denoising. Subsequently, a new denoising approach for 2D ASL data based on total generalized variation (TGV) is presented. This denoising approach is matched to the control-label pairs and includes spatial and temporal information of the whole available dataset in the denoising procedure. The proposed technique is validated on synthetic and in-vivo 2D-ASL data and compared with state-of the art denoising methods.

In Chapter 4 the developed denoisig method is extended to 3D isotropic and anisotropic data. In addition, a spatial adaptive regularization parameter is integrated in the denoising procedure to take into account the spatial varying noise due to parallel imaging (PI) and the physiological noise from the subject. This enables the automatic denoising of static ASL measurements.

In chapter 5 we introduce the concept of variational denoising for dynamic ASL data by using infimal convolution of total generalized variational functionals. We given a short introduction to functional arterial spin labeling (fASL) and discuss and validate the influence of the proposed method on fASL and multi-post-labeling delay (PLD) data.

Chapter 6 presents a pipeline for processing, analyzing and monitoring fASL data in real time. We validated the proposed pipeline on task basked fASL data with and without neurofeedback (NF) presentation. The NF allowed the subjects to control their own brain activation during a finger tapping experiment.

In chapter 7 a time-dependent acquisition scheme for accelerating 3D-gradient and spin echo (GRASE) ASL acquisitions is introduced and combined with a spatio-temporal variational reconstruction approach. The proposed method is validated on motion free and motion-corrupted datasets.

A conclusion and outlook to future work is given in chapter 8.

2

Arterial Spin Labeling

Contents

2.1 Brain Perfusion Imaging

Perfusion is one of the most fundamental physiological processes and delivers essential nutrients such as oxygen and glucose to the tissue capillary bed and clears waste metabolic products like carbon dioxide or lactic acid. A disruption or alteration in perfusion can be dramatic, especially in the brain, which is a particularly highly perfused organ. The human brain receives approximately 15% of the cardiac output at rest which corresponds on average to 800 *ml* of blood per minute [220]. It accounts for approximately 20% of the total body oxygen consumption and 25% of the daily energy intake [78]. Since the brain is not able to store energy locally, a continuous supply of oxygenated blood and glucose is necessary to assure proper functioning of the cells and for growth and repair of brain tissue [182, 210]. Even a short interruption or decrease in perfusion can lead to cell death with irreversible tissue damage, and as a consequence to loss in cognitive functions, physical impairment, or death [182]. The cerebral blood flow (CBF) provides information of the amount or volume (ml) of arterial blood delivered to $100g$ of tissue per minute ($ml/100g/min$). The amount of CBF varies from region to region and depends on the metabolic demands of the brain region [19]. A typical value of CBF in a healthy brain is 60 $ml/100g/min$ in gray matter (GM) and 20 $ml/100g/min$ in white matter (WM) [155, 325]. The CBF is determined by the following relationship:

$$CBF = \frac{CPP}{CVR}, \tag{2.1}$$

where CPP is the cerebral perfusion pressure and CVR is the cerebrovascular resistance. The CBF in the brain is tightly coupled to brain metabolism and a local change in perfusion can be an indicator of changes in neural activation [151]. Also drugs [289], caffeine [2], alcohol [268] or nicotine [71] can change the CBF to a certain extent. To compensate variations in the CBF, and to ensure an adequate constant nutritional blood supply, the human organism has two complex regulation mechanism: first the dynamic cerebral autoregulation [182, 275] and second the variation in oxygen extraction fraction (OEF) [65, 188]. The process of autoregulation is shown in Figure 2.1 Stage 1. The dynamic cerebral autoregulation keeps the CBF relatively constant despite moderate variations in perfusion pressure (60 - 120 $mmHg$) [182]. This constant CBF is achieved by contracting or relaxing the smooth muscle cells in the vessel walls [182]. A decrease in CPP leads to a relaxation of the smooth muscle cells and hence a dilatation of the arteries [182]. This reduces the CVR and thereby increases the cerebral blood volume (CBV) to keep the CBF constant [182]. If the cerebral perfusion pressure drops below the autoregulation range ($<$ 60mmHg) the CBF starts to decrease and leads to a hypoperfusion in the brain (Stage 2). In this stage the second compensatory mechanism take effect and starts to increase the oxygen extraction fraction coefficient so that more oxygen can be extracted from the blood to satisfy the metabolic demands of the brain tissue [182]. The increased OEF leads to an increase in the cerebral metabolic rate of oxygen (CMRO2) [65, 182]. If the CPP reduces further, both compensatory mechanism are exploited and the metabolic demands of the brain tissue are no longer satisfied resulting in permanent cell tissue damage [182].

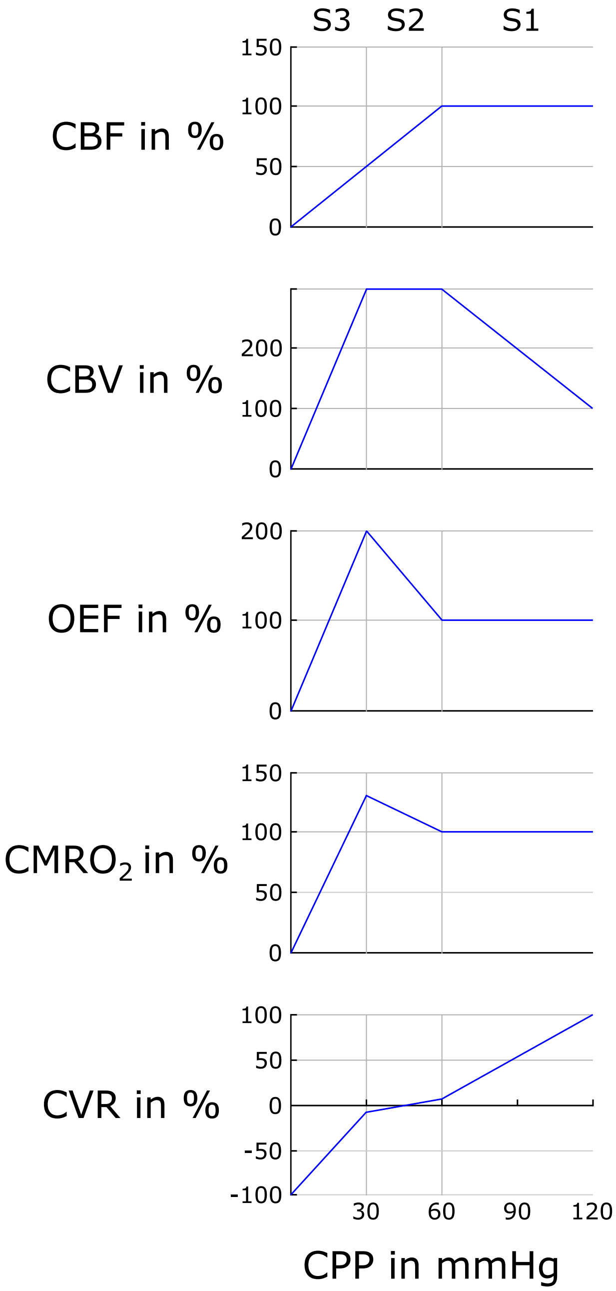

Figure 2.1: Relationship and change (in %) for different cerebral variables in dependence of the cerebral perfusion pressure (CPP). In stage 1 (S1) the dynamic autoregulation process keeps the CBF constant by modifying the cerebral vascular resistance (CVR) and hence the cerebral blood volume (CBV). In stage 2 the CPP drops further which leads to an increase of the oxygen extraction fraction to satisfy the metabolic demands of the brain tissue. A drop in CPP below 30 $mmHg$ (stage 3) can not be compensated by those mechanisms resulting in a deficit in metabolic substrates and hence to cell tissue damage. Figure modified from Nemoto et al. [188].

2.1.1 Importance of Cerebral Blood Flow for Neuroimaging

Measurement of cerebral blood flow provides important information about brain diseases [302], especially those associated with the cerebrovascular system such as cerebral ischemia [38, 321], arterial stenosis and occlusion [302], sickle-cell disease [192], epilepsy [128], or arteriovenous malformations [231]. The CBF provides useful information in the tumor diagnostic and therapy, since the grade of the tumor correlates with the vascular proliferation around the tumor [296]. Neurodegenerative disorders such as Alzheimer are accomplished with local hypo-perfusion areas due to reduced metabolism, which often precedes structural changes such as brain atrophy [324]. Hence, perfusion measurements can serve as early biomarker for Alzheimer [333]. Beside the detection of pathologies, CBF provides important information of metabolic changes, as brain activity requires nutrients and oxygen, which is delivered with the blood. It can therefore be used for cognitive neuroscience and as a biomarker of pharmacological actions [303].

2.1.2 Measuring the Cerebral Blood Flow

For measuring perfusion various imaging techniques were developed, which are all based on tracer kinetics. In general the methods can be divided into two categories: those who use an exogenous agent as a tracer and those who use water protons in the arterial blood as an endogenous tracer. The most commonly used techniques based on an exogenous tracer are positron emission tomography (PET), single-photon emission computer tomography (SPECT), perfusion computed tomography (PCT), xenon-enhanced computed tomography (XeCT), and typically dynamic susceptibility contrast (DSC)-magnetic resonance imaging (MRI). The MRI technique based on an endogenous tracer is called arterial spin labeling (ASL)-MRI and is used in this thesis for obtaining perfusion maps of the brain. [182, 301]

2.2 Arterial Spin Labeling

ASL is a non-invasive MRI technique for measuring perfusion and was invented in 1992 [66]. In the first implementation Detre et al. [66] measured the CBF in a rat brain using water as a freely diffusible tracer [66]. Two years later the same group performed the first successful ASL perfusion measurement of a human brain [68]. A new research area was born, which emerged rapidly over the last two decades and is still evolving. ASL offers distinct advantages over current standard perfusion imaging methods. It is completely non-invasive and highly suitable for studies in the healthy individual, for patients with renal insufficiency, and pediatric or infants [128]. The possibility to quantify the CBF in absolute units permits to trace disease progression and treatment effects and allows the recognition of perfusion changes in pharmacogenetic or longitudinal studies [303]. In addition, the determination of changes in physiological blood flow due to brain activity is of great interest and requires a complete non-invasive technique for repetitive applications in research.

2.3 Main Principle of ASL Imaging

The main principle of ASL imaging compromises three parts (Figure 2.2). In the first step, the arterial blood water is magnetically labeled, typically in a region proximal to the tissue of interest. The blood water spins are inverted using a combination of radio frequency (RF)-pulses and gradients [300]. The second part, called inversion time (TI) or post-labeling delay (PLD), is a waiting period. During this time the labeled blood flows from the labeling plane to the capillaries of interest. After the labeled blood has reached the tissue of interest an image is acquired, the so-called label image. This image contains positive signal contributions from the static tissue and negative signal contributions from the inverted blood. In order to obtain a perfusion weighted image the whole experiment is repeated but without altering the inflowing blood (control condition). This image is known as control image. The perfusion contrast is then achieved by subtracting these two images. The signal of the static tissue cancels out and the remaining signal reflects the amount of labeled spins that have reached the tissue during the PLD. This perfusion signal is in the order of 1-2% of the full tissue signal leading to a limited signal-to-noise ratio (SNR) [204]. Thus, repeated measurements are necessary to gain sufficient image quality, which are typically in the order of tens. A kinetic model based on tracer kinetics is then applied to convert the perfusion weighted image into quantitative units [34, 66]. These steps will be described in more detail in the following sections.

2.4 Labeling Approaches

A crucial part of the ASL experiment is the labeling of the arterial blood water spins. In the first ASL approach the blood spins were labeled using saturation pulses [66]. Shortly thereafter, the saturation pulses were replaced by inversion pulses [300] because they provide doubled signal strength. The amount of successfully inverted or labeled spins, known as labeling efficiency, directly effects the acquired perfusion signal. Thus, a high efficiency of nearly 100% is desirable. Typical values ranges from 70% up to 98% depending on the used labeling scheme [8]. In this section the basic principle of the three major labeling approaches continuous [66, 300], pulsed [77], and pseudo continuous labeling [56] schemes are described. Recently two advanced labeling approaches, velocity selective ASL [74, 189, 309] and acceleration ASL [224] were developed, which are described in section 2.9 ”Advanced ASL methods”.

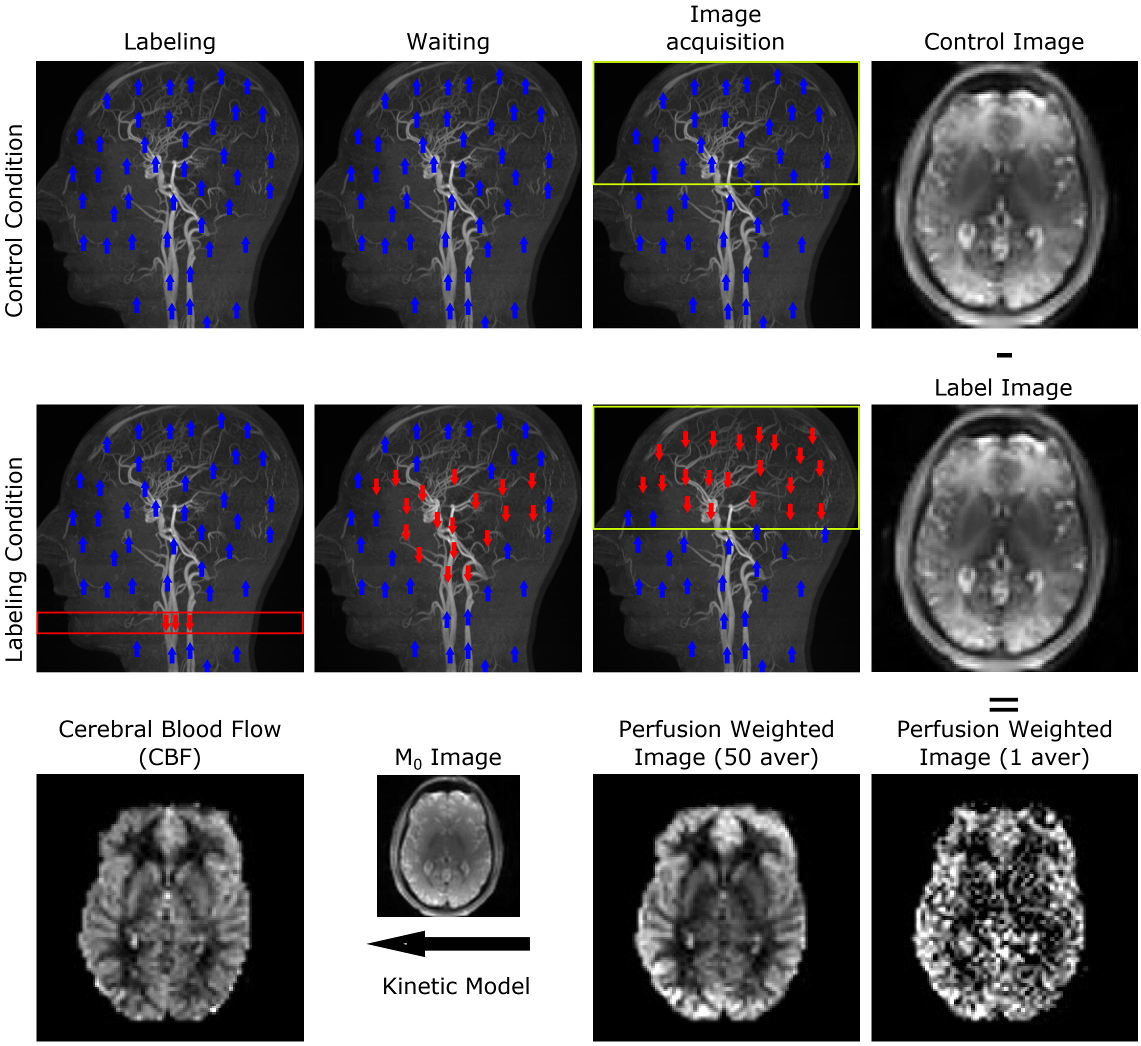

Figure 2.2: Basic principle of the ASL experiment. (1) Labeling condition: Blood moving through the labeling plane (red) gets inverted. During the waiting period the labeled blood flows into the region of interest (yellow). After the labeled spins have reached the tissue an image is acquired, the so called label image. (2) During the control condition a second image is acquired (control image) without altering the inflowing blood. The perfusion contrast is achieved by subtraction the label image from the control image thereby canceling out the signal from the static tissue. From the perfusion weighted image (PWI) a quantitative CBF-map is calculated based on a kinetic model.

2.4.1 Continuous Arterial Spin Labeling (CASL)

The first implementation of ASL used a continuous labeling of the arterial blood known as continous arterial spin labeling (CASL) [66]. Figure 2.3 shows schematically the basic principle of this technique. The labeling of the arterial spins is achieved by applying a long and continuous RF pulse, typically 2-4 s, in combination with a slice-selective gradient proximal to the imaging volume [300]. In contrast to traditional adiabatic inversion, which uses frequency modulated RF pulses, CASL uses flow-driven adiabatic inversion for labeling of the arterial blood spins. This means that the frequency modulation is achieved by applying a constant magnetic field gradient along to the feeding arteries. Consequently, as the blood spins move through the labeling plane the gradient changes the Lamor-frequency from far below resonance to on-resonance, at the center of the labeling plane, to far above resonance. In combination with the main magnetic field and the continuously applied B_1 field the blood water spins experience an rotating effective field B_{eff} from nearly aligned with the static magnetic field (+z axis) to nearly opposite to the static magnetic field (-z axis). This is schematically illustrated in Figure 2.4. If the change in the effective field is slow compared to the precession a spin-locked state is achieved. In this state the spins precess around the effective field and any small offset or change averages out, meaning that the spins follow the change in effective field. As B_{eff} rotates from upwards to downwards, the magnetization gets inverted as the spins move through the labeling plane. [36, 100, 120]

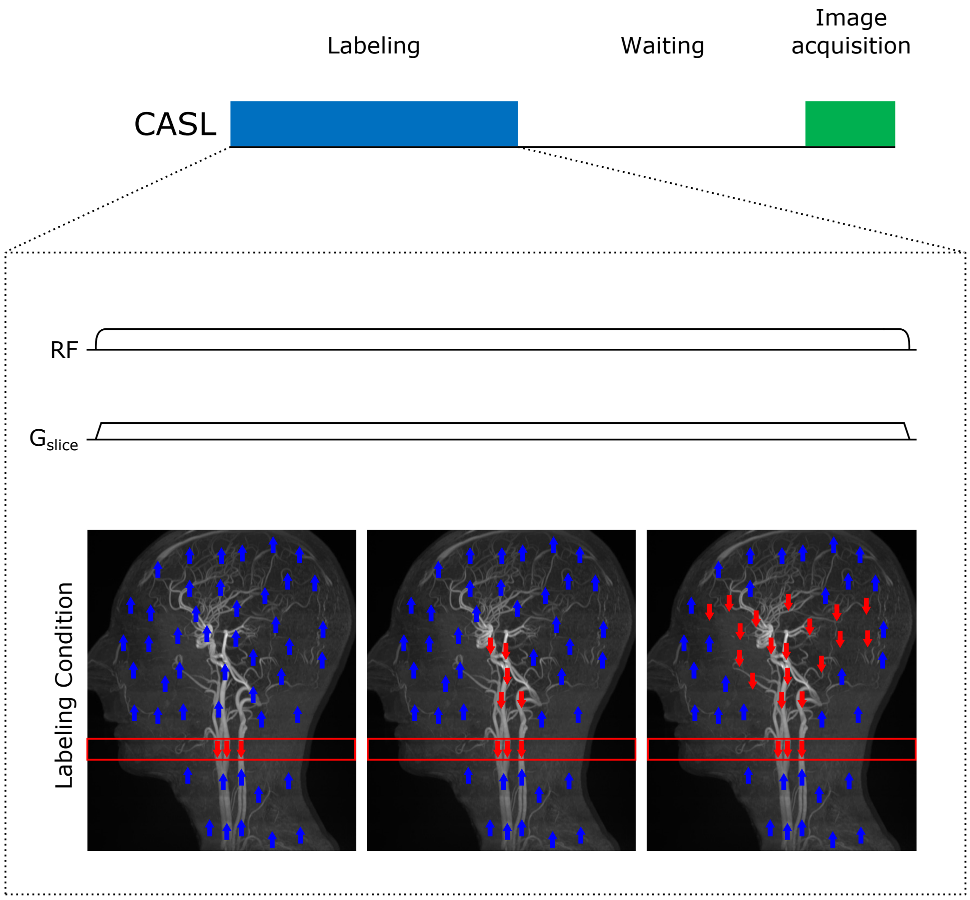

Figure 2.3: Basic principle of continuous ASL. The blood flowing through the labeling plane (red) is continuously inverted by applying a constant RF and slice selective gradient along the feeding arteries. This is known as flow driven adiabatic inversion.

However, to achieve flow driven adiabatic inversion, the spins must obey the adiabatic labeling condition [14, 100, 300]:

$$\frac{1}{T_1}, \frac{1}{T_2} << \frac{G \cdot v}{B_1} << \gamma B_1, \tag{2.2}$$

where T_1 and T_2 are the longitudinal and transversal relaxation times of blood, G is the gradient amplitude, v is the blood flow velocity, B_1 is the applied magnetic field, and γ is the gyromagnetic ratio. From this condition follows that the labeling efficiency in CASL is highly dependent on the blood flow velocity and hence the RF-amplitude and the gradient strength has to be tuned accordingly [306].

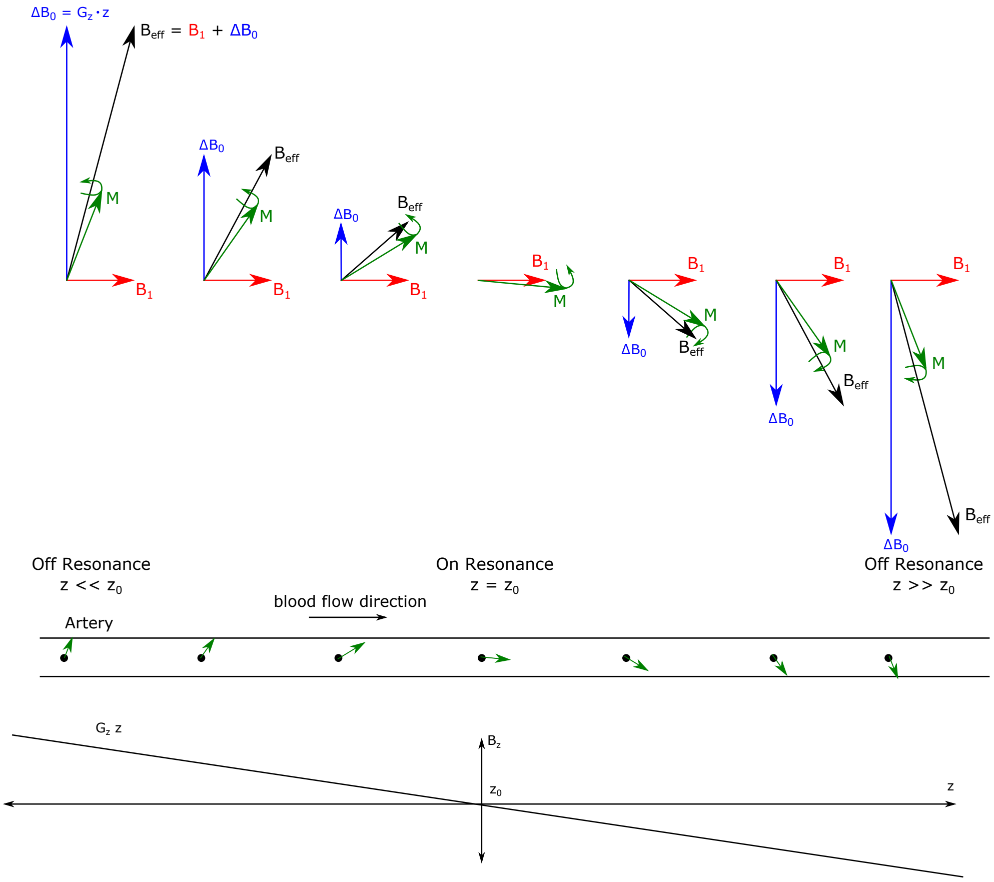

Figure 2.4: Principle of flow driven adiabatic inversion in the reference rotating frame. The RF field B_1 appears constant. The applied gradient along the feeding arteries produces a spatial depended magnetic filed which appears as off-resonance field ΔB_0. The magnetization precesses around the effective field B_{eff}, which is the vector sum of the B_1 and the spatial dependent ΔB_0 field. As the blood spins move along the applied gradient filed the effective field changes from upstream to downstream inverting the blood magnetization.

The continuous labeling over a long period of time allows on the one hand to achieve a steady-state condition of labeled blood in the tissue, thereby increasing the ASL signal but on the other hand produces magnetization transfer effects [66, 300]. Indeed, the long off-resonance pulse saturates bounded protons on macromolecules in the tissue due to their broad resonance frequency. These saturated protons will than exchange its magnetization with that of ”free” water causing a reduction in the free proton magnetization [100]. If the magnetization transfer (MT) effect is only present in the label image, the difference signal would indicate a combination of perfusion and magnetization transfer contrast, leading to an overestimation of CBF [68]. Hence, a control preparation is necessary which produces the same amount of MT contrast but without labeling of the spins [271].

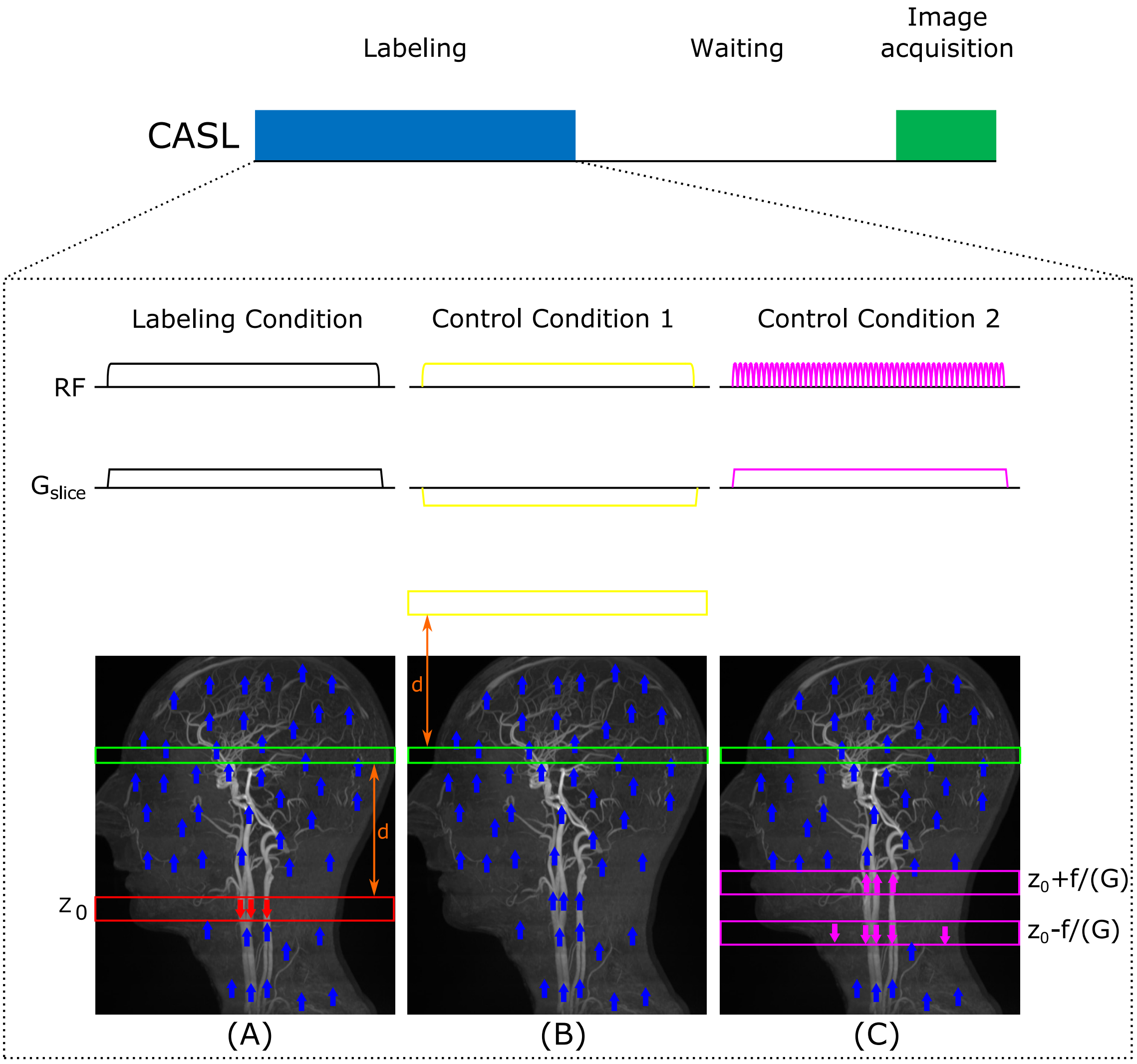

Figure 2.5: Labeling (A) and control (B, C) conditions for a CASL experiment. The control condition 1 can be used for accounting MT effects in single slice acquisition. Control condition 2 uses a double inversion of the inflowing blood to account for MT effects and can therefore be used for multi-slice acquisitions.

Figure 2.5B illustrates the original approach of CASL to control MT effects [300]. To achieve a symmetric off-resonance saturation in control and label image, the inversion plane is shifted with -d outside the brain. This produces the same amount of MT effects but do not alter the inflowing blood, because the inversion plane is located outside the brain.
While this approach works well for single-slice acquisition it is not easy extendable to multi-slice acquisitions, because the long RF pulse is applied concurrently with a gradient and thus renders slice specific MT effects [36]. To mitigate this shortcoming Alsop et al. proposed an amplitude modulated approach [7] (Figure 2.5C). During the control condition the RF pulse with a carrier frequency f_0 is modulated with a sine-wave with frequency f_1 producing two resonances. Thus, the amplitude modulated pulse has two frequency components $f_0 - f_1$ and $f_0 + f_1$ with an offset of $\pm f_1$ from the frequency of the original labeling pulse. Together with the magnetic field gradient the amplitude modulated pulse performs two adiabatic inversions concurrently. Spins flowing through the first resonance gets inverted and they got re-inverted as they flow through the second resonance. In other words, the amplitude modulated RF pulse together with the magnetic field gradient produces two labeling planes with an offset in position of $z = -f_1/(\gamma G)$ and $z = f_1/(\gamma G)$ from the original labeling plane. [7, 271] Both, control and label condition use now the same gradient and RF pulse, exhibiting the same amount of MT contrast and hence enables multi-slice acquisitions. However, the double inversion in the control condition is not ideal and reduces the labeling efficiency by approximately 32% [7]. A more intuitive approach is to use a two-coil setup consisting of a small labeling coil placed in the neck region near the carotid arteries and a second receiving head coil [124, 259, 326]. The spatial range of the produced B_1 field is limited to a localized region around the carotid arteries. Consequently, blood spins in the neck region are successfully inverted but no MT effects are produced in the brain, because the B_1 field does not extend sufficiently far [36]. The second coil is then used for imaging. This approach works well for single and multi-slice acquisition as the control image does not need a MT preparation [236]. In theory this approach is very simple but in practice it requires additional hardware (separate coil and transmit channel) that has to be synchronized with the MRI pulse sequence and wearing an additional neck coil reduces the comfort of subjects [120].

In general, the additional need of specific hardware, the high sensitivity to MT-effects, and the high specific absorption rate (SAR) makes the implementation of CASL for measuring perfusion in human quite challenging. Consequently, CASL has been replaced by another technique called pulsed arterial spin labeling (PASL). [77, 151]

2.4.2 Pulsed Arterial Spin Labeling (PASL)

The basic principle of PASL is shown in Figure 2.6. Instead of applying a continuous RF-pulse, PASL uses a short slab selective adiabatic pulse (typically 10-20 ms) to invert the blood water spins in a broad range of the feeding arteries. The slab is typically 10-15

cm thick resulting in a labeling duration of approximately 0.7 to 1.2 *s* for a healthy subject [308]. However, the exact temporal width of the bolus is unknown and depends on the blood flow velocity, which can be highly different in patients with cerebrovascular disease, or even between different arteries leading to quantification errors in the original approaches [308]. Wong et al. introduced a technique called quantitative imaging of perfusion using a single subtraction (QUIPSS)/quantitative imaging of perfusion using a single subtraction version II (QUIPSS II) [308] to define the temporal width of the bolus in PASL. In QUIPSS II a saturation pulse is applied to the labeling slab at time point TI1 to saturate the inflowing blood during both control and label condition. Thus, the signal contribution after the time TI1 is equal in the control and label condition and cancels out during subtraction. Thereby "cutting" the bolus at a defined temporal width of TI1 across subjects [308]. The principle of this technique is schematically illustrated in Figure 2.6 in pink. An adaptation of QUIPSS II was proposed by the same group one year later, which replaces the slab selective saturation pulse by a train of thin-sliced saturation pulses applied at the distal end of the labeling slab, called QUIPSS II with thin-slice TI1 periodic saturation (Q2TIPS). This smaller pulse is less sensitive to B_1 variations and has a sharper slice profile resulting in an improved bolus width and quantification accuracy [170].
Similar to CASL, the labeling RF pulse produces MT effects, which have to be considered in the control condition. However, this effects are much smaller due to the short pulse duration and can be easily accounted by applying for example an off-resonance RF pulse with the same power during the control condition (Control Condition in Figure 2.6) [304].

Due to its easy implementation, low SAR, and high labeling efficiency ($> 95\%$) [308], many PASL techniques were developed with increasing success in perfusion imaging including: flow-sensitive alternating inversion recovery (FAIR) [144, 152], signal targeting with alternating radio frequency (STAR) [77], proximal inversion with a control for offresonance effects (PICORE) [304], un-inverted flow-sensitive alternating inversion recovery (UNFAIR) [118], unprepared basis and selective inversion (BASE) [226], flow-sensitive alternation inversion recovery excluding radiation damping (FAIRER1) [331], flow-sensitive alternation inversion recovery with an extra radio frequency pulse (FAIRER2) [174], double inversions with proximal labeling of both tag and control images (DIPLOMA) [136], transfer insensitive labeling technique (TILT) [102], quantitative star labeling of arterial regions (QUASAR) [200], and pulsed star labeling of arterial regions (PULSAR) [101]. To give an complete overview of all available techniques is out of scope of this thesis, but the interested reader is referred to [14, 15]. In the following section the three major types of PASL (STAR, PICORE, FAIR) [6] are presented. Their basic principles are shown in Figure 2.7.

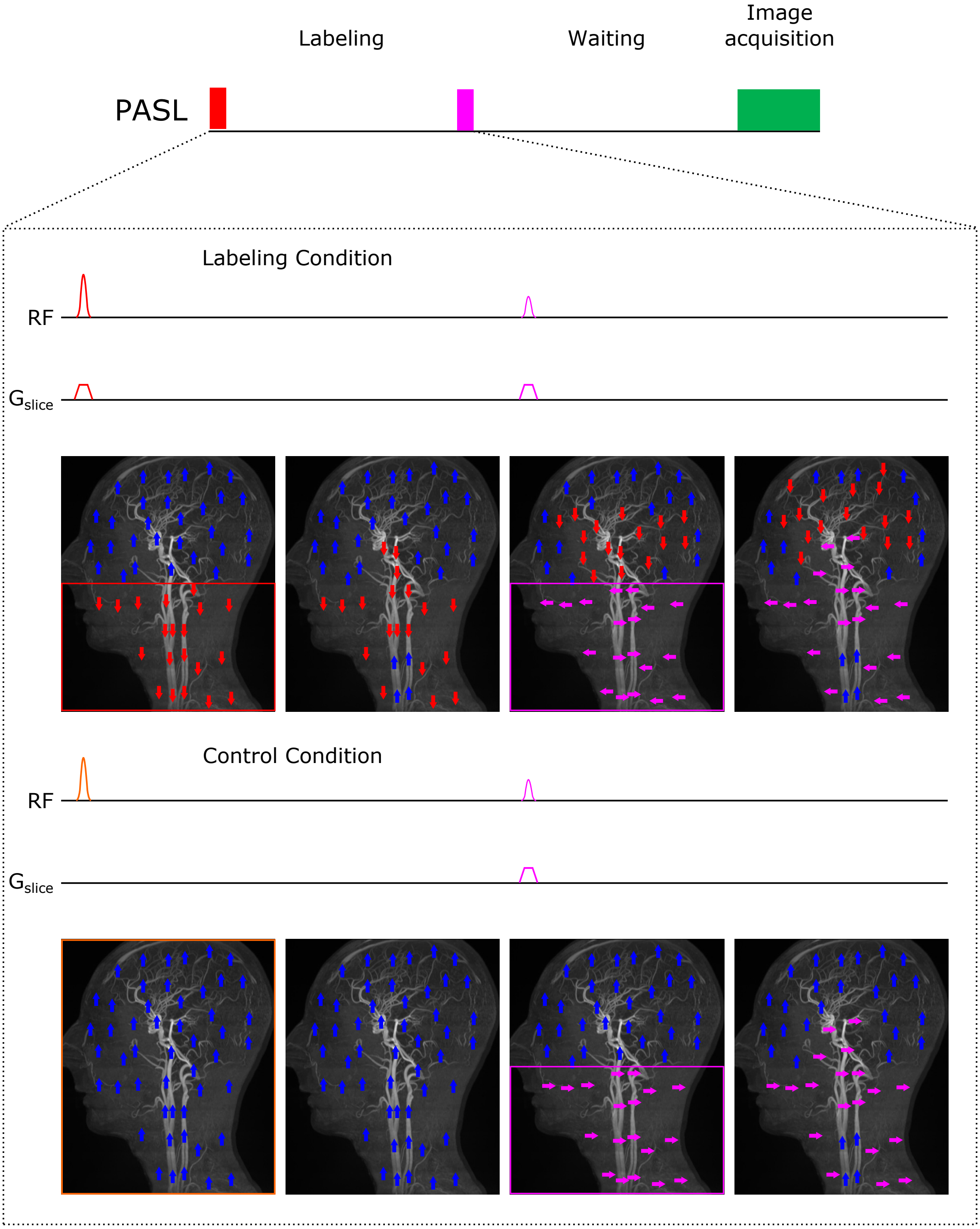

Figure 2.6: Basic principle of PASL with QUIPSS II (pink colour) to control the bolus width. After a predefined time interval $TI1$, a slab selective saturation pulse is applied in the control and label condition. Both, labeled and unlabeled blood spin are saturated producing the same amount of signal in the images. Thus, the labeled bolus is "cutted" at the time point $TI1$.

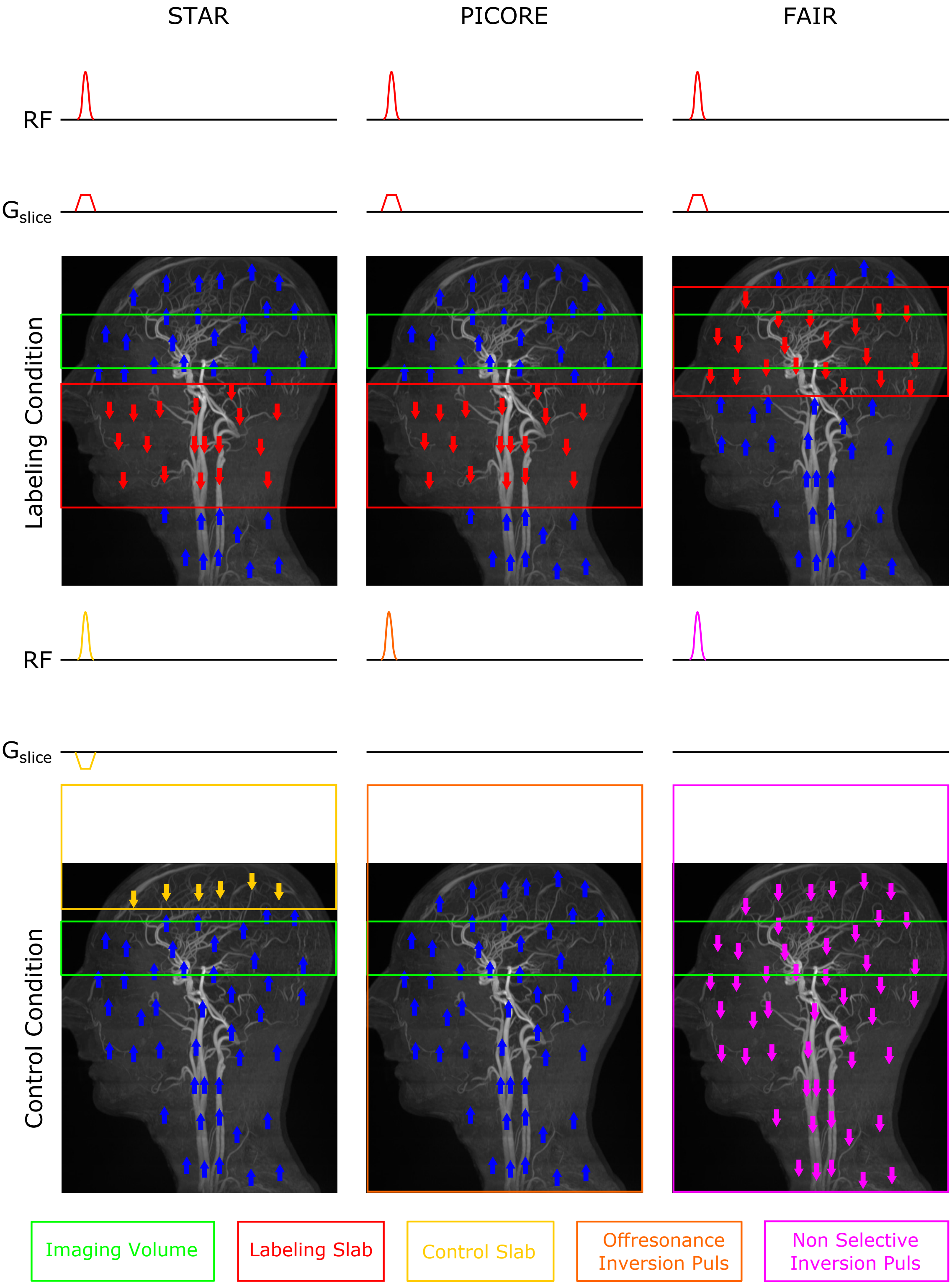

Figure 2.7: Basic principle of the three major PASL techniques.

2.4.2.1 Signal Targeting with Alternating Radio Frequency (STAR)

STAR was the first implementation of PASL [77] (Figure 2.7). It was originally combined with an echoplanar imaging (EPI) readout and thus it is often referred as echoplanar imaging and signal targeting with alternating radio frequency (EPISTAR) in the literature. In STAR the arterial blood is inverted in an area proximal to the imaging region using a short slab selective adiabatic inversion pulse [35, 77]. This RF pulse inverts the inflowing blood but produces additional MT contrast in the label image. Similar to CASL in the control condition the same RF pulse is applied but with negative gradient to account for the MT effect. In case of symmetric MT effects on either side of the imaging region the MT contrast cancels out during the subtraction. Indeed, the inversion labels the spins above the imaging region leading to potential venous contamination if the inversion slab lies within the brain. In addition, the MT effects are only minimized for a single slice [14, 77]. Edelemann and Chen [76] proposed a modified version of STAR to account for MT contrast in multi-slice imaging and potential contamination of inflowing blood inferior to the imaging slice in the control condition. In this updated version, the control condition consists of two slab-selective adiabatic inversion pulses, which are immediately applied to the labeling region. This double inversion leads to no net labeling of the blood spins. In practice, the double inversion is not perfect because some fast spins have already left the labeling slab and spins on the boarder of the labeling slab do not experience full inversion due to imperfect slab profiles [14, 76]. This effects results in quantification errors of the CBF and consequently leads to the development of another technique called PICORE [304].

2.4.2.2 Proximal Inversion with a Control for Offresonance Effects (PICORE)

PICORE is a modification of the original STAR technique (Figure 2.7). It uses the same labeling condition as STAR, inverting the blood in a slab proximal to the imaging slice [304]. In the control condition the RF pulse is applied without a field gradient and the frequency of the RF pulse is additionally shifted so that the imagine plane experience the same off-resonance as in the labeling condition. This ensures equal MT effects for control and label images. Since the RF pulse is non-selective, this technique takes advantage that no inversion of the spins occurs distal to the imaging plane avoiding potential venous inflow. [35, 304]

2.4.2.3 Flow-Sensitive Alternating Inversion Recovery (FAIR)

FAIR was independently developed by Kwong et al. [152] and Kim et al. [144] shortly after STAR (Figure 2.7). In contrast to STAR and PICORE, the labeling is applied symmetrically with respect to the imaging volume and creates positive perfusion contrast (label image has a higher signal than the control image). The symmetric nature of this technique automatically corrects for the MT contrast in the PWI. In the labeling condition a slice, or slab selective inversion pulse is applied to the imaging region. This inverts the blood and tissue spins within the imaging region but leaves the inflowing blood spins unchanged. The control condition uses the same, but non-selective inversion pulse leading to a global inversion of the tissue and blood spins within the range of the RF-transmit coil. Consequently, inflowing blood from both sites of the imaging slice gets labeled. If both RF pulses perfectly invert the spins in the imaging region, the signal from the static tissue is equal and cancels out in the difference image. Hence, the difference image contains only information from the inflowing labeled blood. Due to the positive perfusion contrast, the PWI is achieved by subtraction the control image from the label image, which is different to other PASL and CASL techniques. In practice, the slice selective inversion pulse dose not produce a perfect inversion over the whole region, because the slice-profile is not perfectly rectangular. Thus, in a typical FAIR experiment the spatial width of the slice-selective pulse is twice the width of the imaging slab so that the uniform center of the pulse covers the whole imaging slice. [35, 144]

2.4.3 Pseudo-Continous ASL (pCASL)

Pseudo continous arterial spin labeling (pCASL) is a hybrid labeling method combining the advantages of PASL and CASL and therefore provides a better balance between SNR and tagging efficiency [312]. PCASL was introduced by Dai et al. [56] and Wu et al. [312] and mimics the flow driven adiabatic inversion effect of CASL in a piecewise manner (Figure 2.8). A train of short and equally spaced RF pulses in combination with a gradient field along the direction of blood flow inverts the blood spins. Compared to CASL, the RF duty cycle and the SAR are reduced, and an application on standard MRI scanner without the need of additional hardware is possible [6]. Splitting up the long constant rectangular RF pulse in short successive rectangular pulses leads to additional periodic labeling planes at locations z governed by the spacing of the RF pulses Δt, and the gradient strength G ($z = n/\gamma G \Delta t$) [56]. To suppress the aliased labeling planes, typically a Hanning-shaped pulse in combination with strong gradients during the RF pulse, typically 10 times stronger than for CASL, are applied. This makes the RF pulse spatially more selective and suppresses the aliased planes well, noting that the position of the aliased labeling planes are dependent on the mean gradient G_{aver} ($z = 1/\gamma G_{aver} \delta$). In general, aliased labeling planes are well suppressed if the following condition is met: [56]

$$\frac{G_{max}}{G_{aver}} >> \frac{\Delta t}{\delta} \ , \tag{2.3}$$

where G_{max} is the amplitude of the gradient during the RF pulse, G_{aver} is the average gradient between the center of two successive RF pulses, Δt is the time interval between two RF pulses, and δ is the pulse duration (Figure 2.8). The train of RF pulses generates a pulsed steady stead with an average B_1 field comparable to CASL. During the RF gaps gradient rewinders are used to keep the averaged gradient amplitude low and comparable to CASL (approximately 1 mT/m), ensuring that the adiabatic conditions are met

(Figure 2.8). The net average gradient leads to a phase accumulation of the flowing spins between successive RF pulses. To match the phase evolution, a phase increment of $\Delta\phi = \gamma G_{aver} \Delta z \Delta t$ has to be applied to each following pulse, where Δz is the labeling slice offset from the isocenter [8]. Once the label image has been acquired, a carefully designed control condition is necessary to eliminate residual MT errors. The application of the strong gradient during the RF-pulse train has the advantages that the MT effect is much smaller compared to CASL, because the RF pulse becomes further off-resonant relative to the imaging region [6]. The control condition can be implemented as balanced pCASL [305, 312] or unbalanced pCASL [56] (Figure 2.8). In balanced pCASL the same gradients as for labeling are used but every subsequent RF pulse maintains a 180° phase shift. This is achieved by alternating the sign of subsequent RF-pulses leading to an average B_1 of zero and no effective labeling of the blood spins, while maintaining the same averaged RF power as in the label condition. [56]
In unbalanced pCASL (Figure 2.8) the gradient waveforms are different between label and control condition. Here the term unbalanced might be confusing since the gradients and the RF in the control condition are fully balanced similar to a balanced steady state free precession (bSSFP). The balanced gradients in the control condition eliminate the labeling effect while keeping the same RF power as in the label condition. [312]

In general, the balanced gradients in the control and label condition better matches possible eddy current related artifacts i.e. Wu et al. observed a shift in phase encoding direction between control and label images [312] for the unbalanced case. This might results in subtraction and quantification errors. On the other hand, the unbalanced approach is less sensitivity to off-resonance effects resulting in higher labeling efficiencies [14, 312]. Due to the lower sensitivity to off-resonance effects the unbalanced method is the recommended approach for pCASL experiments [8, 312]. In contrast to CASL the well matched control condition for multi-slice imaging lead to a higher labeling efficiency for pCASL [312].

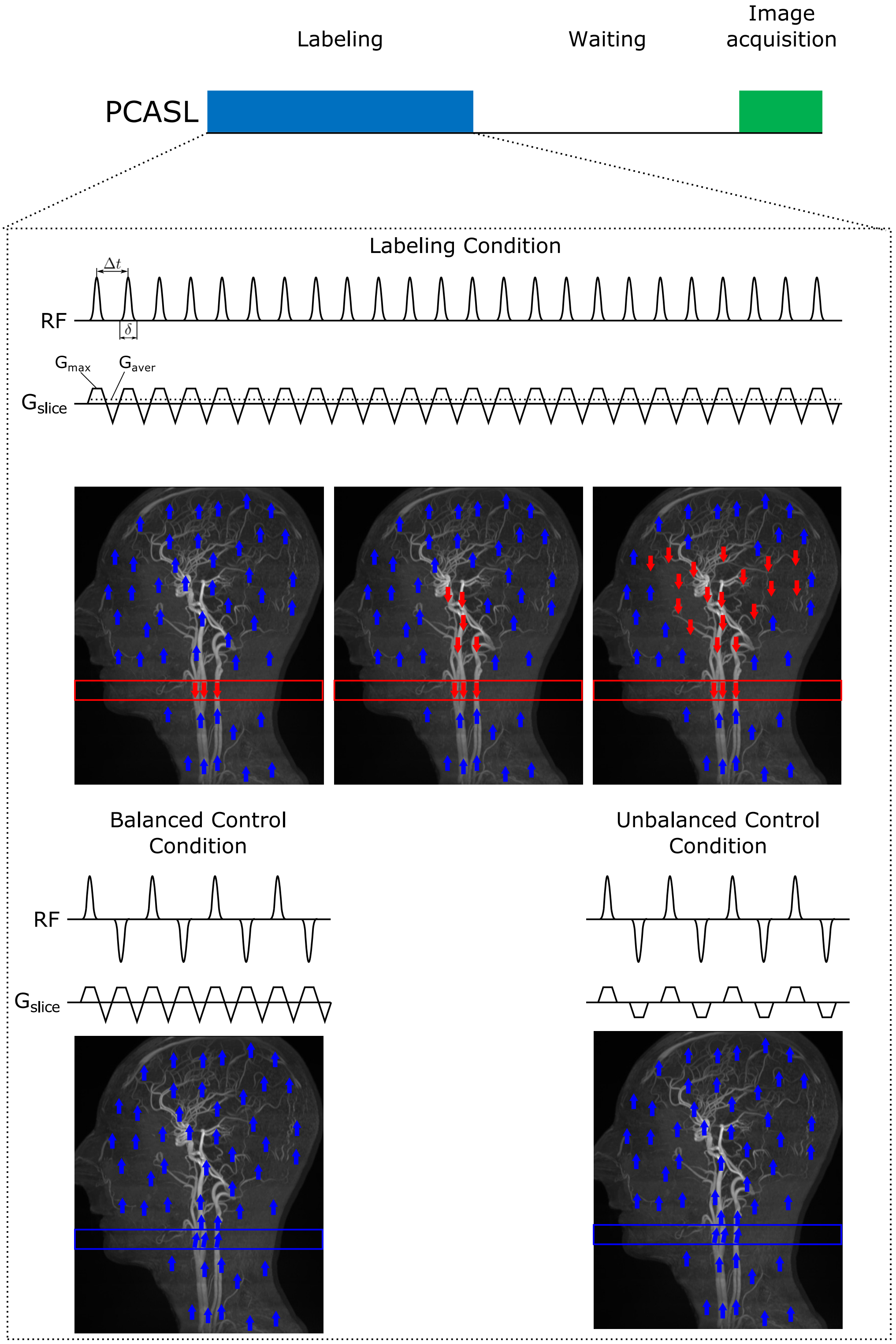

Figure 2.8: Basic principle of pCASL. The combination of short RF pulses with an average gradient along the feeding arteries, leads to a flow driven adiabatic inversion of the blood spin. During the control conditions the same RF power is applied to match MT contrast between control and label condition.

2.4.4 Comparison of pCASL and PASL

In PASL a single adiabatic pulse creates the entire bolus in a few milliseconds, which is very robust to field inhomogeneities [8]. Additionally, it is relative insensitive to blood velocity due to the short pulse duration. The labeling efficiency varies by less than 1% for a velocity range of 0-100 cm/s [308]. It has a very low power deposition, which is especially beneficial for higher field strength. In contrast, pCASL relies on the principle of flow-driven adiabatic inversion and thus is more prone to B_0 inhomogeneities in the labeling plane. In addition, it is highly dependent on the blood velocity resulting typically in a lower labeling efficiency of 85% compared with PASL with 98% [8]. Although the labeling efficiency is higher in PASL, the overall SNR in much lower compared with pCASL. This occurs for two reasons: First, pCASL continuously labels the inflowing blood resulting in a much longer bolus duration with a higher SNR. In PASL the bolus duration is limited by the spatial coverage of the RF-transmit coil leading to an overall reduced SNR [6]. Second, the T_1-decay of the bolus is higher for PASL, because of the large labeling slab some labeled blood is further away from the imaging region. Thus, the bolus is decaying with T_1 before it leaves the distal end of the labeling region leading to a reduced SNR. A direct comparison of PASL and pCASL is shown in Figure 2.9. In summary, the high SNR efficiency (50% improvement compared to PASL) [312], the improved repeatability [48], the well defined bolus duration and the sharp bolus makes pCASL the recommended labeling approach for ASL [8].

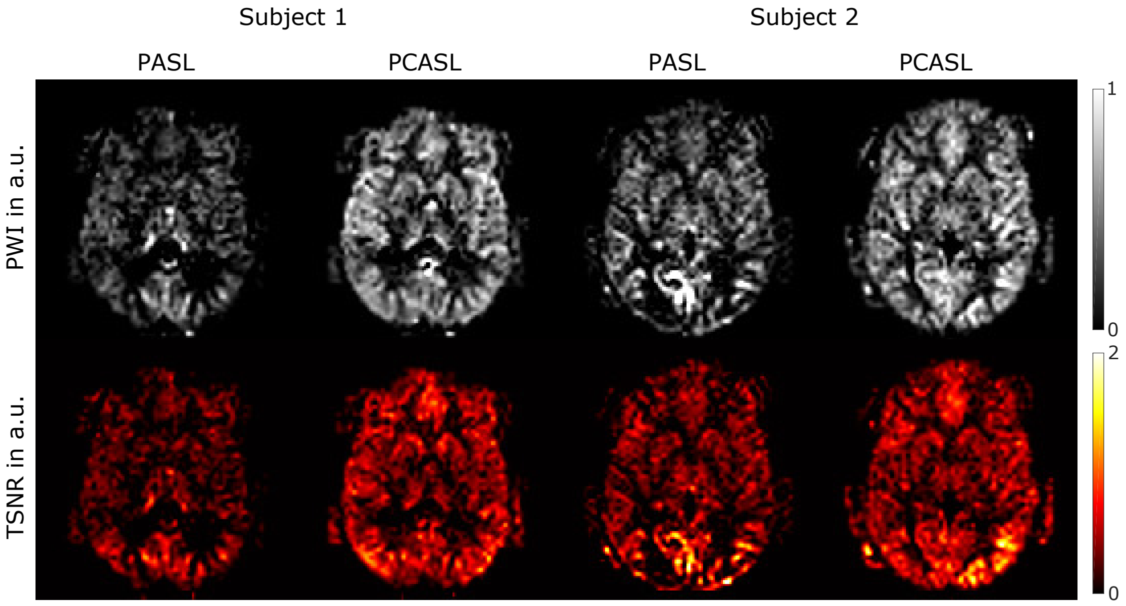

Figure 2.9: Direct comparison of PASL and pCASL using the recommended parameters from the International Society for Magnetic Resonance in Medicine (ISMRM) consortium and perfusion study group [8].

2.5 Labeling Duration and Waiting

After the arterial blood water has been labeled, the bolus needs some time to travel from the labeling plane to the capillaries, where they exchange with the tissue water. Hence, a waiting period called PLD is introduced between labeling and imaging acquisition. The definition of the labeling duration and PLD is slightly different between ASL techniques. Figure 2.10 shows the timing diagram for pCASL and PASL acquisitions. In PASL the bolus is immediately created and the labeled spins travel to the tissue of interest during the time period TI. As previously described, techniques such as QUIPSS II are necessary to achieve a well-defined bolus width. The start of the QUIPSS II block defines the bolus duration TI1, which is analogues to the labeling duration (LD) in CASL/pCASL. The effective waiting period in PASL is then defined as (TI - TI1). This is equal to the definition of PLD in CASL/pCASL. [8, 45]

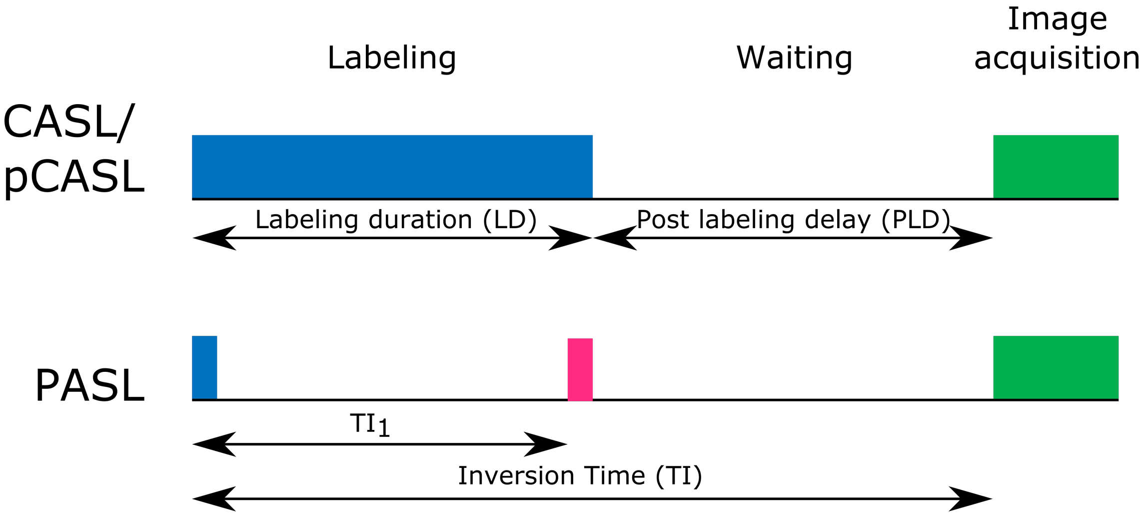

Figure 2.10: Schematic timing diagram for the three major parts of an ASL experiment. The blue block refers to the labeling period, the pink block in PASL refers to QUIPSS II, and the green block to the readout.

The labeling duration depends on the used labeling technique. In general, a high labeling duration is beneficial as this accumulates the tracer in the capillary bed of the measured organ and translates directly in an increased SNR [45]. For pulsed ASL the labeling duration is limited to the spatial coverage of the transmit RF coil and is typically less than 1 s [8, 308]. Hence, the consensus paper recommends a LD of 0.8 s for PASL [8]. The CASL or pCASL approach provides the possibility to label the blood over seconds to create a long sharp bolus. However, the T_1-relaxation of blood, which is 1.65 s at 3T [169], limits the labeling time to a certain extend. For those approaches the consensus paper recommends a labeling duration of 1.8 s, which provides a good trade of between bolus duration and tracer decay [8]. Different studies suggest that an even longer labeling duration of up to 3 seconds can be very beneficial and improves the reliability of the CBF-maps for patients with cerebrovascular disease such as moya-moya [81].

Similar to the labeling duration the post labeling delay is always a compromise. On the one hand a long PLD gives the tracer sufficient time to travel to the capillary bed, maximizing the ASL signal and avoid miss-quantification in CBF. On the other hand, the tracer exponentially-decays during the waiting period with a time constant T_1 of the residing compartment (mostly in the arterial blood compartment with a T_1 of 1.65 s at 3T [169]). The influence of the PLD on the ASL signal is illustrated in Figure 2.11. For a too long waiting period the ASL signal is very small and dominated by noise. If the PLD is too short an angiogram is obtained showing the major vessels in the brain. Therefore, the optimal PLD would be equal or slightly higher than the expected arterial transit time (ATT). The ATT refers to the time it takes for the labeled spins to go from the labeling plane to the tissue of interest. For healthy subjects the ATT is typically in the rang of 1.5 s for young and 2.0 s for old subjects [8, 165]. This advises a PLD of 1.5 s for children, 1.8 s for subjects $<$ 70 years, and 2 s for subjects $>$ 70 years [8]. Especially for clinical applications, where the presence of long ATT is very likely, a careful setting or combination of LD and PLD [8, 320] is very important. For example Fan et al. compared ASL with PET measurements for moya-moya patients. He found a higher correlation between those techniques using a long LD of 3 s and a PLD of 4 s, than using the recommended settings from the consensus paper [81].

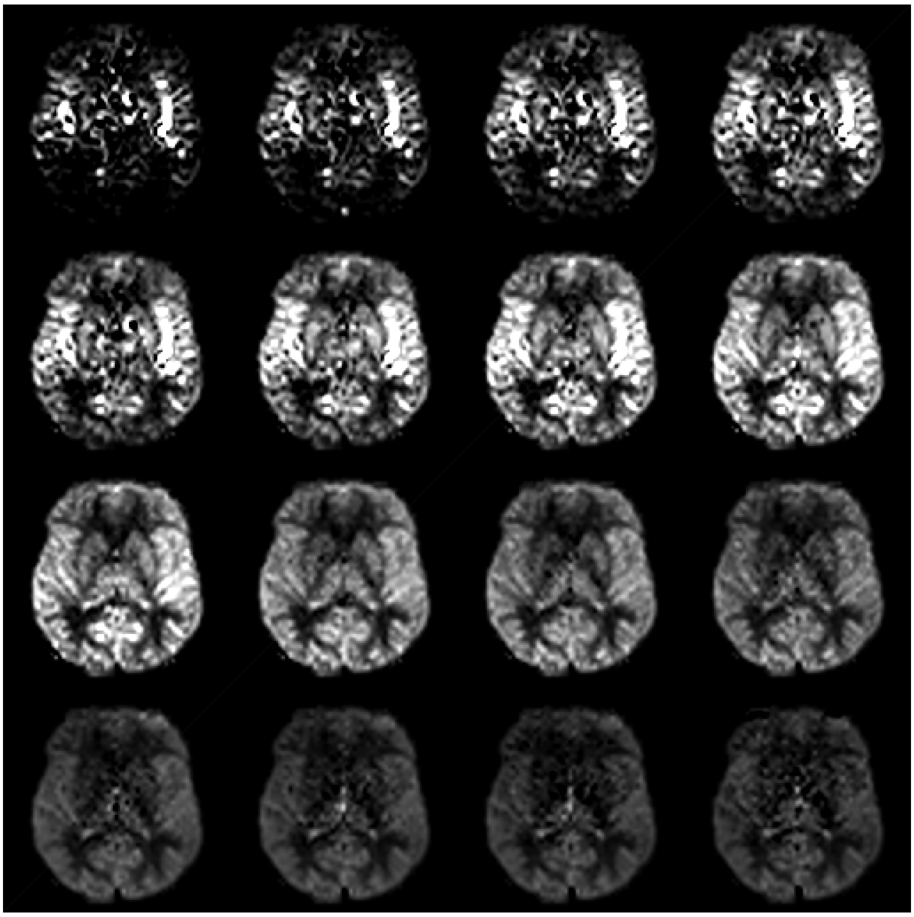

Figure 2.11: PWI at 16 different PLDs using pCASL labeling with a labeling duration of 1800 *ms*. PLD increases (200 *ms*) from left to right and top to bottom, starting with a PLD of 0 *ms*.

2.5.1 Single vs Multi Post Labeling Delay

The recommended clinical ASL protocol uses a single labeling duration and post labeling delay because it is easy to implement and allows to boost the SNR by repeating the measurements [8, 45]. As previously mentioned, two main limitation of single PLD acquisition exists: First the CBF is underestimated in areas where the ATT of the blood is higher than the selected PLD; And second for a too short PLD, or for subjects with prolonged ATT, hyper-perfusion areas are visible. These areas are related to the presence of labeled blood in the vessels, known as vascular artifacts. These vascular artifacts complicate clinical diagnosis in patients with stroke, steno-occlusions of moya-mayo disease [320]. For such cases, the right choice of the PLD is very important to increase the reliability of the CBF-map. In general, the PLD should be longer as the expected ATT in the imaged tissue. In practice, the right choice of the PLD is difficult, because the ATT is not known in advance and varies between healthy subjects and even in patients with the same vascular disease. Alternatively, the ASL signal can be sampled over time, acquiring several images with different PLDs. Typically from a short PLD to a long PLD. By applying a kinetic model to the time series the potential bias in CBF due to unknown ATT can be reduced [8, 34]. In addition, the ATT, another important parameter can be estimated simultaneously (see section 2.8). The ATT can reveal additionally clinical relevant information i.e. distinguishing between a real hypoperfusion and an artificial created hypoperfusion due to prolonged ATT, or identification of boarderzone sign and collateral flow [320]. However, the higher number of PLDs leads to an increase acquisition time. Furthermore, for longer PLDs the SNR decreases due to the T_1-relaxation of blood and the increased repetition time, allowing to acquire a lower number of averages in the same acquisition time. In a time matched acquisition this can lead to a higher bias and error in CBF compared with single-PLD acquisitions [311]. Woods et al. proposed a framework to optimize the multi-PLD protocol for different readout schemes and expected ATT ranges to improve the reliability of CBF and ATT maps [311]. Another approach uses a short low resolution prescan to estimate the expected ATT and adapts the protocol specific to the patients [58]. A smart way to boost the SNR of multi-PLD acquisitions was recently proposed by Guenther et al. [108], called time-encoded ASL, and will be described in section 2.9.3 "Time Encoded ASL".

2.6 Readout Approaches

The third and last block of an ASL experiment is the image acquisition. The first implementation of ASL used a simple two-dimensional spin echo sequence [66]. In this proof of principle study only one single-slice were acquired. It soon became clear that fast imaging techniques are necessary to achieve a good SNR in an acceptable acquisition time. The first fast imaging technique used for ASL imaging in the human brain was EPI [77]. In principle any developed readout technique for MRI is applicable for ASL imaging. The following section describes three most widely used techniques for ASL imaging. These readout approaches are also recommended in the consensus paper [8].

2.6.1 2D Readout Approaches

2.6.1.1 2D - Echo Planar Imaging (EPI)

Multi-slice EPI is one of the most common readout approaches in neuroimaging, in particular for functional magnetic resonance imaging (fMRI), diffusion, and perfusion imaging. It was originally developed by Peter Mansfield in the early eighties [181]. With this snap-shot technique a complete two dimensional image can be acquired within 20-50 ms [20]. The sequence diagram is shown in Figure 2.12. A slice selective excitation pulse (usually 90°) is used to create a free induction decay (FID). The readout (G_{read}) and phase-encoding gradient (G_{phase}) starts with a prephasing gradient causing a phase dispersion of the transverse magnetization. Both prephasing gradients position the k-space trajectory at k_{min} in x and y direction (red point in Figure 2.12). Immediately afterwards, a readout gradient (blue) with different polarity is applied. This causes the spins to partially rephase producing a gradient echo. During this readout gradient the kspace line traversing from -$k_{x,min}$ to $k_{x,max}$ is acquired. The vertical location of the trajectory is modified by applying small phase-encoding gradients (green), known as gradient blips, in between the readout gradients. The followed negative readout gradient (pink) creates a second gradient echo which is acquired while traversing back through the k-space. [20] This process is repeated until the full k-space is acquired. Typically EPI is applied as a multi-slice acquisition and subsequent slices are acquired by repeating the the whole procedure again. For multi-slice ASL imaging, an ascending slice order is recommended as the blood flows from the neck to the brain leading to prolonged ATT for superior slices. Note that this acquisition order prolongs the PLDs for subsequent slices. [8]

While EPI is a very effective imaging method, it does suffer from several artifacts. The T_2^* signal decay during acquisition results in an exponential filtering of the k-space along the phase encoding direction causing blurring in the image space. However, the blurring is not very significant if the acquisition time is small or comparable to the T_2^* decay constant of the tissue, because the windowing function is asymmetric around the k-space. Meaning that high negative frequency components at location $k_{y,min}$ are enhanced compared with the signal at the center k-space (k_0), partially offsetting the diminished positive frequency components at $k_{y,max}$. [35]

In addition to blurring, the narrow bandwidth in the phase encoding direction causes prominent chemical shift artifacts in EPI images. Fat signal arising from the skull marrow or the scalp is shifted in the phase encoding direction [35]. Chemical shift artifacts can be reduced using fat saturation pulses applied immediately before the readout.

One of the most prominent artifacts in EPI is Nyquist ghosting [20, 298]. Nyquist ghosts appear as N/2 shifts of the image in the phase encoding direction and are caused by timing differences between even and odd echos. The even and odd echos are formed by different gradient polarity which are mostly not perfectly balanced due to eddy currents. The eddy currents produces magnetic fields, which in turn delays or advances the time of refocusing. [20, 35] Nyquist ghost are routinely minimized using the reference line approach [115].

Another typical artifacts in EPI are distortions and signal dropouts in the images due to B_0-field inhomogeneities. The field inhomogeneities causes an additional phase offset, consequently leading to errors in the spatial encoding. This miss localization accompanies a displacement in the reconstructed image [35]. The geometric distortions are proportional to the field of view (FoV) in phase encoding direction, echo-spacing, and the B_0 inhomogeneities [20]. Thus, a higher bandwidth, parallel imaging, or advanced shimming techniques can help to reduce the amount of distortions. In addition, field maps can be acquired and used in a post-processing step to minimize the distortions [322]. In addition to distortions, areas of high susceptibility changes such as tissue-air interfaces (sinus cavities) can cause signal dropout in gradient-echo based EPI [35]. The signal dropout can be eliminated by using a spin-echo based EPI sequence. However, this prolongs the readout time and is thus typically not recommended for ASL imaging [45].

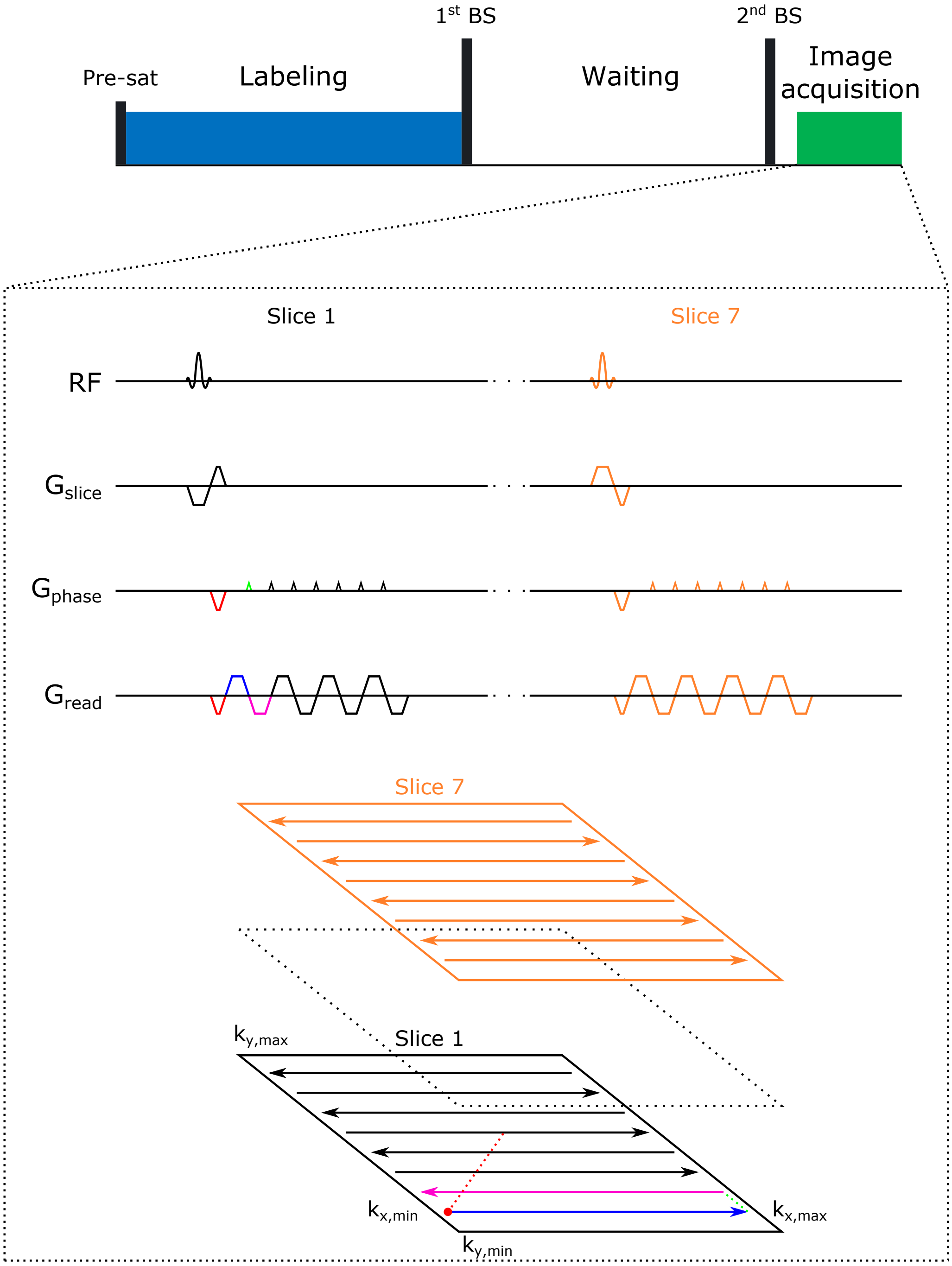

Figure 2.12: Sequence diagram for a multi-slice 2D-EPI readout and corresponding k-space trajectory. Consisting of a slice-selective excitation, followed by pre-phasing gradients (red) and a train of bi-polar readout gradients (first blue, second pink) with small phase blips (first green) during the readout gradient switching.

2.6.2 3D Readout Approaches

2.6.2.1 3D - Gradient and Spin Echo (GRASE)

The gradient and spin echo (GRASE) sequence is a hybrid method combining a rapid acquisition with relaxation enhancement (RARE) with an EPI readout. It was proposed by Oshia and Feinberg [194] as a fast 2D readout alternative to EPI. In their original work the full k-space was acquired by alternating refocusing pulses and short EPI-trains. So, during each spin-echo a short number of gradient echos are created, minimizing the off-resonance effects compared with EPI. Since ASL is a low SNR technique, the original 2D readout was extended to 3D, including a slab selective excitation in combination with a second phase encoding direction. The larger slab contains a higher number of protons which increases the SNR [109]. Figure 2.15 shows the pulse diagram for the 3D GRASE readout. A slab selective excitation pulse (usually 90°) is applied to create a transverse magnetization. After TE/2 a refocusing pulse is applied to form a spin echo at time point TE. Right before and after the refocusing pulse, additional crusher gradients (blue) are used to spoil the FID. During the spin echo an EPI readout is applied, producing a train of gradient echos thereby acquiring one kspace partition. Before the next refocusing pulse is applied all gradients are fully balanced. The second partition is acquired by applying again a refocusing pulse followed by an EPI readout. It becomes clear that the total number of echos is given by the number of created spin-echos multiplied by the number of gradient echos. Typically a center out acquisition ordering is used to achieve higher SNR, meaning during the first spin echo the center partition ($k_z = 0$) is acquired, followed by a zig-zag acquisition of the subsequent partitions (+1/-1/+2/-2 etc.). [20, 194]

The 3D GRASE readout has inherently the same problems as the previous described EPI acquisition. In addition, the longer echo train length leads to an exponential filtering of the k-space along the second phase encoding direction leading to blurring in the image space. The amount of blurring depends on the k-space acquisition order and echo train length. This effect is illustrated in Figure 2.14 for 3 different echo train length. The amount of blurring and the sensitivity to off-resonance effects can be reduced by using segmented acquisitions as recommended by the consensus paper [8]. In addition, variable flip angle approaches [162], parallel imaging techniques [73], or deblurring methods [94] were proposed to account for this effect and will be discussed in more detail in chapter 7.

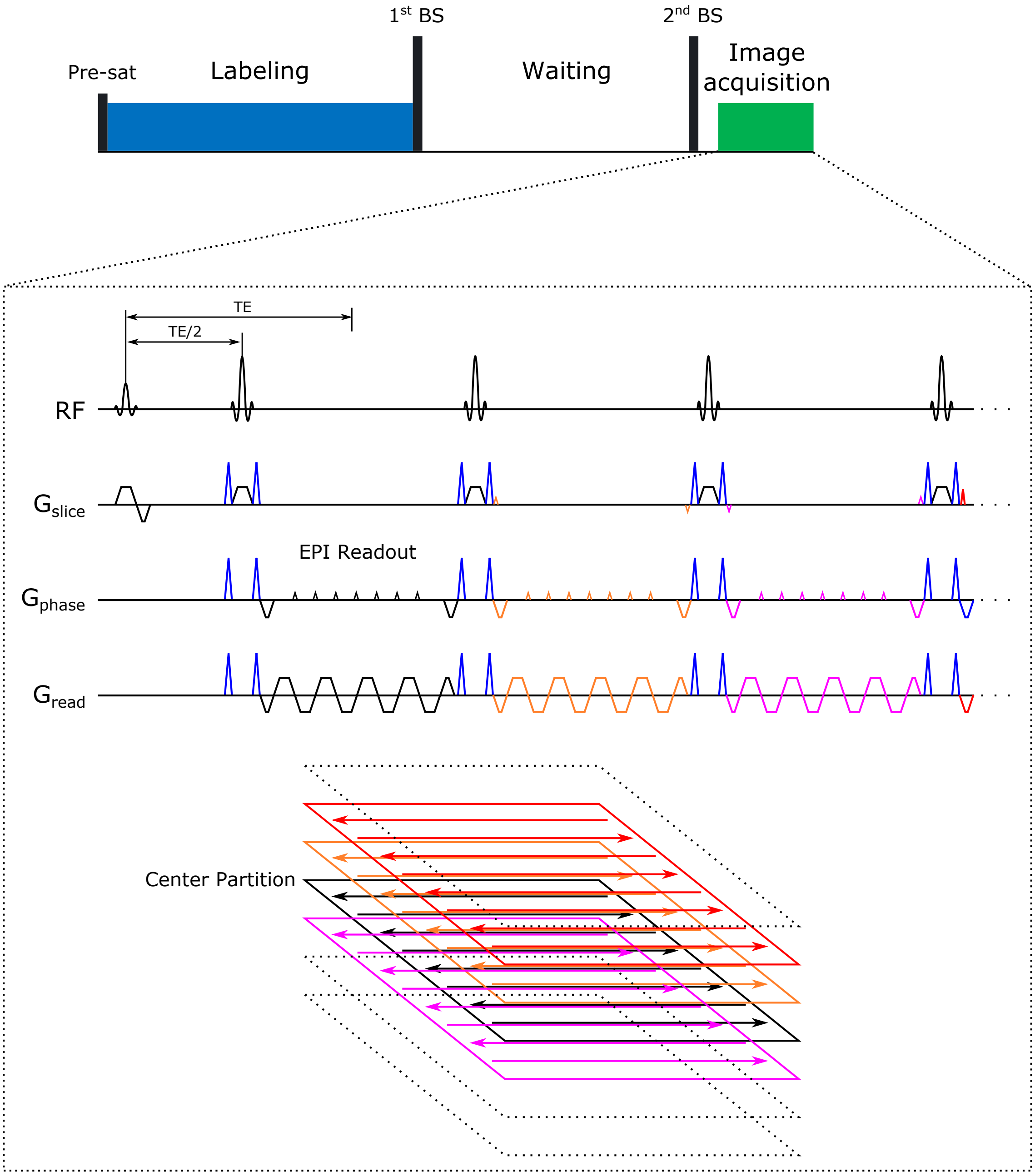

Figure 2.13: Sequence diagram for a 3D-GRASE readout and corresponding k-space trajectory. During each spin echo one k_z plane is acquired using an EPI readout. Crusher gradients (blue) are applied to spoil the FID and gradients are fully balanced between successive RF refocusing pulses.

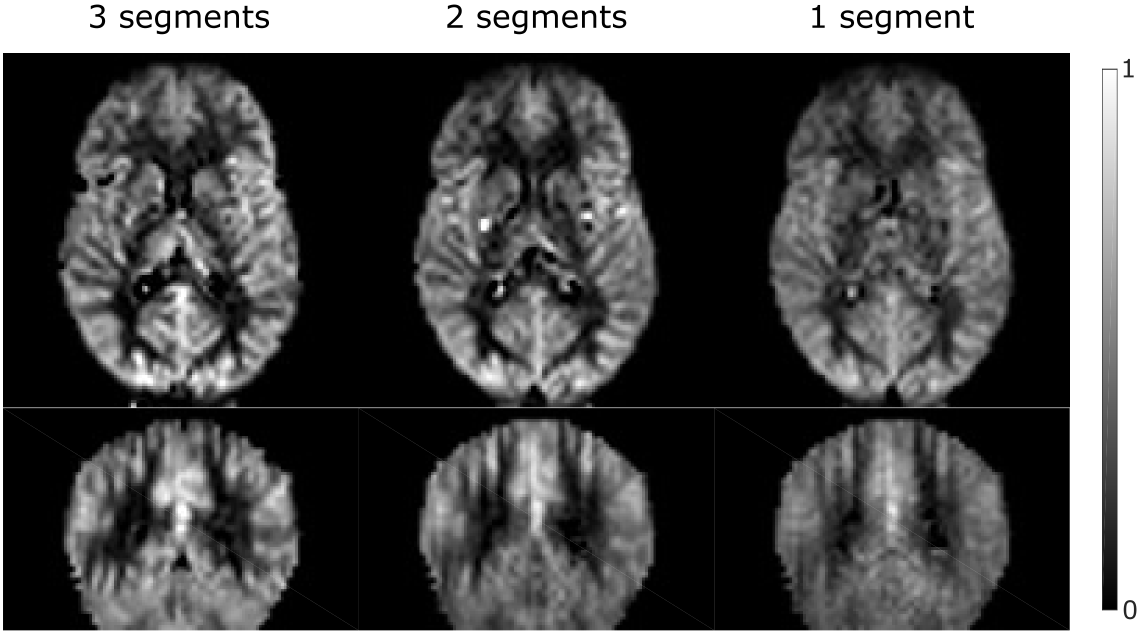

Figure 2.14: Influence of echo train length on the CBF-maps. Echo-train length (segments) from left to right: 270 *ms* (3), 405 *ms* (2) and 810 *ms* (1). A longer echo train leads to a broader point spread function (PSF) accompanied by a stronger blurring.

2.6.2.2 3D - Rapid Acquisition with Relaxation Enhancement Stack of Spirals

3D RARE-stack of spirals (SoSP) is another technique for acquiring a whole volume within a single shot [133, 283]. It is based on the same principle as the GRASE acquisition but replaces the EPI readout with a spiral readout in between the refocusing pulses. Figure 2.15 shows the pulse diagram of the RARE-SoSP acquisition. A slab selective excitation pulse followed by a refocusing pulse is applied to generate a spin echo. Again, before and after the refocusing pulse crusher gradients (blue) are used to spoil the FID. During the spin echo a spiral trajectory is acquired. This is achieved by modulating the amplitude of the sinusoid phase and readout gradient. At the beginning of the readout both gradients are zero, hence the spiral trajectory starts at the k-space center. As the readout progresses, the amplitude of the gradient increases until the maximum k-space radius is reached. Then, rewinding gradients are used to bring the trajectory back to the k-space center. [20] The missing phase encoding steps leads to a much faster readout compared with EPI, thereby reducing the echo time and potentially signal dropout artifacts. However, B_0 inhomogeneities leads to blurring in the images, which is difficult to correct in postprocessing. [45] In addition, advanced reconstruction methods are necessary for obtaining the image from the non-Cartesian trajectory [14]. A detailed comparison of 3D RARE-SoSP with 3D GRASE is given in Vidorreta et al. [281]. The authors conclude that the 3D-RARE-SoSP outperforms 3D-GRASE due to higher spatial and temporal SNR and reduced through plane blurring due to its shorter effective echo time. However, these

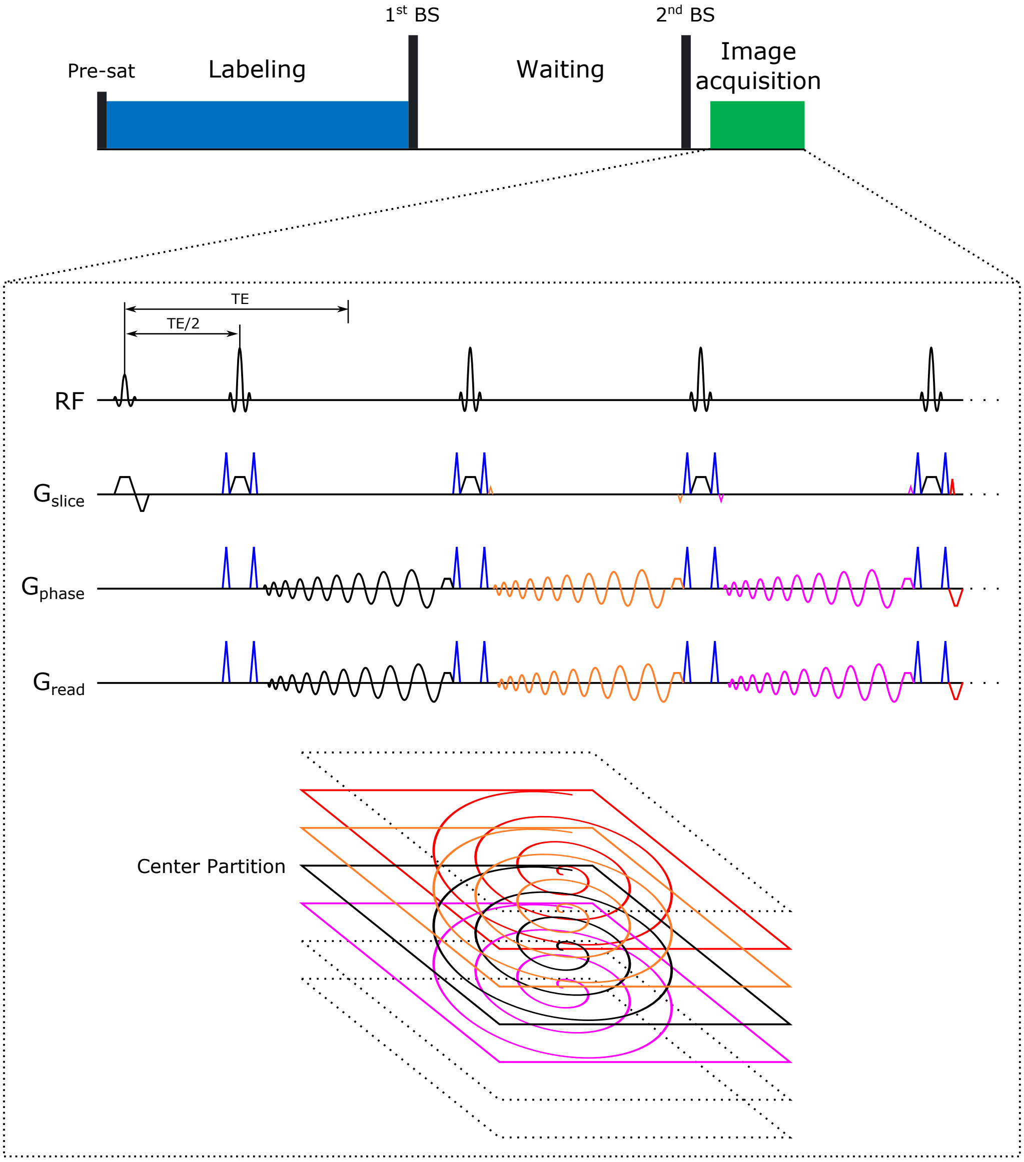

Figure 2.15: Sequence diagram for a 3D-RARE-SoSP readout and corresponding k-space trajectory. During each spin echo one k_z plane is acquired using a spiral readout. Crusher gradients (blue) are applied to spoil the FID and gradients are fully balanced between successive RF pulses.

advantages comes at the cost of slightly increased in-plane blurring due to off-resonances and missing sampling of high frequency components [8, 281]. Note that we described an equally spaced spiral readout. Modifications such as variable density spiral readout [43] exists, which provides higher SNR and additionally allows to extract motion information from the dense sampled k-space center between averages [257].

2.6.3 2D vs 3D Readout

As previously mentioned 2D and 3D readouts have its own advantages and disadvantages. The consensus paper recommends segmented 3D readouts, either GRASE or RARE-SoSP [8]. The 3D readouts provides a higher SNR and allows efficient background suppression of the static tissue (see section 2.7) compared with 2D readouts. This increases the spatial and temporal SNR, resulting in a higher image quality. However, segmented readouts are prone to motion-artifacts and if excessive motion is expected a fast 2D acquisition is preferable [8]. Figure 2.16 shows the typically image quality of a CBF-map acquired with a 2D-EPI and a 3D-GRASE readout. The acquisition time was kept constant with 5 minutes.

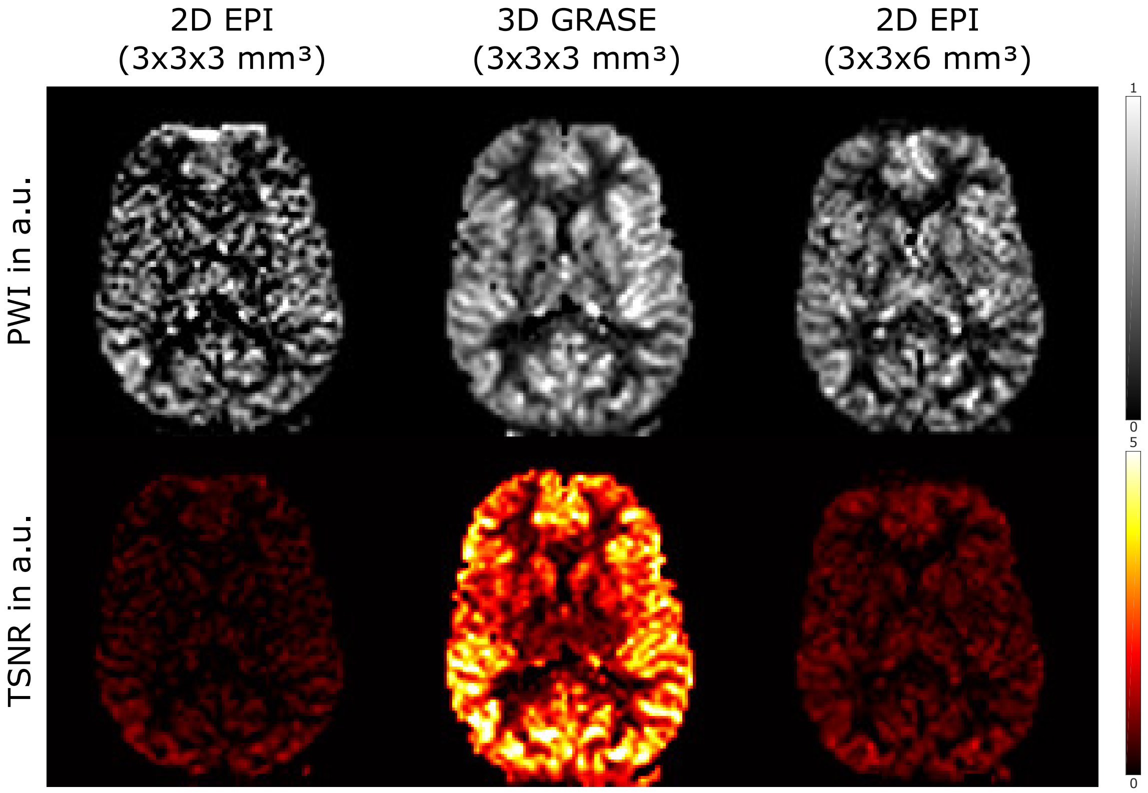

Figure 2.16: Comparison of CBF-maps obtained with a 2D-EPI and a 3D-GRASE readout. The CBF-maps from the 3D-GRASE show a higher temporal signal to noise ratio (TSNR) and hence a better image quality.

2.7 Background Suppression

In an ideal ASL experiment the signal intensity of static tissue is identical in the control and label condition and cancels out in the subtraction process. The remaining signal intensity in the difference image is proportional to the perfusion. Typically, the ASL signal is in the order of 1% due to the low amount of blood volume (3-5%) in a given voxel [14]. Thus, even a small fluctuation of the tissue signal will swamp the effect of perfusion. ASL measurements are therefore very sensitive to changes in the tissue signal. In practice, these fluctuations are many times higher than the ASL signal and are caused by physiological effects and subject motion. As the degree of variations scales with the tissue signal, techniques eliminating the unwanted signal while retaining the ASL signal are of high importance. [8, 14, 96, 283] This techniques are called background suppression and leads to increased temporal stability and accompanied increased quality of the CBF-maps [96, 179, 318].

The background suppression technique employes a carefully designed combination of pre-saturation and inversion pulses to eliminate the contribution of static tissue signal at the time of imaging. An example timing diagram using one pre-saturation and two background suppression (BS) pulses is shown in Figure 2.17. The degree of signal attenuation is a function of the longitudinal tissue relaxation time T_1 and the number of used inversion pulses i.e. with 2 inversion pulses the magnetization of two different tissue types can be eliminated at imaging time. [8, 14, 96]

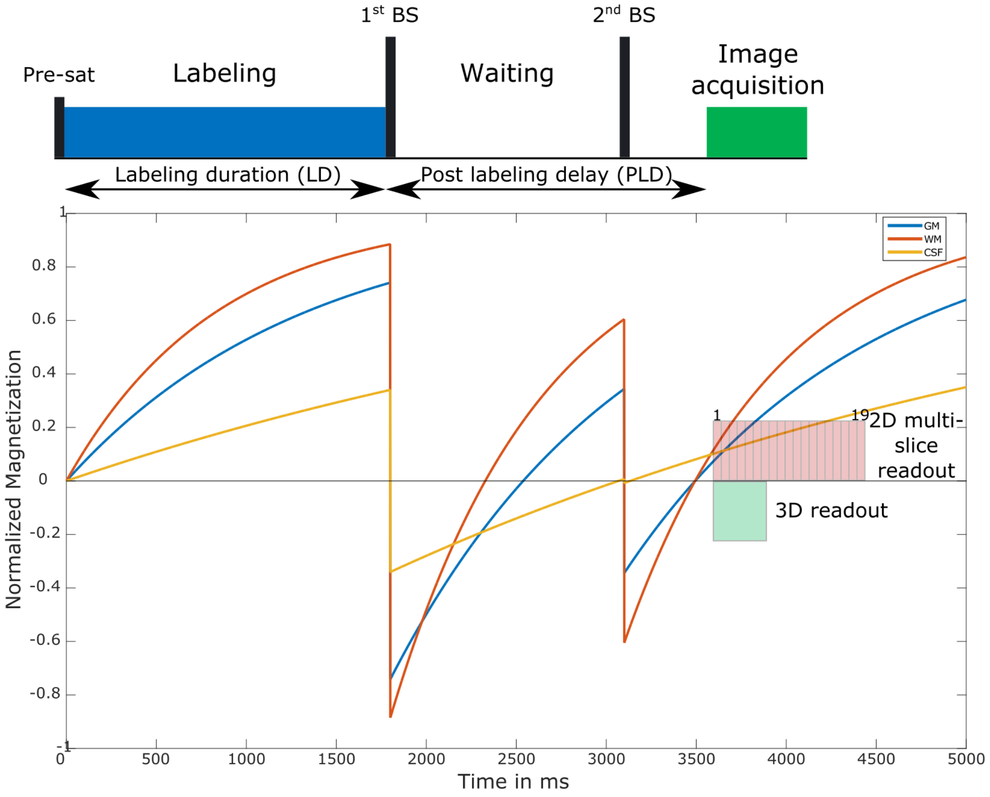

Figure 2.17: Timing diagram for BS in an ASL experiment with the corresponding signal evolution of GM, WM, and CBF tissue magnetization. For the 3D acquisition the BS is optimal for the whole volume, whereas in the multi-slice 2D readouts the signal evolution results in a poorer BS for subsequent slices.

As illustrated in Figure 2.17 the background suppression is only optimal at one point of time. Thus, for multi-slice 2D-readouts the degree of BS decreases from slice to slice. Usually the images are acquired in ascending order leading to a perfect background suppression for the most caudal slice and the worst BS for the most rostal slice. Accompanied with the imperfect BS is a reduced TSNR for upper slices and a contrast change in subsequent acquired images. This cause several additional problems if through plane motion occurs (see section 2.10.2 ”Background Suppression”). In contrast, 3D readouts provides an optimal background-suppression for the whole acquisition volume.
ASL experiments conducted with BS have typically a much higher TSNR and are thus highly recommended by the consensus paper in combination with 3D-readouts [8]. Figure 2.18 shows the benefit of background suppression using one pre-saturation and two inversion pulses in combination with a 3D-GRASE readout. However, there are also quantification issues accompanied by BS, which are discussed in section 2.10.2 ”Background Suppression”.

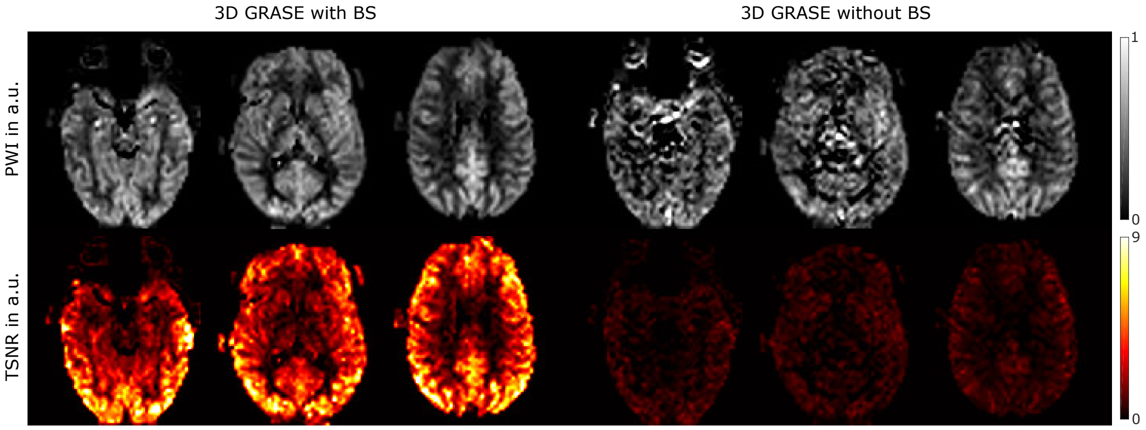

Figure 2.18: Effect of BS on an ASL experiment using a 3D-GRASE readout. BS increases the TSNR and is accompanied with an improvement in image quality.

2.8 Quantification Models

One of the main advantages of ASL is the possibility of absolute quantification. This feature has led to the rapid development of ASL over the past two decades. In ASL, the difference signal between control and label image is proportional to the amount of blood delivered to the tissue. To obtain quantitative values of perfusion from the difference image a detailed model that combines kinetics and relaxation is necessary [35]. The current standard approach for modeling the ASL signal is based on a single compartment model [34, 66]. This basic model is recommended by the consensus paper and will be discussed in more detail throughout this section [8].

2.8.1 Bloch Equation Model

The first approach for modeling the ASL signal was introduced by Detre et al. in 1992 [66] and is known as Bloch equation model or as T_1-quantification model [51, 66]. In this model, the Bloch equation for the longitudinal magnetization was modified by including flow effects (equation 2.4). The delivery term $fM_a(t)$ describes the flow of magnetization into the voxel and the clearance term $fM_v(t)$ the decrease of magnetization due to outflow of the labeled blood.

$$\frac{dM_t(t)}{dt} = \frac{M_0 - M_t(t)}{T_1} + f\left(M_a(t) - M_v(t)\right), \tag{2.4}$$

where M_t is the longitudinal magnetization of tissue, M_0 is the equilibrium longitudinal magnetization of tissue, T_1 is the relaxation time constant of tissue, M_a and M_v are the longitudinal magnetization of arterial and venous blood, and f is the cerebral blood flow. This model assumes that labeled blood is provided by an uniform plug flow and that the exchanges of tissue water and labeled blood water is instantaneously within the voxel i.e. assuming a well mixed compartment [51, 66]. Thus, the venous outflow of the magnetization is equal to the tissue concentration divided by the blood-tissue partition coefficient λ ($M_v(t) = M_t(t)/\lambda$). The blood-tissue partition coefficient is necessary to take into account the slightly different water content of blood and tissue and is derived from the PET literature [14]. Plugging in the difference signal ($\Delta M_t = M_{t,C} - M_{t,L}$) in equation 2.4 and by assuming equal longitudinal magnetization in both images we obtain the following equation:

$$\frac{d\Delta M_t(t)}{dt} = -\frac{\Delta M_t(t)}{T_{1app}} + f\Delta M_a(t), \tag{2.5}$$

where $\frac{1}{T_{1app}} = \frac{1}{T_1} + \frac{f}{\lambda}$. From this follows that the perfusion signal decays with the relaxation time constant T_{1app}.

2.8.2 General Kinetic Model

The previous described model has several simplifications leading to potential quantification errors. This includes variable transit time of the bolus, changes in T_1 as labeled water exchanges between blood and tissue, and incomplete water extraction [34]. Buxton et al. formulated a general kinetic model to account for those systematic errors in ASL [34]. This general kinetic model is based on tracer kinetics theory. The tracer considered here, are labeled blood spins traveling through the vascular system. Hence, the measured signal is a quantity of magnetization provided by the blood flow. The amount of labeled blood spin in a voxel at timepoint t depends on the history of delivered magnetization by arterial blood flow, the longitudinal relaxation, and the clearance of magnetization by venous outflow. [34] To describes these processes Buxton formulated three functions: (1) The arterial input function (AIF) $c(t)$ describes the amount of labeled water molecules arriving in a voxel at time t. (2) The residue function $r(t-t')$ is the fraction of labeled water molecules that were delivered to the voxel at time t' and is still present at time t [34]. (3) The magnetization relaxation function $m(t-t')$ describes the decrease in longitudinal magnetization due to the T_1 relaxation between timepoints t and t' [34]. With the definition of these function the measured ASL signal at timepoint t is given by:

$$\begin{aligned} \Delta M(t) &= 2M_{0b}f\int_0^t c(t^{'})r(t-t^{'})m(t-t^{'})dt^{'} \\ &= 2M_{0b}f\left\{c(t)\otimes[r(t)m(t)]\right\} \ , \end{aligned} \tag{2.6}$$

where M_{0b} is the blood equilibrium magnetization and f is the CBF. This general model provides a flexible quantification approach for ASL data. It takes into account different arterial input functions for PASL, CASL, and pCASL, the transit delay of the bolus, and additionally different exchange mechanism (single or multi-compartment) by choosing appropriate forms of the delivery function, residue function, and magnetization relaxation function [34]. From this general kinetic model the de facto standard ASL model was derived by Buxton et al. [34] by making three major assumptions:

1. It is assumed that the labeled blood water arrives the voxel via uniform plug flow. Thus, the bolus is well defined with a temporal width according to the labeling duration τ and reaches the voxel after the arterial transit delay Δt. This is described by the AIF $c(t)$ as follows [34]:

$$c(t) = \begin{cases} 0 & & t < \Delta t, \\ \alpha e^{-t/T_{1,b}} & \text{(for PASL)} & \Delta t \le t < \Delta t + \tau, \\ \alpha e^{-\Delta t/T_{1,b}} & \text{(for pCASL/CASL)} & \Delta t \le t < \Delta t + \tau, \\ 0 & & \Delta t + \tau \le t. \end{cases} \tag{2.7}$$

   The labeling efficiency α accounts for imperfect inversion of the blood magnetization. Note that for PASL the bolus is not uniform (box car-function) because some blood has already been decayed with $T_{1,b}$ as it leaves the labeling plane. The time course of the AIF is shown in Figure 2.19 for PASL and CASL/pCASL using the recommended labeling parameters of 0.8 s and 1.8 s respectively [8].

2. The water exchange between tissue and blood is described by single compartment kinetics. This means, that the labeled water exchanges instantaneously with tissue leading to a constant tissue concentration within the voxel. Equal to the Bloch equation model, the venous outflow is given by $M(t)/\lambda$ to account for the different water content in blood and tissue. With this assumption the residue function $r(t)$ is described by [34]:

$$r(t) = e^{-ft/\lambda}. \tag{2.8}$$

3. The labeled blood water magnetization decays initially with the relaxation time constant of blood ($T_{1,b}$). As soon as the labeled water molecules have reached the tissue, the magnetization decays with the relaxation time constant of tissue T_1 [34]. The magnetization relaxation function $m(t)$ is

$$m(t) = e^{-t/T_1} \ , \tag{2.9}$$

assuming a T_1 of 1.33 s [34], and shown in Figure 2.19.

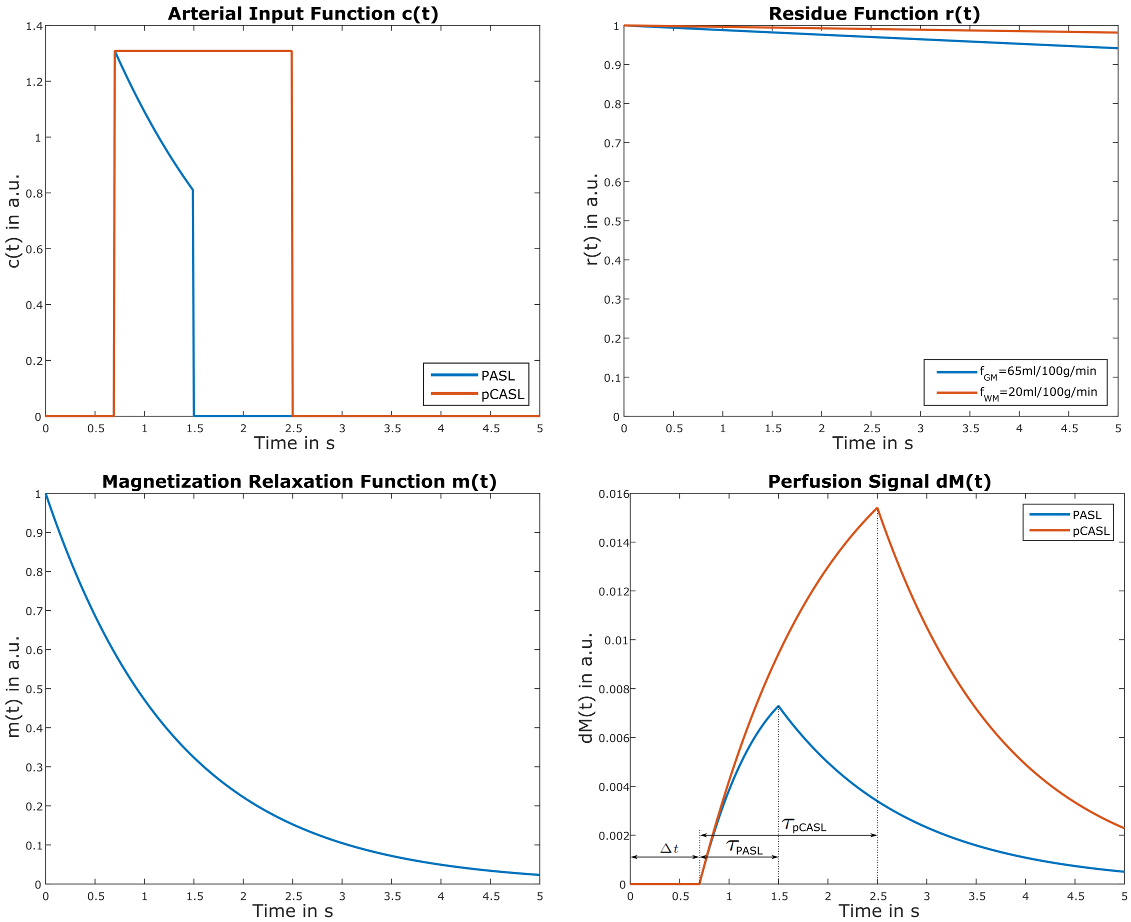

Figure 2.19: Time course of the arterial input function c(t) in a simulated GM voxel for PASL and pCASL using the recommended labeling duration of 0.8 s and 1.8 s respectively. The residue function r(t) and the magnetization relaxation function m(t) of arterial blood in dependence of the time are plotted. The bottom right plot shows the perfusion signal evolution $dM(t)$ using the general kinetic model with the three shown functions for PASL and pCASL.

With these assumptions the signal evolution of the difference image measured with

PASL is given by

$$\Delta M(t) = \begin{cases} 0 & t < \Delta t, \\ 2\alpha M_0/\lambda f\,(t-\Delta t)\,e^{-t/T_{1,b}} q_p(t) & \Delta t \leq t < \Delta t + \tau, \\ 2\alpha M_0/\lambda f \tau e^{-t/T_{1,b}} q_p(t) & \Delta t + \tau \leq t, \end{cases} \tag{2.10}$$

with

$$q_p(t) = \begin{cases} 0 & t < \Delta t, \\ \frac{e^{kt}\left(e^{-k\Delta t} - e^{-kt}\right)}{k(t-\Delta t)} & \Delta t \leq t < \Delta t + \tau, \\ \frac{e^{kt}\left(e^{-k\Delta t} - e^{-k(\tau+\Delta t)}\right)}{k\tau} & \Delta t + \tau \leq t\ , \end{cases} \tag{2.11}$$

$$k = \frac{1}{T_{1,b}} - \frac{1}{T_{1app}}, \tag{2.12}$$

$$\frac{1}{T_{1app}} = \frac{1}{T_1} + \frac{f}{\lambda}. \tag{2.13}$$

In case of CASL/pCASL, the signal evolution of the difference image is described by

$$\Delta M(t) = \begin{cases} 0 & t < \Delta t, \\ 2\alpha M_0/\lambda f T_{1app} e^{-\Delta t/T_{1,b}} q_{ss}(t) & \Delta t \leq t < \Delta t + \tau, \\ 2\alpha M_0/\lambda f T_{1app} e^{-\Delta t/T_{1,b}} e^{-(t-\tau-\Delta t)/T_{1app}} q_{ss}(t) & \Delta t + \tau \leq t, \end{cases} \tag{2.14}$$

with

$$q_{ss}(t) = \begin{cases} 0 & t < \Delta t, \\ 1 - e^{-(t-\Delta t)/T_{1app}} & \Delta t \leq t < \Delta t + \tau, \\ 1 - e^{-\tau/T_{1app}} & \Delta t + \tau \leq t\ . \end{cases} \tag{2.15}$$

Figure 2.19 shows the ASL signal evolution over time for PASL and pCASL using the recommended labeling duration of 0.8 s and 1.8 s respectively [8]. The single compartment model is currently standard for CBF quantification with ASL [8] and used throughout this thesis. However, the assumption of a well mixed compartment does not hold in practice. In reality, the labeled water will remain for some time in the vessels decaying with $T_{1,b}$ before it exchanges with water from the extravascular space decaying with T_1. The difference in $T_{1,b}$ and T_1 leads to quantification errors. In addition, the assumption that all the labeled blood water exchanges with the tissue reaching an equilibrium is incorrect [196]. Meaning that some of the labeled water will pass through the voxel without exchanging with tissue [123, 196]. Parkes et al. proposed a two-compartment model, to correct for this two assumptions [196, 198]. This model consists of an additional extravascular compartment within the voxel. The water exchange between the water and blood compartment occurs through a semipermeable membrane [123, 196].

Both, the single and two compartment model assumes that the bolus is well defined and at least for CASL/pCASL has a box car shape [123]. However, in reality the bolus gets smoothed as it travels from the neck to the brain capillary. This smoothing is referred as bolus dispersion and caused by the narrower vessels, branching, and cardiac pulsation [45]. Several approaches were proposed to account for this effect using a dispersions kernel [46, 95, 132]. The most accurate approximation of the bolus dispersion was achieved using a gamma-variate function [46].

2.9 Advanced ASL Methods

ASL has gained increased popularity over the last years leading to the development of new labeling, encoding, and quantification techniques. With these methods a great progress in SNR, robustness, and acquisition speed has been made. The following section provides a brief overview of four very promising approaches in ASL. For a general overview of recent progresses in ASL the reader is referred to two recently published review papers from Van Osch et al. [279] and Hernandez-Garcia et al. [123].

2.9.1 Velocity and Acceleration Selective ASL

In the current standard labeling approaches (PASL and pCASL) the labeling plane is located proximal to the imaging region. This causes a transit delay for the labeled blood to flow from the labeling plane to the tissue of interest. In cerebrovascular diseases this transit delay is often much longer than the longitudinal relaxation rate of blood due to slower blood flow, collateral flow, or stenosis [14]. This inhibits accurate measurement of the perfusion. Velocity selective arterial spin labeling (VSASL) was introduced to address this issue [189, 309]. In VSASL all spins flowing above a predefined velocity-threshold v_{enc} are labeled independent of the position. In principle, this approach removes the gap between labeling plane and tissue. The basic principle is illustrated in Figure 2.20. The first spatially non-selective 90° pulse tips the magnetization into the transverse plane, followed by two adiabatic non selective inversion pulses surrounded by gradients. The gradients have a net zero moment leaving stationary spin unaffected but leading to a dephasing of moving spins above a defined threshold v_{enc}. The last spatially non-selective $-90°$ pulse returns the magnetization into the longitudinal plane. This four-pulse velocity encoding scheme saturates moving spins above the velocity v_{enc} while leaving stationary spins largely unaffected and additionally corrects for phase shifts due to B_0 inhomogeneities. During the control condition the same pulse scheme is applied but without velocity-sensitizing gradients. [14, 123, 279, 309]

As for the standard approaches, the signal in the difference image is proportional to the perfusion. The disadvantage of VSASL is that all spins flowing above the defined velocity threshold are labeled, independent of the location in the vascular system. This leads to a venous contamination in the perfusion maps. From the physiology it is well known that blood flowing from large arteries to capillaries decelerates while blood flowing from capillaries to veins accelerates. [14, 123, 279, 309] To minimize the venous contamination, Wong et al. came up with the idea of applying a second velocity selective ASL module short before the readout [309]. This module again saturates spins above v_{enc} short before the label image is acquired. During the control condition only the second velocity selective module is applied with velocity sensitizing gradients. This ensures that only spins that had a velocity $v > v_{enc}$ at time of labeling and $v < v_{enc}$ at the time of imaging gives contrast in the PWI. In addition, the time between the first and second velocity module defines the temporal width of the bolus, similar to QUIPSS II. This approach is known as dual VSASL and allows the quantification of CBF in absolute units. [309]

The great potential of this method lies in the spatial non-selective labeling. This allows measurements in steno-occlusive or Moyamoya disease, where for traditional spatial-selective methods the magnetization is already decayed due to the long ATT. For example, Zaharchuk showed that the VSASL shows similar results to a pCASL approach with a very long PLD (3000 ms) but with reduced acquisition time [320].

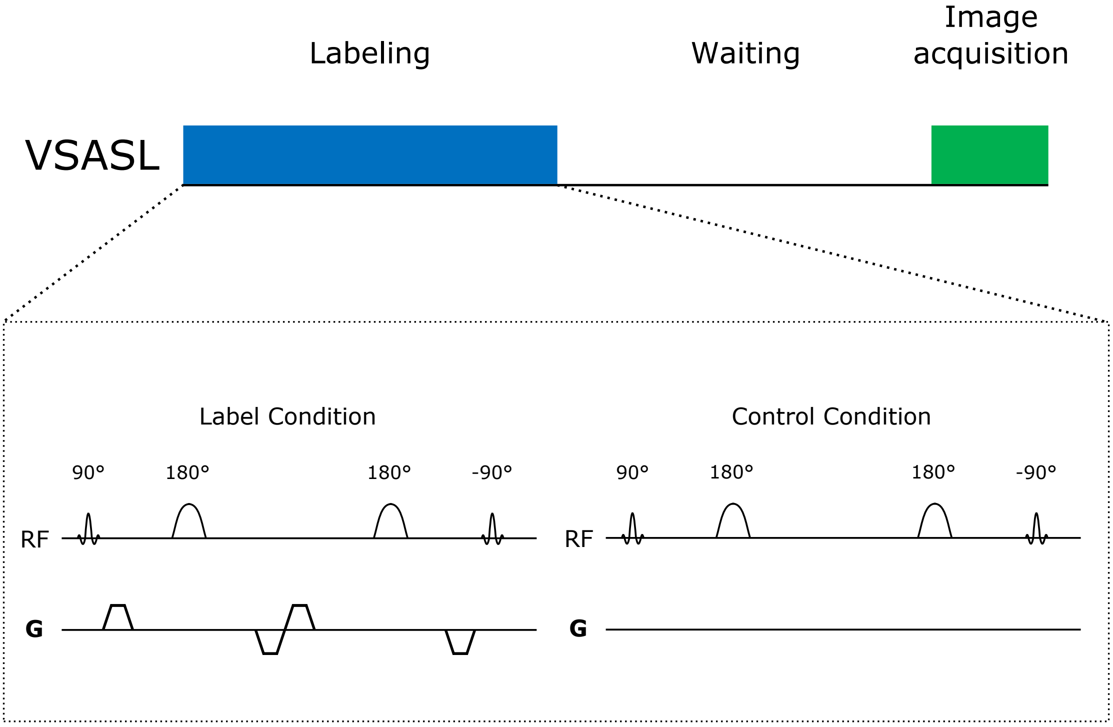

Figure 2.20: Schematic overview of the velocity selective labeling module [309]. The velocity sensitized gradients are embedded in a four pulse scheme to correct for B_0 inhomogeneities. During the control condition the same RF pulses are applied but without velocity encoding gradients.

An alternative approach to distinguished between arterial and venous blood was proposed by Schmid et al. [224]. This approach labels blood that accelerates or decelerates in the vascular tree and is referred as acceleration selective arterial spin labeling (AccASL). A change in blood velocity occurs due to tortuosity of the vessels, differences in cardiac cycle or changes in vessel diameter [224, 279]. This effects are most prominent on the arterial side of the vascular system labeling mainly arterial blood. Figure 2.21 shows schematically the pulse sequence. The basic principle is similar to VSASL but the gradients and pulses are designed so that their zeroth and first order gradient moments are zero. Hence, stationary spin as well as spins with a constant velocity rephases during the labeling module, whereas accelerated or decelerated blood above a certain threshold A_{enc} gets saturated [224]. Both VSASL and AccASL are very promising techniques and still under active research at the time of writing [123].

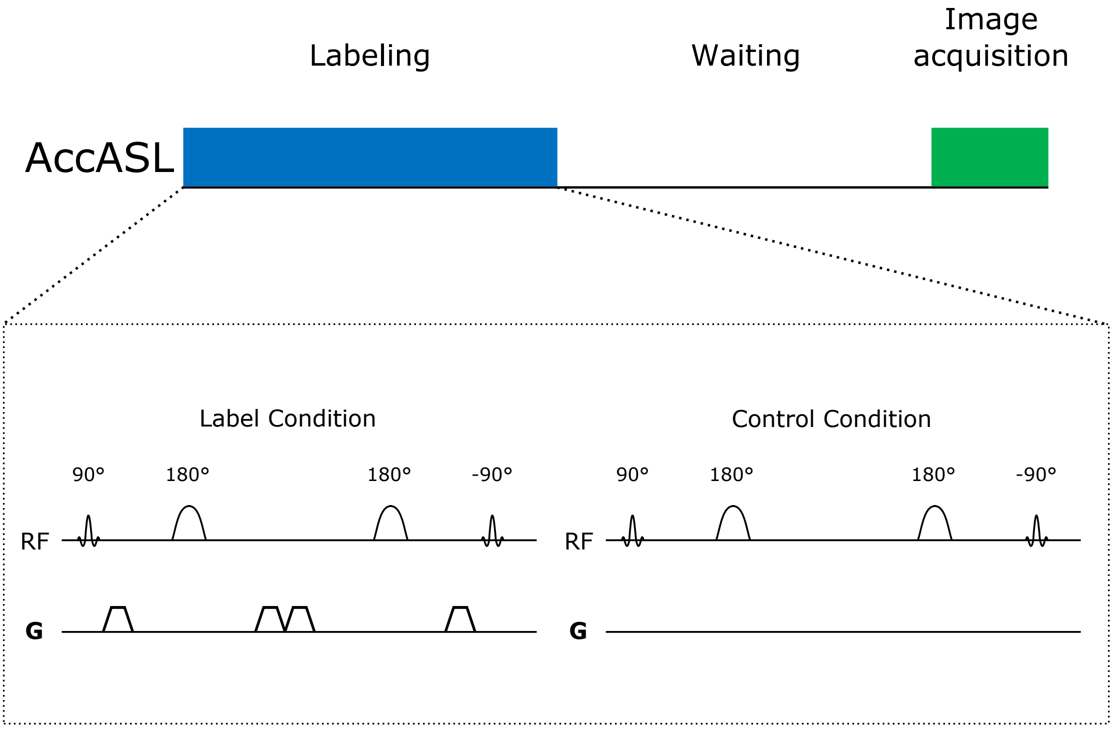

Figure 2.21: Schematic overview of the acceleration selective labeling module [224]. The gradients and RF pulses are designed so that static and moving spins rephase but accelerated or decelerated spins accumulate a phase. During the control condition the same RF pulses are applied but without acceleration-sensitizing gradients

2.9.2 Vessel Encoded ASL (VE-ASL)

Region selective ASL provides perfusion maps of flow territories (Figure 2.22) by selectively labeling one of the major arteries [119]. The visualization of flow territories is important for many application in clinical routine. In embolic stroke the location of the blood clot can be determined [14]. In tumors, or in arterio-venous malformation vessel encoded arterial spin labeling (VE-ASL) has the potential of identifying the feeding artery. This can provide important information for treatment monitoring, therapy decision, or surgical intervention [163]. Studies in healthy subjects show that the territories supplied by the internal carotid artery (ICA) or vertebral arteries strongly vary due to incomplete configurations or differences in the circle of Willis [119, 163]. Such information may be important for acute stroke where these modifications could impair the collateral blood supply [163]. The current gold standard in clinical routine is digital subtraction angiography (DSA), which allows to image a single artery by injecting a contrast agent via a catheter [163]. This method is invasive, time-consuming, and requires x-ray for imaging [163]. In a study comparing DSA with region selective ASL in Moyamoya patients a comparable diagnostic value was found for VE-ASL. Beside the perfusion weighted flow territory maps, dynamic angiographic images can be obtained with VE-ASL. This allows to study the inflow of blood in a specific territory. Three different approaches exists for obtaining flow territory maps with ASL. The most common method is based on a PASL sequence. The labeling slab is rotated and translated in such a way that only blood in a single artery is labeled [119]. The second approach, known as super selective pCASL, uses additional time-varying gradients to selectively label blood in one artery [57, 117]. In principle, this approach is not limited to the major arteries, it can be applied to every artery but requires a careful planning based on high resolution structural and angiographic images [14]. The third approach is called vessel encoded ASL [305]. In this approach the vessels are labeled in a spatial different manner following a Hadamard matrix and the corresponding maps are obtained by decoding the images [279].

2.9.3 Time Encoded ASL (TE-ASL)

Time encoded ASL is a smart way to obtain perfusion weighted images at multiple time points. Instead of acquiring sequentially control and label images at different PLDs, the PLDs are directly encoded in the pCASL module. Figure 2.23 shows this time-encoding process [108]. The basic idea of this method is to divide the labeling module into N sub-blocks or sub-boli, and assign each block a labeling or control condition according to the entries of a N^{th} order Hadamard matrix. The positive entries of this matrix corresponds to labeling and the negative entries to control condition. Each row of the Hadamard matrix is independent and hence encodes the ASL image in an unique way. [108, 279, 286]
The principle of Hadamard encoding is illustrated in Figure 2.23 for a Hadamard 4 matrix:

$$H_4 = \begin{pmatrix} 1 & 1 & 1 & 1 \\ 1 & -1 & 1 & -1 \\ 1 & 1 & -1 & -1 \\ 1 & -1 & -1 & 1 \end{pmatrix}. \tag{2.16}$$

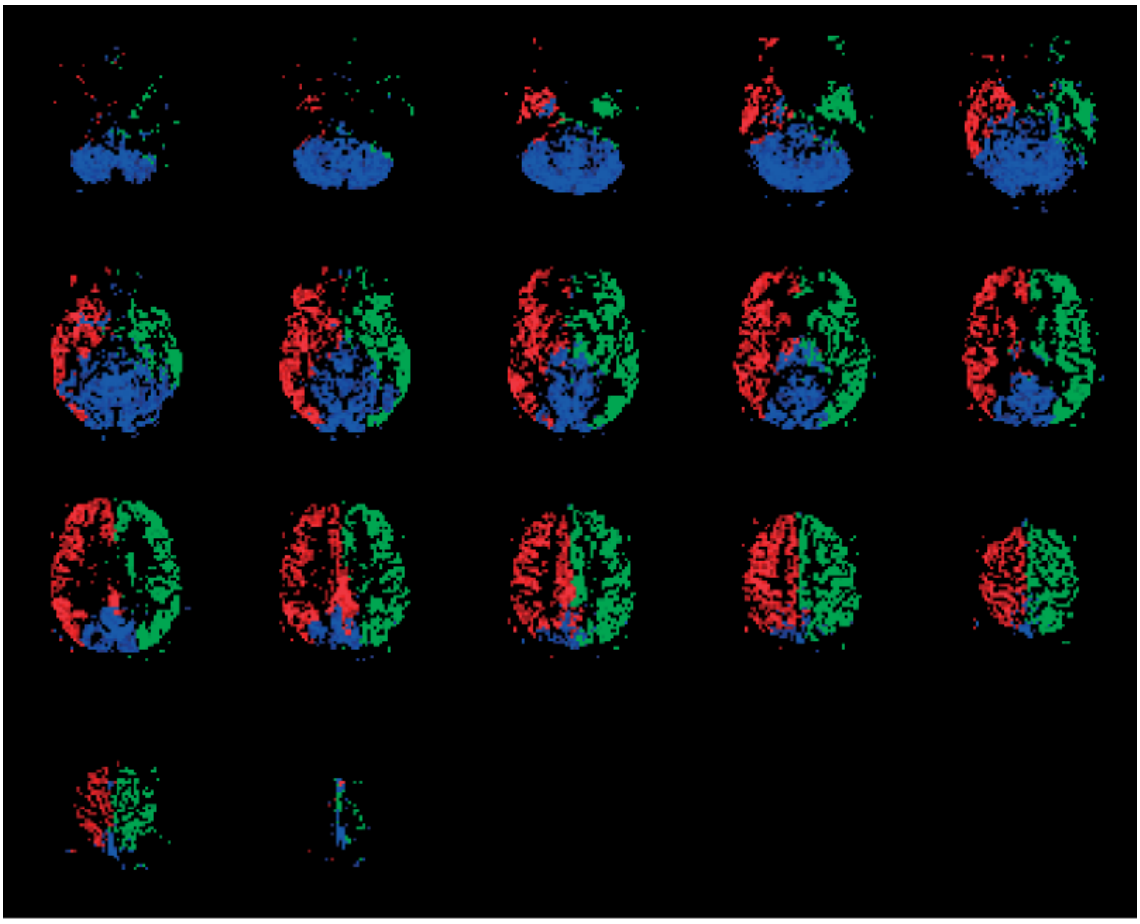

Figure 2.22: Example perfusion maps of flow territories obtained by selectively labeling the left ICA (green), right ICA (red) and the basilar artery (blue). Figure taken from [223].

For obtaining the PWI time series the N acquired encoded images are subtracted or added according to the entries of the N columns in the Hadamard matrix (i.e. 1 corresponds to add and -1 to subtract). This step is known as decoding step (equation 2.17) and can be described by a matrix-vector multiplication [286].

$$(PWI_1, ..., PWI_N) = (IMG_1, ..., IMG_N) \cdot H_N. \tag{2.17}$$

Since each column of the matrix represents one labeling-block or subbolus, the decoding of the N^{th} column leads to a perfusion weighted image that contains only the contribution of the N^{th} subbolus. The corresponding PLD is given by the end of the N^{th} subbolus until image acquisition i.e. for the Hadamard-4 example in Figure 2.23 all 3 PWIs have equal LD defined by the block-length but different effective PLDs. The first or longest PLD for PWI_1 ranges from the end of the first subbolus to the image acquisition. The shortest and last PLD for PWI_3 is given by the end of the last subbolus to the image acquisition. The first column of the Hadamard matrix contains only control or label

state. Thus, the first images is always an averaged control or label image (depending on the state) and only $N-1$ perfusion weighted images can be obtained. [286]
This special encoding is much more efficient than acquiring sequential multi-PLD images where $2(N-1)$ images are necessary to obtain the same number of temporal information. In addition the decoding process inherently averages the images leading to an reduction of $\sqrt{(N/2)}$ in the noise standard-deviation. This makes TE-ASL a highly temporal and SNR efficient method to sample the ASL signal [108, 279].
In the original implementation the k-blocks were equally spaced. This results in a short LD in combination with a very long PLD for the first PWIs reducing the quantification accuracy [59, 110]. Several variants of time-encoded ASL were proposed to improve the parameter estimation including the free-lunch [262], T_1-adjusted [262], or hybrid time-encoded scheme [310]. In the free-lunch approach the first block or subbolus is typically 1.8-2.0 s long while the remaining blocks are equally split up during a time window of 1.8 s. Thus the first column delivers a perfusion weighted image with a LD of 1.8-2.0 s and a PLD of 1.8 s which is equal to the recommended single-PLD acquisition [8]. The addition $N-2$ PWIs can be obtained for free (without additional scan time) yielding an additional ATT map [262]. The T_1-adjusted approach divides the blocks in a sophisticated way, so that the signal contribution of each block is equal at the time of imaging. Thus, the T_1-decay of the tracer is compensated and the SNR is preserved over all images [262]. The hybrid time-encoded scheme uses one of the three previous defined time-encoding schemes as a basis and combines this with sequential PLD acquisition i.e. repeating the T_1-adjusted approach three times with different PLDs between the encoding module and readout [310].

Compared with traditional-sequential ASL acquisitions time-encoding acquisitions are much more sensitive to motion and artifacts. The decoding process involves the whole number of time-encoded images. Thus, if only one acquired image is corrupted with motion or artifacts all decoded images are affected. In contrast, in the sequential image acquisition the affected image-pair can be discarded leading to a negligible loss in SNR and information [279]. To reduce the sensitivity to motion-artifacts Samson-Himmelstjerna et al. proposed a Walsh-ordered Hadamard matrix for encoding the ASL images [286]. This matrix rearranges the rows of a classical Hadamard matrix according to the number of equal signs. In that case the Hadamard matrix can be divided into fully decodable Hadamard submatrices, i.e. for a Hadamard 8 matrix a Hadarmad 2 matrix can be obtained after two acquisitions by summing up the corresponding labeling blocks (see Figure 2.24) [286]. In addition, a post-processing strategy have been proposed by modeling the encoded signal in a Bayesian framework [285]. This technique allows the estimation of CBF and ATT from a fewer number of encoded images i.e. if one or two images were discarded due to motion or artifacts [285].

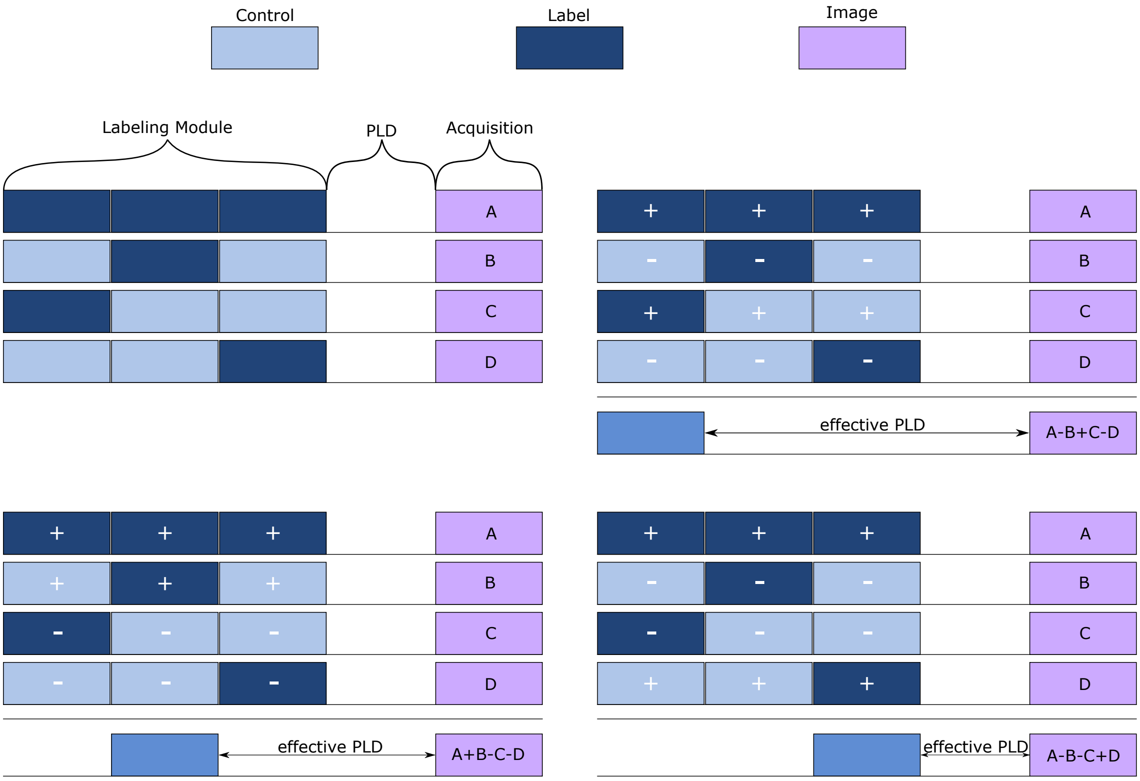

Figure 2.23: Schematic representation of the time encoded ASL using a Hadamard 4 matrix. The decoded images are obtained by adding or subtracting the encoded images according to the column entries in the Hadamard matrix. Figure modified from [279]

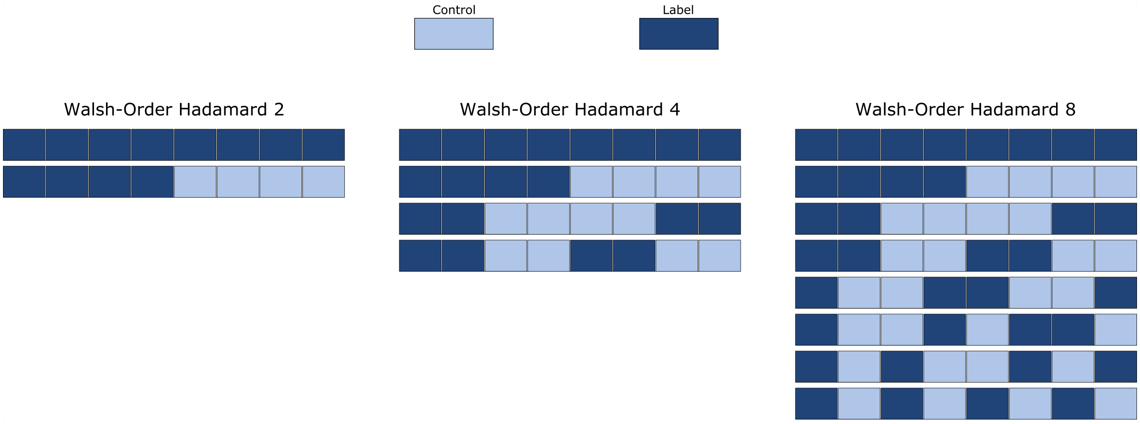

Figure 2.24: Schematic representation of the Walsh-ordering of a Hadamard 8 matrix. After 2 encoding steps a Hadamard 2 matrix, after 4 encoding steps a Hadamard 4 matrix and after 8 encoding steps a Hadamard 8 matrix is obtained. Figure modified from [286]

2.10 Challenges of ASL Imaging

At present, there are numerous challenges for perfusion measurements with ASL. This section provides an overview of these challenges and presents recent developments in this field.

2.10.1 Signal to Noise Ratio and Partial Volume Effects

The major drawback of ASL imaging is the low signal to noise ratio. In gray matter, perfusion replaces approximately 1% of the water protons by labeled blood water in 1 *s* (assuming an average CBF of 65m/100g/min) [14]. Thus, a bolus duration of 1 *s* leads to a ASL signal strength of approximately 1%. In an ideal experiment, this small signal strength would be enough for accurate perfusion measurement. In practice, the ASL signal is affected by several sources of noise including thermal noise, hardware instability, physiological noise, and subject motion. The most prominent source is physiological noise and subject motion, which is several factors higher than the original ASL signal [14]. A detailed explanation concerning the noise in ASL imaging will be given in chapter 4. Improvements in SNR were achieved through the use of advanced hardware [263], sophisticated labeling [56] and readout schemes [109, 283], background suppression techniques [179, 318], and post-processing methods such as motion-correction, outlier detection and denoising [84, 293, 294, 299], which will be described in chapter 3. Beside this sophisticated methods, a very effective way to improve the SNR in ASL images is to increase the voxel size. A larger voxel contains more protons and thus increases the ASL signal. Figure 2.25 shows the impact of the voxel size on the SNR of ASL imaging.

To achieve a reasonable SNR in a feasibly time, ASL images are typically acquired with a low spatial resolution. The consensus paper recommends a resolutions of 3-4 *mm* in-plane and 4-8 *mm* through-plane [8]. This coarse spatial resolution is prone to partial volume effects (PVE) in the CBF images leading to blurring and significant quantification errors in the gray and white matter [160, 276]. The cross-contamination leads to an underestimation of GM and an overestimation of WM CBF [276]. This is problematic for applications in different diseases and in case of group studies especially in age-related [12, 84] and activation studies [29]. To reduce the influence of partial volume effects several methods were proposed based on high resolution T_1 weighted images [11, 160, 202]. Prerequisites of these methods are accurate segmentation as well as subsequent registration with the ASL image. However, these two steps are often prone for errors and the effect of PVE correction comes at the cost of a bias and spatial smoothing [84]. For a detailed study of accuracy and influence factors of PVE on ASL images the reader is referred to a recent systematic study [203, 330]. A more direct way to avoid partial volume effects is to increase the resolution in the ASL images, but this comes with the hurdle of a reduced SNR. Hence, there is always a compromise between SNR and PVE in ASL imaging.

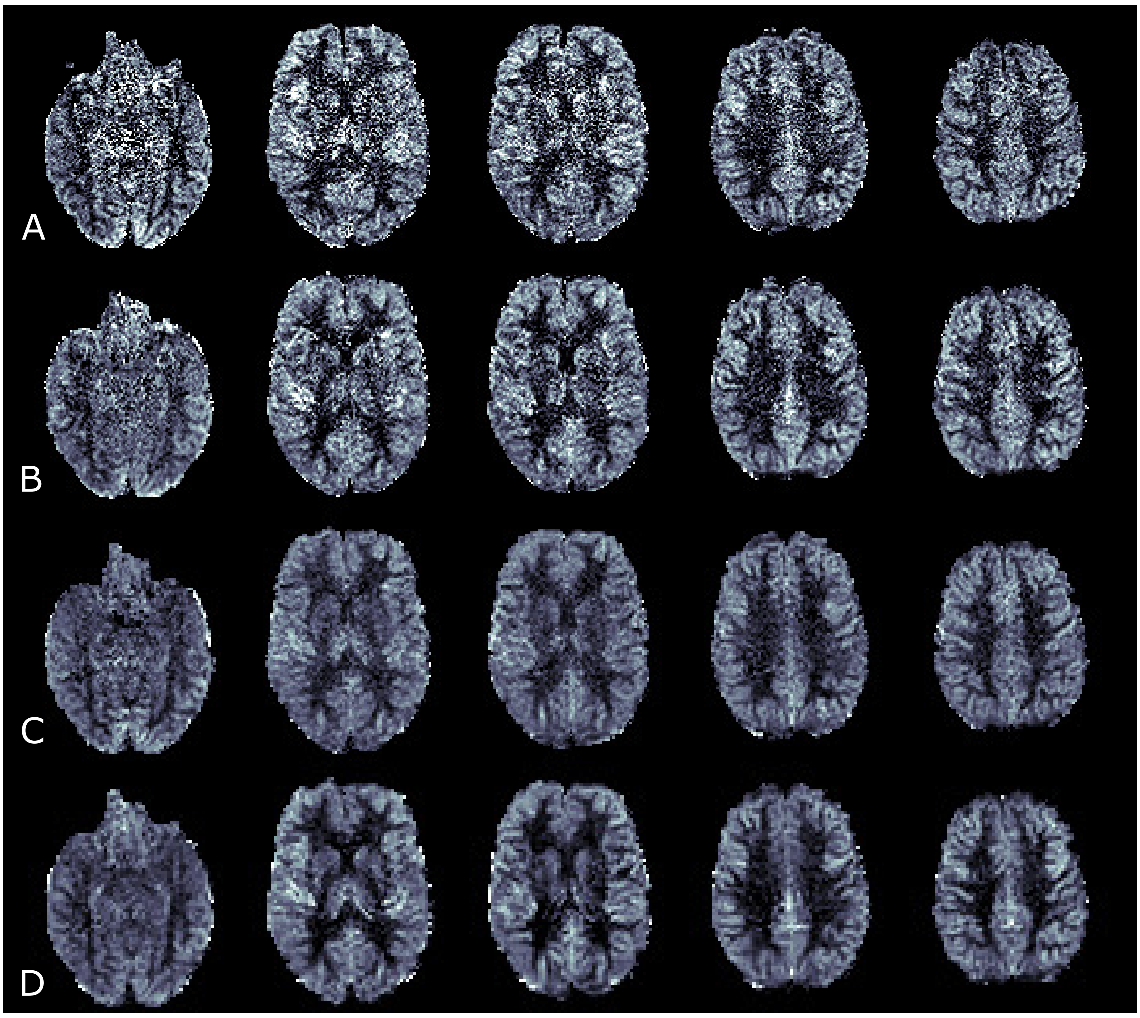

Figure 2.25: Influence of voxel size on the SNR of ASL images. Top to bottom: 1.6 *mm*, 2.0 *mm*, 2.5 *mm* and 3 *mm* isotropic resolution

2.10.2 Background Suppression

Background suppression greatly improves the temporal stability of ASL images. However, three important points have to be considered using background suppression for ASL. First, a trade-off between the number of inversion pulses and suppression of static tissue has to be chosen. More pulses allow a wider range of tissue types (wider range of T_1-values) to be suppressed. On the other hand each BS pulse reduces the labeling efficiency by approximately 5% or more i.e. Shin et al. found that the inversion efficiency can vary from 77 to 95% between subjects and is reciprocal related to the amount of CBF [232]. This reduces the SNR and leads to significant quantification errors in the quantification process.

Second, the background suppression is only optimal at one point in time. Thus, 3D-readouts deliver the same effective BS over the whole imaging slab while for 2D-readouts the BS is only optimal for the first acquired slice. The subsequent acquired slices experience a lower effective BS due to the T_1-relaxation of static tissue. Consequently, the contrast between adjacent images changes and the temporal instability increases for ascending slices. This could produce significant subtraction errors if through plane motion occurs. Approaches were proposed to solve this issue to a certain extend [230, 258]. A combination of background suppressed ASL imaging with prospective motion correction strategies using navigator echos [228, 334] or an optical tracking system [5] could solve this issue.

Third, a too high BS would directly affect the motion correction as the change in contrast is lost [45]. Again this point could potentially be solved by using prospective motion correction approaches.

The current recommended BS strategy consists of one pre-saturation followed by 2 BS pulses which shows a good trade off between suppression of ASL signal and loss in inversion efficiency [8].

2.10.3 Motion

ASL is very sensitive to motion due to the pair-wise subtraction of label and control images. Even an small miss-registration between successive pairs can mask the perfusion signal leading to severe artifacts. Background suppression techniques are typically used to reduce the influence of motion to a certain extent [179, 318]. In addition, adequate fixation of the subject during the acquisition is highly recommended to prevent motion. However, even with appropriate head fixation an involuntary movement can occur. During the last years, several techniques were proposed to correct the potentially subject motion.

In general, motion correction refers to a technique that realigns images to minimize the effect of motion. Currently, motion-correction is a standard ASL preprocessing step. It can be either applied by realigning all image to the first image of the ASL time series or by using the mean image as reference [293, 294]. This retrospective method works well for inter-scan motion, however, for current recommended segmented readout approaches motion can occur in between the acquisition of segments. Inter-segment motion leads to misalignments in k-space which directly affects the reconstruction quality of the images. Unfortunately, this cannot be corrected using image-based motion-correction approaches and is exemplary illustrated in Figure 2.26. Tan et al. proposed a hybrid acquisition strategy to account for inter-segment motion by combining 3D-GRASE with periodically rotated overlapping parallel lines with enhanced reconstruction (PROPELLER) [260]. Alternatively prospective or real-time motion correction strategies can be used. Here, the motion parameters are either estimated by motion sensitive navigator echoes [228, 334] or by an optical tracking systems [5]. If motion occurs, the gradients are updated accordingly so that the mismatch is corrected. Besides the advantage of improved motion robustness the drawback of a lower temporal resolution still remains, which limits its applications to perfusion based functional MRI or multi-PLD ASL [34]. An alternative approach would be to accelerated the acquisition and acquire whole brain images within a single shot to avoid inter-segment motion. Several accelerated acquisitions were proposed, which are discussed in more detail in chapter 7.

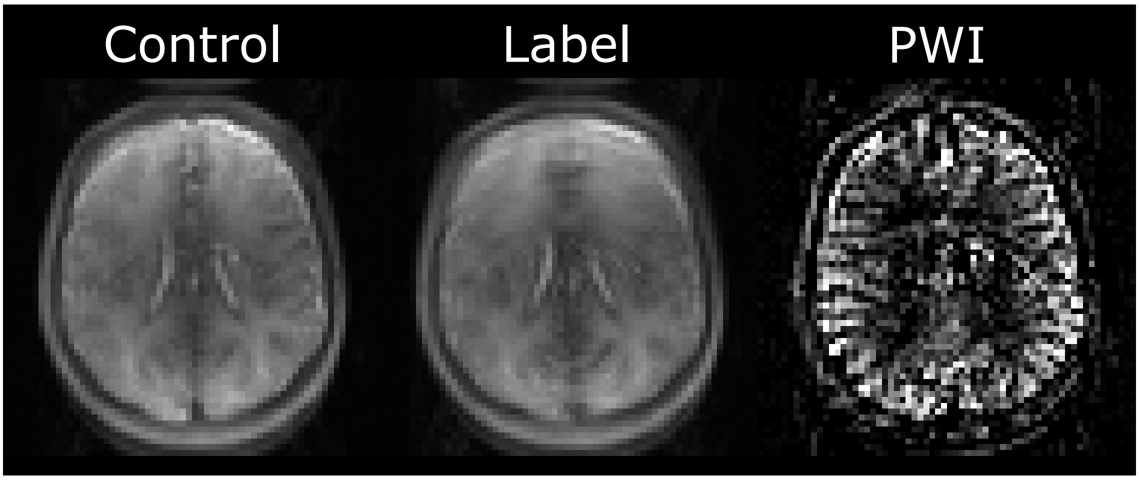

Figure 2.26: Effect of inter-segment motion on control, label and perfusion weighted image

2.10.4 Labeling Robustness and Labeling Efficiency

In general, a labeling method complying the following criteria is desirable: (1) high labeling efficiency close to 100%, (2) providing a long and sharp bolus, (3) being robust against system imperfections, (4) providing consistent labeling efficiency across a reasonable physiological range, (5) and has a minimal SAR [45]. In practice, this ideal labeling technique is not feasible, but the current recommended labeling scheme pCASL provides a good trade-off between these requirements. pCASL has a well defined bolus shape and labeling duration leading to a 50% higher SNR compared with PASL and in contrast to CASL a reduced SAR, RF duty-cycle, and higher labeling efficiency [8, 312]. The labeling efficiency is an important parameter for the quantification of the CBF and is assumed to be 85% for pCASL and 98% for PASL [8]. However, pCASL is based on the principle of flow induced adiabatic inversion, which is highly dependent on the blood velocity [56]. A too high blood velocity leads to a fast change of the effective field violating the adiabatic condition. If the blood velocity is too low, T2-relaxation occurs during inversion compromising the labeling efficiency [14, 56, 327]. Thus, the labeling efficiency is only optimal in a certain range of velocities. Unfortunately, the blood velocity varies strongly across the cardiac cycle, between arteries, healthy subjects, and cerebrovascular disease, which can result in a bad labeling efficiency accomplished with a low SNR and an underestimation of the CBF [91, 280, 313]. Several methods were proposed to account for this effect. First, the pCASL sequence parameters can be adjusted according to the measured flow velocity [273]. Second, the robustness and efficiency can be increased by carefully optimizing the labeling scheme. For example Zhao et al. showed that an unbalanced pCASL with a low average gradient (0.5 mT/m) in combination with a low slice-selective gradient and highest feasible B_1 improves the labeling efficiency [329]. Third, by dynamically varying the RF amplitude according to the velocity change in the cardiac cycle (increasing the amplitude as the velocity increases) [173]. In addition, the labeling efficiency can be estimated from a separate scan [49, 279], directly from the ASL scan [50], or by using phase contrast angiography in combination with a segmented T_1 weighted image [10, 279]. The estimated parameter can than be included in the quantification process to avoid potential errors [279].

Another influence factor in pCASL is the position of the labeling plane. Several studies suggest that the labeling plane should be perpendicular to the feeding arteries to ensure that the z-gradient is in line with the flowing blood spins. In addition, positions close to vessel crossings or tortuosities such as the bifurcation should be avoided [9, 10, 239, 282]. Indeed, the best way would be to acquire a short angiogram of the feeding arteries prior to the ASL measurement, but this comes at the cost of additional scan time. In time critical applications anatomical landmarks could be used such as positioning the labeling plane 85 mm below the anterior commissure posterior commissure (ACPC) line [10] or 40 mm below the distal end of the cerebellum [282].

Another major issue of pCASL is the high sensitivity to off-resonance effects caused by susceptibility variations. For example dental implants or air/tissue boundaries lead to B_0 inhomogeneities in the labeling plane. Like in CASL, a B_0 field variation will shift the labeling plane depending on the strength of the B_0 variation. This has a little effect on the inversion efficiency for CASL because the bandwidth is typically in the order of kilohertz satisfying the adiabatic conditions even with off-resonance [14]. However in pCASL, during the time gaps of the RF pulses, off-resonance spins will experience phase shifts depending on the strength of the B_0 inhomogeneities. Consequently the spins lose phase coherence with the RF pulse train. This can significantly reduce the labeling efficiency i.e. an offset of 200Hz can reduce the labeling efficiency up to 40% [306, 329]. Several approaches have been proposed to reduce this effect: First, a multi-phase pCASL approach [142] which increments the phase between each RF pulse over successive cycles in equal steps (4 or 8) from 0 to 2π. The obtained images are then fitted to a model to retrieve the CBF. [21, 142] Second, correcting phase offsets at the labeling plane using field maps and adding additional phase and gradient terms accordingly [21, 135, 171]. Third, performing shimming at the labeling plane [56, 262] and fourth, by performing prescans, including a short multi-phase pCASL scan, to determine the phase offset for each vessel in the labeling plane [233].

An example of a subject with a poor labeling efficiency in the left ICA using pCASL is illustrated in Figure 2.27. The poor labeling efficiency causes reduced CBF values in the flow territory of the ICA. In contrast, PASL provides a CBF-map with good quality but shows a hyperperfusion in the occipital lobe. This hyperperfusion is caused by the shorter PLD and often visible in PASL images [209]. PASL is more robust against field inhomogeneities because the RF pulse is applied with a strong gradient and hence has typically a large RF bandwidth. In addition, it is relative insensitive to flow velocity due to the short pulse duration [308]. Studies have demonstrated that PASL has a labeling efficiency of 98%. The missing 2% are related to the T_2 relaxation occurring during the RF period of 10-20 ms [14, 308].

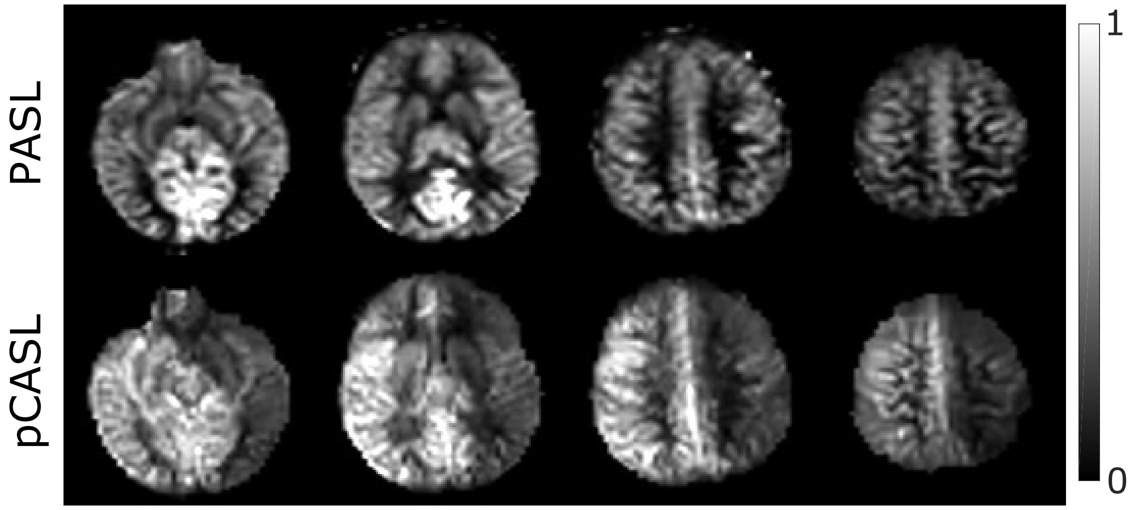

Figure 2.27: Effect of reduced labeling efficiency in the left ICA using pCASL scanning. This reduction is caused by a tortuous artery in the labeling plane. The PASL images show homogeneous CBF but arterial artifacts in the occipital region, due to the shorter PLD.

In summary, a high labeling efficiency is not only important for improving the SNR and image quality, it is also necessary to get an robust labeling over a wide range of field inhomogeneities and blood velocities. Otherwise, it may affected the quantitative CBF values potentially leading to significant differences in group studies or in disease progression studies [324].

2.10.5 Quantification Issues

The quantification models rely on several assumptions and require calibration factors to estimate the CBF from the ASL images. This includes the longitudinal relaxation time of blood ($T_{1,b}$) and tissue ($T_{1,t}$), the blood-brain partition coefficient (λ), the labeling efficiency (α), the amount of inversion efficiency if BS is applied, and the bolus length. These parameters can be either measured during the experiment or values based on literature can be chosen [14]. For simplicity, parameters from the literature are typically used and assumed to be constant through the brain and even through the population. In practice this assumption does not hold, leading to significant quantification errors in CBF. A recent work of Bladt et al. [26] showed that within a 5 minute scan more accurate CBF-maps can be acquired by reducing the number of averages and using the gained time to measure the relaxation time of blood and the labeling efficiency. This chapter summarizes the main influence factors on CBF quantification using the single compartment model [8, 34]. Note that the effect of background suppression, delayed arterial transit times, and the influence factors on the labeling efficiency with associated correction methods were already discussed in the previous sections.

2.10.5.1 Calibration Image and Blood Brain Partition Coefficient

The key for absolute perfusion quantification in ASL is the knowledge of the tracer concentration. In other words, we need the magnetization of arterial blood water for the estimation of CBF. In ASL literature, two different approaches exists for determining the equilibrium magnetization of arterial blood water. [45] It can be either estimated voxelwise from the tissue magnetization (equation 2.20), as recommended by the consenus paper [8], or by using a global value estimated from an reference region (equation 2.19) [45]. For both approaches the equilibrium magnetization of tissue is necessary, which is typically obtained from an addition acquisition using a long repetition time (TR) and without BS or labeling. This tissue magnetization M_{0t} is then related to the arterial blood magnetization M_{0b} via the partition coefficient λ [45]:

$$M_{0b} = \frac{M_{0t}}{\lambda}. \tag{2.18}$$

The parameter λ accounts for the difference in water content between blood and tissue. The units are quoted as ml blood/ml water or as ml blood/g tissue. Typical values for λ are 0.98 for GM, 0.82 for WM, 1.15 for cerebrospinal fluid (CSF), and 0.9 for whole brain [45]. In case of the reference region approach, M_{0b} is estimated by dividing the averaged tissue magnetization in an homogenous regions (GM, WM or CSF) by the corresponding λ:

$$M_{0b} = \frac{\langle M_{0t} \rangle_{rt}}{\lambda_{rt}}. \tag{2.19}$$

It should be noted that M_{0t} has to be corrected for the receiver coil profile. For the voxelwise approach the tissue magnetization is typically divided voxelwise by the partition coefficient to obtain M_{0b}:

$$M_{0b}(x,y) = \frac{\langle M_{0t}(x,y) \rangle_{rt}}{\lambda_{rt}}. \tag{2.20}$$

For simplicity the whole brain partition coefficient is used in this approach [8]. However, as previously mentioned λ varies for different tissue types and more accurate values can be obtained by weighting λ with the partial volume (PV) estimates [45, 208]. In a recent work, the influence of different calibration methods on CBF quantification were investigated [208]. The authors concluded that the voxelwise calibration method recommended by the consensus paper [8] delivers the most accurate results with a high reproducibility. The authors argued that this approach is simple to implement and corrects the coil sensitivity variations intrinsically [208]. Therefore, this approach is used throughout this thesis.

2.10.5.2 T_1 of blood ($T_{1,b}$)

In ASL the labeled water molecules travel from the labeling plane through the arterial vessels to the capillary bed, where they exchange with tissue. During this period the longitudinal magnetization decays with the relaxation rate of blood $T_{1,b}$. For robust quantification, this relaxation effect has to be taken into account and the exact value of $T_{1,b}$ is necessary. Current studies and also the consensus paper assume a $T_{1,b}$ of 1.65 s at 3T and 1.35 s at 1.5T [8]. However, it is well known that $T_{1,b}$ depends on the hematocrit, which is slightly different between subjects i.e. female subjects have a lower hematocrit value than men, leading to a higher $T_{1,b}$ [279]. Moreover, many diseases such as sickle-cell disease may influence the $T_{1,b}$ [272]. This can results in a faster or slower tracer decay accompanied by quantification errors [279]. To account for these potentially errors, an additional pre-scan can be performed for measuring $T_{1,b}$ in the individuals [158]. This is especially important in group studies where an assumed constant $T_{1,b}$ can lead to significant differences in CBF [279].

2.10.5.3 T_1 of tissue ($T_{1,t}$)

Beside the relaxation time of blood, another important parameter for accurate quantification is the relaxation time of tissue $T_{1,t}$. The single compartment model assumes that labeled water decays with $T_{1,t}$ as soon as it enters the imaging voxel. In ASL studies, typically a single $T_{1,t}$ value is used for the whole brain, ranging from 1.33 s to 1.45 s for 3T [14]. In practice, $T_{1,t}$ varies strongly between different tissue types [14], subjects [288], and diseases [288]. These variations can lead to large quantification errors in CBF. If possible, an additional T_1-map should be acquired and considered in the quantification model to reduce this potential source of error [14]. For multi-PLD acquisitions with different BS timings the $T_{1,t}$-map can be directly estimated from the control image time series [228].

3

Variational Denoising for 2D Arterial Spin Labeling Perfusion Data

This chapter is based on the following publication:

> S. M. Spann, K. S. Kazimierski, C. S. Aigner, M. Kraiger, K. Bredies, and R. Stollberger. Spatio-temporal TGV denoising for ASL perfusion imaging. *NeuroImage*, 157:81–96, aug 2017, doi: 10.1016/j.neuroimage.2017.05.054

Contents

3.1 Introduction

The intrinsically low signal-to-noise ratio (SNR) is currently one of the most drawbacks of arterial spin labeling (ASL) imaging preventing its application in the clinical diagnosis. During the last years improvements were achieved through advanced sequence and labeling approaches for ASL such as pseudo-continuous labeling [56] or 3D imaging techniques [109, 283]. In addition, the continued advancements of magnetic resonance imaging (MRI) hardware provide one solution to the limited signal. Several studies indicated the potential of higher field strength for ASL MRI due to the higher SNR and prolonged T_1 of blood and tissue [16, 97, 205, 263, 291]. However, ASL at stronger fields presents several challenges: stronger susceptibility artifacts, higher SAR, and compromised labeling efficiency due to inhomogeneities in B_1 and B_0 fields [263]. Beside sequence and hardware improvements, data post-processing methods have become increasingly important for addressing some limitations in ASL. In particular, motion correction algorithm [293, 294], temporal filtering methods, and outlier correction approaches [18, 83, 183, 234, 261, 293] were successfully applied to ASL and provide increased SNR, improved perfusion quantification, and increased reproducibility [84] by eliminating corruptions in the acquired data. Additional improvements were achieved using non-linear denoising methods for the images. Several groups have studied the performance of denoising techniques applied to ASL images. Different denoising strategies were proposed, for example denoising in the wavelet domain [22, 299], in the image domain using adaptive filtering [299], non-local means filtering [202], combination of non-local means filtering with wavelet domain filtering [161], or total variation denoising in combination with tissue partial volume effect correction [202]. All denoising methods use the perfusion weighted image (control - label) as input for denoising to improve the robustness of the cerebral blood flow (CBF) quantification [84]. In this chapter different types of total generalized variation (TGV) [31] denoising methods for ASL are developed and their performance are investigated. The first method is a TGV-denoising applied on the averaged perfusion weighted image (PWI) using L^1 and L^2 data-fidelity norms, similar to the previous published denoising methods. Second, an extension including the PWI time series directly in the denoising procedure and third, a denoising approach that is matched to the label/control image time series of ASL MRI is investigated. The third TGV-based denoising approach combines temporal and spatial information of the whole available dataset for improving the quality of ASL images. The incorporation of temporal information in the denoising process may be beneficial for detecting outliers. The performance of this novel technique and its influence on the CBF quantification is evaluated on synthetic and experimental in-vivo high and standard resolution pulsed arterial spin labeling (PASL) data with varying numbers of control-label pairs. Additionally, the proposed method is compared to recently published and well established denoising techniques.

3.2 Theory

3.2.1 Variational Methods for Image Denoising

Denoising is a fundamental image processing technique with the aim of recovering or estimating the original image from a noisy observed image. The problem can be modeled as follows

$$d(x, y) = u(x, y) + n(x, y) \ , \tag{3.1}$$

where $d(x, y) \in \Re^{N_x \times N_y}$ is the observed corrupted noisy image, $u(x, y) \in \Re^{N_x \times N_y}$ is the clean noise free image, and $n(x, y) \in \Re^{N_x \times N_y}$ is the additive noise which represents the unwanted information and degrades the image quality. We denote by x and y the pixel location and by N_x and N_y the image size. Over the last decades denoising approaches have been extensively studied with the aim to remove noise while preserving small textures, fine details, and edges. Especially in MRI this detail preservation is important for clinical diagnostics. The estimation of the original image u from the noisy one d is an inverse problem. The solution of this problem is not trivial because in practice only little is know about the noise n in the image i.e. only a guess of the noise distribution or the mean and variance. Since the noise n is random the problem can be solved using probability theory. From a statistical point of view, the maximum likelihood (ML) estimate yields optimal results for a given distribution [82]

$$u^* \in \arg\max_u \, P\left(d \mid u\right), \tag{3.2}$$

where u is the estimated image and d is the measured data or image. By assuming independent identical distributed sample points, which is true for single-coil MRI measurements, the maximum likelihood is given by

$$\begin{aligned} u^* &= \arg\max_u \, P\left(d \mid u\right) \\ &= \arg\max_u \frac{1}{\sqrt{2\pi\sigma^2}} exp\left(-\frac{1}{2\sigma^2}\sum_{i,j} u - d\right), \end{aligned} \tag{3.3}$$

where σ^2 is the noise variance. By omitting constant terms and applying the log, the solution of this problem leads to the well known least squares solution where the sum of squared error between the estimated image and the denoised image is minimized. [82]

$$u^* = \arg\min_u ||u - d||_2^2 \tag{3.4}$$

The simplest and fastest type of noise removal approach relying on the maximum likelihood principle is the linear mean filter. In this filter the signal intensity is assumed to be constant within a region and the single pixel values are statistically independent observations [214]. By averaging all signal intensities within the region the noise is reduced, however, edges are blurred and fine details can be lost. In a probabilistic setting, a way to improve the detail preservation is using filtering approaches which incorporate prior information of the images. These kind of algorithms are known as variational denoising methods. The motivation for variational image denoising methods is based on Maximum-a-Posteriori (MAP) probability estimation. By knowledge of the degradation model $P(d \mid u)$ and an adequate prior $P(u)$ the most likely image given the observed data and prior can be estimated by maximizing [82]

$$\begin{aligned} u^* &\in \arg\max_u \, P(u \mid d) \\ &\in \arg\max_u \, P(d \mid u) \; P(u) \\ &\in \arg\min_u - logP(d \mid u) - logP(u). \end{aligned} \tag{3.5}$$

The term $-logP(y \mid u)$ is often referred as data fidelity term $D(u, d)$ that denotes the difference between the original and noisy image and the term $-logP(u)$ as regularization term $R(u)$, which contains the prior information or assumption on the likelihood of a solution u. Hence, equation 3.5 can be generally written as

$$u^* \in \arg\min_u \, D(u, d) + R(u). \tag{3.6}$$

For the data-fidelity term, the optimal solution from a statistical point of view is given by the maximum likelihood estimation, which is for example the L^2 norm for Gaussian noise statistics (equation 3.3) or the L^1 norm for Laplacian noise statistics. The choice of the prior distribution of the image $P(u)$ is a critical and challenging part because it defines the appearance of the images. The major problem is that the prior knowledge is often only qualitative in nature i.e. we can describe the images encountered in medical imaging as smooth areas divided by jumps or cliffs. The idea is now to formalize mathematically a function or prior, which produces low values for images belonging to the model, and producing high values for images not belonging to the model. Many different priors have been proposed over the past years i.e. Gaussian priors, Laplacian priors or impulse prior densities, and Markov random fields (MRF) priors. In the following subsection three prominent priors for image denoising are described.

3.2.1.1 Tikhonov-Phillips Regularization

Tikhonov and Phillips proposed to use a Gaussian or smoothing prior on the image u and formalized a general regularization framework [206, 266]:

$$u^* \in \arg\min_u ||Au - d||_2^2 + \frac{\lambda}{2} ||\Gamma u||_2^2 , \tag{3.7}$$

where the first norm proposes a solution in the maximum likelihood sense (equation 3.3) and for image denoising the linear operator A is the identity operator I. The second norm is the regularization term with the linear regularization operator Γ and the regularization parameter λ. [138] By assuming Γ being the identity operator I, the Tikhonov regularization corresponds to a Gaussian prior with zero mean and $\frac{1}{\lambda}$ variance

$$P(u) = N\left(u; 0; \frac{1}{\lambda} I\right) = \left(\frac{\lambda}{2\pi}\right)^{\frac{D}{2}} exp\left(-\frac{\lambda}{2} ||u||_2^2\right) . \tag{3.8}$$

By omitting the constant term the prior is

$$P(u) \propto exp\left(-\frac{\lambda}{2}\left|\left|u\right|\right|_2^2\right), \tag{3.9}$$

leading to the following regularization term

$$R(u) = -logP(u) = \frac{\lambda}{2}\left|\left|u\right|\right|_2^2. \tag{3.10}$$

This regularization penalizes the L^2 norm of the image u. While this is a good regularization approach for parameter estimation it is not well suited for image denoising because it is only performed on a voxel by voxel basis. Hence, it does not take into account neighborhood information leading to no effective noise removal [39]. Since MRI images show a high degree of spatial regularity [39], a useful prior should take into account the neighborhood information of images. In this case, the regularization operator Γ can be defined as a discrete 2D gradient operator (equation 3.12), which is also known as H1-regularization:

$$R(u) = -logP(u) = \frac{\lambda}{2}\left|\left|\nabla u\right|\right|_2^2 \ , \tag{3.11}$$

where ∇ is the discrete 2D gradient operator ($\nabla : \Re^{N_x \times N_y} \mapsto \Re^{N_x \times N_y \times 2}$) defined as

$$(\nabla u)_{i,j} = \begin{pmatrix} (\partial_x^+ u)_{i,j} \\ \left(\partial_y^+ u\right)_{i,j}, \end{pmatrix} \tag{3.12}$$

where ∂_x^+ and ∂_y^+ are the discrete forward differences as defined in the Appendix C.1.1. The introduced gradient of the image takes now the spatial neighborhood into account and leads to a superior noise removal compared to the Tikhonov-regularization [39]. However, the L^2-norm penalizes the gradient belonging to edges very strong leading to an oversmoothing in the images. A good prior for image denoising should ensure spatial regularity but should also preserve edges [39]. To ensure this the L^2 norm can be replaced by a sparsity promoting norm for example a L^1 or L^0 norm [13]. One of the first approaches in this direction was done by Rudin et al. [218] by using a L^1 norm and is known as total variation (TV) [218].

3.2.1.2 Total Variation (TV)

The TV minimization for image denoising was introduced by Rudin, Osher, and Fatemi and is also known as ROF-model [218]. It is based on the principle that noise corrupted images or signals have a high total variation, which means in the discrete setting that the sum of the absolute gradient is high. The TV allows for discontinuities between objects, but eliminates oscillations. TV is the L^1 norm of the image gradient and is defined in a discrete setting as the following functional

$$R(u) = TV(u) = \left|\left|\nabla u\right|\right|_1, \tag{3.13}$$

with the discrete 2D gradient operator ∇ defined in equation 3.12. This L^1-penalization of the gradient leads to superior results compared to Tikhonov-regularization with a well preservation of object boundaries while eliminating noise. However, the main and crucial disadvantage of TV is that it tends to produce the so called stair-casing artifacts [70]. This means that the functional enforces piecewise constant regions and hence, smooth regions in the original image are represented as piecewise constant areas. In order to alleviate this disadvantage, several methods using higher order derivatives were proposed such as infimal-convolution functional [40], gradient and laplacian operators [42], or the total generalized variation functional [31].

3.2.1.3 Total Generalized Variation (TGV)

The TGV was introduced in 2010 by Bredies et al. [31]. It is a generalized version of TV, which involves and balances higher order derivatives of the images up to a certain order. This allows the reconstruction of piecewise affine or piecewise smooth solutions and thereby avoids the stair-casing artifacts of TV leading to an enhanced image quality of natural [31] and MRI [147] images. The dual version of the k-th order TGV functional is given by

$$\begin{aligned} TGV_{\alpha}^{k}(u) = \sup \Bigg\{ \int_{\Omega} u \operatorname{div}^{k} v \, \mathrm{dx} \mid v \in C_{c}^{k}\left(\Omega, \operatorname{Sym}^{k}\left(\Re^{d}\right)\right), \\ \left|\left|\operatorname{div}^{l} v\right|\right|_{\infty} \leq \alpha_{l},\ l = 0, \ldots, k-1 \Bigg\}, \end{aligned} \tag{3.14}$$

where $C_c^k\left(\Omega, \operatorname{Sym}^k\left(\Re^d\right)\right)$ denotes the space of compactly supported symmetric tensors fields with $\Omega \subset \Re^d$, div^k is the k-th order divergence operator of the tensor field (defined for first and second order in Appendix C.1.7 and C.1.8) and α_l are positive weights [31]. The higher order derivatives favor piecewise polynomial solutions with the degree of polynomials less than or equal to k-1. For example a first order TGV corresponds to a TV ($TGV^1(u) = TV(u)$) and enforces piecewise constant regions, a second-order TGV enforces piecewise affine regions, and a third order TGV enforces piecewise smooth regions etc. [323]. However, a higher order comes at the cost of a higher computational burden. Bredies et al. [31] showed that a TGV^2 faithfully restores smooth images and avoids the stair-casing effect of TV. The third order TGV (TGV^3) reconstructs regions of high curvature better but at the cost of more regularized transitions at edges. For many applications the second order TGV is sufficient and delivers meaningful results while keep the computational burdened low [31]. Therefore, it is normally applied for image enhancement of natural and MRI images and we focus on this definition.

$$R(u) = TGV_{\alpha_1,\alpha_0}^2(u) \quad = \min_{v} \left\{ \alpha_1 \left|\left|\nabla u - v\right|\right|_1 + \alpha_0 \left|\left|\epsilon v\right|\right|_1 \right\}, \tag{3.15}$$

where ∇ is the 2D discrete gradient (equation 3.12) and ϵ is the symmetrized gradient operator defined as follows:

$$\epsilon : v = (v^1, v^2) \in \Re^{N_x \times N_y \times 2} \mapsto \Re^{N_x \times N_y \times 3} \tag{3.16}$$

$$(\epsilon v)_{i,j} = \begin{pmatrix} \left(\partial_x^- v^1\right)_{i,j} \\ \frac{1}{2}\left(\left(\partial_x^- v^2\right)_{i,j} + \left(\partial_y^- v^1\right)_{i,j}\right) \\ \left(\partial_y^- v^2\right)_{i,j} \end{pmatrix} = \begin{pmatrix} w^1 \\ w^2 \\ w^3 \end{pmatrix} \tag{3.17}$$

From equation 3.15 it is evident that the TGV^2-functional automatically balances between first order TV and second-order TV in the minimization problem i.e. if v is zero the symmetrized gradient ϵv is zero and $TGV^2(u) = \alpha_1 \left|\left|\nabla u\right|\right|_1$, whereas if $v = \nabla u$ the first part of the TGV functional becomes zero resulting in $TGV^2(u) = \epsilon(\nabla u))$. In reality the tensor v is somewhere between 0 and ∇u. The TGV^2 functional was successfully applied in several MRI applications from reconstruction [147] to denoising [147] over diffusion tensor imaging [274] and is used in the following section for ASL image denoising and in chapter 7 for ASL image reconstruction.

3.2.2 Total Generalized Variation for ASL Denoising

3.2.2.1 TGV Denoising using L^1/L^2 Data Norm for ASL

In ASL imaging the aim is to enhance the SNR and image quality of the perfusion weighted image. This can be achieved in two different ways: Either by denoising the control image c and label image l and by calculating the PWI from those denoised images, or by applying the denoising approach directly to the perfusion weighted image (C-L). Wells et al. studied the influence of different denoising approaches for ASL images and they argued that the PWI reveals many sharp boundaries between regions of contrasting CBF, which may not be apparent in the base (C, L) images, limiting the benefit of edge-preserving filters [299]. Therefore, we focus on directly denoising the PWI by solving the following minimization problem:

$$u^* \in \arg\min_u \frac{\lambda}{2} \left|\left|u - d_u\right|\right|_2^2 + TGV_{\alpha_1,\alpha_0}^2 (u), \tag{3.18}$$

where $u \in R^{N_x x N_y}$ is the denoised perfusion weighted image and $d_u \in R^{N_x x N_y}$ the averaged noisy PWI. A numerical solution of the minimization problem can be found in Appendix C.2. One notices that in ASL imaging always repeated measurements are performed to achieve a reasonable SNR. Therefore, instead of prior averaging of the perfusion weighted images over the time, one could include this directly in the optimization procedure to make use of this additional temporal information. In this case an additional operator $\varsigma : R^{N_x x N_y} \mapsto R^{N_x x N_y x N_t}$ is introduced in the data-fidelity term which leads to the following minimization problem:

$$u^* \in \arg\min_{u} \frac{\lambda}{2} \left|\left|\varsigma u - d_u\right|\right|_2^2 + TGV^2_{\alpha_1,\alpha_0}\left(u\right), \tag{3.19}$$

where again $u \in R^{N_x x N_y}$ is the denoised perfusion weighted image and $d_u \in R^{N_x x N_y x N_t}$ is now the corresponding PWI time series (averages). The operator ς replicates the image (u) N_t times over the temporal dimension so that $\varsigma u \in R^{N_x x N_y x N_t}$. A minimization of the defined data fidelity term leads now to the element-wise mean over the temporal dimension. In the above algorithm, the L^2 norm of the data fidelity term can be replaced by a L^1 norm leading to the element-wise median with respect to the temporal dimension. Since ASL images are often corrupted with outliers, this could be very beneficial for improving the robustness leading to the following optimization problem:

$$u^* \in \arg\min_{u} \lambda \left|\left|\varsigma u - d_u\right|\right|_1 + TGV^2_{\alpha_1,\alpha_0}\left(u\right). \tag{3.20}$$

The defined minimization problems are non-smooth but convex and can be efficiently solved with a first order primal dual algorithm as described in section 3.2.2.3 "Numerical Solution". The numerical solution and corresponding algorithm are given in Appendix C.2.

3.2.2.2 Extension to C/L Denoising

Instead of denoising the perfusion weighted time series, equation 3.20 can be extended by including the whole available ASL data. Mathematically, the aim is to recover an estimate of the control data c and label data l from the given measured control data d_c and label data d_l. In order for c and l to be a robust estimated of d_c and d_l, it should minimize $||\varsigma c - d_c||_1$ and $||\varsigma l - d_l||_1$ similar to the PWI denoising in equation 3.20. Next, l should adhere to the image model proposed above. Therefore, it should minimize $TGV^2_{\alpha_1,\alpha_0}(l)$. In a last step, one is tempted to propose that c should also adhere to the image model by minimizing a related TGV functional. However, one observes that the images c and l have a much higher dynamical range than the difference of the denoised images. Furthermore, the difference of these images is the key quantity in ASL applications. Therefore, far superior results are to be expected if one forces the difference to adhere to the image model by minimizing $TGV^2_{\alpha_1,\alpha_0}(c-l)$. Altogether, c and l should be chosen so that the functional

$$(c^*, l^*) \in \arg\min_{c,l} \frac{\lambda_c}{M} \left|\left|\varsigma c - d_c\right|\right|_M^M + \frac{\lambda_l}{M} \left|\left|\varsigma l - d_l\right|\right|_M^M + TGV^2_{\alpha_1,\alpha_0}\left(l\right) + TGV^2_{\alpha_1,\alpha_0}\left(c-l\right) \tag{3.21}$$

is minimal, where M defines the norm for the data-fidelity term and is either 1 for the L^1 norm or 2 for the squared L^2 norm. Note, that by a similar argument the term $TGV^2_{\alpha_1,\alpha_0}(l)$ could also be replaced by $TGV^2_{\alpha_1,\alpha_0}(c)$. In our experience, the difference between both cases is negligible. The regularization parameters λ_c and λ_l allow a weighting between data fidelity versus regularization. This parameters are chosen according to the noise level of the datasets. Since the expected noise level in control and label image is nearly the same, the same regularization parameters are used for both data terms. In order to control the weighting between the two TGV functional an additional parameter $w \in (0,1)$ is introduced leading finally to the following functional

$$\begin{aligned}(c^*, l^*) \in \arg\min_{c,l} \frac{\lambda}{M} \|\varsigma c - d_c\|_M^M + \frac{\lambda}{M} \|\varsigma l - d_l\|_M^M + \\ \gamma_1(w) TGV^2_{\alpha_1,\alpha_0}(l) + \gamma_2(w) TGV^2_{\alpha_1,\alpha_0}(c-l)\,.\end{aligned} \tag{3.22}$$

The weights are chosen as described in [222] to ensure that the overall costs of the functional does not reduce to zero:

$$\gamma_1(w) = \frac{w}{\min(w, 1-w)}, \qquad \gamma_2(w) = \frac{(1-w)}{\min(w, 1-w)} \tag{3.23}$$

This minimization problem is non-smooth but convex and can be efficiently solved with the primal-dual algorithm described in the following section. The reformulation and numerical solution is given in Appendix C.2.

3.2.2.3 Numerical Solution

Any optimization method for non-smooth convex problems can be employed to solve the minimization problem presented in the last section. A well suited algorithm, which ensures global convergence, is the primal-dual algorithm [41]. With this general algorithm any kind of convex minimization problems of the following form

$$\min_x \; F(Kx) + G(x) \tag{3.24}$$

can be efficiently solved, where F and G are convex functions and K is a linear operator. By using the convex conjugate (equation 3.28) the primal problem 3.24 can be transformed into a saddle-point problem as follows:

$$F(Kx) = \max_y \langle Kx, y\rangle - F^*(y) \quad \longrightarrow \quad \min_x \max_y \langle Kx, y\rangle + G(x) - F^*(y)\,, \tag{3.25}$$

with F^* being the convex conjugate of F. The solution of this convex-concave saddle point problem is obtained with the primal-dual algorithm presented in [41], which alternates a proximal gradient descent in the primal and a proximal gradient ascent step in the dual direction (see Algorithm 1). The stepsizes in the primal and dual direction are defined by τ and σ respectively.

Algorithm 1 Primal Dual Algorithm

```
Initialization: Choose $\tau, \sigma > 0$ so that $\tau\sigma \left|\left|K\right|\right|_2 < 1$, $\left(x^0, y^0\right) \in \Re_x^N \times \Re_y^N$ and set $\bar{x}^0 = x^0$
For $n \geq 0$, compute $x^n$,$y^n$,$\bar{x}^n$ as follows:
    $$\begin{cases} y^{n+1} = \left(I + \sigma\partial F^*\right)^{-1}\left(y^n + \sigma K\bar{x}^n\right) \\ x^{n+1} = \left(I + \tau\partial G\right)^{-1}\left(x^n - \tau K^* y^{n+1}\right) \\ \bar{x}^{n+1} = 2x^{n+1} - x^n \end{cases} \qquad (3.26)$$
```

In the above algorithm the expressions $\left(I + \sigma\partial F^*\right)^{-1}$ and $\left(I + \tau\partial G\right)^{-1}$ are the proximal maps of F^* and G, and K^* is the adjoint operator to K. The algorithm ensures global convergence if the stepsizes τ, σ satisfy $\tau\sigma \left|\left|K\right|\right|_2 < 1$ and it is well suited for our convex but non-smooth problems [41]. All necessary steps in this algorithm reduce to simple arithmetic operations, which can be implemented highly parallelized on a GPU for a fast calculation. [130] For solving the problems defined in section 3.2.2, the primal problem has to be reformulated into a saddle-point problem. This is exemplary carried out for the full TGV problem formulated in equation 3.22 using the L^1 norm. For the other two problems, the numerical solution is given in Appendix C.2. With the definitions of the gradient (equation 3.12), symmetrized gradient (equation 3.17) and the introduced weighting function (equation 3.23) the full optimization problem of equation 3.22 is given by

$$\begin{aligned} &\min_{c,l} \lambda \left|\left|\varsigma c - d_c\right|\right|_1 + \lambda \left|\left|\varsigma l - d_l\right|\right|_1 + \\ &\min_{q_1} \gamma_1(w)\alpha_1 \left|\left|\nabla l - q_1\right|\right|_1 + \gamma_1(w)\alpha_0 \left|\left|\epsilon q_1\right|\right|_1 + \\ &\min_{p_1} \gamma_2(w)\alpha_1 \left|\left|\nabla\left(c - l\right) - p_1\right|\right|_1 + \gamma_2(w)\alpha_0 \left|\left|\epsilon p_1\right|\right|_1 . \end{aligned} \tag{3.27}$$

As previously mentioned this problem has to be reformulated into a saddle point problem. This is achieved by calculating the convex conjugates of the functions. The Fenchel conjugate or convex conjugate of a function $f(x)$ is defined as

$$f^*(y) = \sup_x \langle x, y\rangle - f(x). \tag{3.28}$$

Let $f(x)$ be any kind of norm $||\cdot||$, then the Fenchel conjugate is given by

$$f^*(y) = \begin{cases} 0 & \left|\left|y\right|\right|_* \leq 1 \\ +\infty & \left|\left|y\right|\right|_* > 1. \end{cases} \tag{3.29}$$

Here, $\left|\left|y\right|\right|_*$ is the dual norm of a norm $||\cdot||$ defined as

$$||y||_* = \max_{||x|| \leq 1} \langle x, y \rangle . \tag{3.30}$$

In general, the dual of the L^p norm $(||\cdot||_p)$ is the L^q norm $(||\cdot||_q)$ with $1/p + 1/q = 1$. For example, the dual norm of the L^1 norm is the infinity norm and the L^2 norm is again a L^2 norm in the dual formalism. The Fenchel conjugate of the L^1 norm is given by

$$f^*(y) = I_{||\cdot||_\infty \leq 1}(y) = \begin{cases} 0 & ||y||_\infty \leq 1 \\ +\infty & ||y||_\infty > 1, \end{cases} \tag{3.31}$$

where $I_{||\cdot||_\infty \leq 1}(y)$ is the indicator function. By using the defined Fenchel conjugate (equation 3.28), the TGV functional can be transformed into a saddle point problem. The first part of the functional yields

$$\min_{q_1} \gamma_1(w)\alpha_1 \, ||\nabla l - q_1||_1 \quad \longrightarrow \quad \min_{q_1} \quad \max_{q_2} \langle \nabla l - q_1, q_2 \rangle - I_{||\cdot||_\infty \leq \alpha_1\gamma_1}(q_2) , \tag{3.32}$$

and the second part yields

$$\min_{q_1} \gamma_1(w)\alpha_0 \, ||\epsilon q_1||_1 \quad \longrightarrow \quad \min_{q_1} \quad \max_{q_3} \langle \epsilon q_1, q_3 \rangle - I_{||\cdot||_\infty \leq \alpha_0\gamma_1}(q_3) . \tag{3.33}$$

Combining now equation 3.32 and 3.33, the primal-dual formulation of the whole TGV functional can be obtained.

$$TGV(l) = \min_{q_1} \max_{q_2,q_3} \langle \nabla l - q_1, q_2 \rangle + \langle \epsilon q_1, q_3 \rangle - I_{||\cdot||_\infty \leq \alpha_1\gamma_1}(q_2) - I_{||\cdot||_\infty \leq \alpha_1\gamma_1}(q_3) \tag{3.34}$$

Similar, the data-fidelity term can be reformulated as follows:

$$\max_{l} \lambda \, ||\varsigma l - d_l||_1 \quad \longrightarrow \quad \min_{l} \quad \max_{l_2} \langle \varsigma l - d_l, l_2 \rangle - I_{||\cdot||_\infty \leq \lambda}(l_2) \tag{3.35}$$

With the defined data-fidelity term and TGV functional the reformulation of the full optimization problem is given by

$$\begin{aligned} \underset{c,l,p_1,q_1}{min} \quad \underset{c_2,l_2,p_2,p_3,q_2,q_3}{max} \quad & \langle \varsigma c - d_c, c_2 \rangle - I_{||\cdot||_\infty \leq \lambda}(c_2) + \langle \varsigma l - d_l, l_2 \rangle - I_{||\cdot||_\infty \leq \lambda}(l_2) + \\ & \langle \nabla (c - l) - p_1, p_2 \rangle - I_{||\cdot||_\infty \leq \alpha_1\gamma_2}(p_2) + \\ & \langle \epsilon p_1, p_3 \rangle - I_{||\cdot||_\infty \leq \alpha_0\gamma_2}(p_3) + \\ & \langle \nabla (l) - q_1, q_2 \rangle - I_{||\cdot||_\infty \leq \alpha_1\gamma_1}(q_2) + \\ & \langle \epsilon q_1, q_3 \rangle - I_{||\cdot||_\infty \leq \alpha_0\gamma_1}(q_3) . \end{aligned} \tag{3.36}$$

In the above saddle point problem the primal variables are given by $\mathbf{x} = (c, l, p_1, p_2)$, the corresponding dual variables by $\mathbf{y} = (p_2, p_3, q_2, q_3, c_2, l_2)$ and the operator K by

$$K = \begin{pmatrix} \nabla & -\nabla & -Id & 0 \\ 0 & 0 & \epsilon & 0 \\ 0 & \nabla & 0 & -Id \\ 0 & 0 & 0 & \epsilon \\ \varsigma & 0 & 0 & 0 \\ 0 & \varsigma & 0 & 0 \end{pmatrix}. \tag{3.37}$$

The functional $G(x) = 0$ and the Fenchel conjugate $F^*(y)$ is

$$\begin{aligned} F^*(y) = {} & \langle d_c, c_2 \rangle + \langle d_l, l_2 \rangle + I_{||\cdot||_\infty \le \lambda}(c_2) + I_{||\cdot||_\infty \le \lambda}(l_2) + I_{||\cdot||_\infty \le \alpha_1 \gamma_2}(p_2) + \\ & I_{||\cdot||_\infty \le \alpha_0 \gamma_2}(p_3) + I_{||\cdot||_\infty \le \alpha_1 \gamma_1}(q_2) + I_{||\cdot||_\infty \le \alpha_0 \gamma_1}(q_3)\,. \end{aligned} \tag{3.38}$$

In the iterative primal dual scheme also the adjoint operators are required. The adjoint operator of K is given by K^*.

$$K^* = \begin{pmatrix} \nabla^* & 0 & 0 & 0 & \varsigma^* & 0 \\ -\nabla^* & 0 & \nabla^* & 0 & 0 & \varsigma^* \\ -Id & \epsilon^* & 0 & 0 & 0 & 0 \\ 0 & 0 & -Id & \epsilon^* & 0 & 0 \end{pmatrix}, \tag{3.39}$$

where ∇^* is the negative divergence $\nabla^* = -\mathrm{div}^1$ (equation 3.40), ϵ^* the negative symmetrized divergence operator $\epsilon^* = -\mathrm{div}^2$ (equation 3.41), and ς^* the collapse-operator (equation 3.42).

$$\begin{gathered} \mathrm{div}^1 : \Re^{N_x \times N_y \times 2} \mapsto \Re^{N_x \times N_y} \\ \left(\mathrm{div}^1 v\right)_{i,j} = \left(\left(\partial_x^{*+} v^1\right)_{i,j} + \left(\partial_y^{*+} v^2\right)_{i,j} \right) \end{gathered} \tag{3.40}$$

$$\begin{gathered} \mathrm{div}^2 : \Re^{N_x \times N_y \times 3} \mapsto \Re^{N_x \times N_y \times 2} \\ \left(\mathrm{div}^2 w\right)_{i,j} = \begin{pmatrix} \left(\partial_x^{*-} w_1\right)_{i,j} + \left(\partial_y^{*-} w_3\right)_{i,j} \\ \left(\partial_x^{*-} w_3\right)_{i,j} + \left(\partial_y^{*-} w_2\right)_{i,j} \end{pmatrix} \end{gathered} \tag{3.41}$$

$$\begin{gathered} \varsigma^* : \Re^{N_x \times N_y \times N_t} \mapsto \Re^{N_x \times N_y} \\ \varsigma^* x = \sum_{t=1}^{N_t} x[t] \end{gathered} \tag{3.42}$$

The final update scheme for the primal dual algorithm of the saddle point problem 3.36 is defined in Algorithm 2.

Algorithm 2 Primal Dual Algorithm for L^1 ASL-TGV denoising

```
Input: $d_c$, $d_l$
Output: $c$, $l$
Initialize: $p_1^0$, $p_2^0$, $p_3^0$, $q_1^0$, $q_2^0$, $q_3^0$, $c^0$, $c_2^0$, $l^0$, $l_2^0$, $\overline{c}^0$, $\overline{l}^0$, $\overline{p}_1^0$, $\overline{q}_1^0$, choose $\tau$,$\sigma > 0$

for $n = 0$ until maxIter
    Dual Update:
    $p_2^{n+1} = P_{\alpha_1,\gamma_1}\left(p_2^n + \sigma\left(\nabla\overline{c}^n - \nabla\overline{l}^n - \overline{p}_1^n\right)\right)$
    $p_3^{n+1} = P_{\alpha_0,\gamma_1}\left(p_3^n + \sigma\epsilon\overline{p}_1^n\right)$
    $q_2^{n+1} = P_{\alpha_1,\gamma_2}\left(q_2^n + \sigma\left(\nabla\overline{l}^n - \overline{q}_1^n\right)\right)$
    $q_3^{n+1} = P_{\alpha_0,\gamma_2}\left(q_3^n + \sigma\epsilon\overline{q}_1^n\right)$
    $c_2^{n+1} = P_\lambda\left(c_2^n + \sigma\left(\varsigma\overline{c}^n - d_c\right)\right)$
    $l_2^{n+1} = P_\lambda\left(l_2^n + \sigma\left(\varsigma\overline{l}^n - d_l\right)\right)$

    Primal Update:
    $c^{n+1} = c^n - \tau\left(\nabla^* p_2^{n+1} + \varsigma^* c_2^{n+1}\right)$
    $l^{n+1} = l^n - \tau\left(-\nabla^* p_2^{n+1} + \nabla^* q_2^{n+1} + \varsigma^* l_2^{n+1}\right)$
    $p_1^{n+1} = p_1^n - \tau\left(-p_2^{n+1} + \epsilon^* p_3^{n+1}\right)$
    $q_1^{n+1} = q_1^n - \tau\left(-q_2^{n+1} + \epsilon^* q_3^{n+1}\right)$

    Extrapolation step:
    $\overline{c}^{n+1} = 2c^{n+1} - c^n$
    $\overline{l}^{n+1} = 2l^{n+1} - l^n$
    $\overline{p}_1^{n+1} = 2p_1^{n+1} - p_1^n$
    $\overline{q}_1^{n+1} = 2q_1^{n+1} - q_1^n$
```

3.3 Methods

3.3.1 ASL Acquisition

The ASL experiments were carried out on a 3T magnetic resonance (MR) system (Magnetom Skyra, Siemens Healthcare, Germany). Pulsed ASL measurements were performed on eight healthy subjects (25.5 ± 1.2 years old with a range of 24-28, 4 women) using PICORE [304] - Q2TIPS [170] with a 32-channel head coil. Small wedge sponges were placed between the patient's head and the coil to reduce motion during the acquisition. Caffeine and tobacco ingestion were avoided before the MR acquisition to preclude alterations on the global and regional CBF [2, 71, 284].

The following acquisition parameters were used: 12 slices, 3.6 *mm* thickness, distance factor 25%, matrix 128 x 128, field of view (FoV) 230 x 230 mm^2, in-plane resolution 1.8 x 1.8 mm^2, 6/8 partial Fourier, generalized autocalibrating partial parallel acquisition

(GRAPPA)-factor 2 and pre-scan normalization. Imaging was conducted with single-shot echoplanar imaging (EPI) with repetition time (TR)/echo time (TE) = 2800/19 ms, flip angle = 90°, bolus or labeling duration (TI1) = 800 ms, labeling inversion time TI_2 = 1800 ms, labeling slab thickness 100 mm, 2 cm gap between labeling slab and image slice, ascending slice order and bandwidth = 1630 Hz/px. To compute an unfiltered reference perfusion weighted image, 500 control/label-pairs (C/L-pairs) and one proton density weighted (M_0) image were acquired within a total scanning time of 45 min.

In addition, standard resolution ASL images from 2 subjects with the following parameters were acquired: 12 slices, 6 mm thickness, distance factor 25%, matrix = 64 x 64, FoV = 192 x 192 mm^2, in-plane resolution 3 x 3 mm^2, 6/8 partial Fourier, bandwidth = 1630 Hz/px and pre-scan normalization. All other imaging parameters were the same as for the high resolution ASL dataset. To compute an unfiltered reference perfusion weighted image, 100 C/L-pairs and one proton density weighted image were acquired within a total scanning time of 9 min 25 s.

3.3.2 Anatomical Data Acquisition

Additionally, anatomical T_1 weighted images were acquired for each subject using a 3D magnetization prepared - rapid gradient echo (MPRAGE) sequence with 1 x 1 x 1 mm^3 resolution, FoV = 256 x 256 mm^2, 144 slices, GRAPPA-factor = 4, TR/TE/inversion time (TI) = 1910/1.81/1000 ms, flip angle = 8°, acquisition time = 2 min 53 s.

3.3.3 Anatomical Data Processing

For each subject, the acquired T_1 weighted image was segmented into white matter (WM), gray matter (GM) and cerebrospinal fluid (CSF) regions using statistical parameter mapping v 12 (SPM12)[1] (Wellcome Trust Centre for Neuroimaging, London, UK). The results of the segmentation process were tissue partial volume (PV)-content maps defining the amount or content of GM, WM, and CSF in each voxel. These tissue PV-content maps and the T_1 weighted images were coregistered to the ASL space using the first ASL-image as a reference. Afterwards the resulting coregistered tissue PV-content maps were used to create a brain mask. The CSF, WM, and GM PV-content maps were summarized resulting in a single PV-content map. In this map all voxels with a tissue PV-content greater than 0.1 were included in the brain mask, which delivers good results.

3.3.4 Numerical Phantom

High resolution synthetic image sets were generated from one subject (subject 8) based on the acquired M_0 image and the coregistered WM and GM PV-content maps [22]. In order to create a noise free CBF-map, CBF values of 20 $ml/100g/min$ and 65 $ml/100g/min$ [155, 325], reported for the normal human brain, were assigned to the WM (f_{WM}) and GM

---

[1] www.fil.ion.ucl.ac.uk/spm

(f_{GM}) voxel respectively. To incorporate realistic partial volume effects in the synthetic images, the GM, and WM PV-content maps were multiplied using the following equation:

$$f(x,y,z) = f_{GM}P_{GM}(x,y,z) + f_{WM}P_{WM}(x,y,z), \tag{3.43}$$

where $P_{GM}(x,y,z)$ is the PV-content map of GM defining the content of GM in the voxel at location (x,y,z), $P_{WM}(x,y,z)$ is the PV-content map of WM defining the content of WM in the voxel at location (x,y,z).

The control image C was assumed to be the M_0 image and the label image L was calculated in each voxel by using a general kinetic model [34]

$$L(x,y,z) = C(x,y,z) - \frac{2 \cdot \alpha \cdot M_0(x,y,z) \cdot f(x,y,z) \cdot TI_1 \cdot e^{-\frac{TI_2}{T_{1,b}}}}{\lambda}, \tag{3.44}$$

where α is the labeling efficiency and set to 0.98 [308], TI_1 is the labeling duration and set to 800 ms, TI_2 is the labeling inversion time and set to 1800 ms [8]. M_0 is the acquired proton density image, λ is the blood-brain partition coefficient and set to 0.9 ml/g [125], $T_{1,b}$ is the longitudinal relaxation time of blood at 3T and set to 1650 ms [169] and $f(x,y,z)$ is the synthetic CBF-map generated as described in equation 3.43. The computed synthetic CBF-map, the control, and label image are illustrated in Figure 3.1.

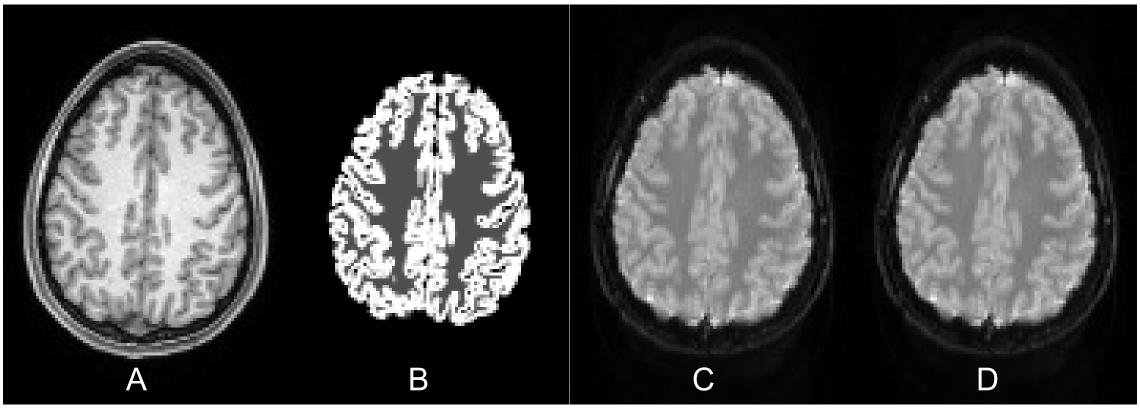

Figure 3.1: Coregistered and resampled T_1 weighted image in the ASL space (A) with voxel dimensions of 1.8 x 1.8 x 3.6 mm^3 of subject 8. Synthetic, noise free CBF-map (B) created from the coregistered white and gray matter PV-content maps. Noise free synthetic control (C) and label image (D).

To compute a synthetic dataset with a realistic noise level, the standard deviation over the 500 repetitions was estimated from the acquired high-resolution C and L images for each voxel. Subsequent Gaussian noise with a standard deviation previously estimated was added to each voxel of the synthetic noise free C and L images. This step was repeated 500 times to generate a synthetic data pool containing 500 C/L-pairs. The benchmark for the synthetic datasets consisted of 50 trials with 40, 50, 60, 80 and 100 randomly selected image pairs out of a data pool of 500.

3.3.5 ASL Data Processing

ASL image preprocessing was performed on the high and standard resolution in-vivo datasets using SPM12, MATLAB 2015b (The MathWorks, Inc., Natick, Massachusetts, USA), ASL-toolbox [293, 294], and in-house MATLAB scripts. Prior to spatial denoising, ASL datasets were preprocessed using the steps and algorithm recommended by Fazlollahi et al. [84]. First, the acquired ASL images were motion corrected using the ASL-toolbox. This involves realigning of all ASL images, including all label and control images, to the first ASL image (L) in the time series for estimating the rigid motion time course. Subsequently, errors in realignment resulting from the control/label intensity difference were regressed out from the motion time course as described by Wang et al. [293] and finally the clean motion parameters were used for motion-correction. In a second step the whole ASL time series was de-trended to remove baseline drifts. Therefore, a first order high-pass Butterworth filter with a cutoff frequency of 0.01Hz was applied to the ASL-image time series (L/C/L/C...) as described in [293, 295]. Third, residual motion artifacts and global signal fluctuations were regressed out of the ASL image time series at each voxel [293]. Prior to spatial denoising outlier C/L-pairs were removed using Z-score thresholding [261].

3.3.6 In-Vivo Dataset

The motion corrected, de-trended and outlier removed C/L-pairs served as a basis for all subsequently applied denoising methods. For the high resolution in-vivo dataset of subject 8, which was used to create the synthetic dataset, benchmarking was performed similar to the synthetic dataset and consisted of 50 trials with 40, 50, 60, 80 and 100 randomly selected image pairs out of a data pool of 500. For the best performing TGV approach as well as for all reference denoising methods additional benchmarking was performed using the remaining 7 high resolution in-vivo datasets. This consists of 50 trials with 50 randomly selected image pairs out of the acquired 500. In addition for the two standard resolution datasets, benchmarking was performed using 50 trials with 5, 8, 12, 15, 20 and 25 randomly selected image pairs out of a data pool of 100.

3.3.7 Parameter Choice

Previous studies [30, 148, 222] have shown, that setting the ratio α_1/α_0 to $1/\sqrt{2}$ yields robust results and this ratio is used throughout this work. For the CL-approaches the model parameter s, which controls the weighting between the first TGV and the second TGV functional, was fixed for the high-resolution and low resolution in-vivo and synthetic dataset by evaluating a range of parameters with respect to the structural similarity index [292]. The regularization parameter λ was optimized using a fixed s for different numbers of C/L-pairs. For the training of the two parameters slice 6 of subject 8 was used for the high-resolution in-vivo dataset and slice 6 was used for the synthetic dataset. Exemplary results of the parameter tuning are shown for the CL-T-L1 approach in Figure 3.2

using the in-vivo dataset. For all approaches the used model and regularization parameters for the high-resolution synthetic and in-vivo dataset are summarized in Table 3.1. For all experiments the number of iterations was set to 1 000.

Table 3.1: Optimized model and regularization parameters for the different TGV approaches

N	PWI L1	PWI L2	PWI-T-L1	PWI-T-L2	CL-T-L1		CL-T-L2	
	λ	λ	λ	λ	s	λ	s	λ
Synthetic Data								
40	1.375	3.050	1.90	0.155	0.475	2.15	0.5	0.200
50	1.475	3.325	1.90	0.135	0.475	2.25	0.5	0.200
60	1.525	3.675	1.85	0.125	0.475	2.45	0.5	0.200
80	1.525	4.050	1.85	0.100	0.475	2.75	0.5	0.175
100	1.575	4.075	1.85	0.100	0.475	3.00	0.5	0.150
In-Vivo Data								
40	1.375	1.025	2.25	0.040	0.4	4.25	0.45	0.1250
50	1.500	1.325	2.55	0.050	0.4	4.50	0.45	0.0975
60	1.525	1.425	2.55	0.045	0.4	4.75	0.45	0.0975
80	1.625	1.750	3.00	0.040	0.4	5.75	0.45	0.0825
100	1.625	2.475	3.25	0.045	0.4	6.50	0.45	0.0900

3.3.8 Reference Denoising Methods

We chose state of the art denoising methods which were successfully applied to ASL perfusion images in the past: Wavelet-based-Wiener (WbW) [22], iterative-soft thresholding [60], adaptive Wiener (aWNR) [299], Anisotropic Diffusion (AD) [299], DT-CWT ONLM [161], spatio-temporal low rank total variation (STLRTV) [83] and additional block matching 3D (BM3D) [54]. Each of the denoising filters is parameter dependent and the choice of the right parameter has a major impact on the denoising result. For the choice of the parameters we decided to maximize the SSIM between the gold standard and denoised image to evaluate the performance of each filter in a fair way, rather than using an empiric optimization by visual inspection. Compared to the root mean squared error (RMSE), the SSIM includes both the structure and the contrast of the image and therefore reflects the visual interpretation of the human eye in a better way [292]. Some of the filters have noise-dependent parameters, for which the noise was estimated for each voxel over the number of repetitions. The mean standard deviation σ over all pixels within the brain mask was computed and used as standard deviation [202].

3.3.8.1 Temporal Mean Filter

A perfusion weighted time series was calculated from the motion corrected, detrended and outlier cleaned control/label series by pairwise subtraction of the C/L-pairs. The single

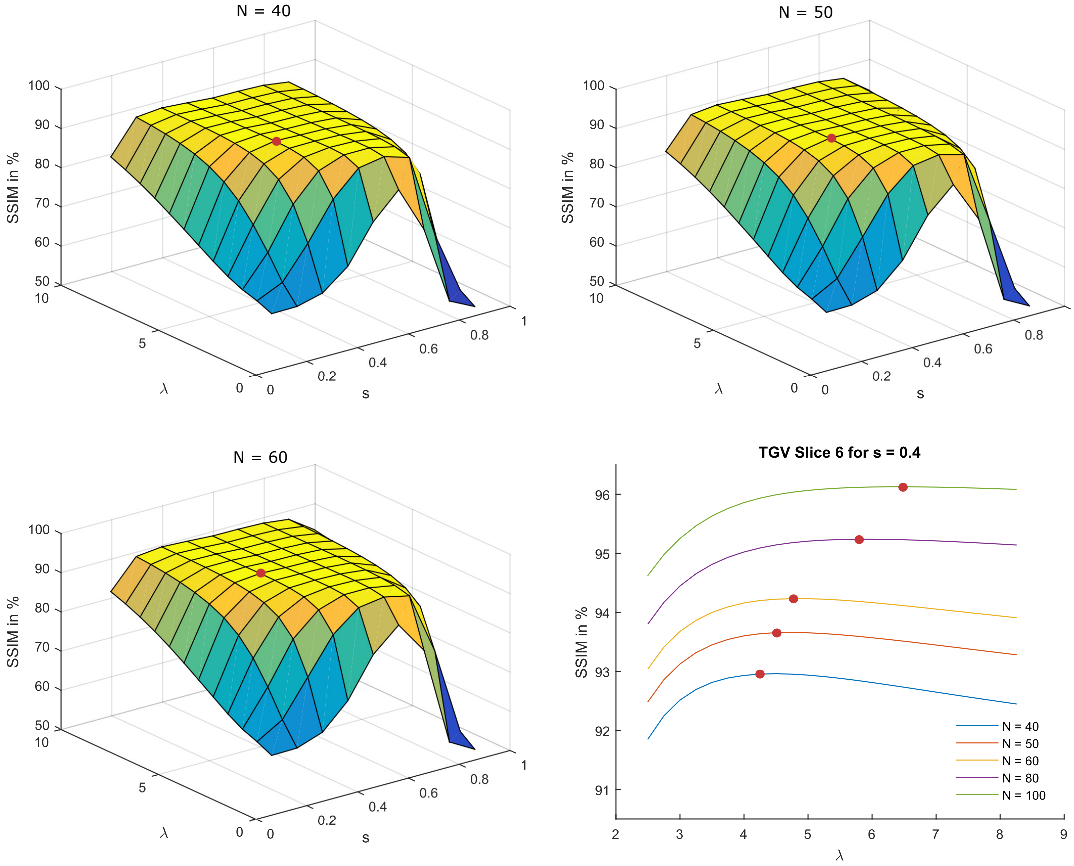

Figure 3.2: Results of the parameter learning for the CL-T-L1 approach on high resolution in-vivo images using 40, 50 and 60 C/L-pairs for slice 6 of subject 8. The red point indicates the maximum structural similarity index (SSIM)-value. The maximum value is achieved setting the parameter s to 0.4. The parameter λ depends on the noise level.

perfusion weighted images are so noisy, that the benefit of applying one of the highly sophisticated reference filters on these single images is very low. Furthermore, due to the subtraction of control and label images a separate denoising of these images leads to flatter edges compared to denoising the perfusion weighted image themselves [299]. Therefore, a mean perfusion weighted image was generated by averaging the perfusion weighted time series. This mean perfusion weighted image serves as basis for all following reference denoising methods with the exception of the STLRTV-filter which uses the perfusion weighted time series as input for denoising.

3.3.8.2 Anisotropic Diffusion (AD) Filter

The AD filter method was implemented in MATLAB [299]. For optimal performance of the filter the diffusion step time was set to 0.25 and the conduction coefficient K and the number of iterations were optimized as described above. Exemplary results of the parameter optimization process are shown in Figure 3.5.

3.3.8.3 Adaptive Wiener (aWNR) Filter

An adaptive Wiener filter based on the mean and variance in the local neighborhood of each voxel was implemented in MATLAB [299]. The kernel size and the global noise variance were optimized to ensure that the filter delivers best possible results.

3.3.8.4 Iterative Soft Thresholding (Wav(S))

The iterative soft thresholding algorithm [60] was implemented in MATLAB for the LeGall 5/3 wavelet [154]. The number of iterations was set to 5000 and the threshold factor was optimized.

3.3.8.5 Wavelet based Wiener (WbW) Filter

The WbW filter [22] was implemented in MATLAB using the Wavelet Toolbox. For the best possible performance the threshold factor was optimized.

3.3.8.6 Block Matching 3D (BM3D) Filter

The MATLAB implementation of the BM3D filter [54] was used for denoising[2]. The filter profile was set to "high" and the noise standard deviation σ was estimated as described above and scaled by a factor c to ensure best possible results in case that the noise level was not estimated sufficiently well.

3.3.8.7 Non-Local Means Combined Dual-Tree Complex Wavelet Transform (DT-CWT ONLM) Filter

The MATLAB version of the DT-CWT ONLM filter [161] was used[3]. All 6 parameters (M1, M2, α_1, α_2, β_1 and β_2) were optimized to ensure the best possible performance.

3.3.8.8 Spatio-Temporal Low Rank Total Variation (STLRTV) Filter

The STLRTV filter was implemented in MATLAB as described in [83]. For the best possible performance of the filter the parameters λ_{TV} and λ_{rank} were optimized.

3.3.9 Quantification of CBF

For the quantification of the CBF a general kinetic model was applied [34]. According to this model, the cerebral blood flow in ml/100g/min can be calculated in each voxel using the following equation:

---

[2] http://www.cs.tut.fi/ foi/3D-DFT

[3] https://www.nitrc.org/projects/dt-cwt-nlm

$$f(x,y,z) = \frac{\lambda \cdot \Delta M(x,y,z)}{2 \cdot \alpha \cdot M_0(x,y,z) \cdot TI_1 \cdot e^{-\frac{TI_2}{T_{1,b}}}}, \tag{3.45}$$

where ΔM is the denoised difference image and M_0 is the acquired proton density image smoothed with a Gaussian filter (full width at half maximum (FWHM) = 3 mm) as recommended by the consensus paper [8]. The total delay time TI_2 was set to 1800 ms for the leading slice. Because of using a multi-slice EPI readout with ascending slice order, an extra delay of 80 ms was added to TI_2 for each further slice acquired. [8] All other parameters were set to the same values as described in the section 3.3.4 "Numerical Phantom".

3.3.10 Evaluation

Two common metrics were used as a measure of denoising quality, the SSIM [292] and the peak signal-to-noise ratio (PSNR) [83, 161]. In case of the synthetic dataset the noise free CBF-map served as gold standard. For the experimental dataset the gold standard CBF-map was computed from the 500 C/L-pairs for the high resolution dataset and from the 100 C/L-pairs for the standard resolution dataset. All evaluation steps were performed on both, synthetic and experimental dataset.

3.3.10.1 Structural Similarity Index (SSIM)

Image structure degeneration and contrast difference between the gold standard CBF-map and the denoised CBF-map were analyzed using the quantitative structural similarity index [292].

3.3.10.2 Peak Signal-to-Noise Ratio (PSNR)

Peak signal-to-noise ratio, $PSNR = 20log_{10}(MAXi/RMSE)$, was used to evaluate the denoising results within the brain mask [83, 161]. RMSE denotes the root mean square error between the ground truth CBF-map and the denoised CBF-map and MAXi represent the maximum intensity value in the ground truth CBF-map.

3.4 Results

3.4.1 TGV Performance

Figure 3.3 shows the performance comparison of the different TGV based denoising methods for the synthetic dataset in dependence of averages. For all methods the quality of the CBF-maps can be improved compared to the standard mean filter. By including successive more information of the acquired ASL dataset the visual quality as well as the quantitative metrics can be improved. The L^1 norm performs better than the L^2 norm if additional temporal information is included.

Figure 3.7 shows typical high resolution CBF-maps from subject 8 before and after denoising using 40, 50, 80 and 100 C/L-pairs together with the gold standard CBF-map generated from all 500 C/L-pairs. Similar to the synthetic dataset the visual image quality and the quantitative metrics increases by incorporating additional information in the denoising process. The best performance is achieved using the CL-T-L1 approach. This method is compared with the reference denoising methods in the subsequent section.

3.4.2 Reference Denoising Methods

Figure 3.5 shows exemplary results of the optimization procedure for each reference denoising method. This figure clearly indicates that the parameters of each reference filter vary between subjects and also among slices of the same subject. To ensure best possible denoising results of the reference filters, the filter parameters were optimized for each subject and slice. It should be noted, that in contrast to the reference filtering methods our proposed method used the same parameters for all in-vivo datasets listed in Table 3.1.

Figure 3.6 shows exemplary the noise free, the noisy, and denoised synthetic CBF-maps using 40 (row A), 50 (row B), 80 (row C), and 100 (row D) C/L-pairs. Qualitative comparison of the CBF-maps shows a lower level of noise in all denoised CBF-maps compared to a simple mean filter. Further, as expected the visual quality of each CBF-map increases with increasing number of C/L-pairs. It can be seen that the various denoising techniques result in different noise removal performance and varying degree of spatial smoothing. In comparison to the reference denoising approaches the proposed TGV based method (CL-T-L1) shows improved noise removal, especially in the WM, while small features are still retained. Furthermore, the proposed method shows fewer overestimated CBF values, especially for low SNR (40 and 50 C/L-pairs) datasets.

Figure 3.7 shows typical high resolution CBF-maps from subject 8 before and after denoising using 40, 50, 80 and 100 C/L-pairs together with the gold standard CBF-map generated from all 500 C/L-pairs. Similar to the results of the synthetic datasets, the visual quality of the CBF-maps was improved in different ways. Furthermore, the proposed CL-T-L1 approach removes local outliers in the difference image, which were neither detected by the outlier algorithm nor by one of the seven reference denoising methods, as indicated by a red arrow in Figure 3.7. Such artificial outliers could be misleadingly interpreted as a hyper perfusion showing a clear benefit of the proposed method.

Additionally, Figure 3.8 shows a quantitative evaluation of all denoising approaches. The mean SSIM and mean PSNR are given for a different number of C/L-pairs of the high resolution synthetic and in-vivo dataset of subject 8. All denoising results are reported within the generated brain mask. As expected, the PSNR and SSIM increase with increasing numbers of control and label pairs. For low as well as high SNR the proposed approach yields the largest improvement in PSNR and in SSIM. These quantitative results

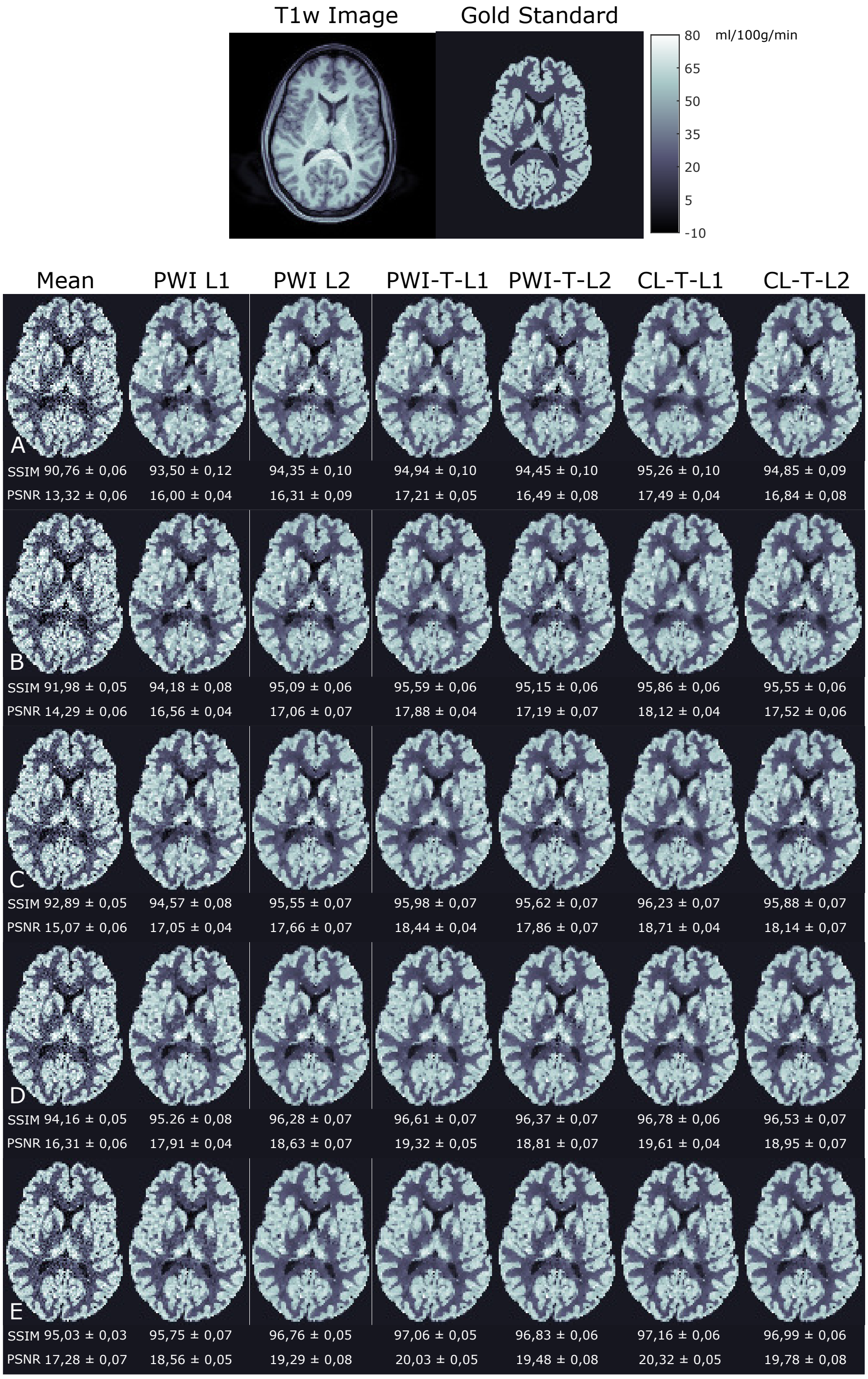

Figure 3.3: T_1 weighted image, gold standard CBF-map, noisy CBF-map and CBF-map calculated from the denoised difference image using 40 C/L-pairs (row A), 50 C/L-pairs (row B), 60 C/L-pairs (row C), 80 C/L-pairs (row D) and 100 C/L-pairs (row E) for slice 3 of the synthetic dataset. Additionally, the quantitative metrices SSIM and PSNR, averaged over all slices and runs are given for each denoising method. A qualitative and quantitative improvement is clearly visible going from the easiest methods performed on the difference image (PWI-L1 and PWI-L2) to the methods including also temporal information of the difference image (PWI-T-L1 and PWI-T-L2) to the methods using all available information simultaneously (CL-T-L1 and CL-T-L2).

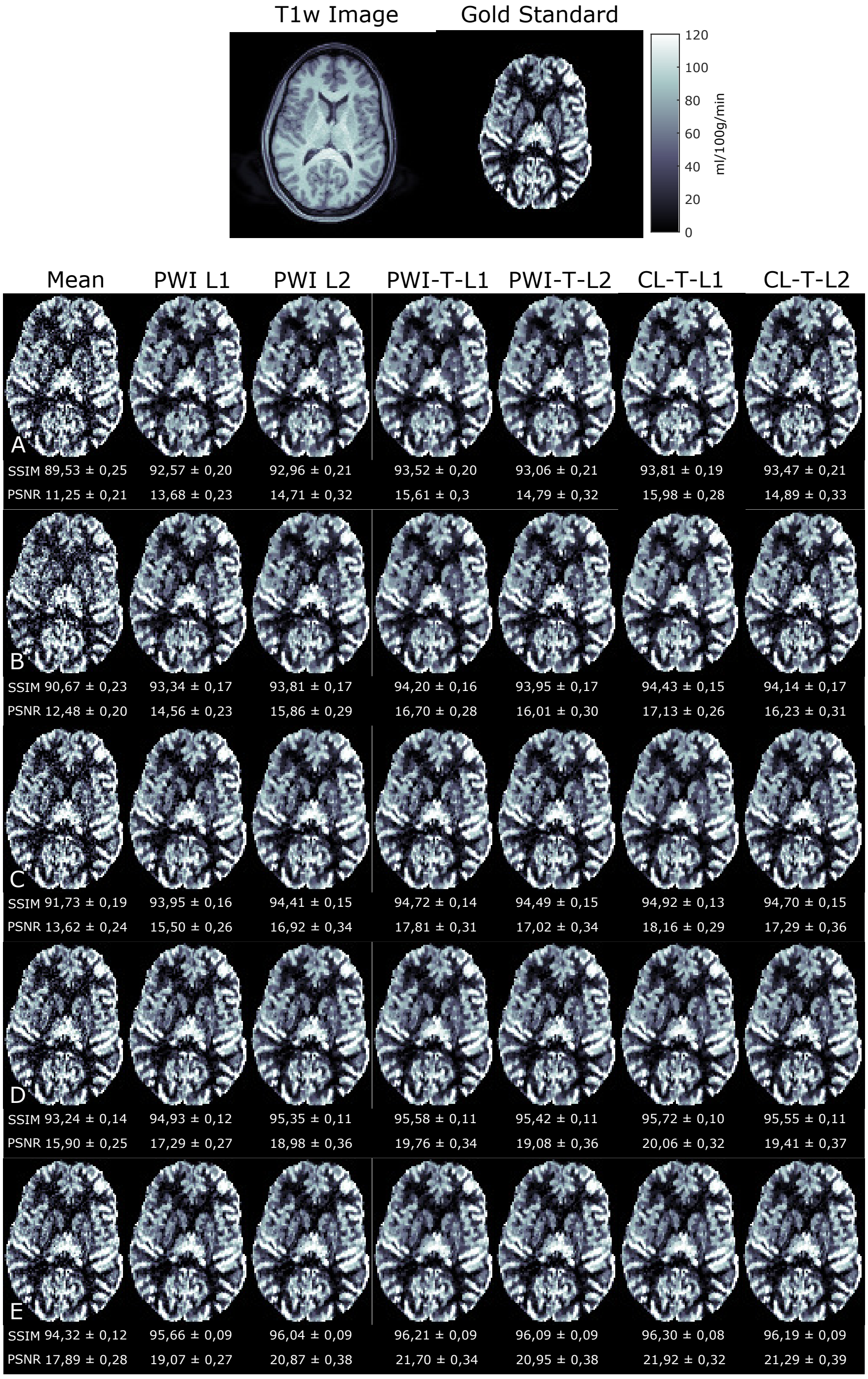

Figure 3.4: Top row shows the T_1 weighted image and the gold standard CBF-map calculated from 500 C/L-pairs from the in-vivo dataset of subject 8. Row A to E shows the noisy CBF-map and the CBF-map calculated from the denoised difference image using 40 C/L-pairs (row A), 50 C/L-pairs (row B), 60 C/L-pairs (row C), 80 C/L-pairs (row D) and 100 C/L-pairs (row E). Additionally the quantitative metrices SSIM and PSNR, averaged over all slices and runs are given for each denoising method. A qualitative and quantitative improvement is clearly visible going from the easiest methods performed on the difference image (PWI-L1 and PWI-L2) to the methods including also temporal information of the difference image (PWI-T-L1 and PWI-T-L2) to the methods using all available information simultaneously (CL-T-L1 and CL-T-L2).

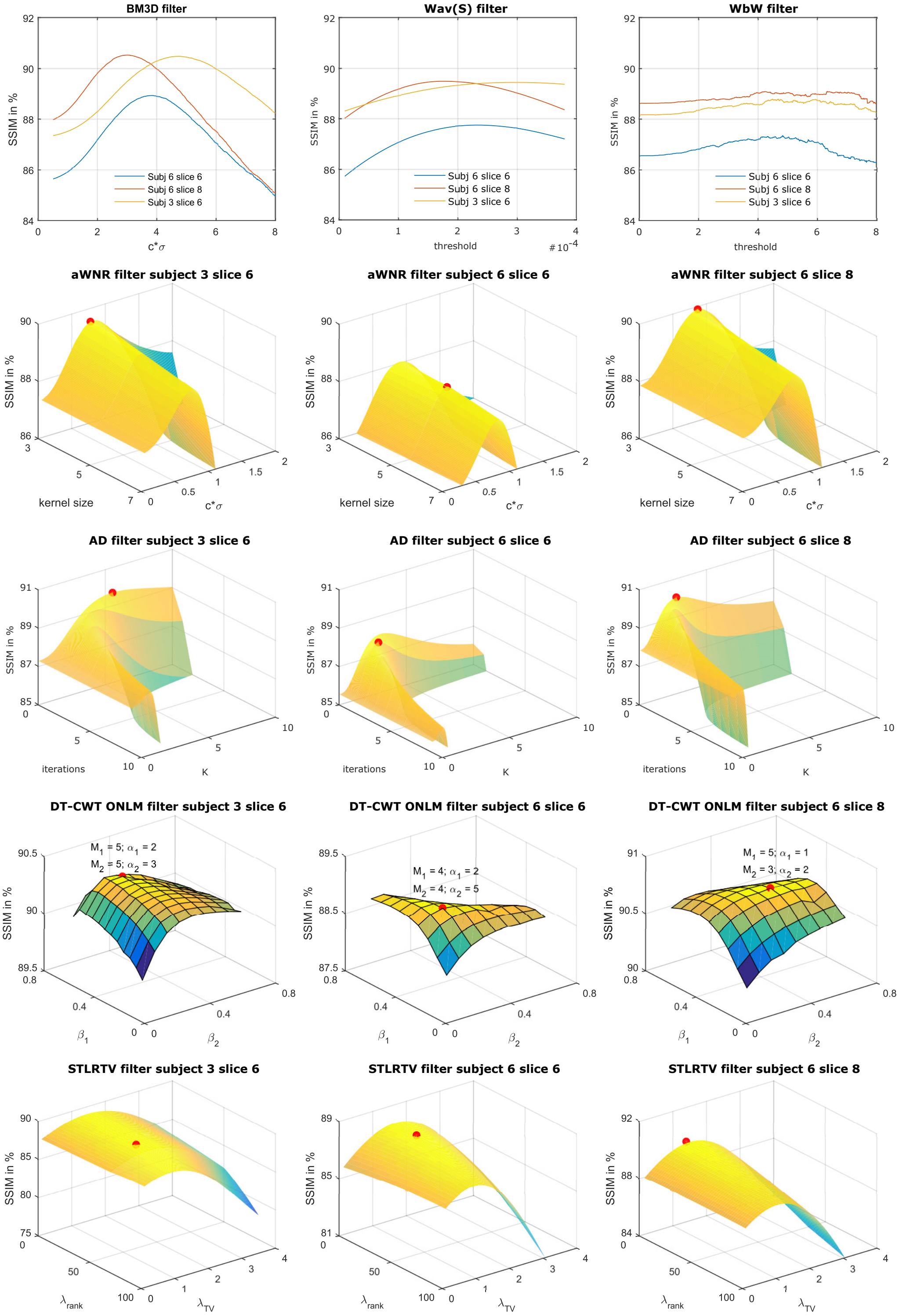
BM3D filter

Wav(S) filter

WbW filter

aWNR filter subject 3 slice 6

aWNR filter subject 6 slice 6

aWNR filter subject 6 slice 8

AD filter subject 3 slice 6

AD filter subject 6 slice 6

AD filter subject 6 slice 8

DT-CWT ONLM filter subject 3 slice 6

DT-CWT ONLM filter subject 6 slice 6

DT-CWT ONLM filter subject 6 slice 8

STLRTV filter subject 3 slice 6

STLRTV filter subject 6 slice 6

STLRTV filter subject 6 slice 8

Figure 3.5: Results for the reference denoising methods using 3 different slices from the high resolution dataset. In the 3D plots, the maximum is indicated by a red point for a clearer visualization. The optimal parameter for each filtering method varies between different slices of the same subject and also between different subjects.

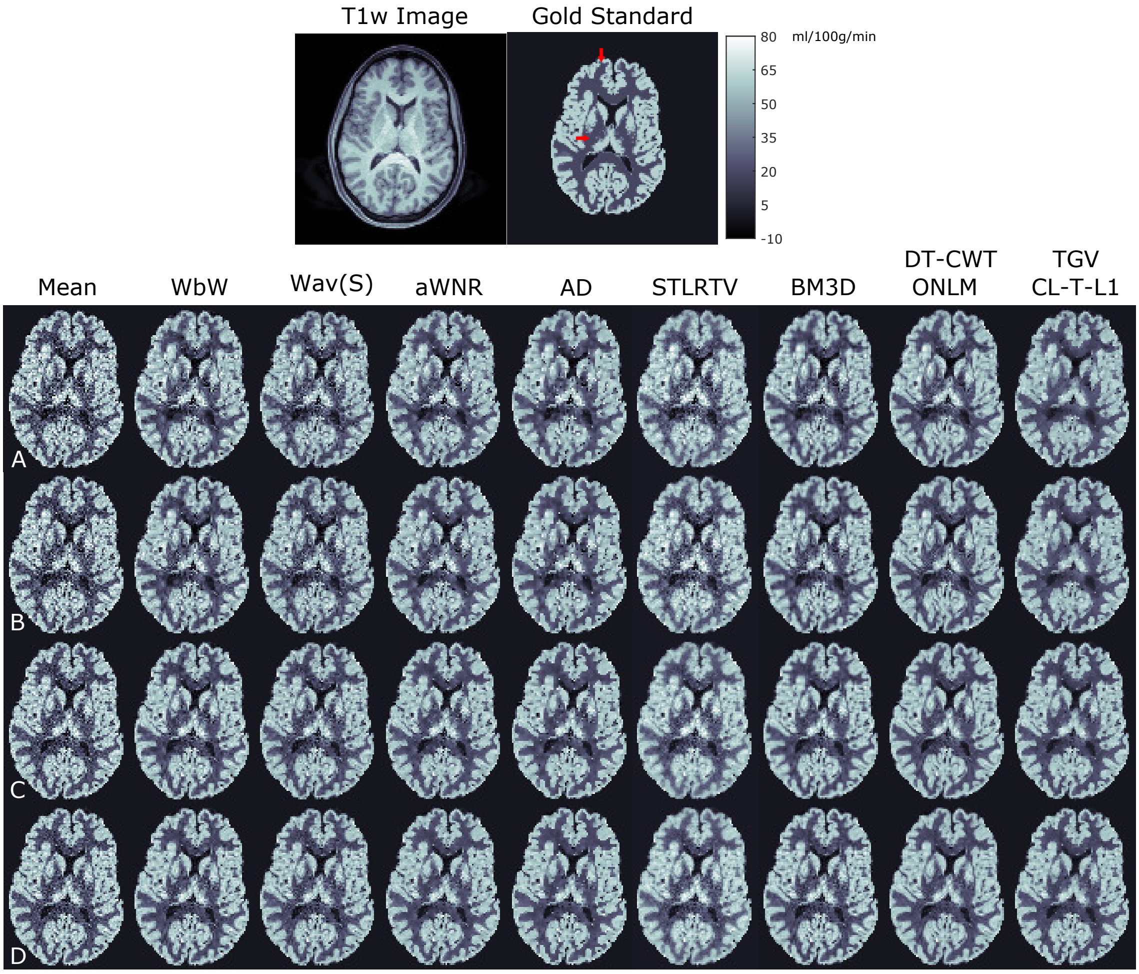

Figure 3.6: T_1 weighted image, gold standard CBF-map, noisy CBF-map and CBF-map calculated from the denoised difference image using 40 C/L-pairs (row A), 50 C/L-pairs (row B), 80 C/L-pairs (row C) and 100 C/L-pairs (row D) for slice 3 of the synthetic dataset. Areas were the performance of the TGV denoising approach was superior compared to the reference denoising methods are indicated with a red arrow.

are consistent with the qualitative results in Figure 3.6 and 3.7.

Figure 3.9 shows the mean SSIM and mean PSNR for a different number of C/L-pairs of the high resolution synthetic and in-vivo dataset of subject 8. All denoising results are reported within the segmented GM and WM mask.

Figure 3.10 shows a representative high resolution CBF-map of each of the remaining seven subjects (subject 1 to subject 7) before and after denoising using 50 C/L-pairs. The filtering results are similar to the denoising results of subject 8.

Figure 3.11 shows the mean SSIM and mean PSNR for the high-resolution in-vivo dataset of the remaining 7 subjects using 50 C/L-pairs at optimal filter parameter settings. The CL-T-L1 approach shows an averaged higher PSNR of 1.1 dB and an averaged higher

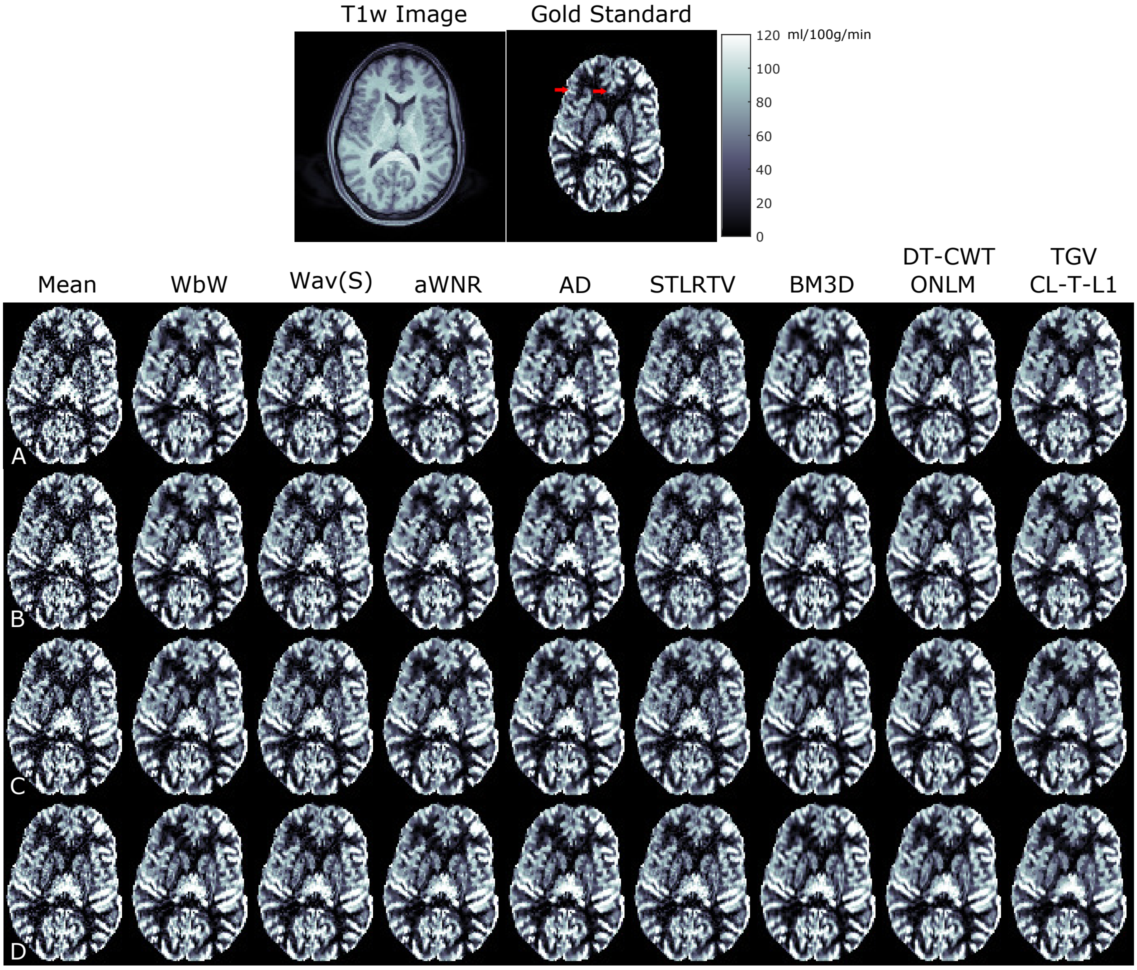

Figure 3.7: Top row shows the T_1 weighted image and the gold standard CBF-map calculated from 500 C/L-pairs of the high resolution in-vivo dataset of subject 8. Row A to D show the noisy CBF-map and the CBF-map calculated from the denoised difference image using 40 C/L-pairs (row A), 50 C/L-pairs (row B), 80 C/L-pairs (row C) and 100 C/L-pairs (row D). The red arrows indicate areas were the TGV (CL-T-L1) approach is more comparable with the gold standard CBF-map than the CBF-maps from the reference denoising methods.

SSIM of 0.6% compared to the best performing reference denoising technique. It should be noted that for the proposed method the same parameters were used for all subjects. The subjects were sorted in ascending order by PSNR.

Figure 3.12 shows exemplary the standard resolution CBF-maps before and after denoising from subject 1 for a different number of C/L-pairs. The gold standard CBF-map was calculated from the 100 C/L-pairs. The denoising results for the standard resolution dataset are similar to the results of the high-resolution datasets, with the greatest improvement in visual quality using the proposed TGV based approach (CL-T-L1).

Figure 3.13 shows the mean SSIM and mean PSNR for the two standard-resolution in-vivo datasets for different numbers of C/L-pairs. The SSIM and PSNR improvement

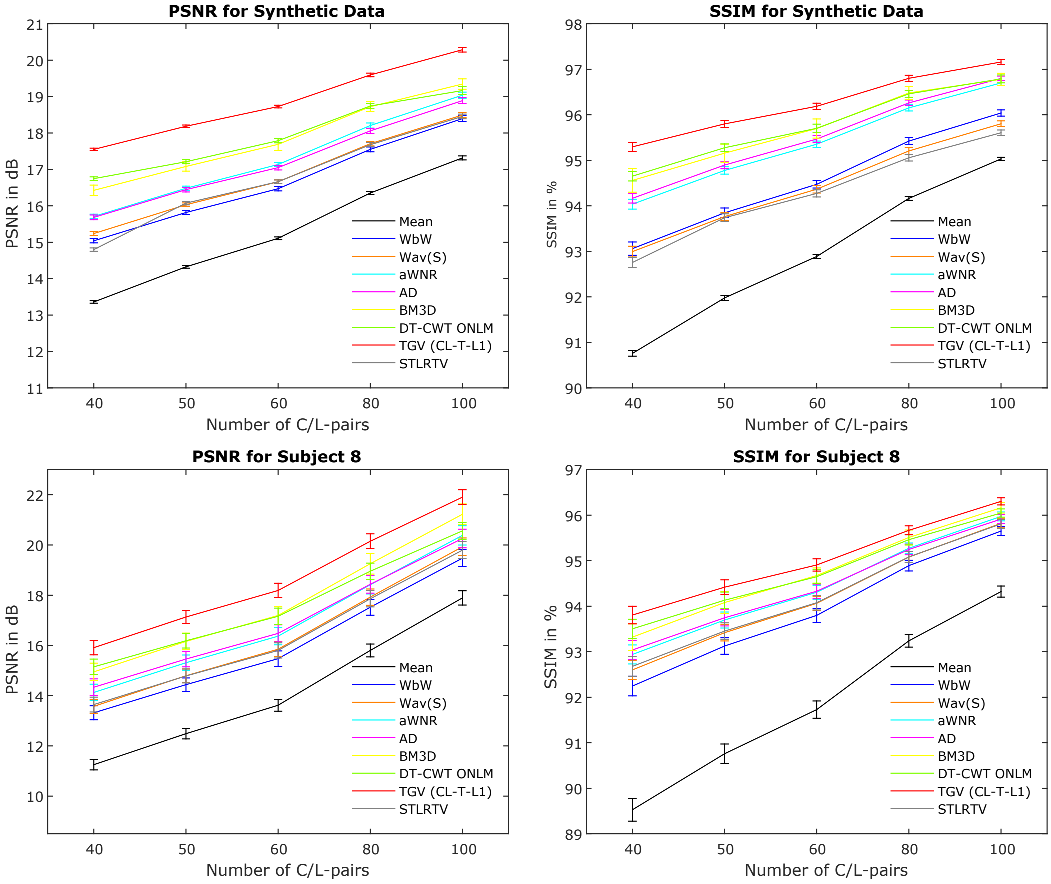

Figure 3.8: Mean SSIM and PSNR for different numbers of C/L-pairs from high-resolution in-vivo and synthetic data averaged over 50 trials. Error bars denote ±1 standard deviation.

for the different filters are in accordance with the results of the high-resolution datasets and the greatest improvement in PSNR and SSIM can be observed for the TGV denoised CBF-maps.

3.5 Discussion

3.5.1 TGV Denoising Methods

The inherently low SNR of ASL data makes spatial denoising essential for robust CBF quantification. The results of this study demonstrate the potential of using a TGV based denoising approach for ASL imaging. Synthetic and in-vivo images with different SNR levels were considered. Both, synthetic and in-vivo datasets show improved noise suppression for low as well as high SNR regime while retaining small details and edges in the perfusion images. This qualitative improvement is confirmed by the two quantitative metrics SSIM and PSNR.

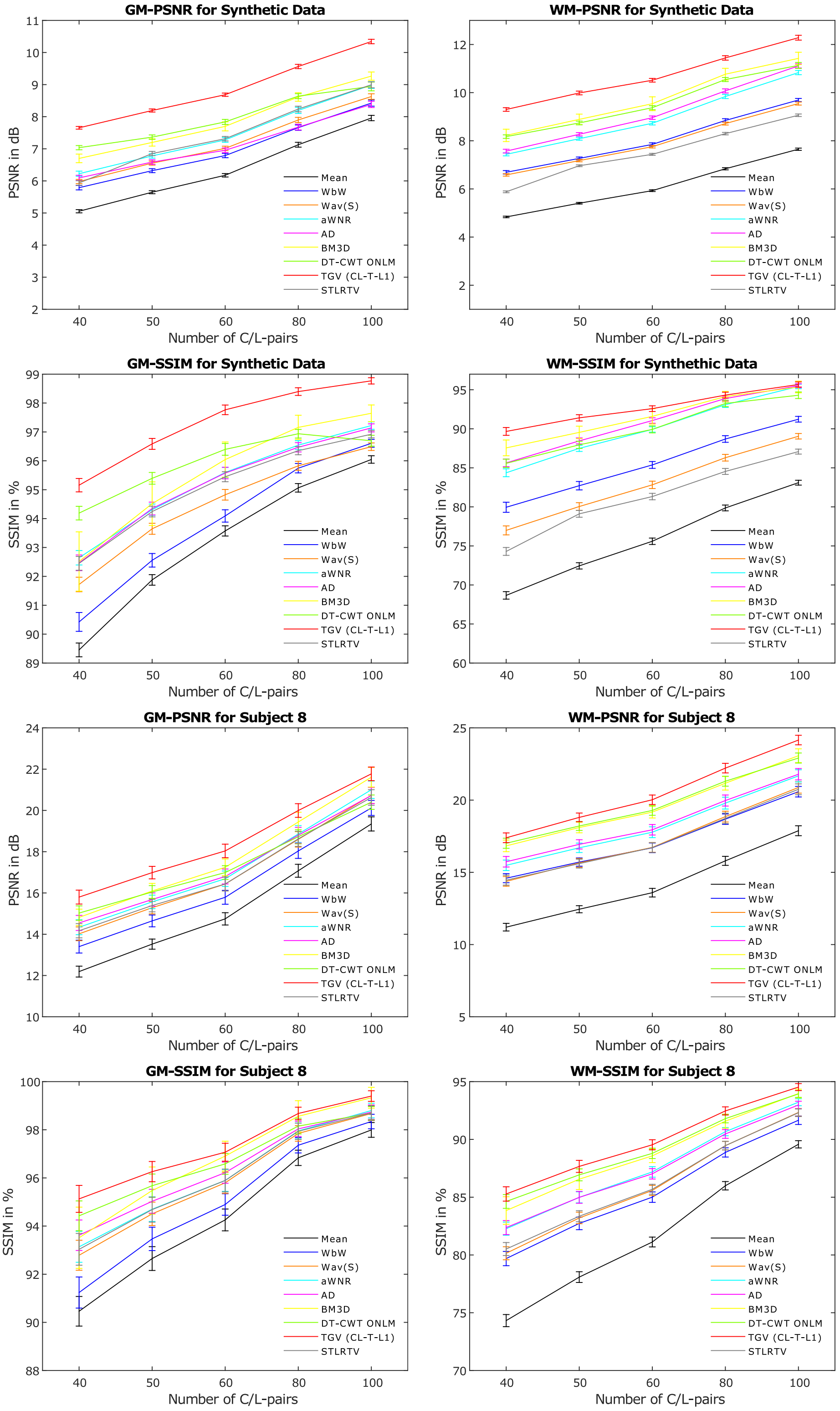

Figure 3.9: Mean SSIM and PSNR in the GM and WM for a different number of C/L-pairs from high resolution in-vivo and synthetic data. The results are averaged over 50 trials and the error bars denote ±1 standard deviation.

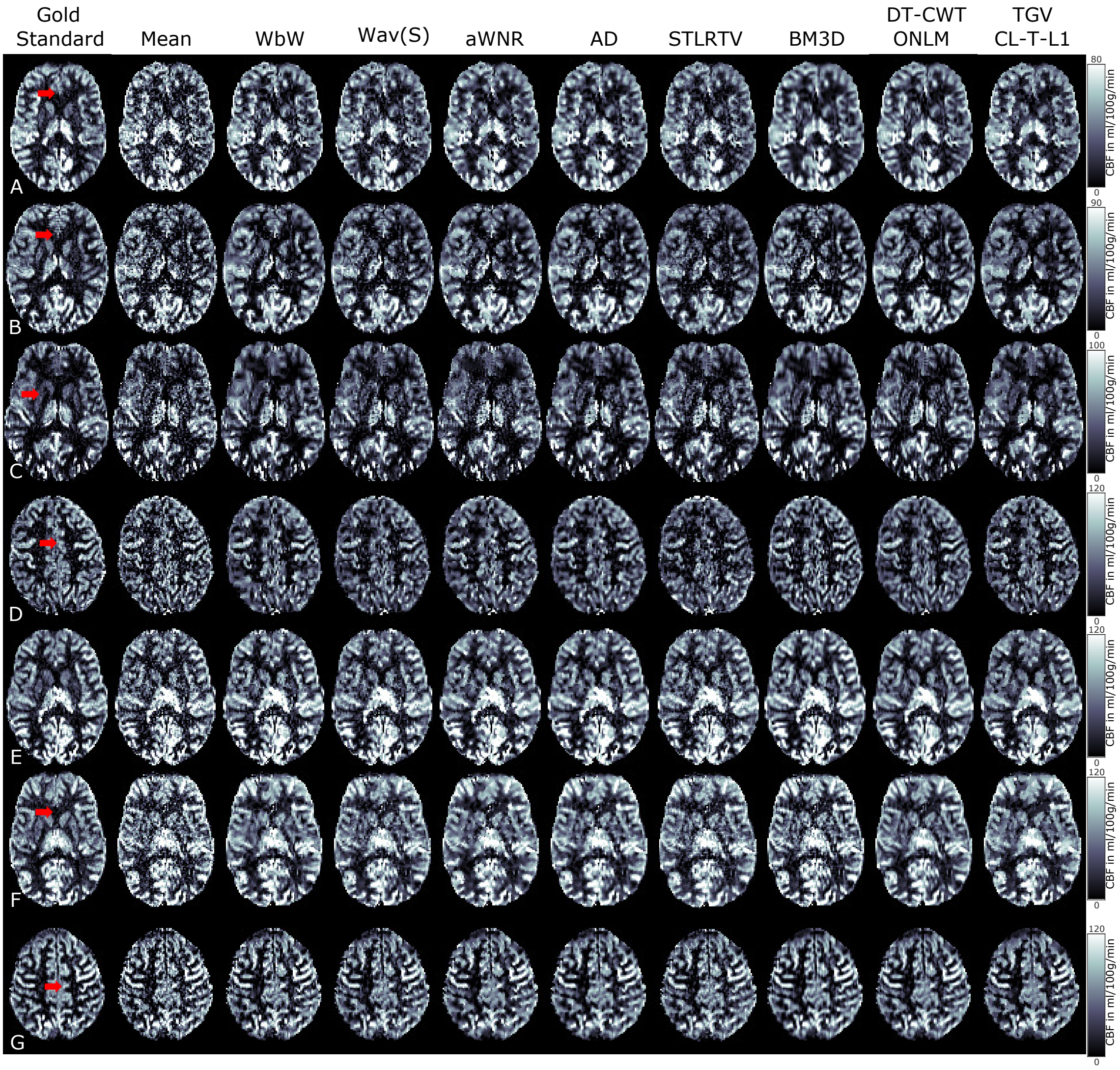

Figure 3.10: Gold standard CBF-map, noisy CBF-map and CBF-map calculated from the denoised difference image using 50 C/L-pairs form subject 1 to 7 (row A to row G). The gold standard CBF-map was calculated from the averaged 500 C/L-pairs. The red arrows indicate areas in the CBF-maps were the proposed approach is more comparable with the gold standard CBF-map than the CBF-maps of the reference denoising methods.

The extension of the simple TGV based approach by incooperating additional information in the denoising procedure improves the results for both, L^1 and L^2 data fidelity term approaches. The inclusion of temporal information is especially beneficial for the L^1 norm approach which reduces outliers in the time series resulting in a significant improvement in image quality. For the L^2 norm approach (PWI-T-L2) the improvement is minor compared to the PWI-L2 approach. Since per definition the used data-fidelity term is the

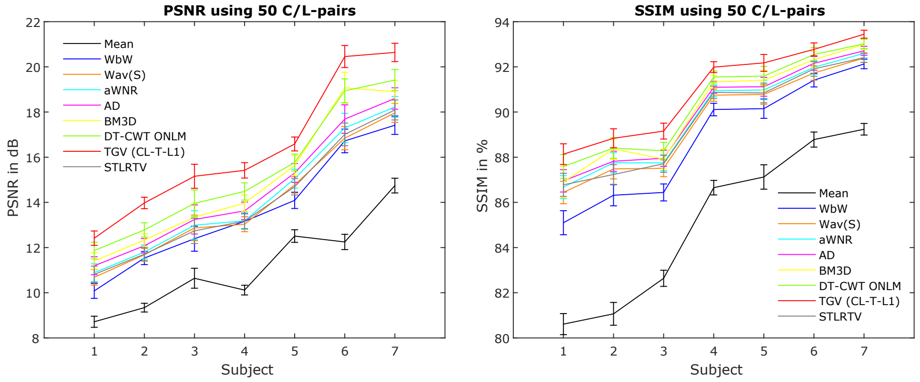

Figure 3.11: Mean SSIM and PSNR using 50 C/L-pairs from the remaining 7 subjects averaged over 50 trials. Error bars denote ±1 standard deviation.

element-wise mean the minor improvement gets clear. For both approaches a further image enhancement is visible by incooperating the whole available dataset, suggesting that the denoising approaches can benefit from the additional information. As expected, the highest improvement in noise suppression is achieved with the CL-T-L1 norm. The L^1 norm is more robust against outliers and takes into account the spatial varying noise in the images, resulting in an improved noise suppression in regions of the capsula interna while preserving sharp edges. In contrast, for the full L^2 model (CL-T-L2) noise still remains in regions of the capsula interna. The L^2 norm penalizes large errors stronger than the L^1 norm. The increased noise level in this region could be reduced by using stronger regularization but this will comes at the cost of blurred edges. Therefore, the L^1 norm is preferred over the L^2 norm for ASL images. The visual impression is confirmed with the qualitative metrices (SSIM and PSNR) showing the highest values for the CL-T-L1 approach.

3.5.2 Comparison to Reference Denoising Methods

The results of the best performing TGV based method (CL-T-L1) were compared with those of seven published denoising approaches. For all denoising methods the filter parameters were optimized with respect to the quantitative metric SSIM, rather than relying on visual quality. This allows comparing the performance of the different filters in a fair way. The utilized parameter optimization strategy might be interesting in general for various denoising algorithms, since it accounts for both structural degradation and differences in contrast. Further, a semi-automatic parameter approach based on the noise variance within an image was implemented [299]. This approach provides moderate results, but degraded visual quality as well as reduced SSIM and PSNR, compared to the presented optimization approach (data not shown). This is due to the fact that the noise variance is often inaccurately estimated or spatially dependent. In contrast to the reference methods, the TGV filtering approach provides superior results by applying

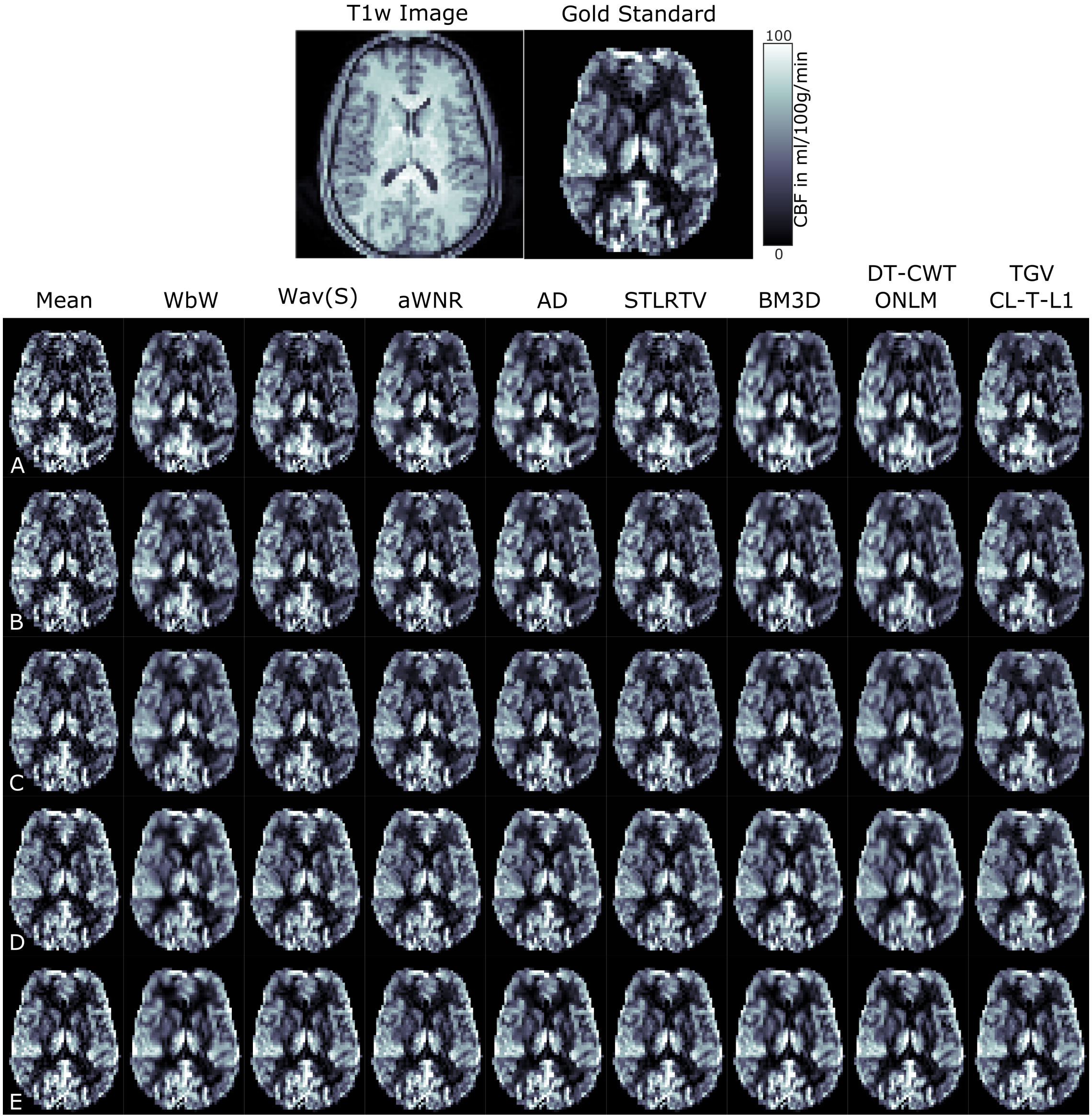

Figure 3.12: Top row shows the T_1 weighted image and the gold standard CBF-map calculated from 100 C/L-pairs of the standard resolution in-vivo dataset of subject 1. Row A to E show the noisy CBF-map and the CBF-maps calculated from the denoised difference image using 8 C/L-pairs (row A), 10 C/L-pairs (row B), 12 C/L-pairs (row C), 15 C/L-pairs (row D) and 20 C/L-pairs (row E).

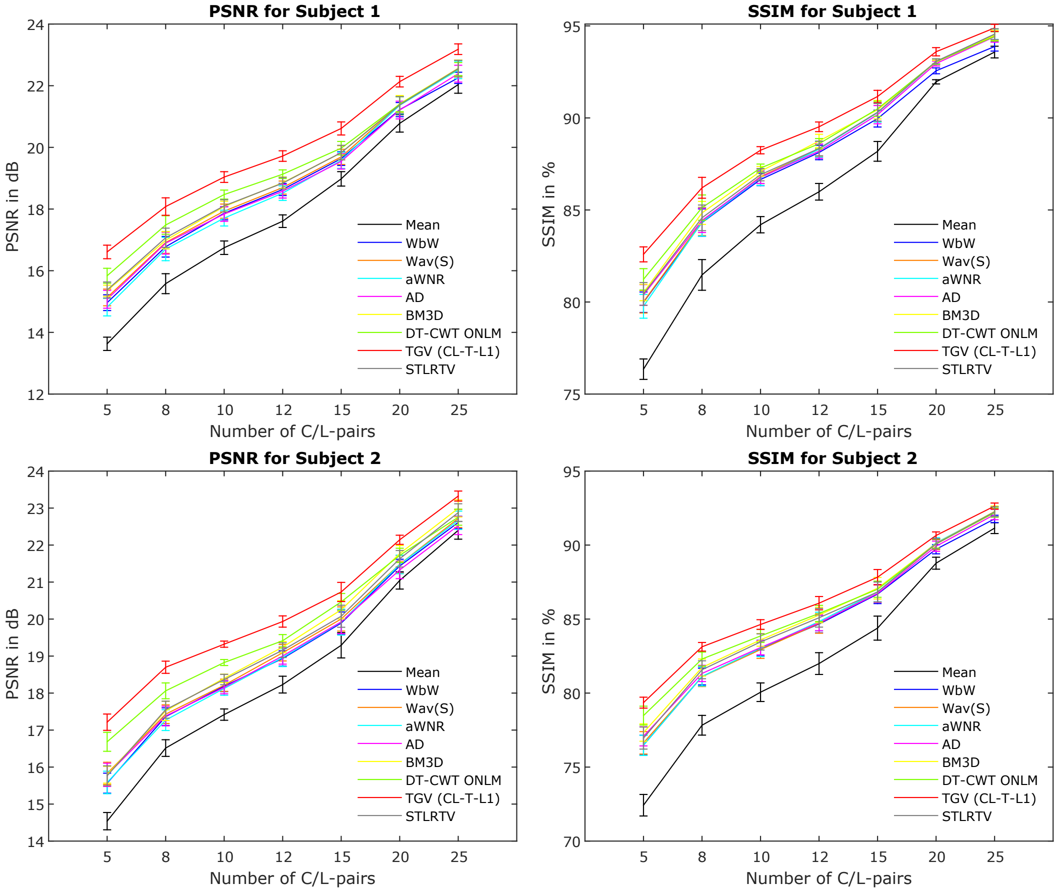

Figure 3.13: Mean SSIM and PSNR for different numbers of C/L-pairs from the two standard resolution in-vivo datasets averaged over 50 trials. Error bars denote ±1 standard deviation.

the same model parameter set for all subjects. The optimal model parameters are very robust against varying numbers of averages. Nevertheless, the regularization parameter λ has to be adapted according to the noise level. In contrast to other methods the proposed method is very robust for a broad range of regularization parameter. Hence, the denoising quality decreases only slightly, especially for datasets with sufficient SNR (Figure 3.2). This property might be attributed to the fact that a general denoising model was applied, which does not depend on self-similarity blocks within an image or on a-priori information such as the noise variance, which is often not accurately estimated. This leads also to the fact, that the same parameters can be used for all in-vivo datasets.

In contrast to other studies which added constant zero mean Gaussian noise to the synthetic dataset spatial dependent noise was considered to generate a more realistic synthetic ASL dataset. A comparison of the two Wavelet based filters (WbW and Wav(S)) with the noise free synthetic CBF-map reveals that the structural degradation is minimal. However, noise is still present in the CBF-maps especially in the WM, where the SNR is approximately 3 times smaller than in the GM. The denoising results using AD or aWNR are superior to the two wavelet based filters but in both cases noise is still present. This is also the case for the STLRTV denoised CBF-maps. It should be noted, that our data is motion-corrected, de-trended and outlier cleared before denoising. This may restrict the benefit of the STLRTV filter compared to non-preprocessed data. For the two block matching filters (BM3D, DT-CW ONLM), based on self-similarity blocks in the difference image, an improved denoising especially in the WM regions can be observed in comparison to the previous filters but this comes at the cost of stronger blurring at the GM/WM boundaries. However, noise is still present in the capsula interna for all denoising methods except for the TGV method. The use of self-similarity blocks within a difference image can be a disadvantage in case of blocks or structures which have only a few similar blocks within the image. These blocks remain noisy, which might be the case for the capsula interna (Figure 3.6). Further, in all reference denoised CBF-maps a hyper perfusion can be observed in the left and right thalamus. In contrary the TGV method resulted in maps which are more comparable to the ground truth. The TGV method shows improved noise removal in the GM and WM as well as in the capsula interna. At the same time edges especially in the frontal lobe are still preserved (red arrow in Figure 3.6). The retaining of structure and of small details is crucial especially for the application of denoising high resolution ASL data. Furthermore, it is essential for the detection of small local CBF changes which might get vanished in situations where denoising introduces a high degree of spatial smoothing. The oversmoothing of the reference filters may restrict its sensitivity in detecting small changes in CBF. Hence, the reference filters are prone to a limited sensitivity in the detection of small lesions or minor changes in CBF. Furthermore, the inherent spatial oversmoothing of the reference denoising methods could impair the sensitivity in group studies where only GM structures or regions are analyzed.

An increased number of C/L-pairs improve the quality of all CBF-maps and leads to a lower structural degradation, especially for the two block matching filters. This indicates that the degree of spatial smoothing is coupled with the degree of noise suppression and SNR. Moreover, the presented study demonstrates that at low SNR level a trade-off between spatial smoothing and noise removal level has to be chosen for all reference denoising approaches. These visual observations are confirmed by the two quantitative metrics SSIM and PSNR, indicating a lower systematic error and minor structural degradation for the TGV based method for all analysis. Both, the visual quality and the quantitative metrics show that for all denoising techniques the benefit of denoising decreases with increasing SNR.

The in-vivo dataset exhibits the same degree of spatial oversmoothing for the reference denoising methods (Figure 3.7), especially for low SNR. An additional feature of the proposed method is its robustness against outliers. This is achieved by applying the L^1 norm together with the temporal dimension in the data term of the functional (equation 3.27). This shows a clear benefit of the proposed method, while all reference methods, except the STLRTV, use only the spatial dimension for denoising. In terms of SSIM and PSNR similar results were obtained for the in-vivo datasets of the remaining 7 subjects. The highest improvements are reported for the proposed TGV method. The differences in PSNR and SSIM between subjects may be due to differences in the CBF. Previous studies [168, 197] found a higher CBF in women than in men. Subjects 1, 2, 3 and 5 are men and subjects 4, 6, 7 and 8 are women indicating a higher PSNR and consequently a higher SSIM for women than men.

Furthermore, we analyzed a principle component analysis (PCA) and independent component analysis (ICA) denoising algorithm [299] for denoising of the perfusion weighted time series. However, we only use a single TI time with no dynamic change in our data. Denoising by reconstructing the image series using only the biggest components of the PCA clearly reduced the temporal variation of the pixels, but leads, after averaging to the same results as a simple mean filtering of the original data. We observed similar results for the ICA denoised images with no additional improvements. Additionally, it is very hard to choose the right independent components as it is not clear how much each component contributes to the signal. Since we average the whole perfusion weighted time series and got similar results as for simple mean filter, we decided not to include the ICA and PCA results in our study.

We additionally evaluated the denoising algorithm for standard resolution ASL data of two subjects. The performance of the evaluated denoising algorithm (Figure 3.12) is the same as for high resolution data with the exception of the STLRTV, which performs better than for the high resolution datasets. This can be due to the higher SNR in the single perfusion weighted images, leading to a higher benefit of the spatial TV and therefore to a better final outcome. However, the proposed TGV based denoising approach is still the best in terms of PSNR and SSIM (Figure 3.13).

In summary the results of the presented study highlights, that the proposed TGV (CL-T-L1) method enables an essential reduction of the acquisition time in the application of high as well as standard resolution PASL. As a consequence, this reduces the risk of motion artifacts and addresses clinical demands. A combination of the proposed TGV denoising method with higher SNR labeling schemes such as pseudo continous arterial spin labeling (pCASL) [56] or 3D readouts such as 3D-gradient and spin echo (GRASE) [109] would lead to a further reduction in acquisition time or may further improve the spatial resolution. The developed algorithm can be easily implemented as an additional preprocessing step besides motion-correction, outlier-detection and temporal filtering and should help increasing the robustness and reproducibility of CBF quantification in clinical studies.

3.6 Conclusion

This study demonstrated that the proposed total generalized variation denoising framework with coupling of control and label pairs, outperforms state of the art denoising techniques. In addition, the new method improved the quantification accuracy of the CBF-maps, for both simulations and experiments. This general TGV model joins spatial and temporal similarity of the label and difference image for robust signal estimation, in case of low as well as high SNR. Consequently, this approach highly satisfies clinical demands in terms of reducing the scan time, motion artifacts and local outliers and increasing the spatial resolution. Compared to other state of the art denoising methods the structural degradation is minimized and local outliers are removed. This makes the TGV denoising approach highly attractive for group or functional ASL studies as well as for detecting anomalies in perfusion.

4

Spatial Adaptive Variational Denoising for ASL Perfusion Data

This chapter is based on the following abstract which was accepted for the ISMRM 2017:

> S. M. Spann, K. S. Kazimierski, C. S. Aigner, and R. Stollberger. A denoising method for arterial spin labeling data based on total generalized variation (TGV) with a spatial varying regularization parameter. In *Proceedings of the 25th Annual Meeting of ISMRM*, Honolulu, 2017

Contents

4.1 Introduction

In the previous chapter an overview and comparison of state-of the art denoising methods with a new TGV based algorithm for 2D arterial spin labeling (ASL) data was considered. Filtering improves the quality of ASL images and allows a significant reduction in acquisition time, which is important in the clinical routine. The investigated filtering methods rely on the assumption that the noise variance is equal across the image i.e. the value of noise variance is stationary and can be characterized by a single value. However, this assumption is often violated in practice leading to suboptimal performance in noise removal.

In ASL noise contributions can be divided in thermal noise and physiological noise. Thermal noise was described by Nyquist [190] and Johnson [140] and is caused by random thermally driven motion of electrons within the radio frequency (RF)-coil and receiver electronics [1, 52]. Thermal noise is stationary, additive and normally distributed with zero mean and can be characterized by a single parameter σ^2. The noise variance ($\sigma^2 \propto 4kTBR$) depends on the temperature T, the readout bandwidth B, and the effective resistance R. Both the imaginary and real signal in k-space are affected by thermal noise. In magnetic resonance imaging (MRI) the complex image is obtained by applying a discrete inverse fourier transform. Since the inverse discrete Fourier transformation (IDFT) is an orthogonal linear transformation, the characteristics of stationary Gaussian noise is well preserved. While this assumption is valid for single RF coil acquisitions [184], it is violated for images obtained form multichannel-coils [114], which are nowadays standard in MRI. The noise in the receiver coils is no longer independent due to electromagnetic coupling leading to cross-correlations in the coils [4, 52]. Furthermore, the development of multi-coils form the basis for parallel imaging (PI) methods to speed up the acquisition [104, 211, 238]. PI reduces the signal-to-noise ratio (SNR) by the square root of the acceleration factor due to reduced data sampling and results in a spatial varying noise enhancement in the image [211]. This effect is described by the g-factor [211] and depends on several factors including the coil geometry, the imaged object, and the acceleration factor [211]. A detailed summary of effects on the noise distributions using multi-coils and parallel imaging is given by Santiago Aja-Fernandez et al. [3]. For ASL imaging a moderate acceleration factor of 2-3 is recommended to reduce the echo train length for 3D-rapid acquisition with relaxation enhancement (RARE)-readouts or the echo time for 2D gradient echo EPI [8]. Typically, phased array coils with 20, 32 or even 64 coils are used leading to non-stationary noise in the images.

Beside thermal noise, physiological noise is the second and dominant source of noise in ASL imaging. Physiological noise refers to all sources of signal variability that are related to the subject physiological processes (being measured) i.e. signal fluctuation due to respiratory and cardiac effects [150], or metabolic effects of neural activity [24]. Breathing can influence the baseline signal up to ± 25% [217] and differences in cardiac cycle lead to changes up to ± 20% [217]. Cardiac related signal fluctuations are due to cerebrospinal fluid (CSF) movement and vessel pulsation [55], which changes the diameter of blood vessels and increases the number of fresh inflowing spins [159]. Li et al. showed that these fluctuations are spatially correlated and changes the global signal intensity in ASL images with the most influence in regions within or near large blood vessels [159].

The effect of breathing on MRI of the brain has been investigated by several groups [212, 213, 277]. Respiration induces B_0 fluctuations in the human brain through changes in magnetic susceptibility associated with movement of the organs in the thorax and abdomen, and due to changes in the oxygen concentrations [212, 213]. B_0 fluctuations causes instabilities in phase and frequency in the MRI signal which in turn leads to signal fluctuations, ghosting, and image displacement [213, 277].

The last source of noise is related to subject motion, which is a critical problem in ASL imaging. The perfusion signal is only 1% of the static tissue signal and obtained by a subtraction of two successively acquired images. Even a small amount of motion, especially at the boarder of two regions, can create substantial changes in the voxel intensity which dominants the ASL signal. In contrast to thermal noise, physiological noise is dependent on the signal intensity and fare away from random. [153]
Considering for those effects in the denoising procedure a spatially varying regularization parameter would be more appropriate than a global. Therefore, we adapt the denoising framework of chapter 3 by including a spatial dependent regularization parameter. The nature of ASL acquisition allows an easy estimation of the spatially variant noise maps by calculating the voxel wise standard deviation over the repeated measurements. The performance of the proposed method is evaluated on synthetic and experimental in-vivo high resolution pulsed arterial spin labeling (PASL) data with 2D-echoplanar imaging (EPI) readout and pseudo continous arterial spin labeling (pCASL) data with 3D-gradient and spin echo (GRASE) readout. The results are compared with the ASL-TGV denoising approach presented in chapter 3.

4.2 Theory

4.2.1 Extension of the ASL-TGV Denoising Approach for 3D Data

In chapter 3 we proposed a variational denoising method for 2D isotropic ASL data. This approach is now extended for 3D isotropic and anisotropic ASL data. Here, an additional third dimension is introduced in the gradient and symmetrized gradient operator of the total generalized variation (TGV) functional. In case of isotropic data the resolution or grid size is equal in all dimension leading to a equally penalization of the discrete gradient and symmetrized gradient operator respectively. However, for anisotropic data an additional spatial weight for each gradient direction is necessary to relate the voxel size to the physical grid leading to

$$TGV^2_{\alpha_1,\alpha_0}(u) = \min_v \left\{\alpha_1 \left|\left|\nabla u - v\right|\right|_1 + \alpha_0 \left|\left|\epsilon v\right|\right|_1\right\}, \tag{4.1}$$

$$\begin{aligned} \nabla : \Re^{N_x \times N_y \times N_z} &\mapsto \Re^{N_x \times N_y \times N_z \times 3} \\ (\nabla u)_{i,j,k} &= \begin{pmatrix} s_x \left(\partial_x^+ u\right)_{i,j,k} \\ s_y \left(\partial_y^+ u\right)_{i,j,k} \\ s_z \left(\partial_z^+ u\right)_{i,j,k} \end{pmatrix}, \end{aligned} \tag{4.2}$$

$$\epsilon : \Re^{N_x \times N_y \times N_z \times 3} \mapsto \Re^{N_x \times N_y \times N_z \times 6}$$

$$(\epsilon v)_{i,j,k} = \begin{pmatrix} s_x \left(\partial_x^- v^1\right)_{i,j,k} \\ s_y \left(\partial_y^- v^2\right)_{i,j,k} \\ s_z \left(\partial_z^- v^3\right)_{i,j,k} \\ \frac{1}{2}\left(s_x \left(\partial_x^- v^2\right)_{i,j,k} + s_y \left(\partial_y^- v^1\right)_{i,j,k}\right) \\ \frac{1}{2}\left(s_x \left(\partial_x^- v^3\right)_{i,j,k} + s_z \left(\partial_z^- v^1\right)_{i,j,k}\right) \\ \frac{1}{2}\left(s_y \left(\partial_y^- v^3\right)_{i,j,k} + s_z \left(\partial_z^- v^2\right)_{i,j,k}\right) \end{pmatrix}, \tag{4.3}$$

where s_x, s_y, s_z are the corresponding weights and $N_x \times N_y \times N_z$ is the size of the 3D volume. Similar to the 2D case the full optimization problem includes data-fidelity terms for control and label data as well as TGV-functionals for label and perfusion images.

$$\begin{aligned} (c^*, l^*) \in \underset{c,l}{\arg\min}\; & \lambda \left|\left|\varsigma c - d_c\right|\right|_1 + \lambda \left|\left|\varsigma l - d_l\right|\right|_1 + \gamma_1 (w)\, TGV^2_{\alpha_1,\alpha_0} (c) + \\ & \gamma_2 (w)\, TGV^2_{\alpha_1,\alpha_0} (c - l) \end{aligned} \tag{4.4}$$

The numerical solution of this convex but non-smooth problem is given by the primal dual splitting algorithm and can be found in appendix C.2.

4.2.2 Extension to Spatial Adaptive Variational Denoising

For considering non-stationary noise in the ASL images the constant regularization parameter λ in the 3D denoising approach (equation 4.4) is replaced with a separate regularization map for control ($\lambda_c \in \Re^{N_x \times N_y \times N_z \times N_t}$) and label ($\lambda_l \in \Re^{N_x \times N_y \times N_z \times N_t}$) data. This regularization maps penalizes deviations now voxel-wise according to the inverse of the temporal standard deviation of the corresponding image. Hence, in voxels with low standard deviation the faithfulness to the original data is high, whereas in voxels with high standard deviation stronger regularization is used, relying more on the model assumption. The full minimization problem reads as follows

$$\begin{aligned} (c^*, l^*) \in \underset{c,l}{\arg\min}\quad & \frac{1}{2} \left|\left|\lambda_c \left(\varsigma c - d_c\right)\right|\right|_2^2 + \frac{1}{2} \left|\left|\lambda_l \left(\varsigma l - d_l\right)\right|\right|_2^2 + \gamma_1 (w)\, TGV^2_{\alpha_1,\alpha_0} (c) + \\ & \gamma_2 (w)\, TGV^2_{\alpha_1,\alpha_0} (c - l)\,. \end{aligned} \tag{4.5}$$

The numerical solution of this problem is given by the primal dual splitting algorithm in appendix C.2.

4.3 Methods

4.3.1 ASL Data

For validation the numerical phantom and the corresponding acquired 2D dataset of section 3.3.1 "ASL Acquisition" were used. In addition, ASL data at 4 different resolutions were acquired from one healthy subject at a 3T magnetic resonance (MR) system (VIDA, Siemens Healthcare, Germany) using a 64 channel head coil. A prototype controlled aliasing in parallel imaging results in higher acceleration (CAIPIRINHA) accelerated 3D-GRASE sequence with pCASL labeling and background-suppression was used [134, 283]. The labeling plane was placed above the carotid bifurcation and below the V3 segment using a short time of flight (ToF) scan for planning [282]. The following parameters were equal for the four acquisitions: field of view (FoV) = 203 x 203 mm, CAIPIRINHA-pattern $2 \times 2^{(1)}$, phase-partial Fourier = 6/8, slice-partial Fourier = 6/8, two background suppression pulses, refocusing flip angle = 180°, labeling duration (LD) = 1800 ms, and post-labeling delay (PLD) = 1800 ms. The additional parameters for each acquisition are summarized in Table 4.1.

Table 4.1: Acquisition parameters for the four ASL datasets

Parameter	Dataset 1	Dataset 2	Dataset 3	Dataset 4
Resolution in mm	1.3x1.3x1.3	1.6x1.6x1.6	2x2x2	2.5x2.5x2.5
TR in ms	3920	4120	4000	3870
TE in ms	26.4	37.1	23.6	16.9
Turbo-factor	10	8	13	13
EPI-factor	29	45	37	29
Slices	48	38	32	26
Segments	4	2	1	1
Repetitions	20	30	38	30
Acquisition time	10 min 36 s	8 min 22 s	5 min 12 s	4 min 4 s

To show the potential of the 3D spatial adaptive regularization approach, an additional high resolution (2x2x2 mm^3) synthetic ASL dataset with non-stationary noise was computed. The generation of this dataset is based on a high resolution (1 mm isotropic) T_1- and proton density (PD)-map (M_0) supplied by MRiLab [164] for MATLAB r2016b (The Mathworks, Natick, MA, USA). Similar to the 2D dataset, cerebral blood flow (CBF)-values of 65 $ml/100g/min$ and 20 $ml/100g/min$ were assigned to gray matter (GM) and white matter (WM) tissues, respectively [72, 155, 201, 325]. In a subsequent step, the high resolution images were downsampled to 2 mm isotropic resolution using tri-linear interpolation, which introduces additional partial volume (PV) effects. From the downsampled CBF-map the perfusion weighted images (PWIs) were calculated using the general kinetic model for pCASL [34] described in section 4.3.4 "Quantification of Cerebral Blood Flow". The control images are assigned to $C = 0.1 \cdot M_0$, which models a background suppression of 90% applied to M_0. The label images are simply given by $L = C - \text{PWI}$. Afterwards spatial dependent Gaussian noise was added to each voxel in the C/L-images as shown in Figure 4.1.

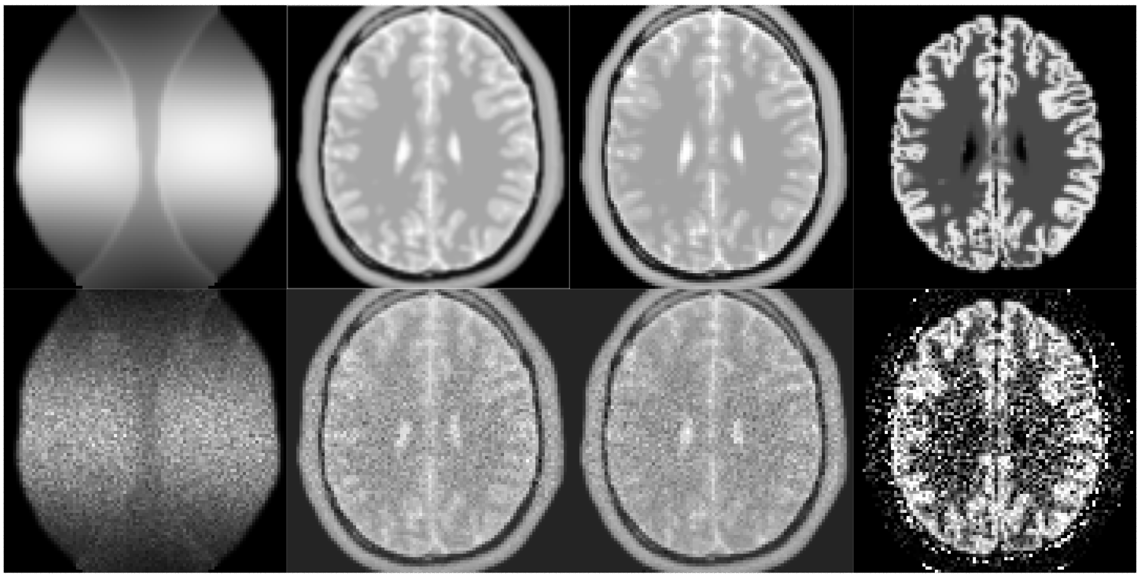

Figure 4.1: Example of generating the ASL dataset with spatial varying noise. Top row from left to right: spatial varying noise map, noise free control image, noise free label image, and noise free CBF-map. Bottom row from left to right: applied non-stationary noise, noisy control image, noisy label image, and noisy CBF-map.

4.3.2 ASL Data Processing

The 2D and 3D datasets were processed using statistical parameter mapping v 12 (SPM12), MATLAB 2015b (The MathWorks, Inc., Natick, Massachusetts, USA), ASL-toolbox [293, 294], and in-house written MATLAB scripts. The preprocessing was performed as previously described in chapter 3 section 3.3.5 "ASL Data Processing" and includes: motion correction [293, 294], de-trending [293, 295], and outlier correction [261]. Subsequently, the ASL images were denoised using the proposed TGV based methods.

4.3.3 Parameter Choice

For the reference denoising method in 2D the parameters and results from the previous chapter were taken. For the extended 3D version, as well as the proposed spatial adaptive denoising method, the parameters were optimized by maximizing the structural similarity index (SSIM) between the noise free synthetic CBF-map and the denoised CBF-map. The spatial dependent regularization parameter-maps were calculated independently in each voxel by estimating the temporal standard deviation. An additional parameter η ensures a correct weighting between the spatial dependent regularization and data faithfulness. For all approaches the optimized parameters were summarized in Table 4.2.

Table 4.2: Optimized model (s) and regularization parameters (η and λ) for the 2D and 3D TGV approaches.

N	2D CL-T-L1		3D CL-T-L1		2D SA-TGV		3D SA-TGV	
	s	λ	s	λ	s	η	s	η
2D Synthetic Data								
40	0.475	2.15	0.5	2.50	0.45	0.35	0.5	0.3
50	0.475	2.25	0.5	2.25	0.45	0.35	0.5	0.3
60	0.475	2.45	0.5	2.00	0.45	0.35	0.5	0.3
80	0.475	2.75	0.5	2.00	0.45	0.35	0.5	0.3
100	0.475	3.00	0.5	2.25	0.45	0.35	0.5	0.3
2D In-Vivo PASL Data								
40	0.4	4.25	0.55	2.625	0.5	0.35	0.55	0.3
50	0.4	4.50	0.55	2.425	0.5	0.35	0.55	0.3
60	0.4	4.75	0.55	2.425	0.5	0.35	0.55	0.3
80	0.4	5.75	0.55	2.925	0.5	0.35	0.55	0.3
100	0.4	6.50	0.55	3.550	0.5	0.35	0.55	0.3
3D Synthetic Data								
25	0.6	2.0	0.6	2.2	0.6	0.325	0.6	5.5
50	0.6	2.25	0.6	2.6	0.6	0.325	0.6	5.5
75	0.6	2.25	0.6	2.4	0.6	0.325	0.6	5.5
3D In-Vivo pCASL Data								
Resolution	s	λ	s	λ	s	η	s	η
1.3 mm iso	0.55	3.5	0.55	3.25	0.6	0.45	0.6	2.0
1.6 mm iso	0.55	3.75	0.55	3.5	0.6	0.45	0.6	2.0
2.0 mm iso	0.55	4.0	0.55	3.75	0.6	0.45	0.6	2.0
2.5 mm iso	0.55	4.0	0.55	3.75	0.6	0.45	0.6	2.0

4.3.4 Quantification of Cerebral Blood Flow

For the quantification of the CBF a general kinetic model was applied [34]. According to this model, the CBF in $ml/100g/min$ can be calculated in each voxel for PASL-Q2TIPS data using the following equation [8]

$$CBF(x,y,z) = \frac{6000 \cdot \lambda \cdot PWI(x,y,z) \cdot e^{\frac{TI_2}{T_{1,b}}}}{2 \cdot \alpha \cdot M_0(x,y,z) \cdot TI_1} \ , \tag{4.6}$$

and for pCASL data using [8]

$$CBF(x,y,z) = \frac{6000 \cdot \lambda \cdot PWI(x,y,z) \cdot e^{\frac{PLD}{T_{1,b}}}}{2 \cdot \alpha \cdot M_0(x,y,z) \cdot T_{1,b} \cdot \left(1 - e^{-\frac{\tau}{T_{1,b}}}\right)} \ , \tag{4.7}$$

where λ is the blood-brain partition coefficient and set to 0.9 ml/g [125], $T_{1,b}$ is the longitudinal relaxation time of blood at 3T and set to 1.65 s [169], α is the labeling efficiency and set to 0.85 for pCASL [56] and 0.98 for PASL [308], τ/TI_1 is the labeling duration and set to 1.8/0.8 s, PLD/TI_2 is the post labeling delay and set to 1.8 s [8], $PWI(x,y,z)$ is the denoised difference image, and M_0 is the acquired proton density image smoothed with a Gaussian filter (full width at half maximum (FWHM) = 3 mm) as recommended [8]. The total delay time TI_2 was set to 1.8 s for the leading slice. For the PASL data an extra delay of 80 ms was added to TI_2 for each further slice acquired in ascending order [8], because of the used multi-slice EPI readout [8].

4.3.5 Evaluation

Two common metrics were used as a measure of denoising quality: the SSIM [292] and the peak signal-to-noise ratio (PSNR) [83, 161]. In case of the synthetic dataset the noise free CBF-map served as gold standard. For the 2D experimental dataset the gold standard CBF-map was computed from the 500 C/L-pairs. Benchmarking consists of 50 trials with 40/50/60/80/100 randomly selected C/L-pairs out of the data pool of 500, for the 2D synthetic and in-vivo dataset of subject 8. For the remaining 7 subjects benchmarking was performed using 50 C/L-pairs. In case of the 3D synthetic dataset benchmarking was performed using 25/50/75 randomly generated C/L-pairs.

SSIM

Image structure degradation and contrast difference between the gold standard CBF-map and the denoised CBF-map were analyzed using the quantitative structural similarity index [292].

PSNR

Peak signal-to-noise ratio, $PSNR = 20\log_{10}(MAXi/RMSE)$, was used to evaluate the denoising results within the brain mask [83, 161]. $RMSE$ denotes the root mean squared error between the ground truth CBF-map and the denoised CBF-map, and $MAXi$ represents the maximum intensity value in the ground truth CBF-map.

ROI Analysis

For the high resolution 3D datasets the denoising performance was evaluated by creating box-plots of the GM- and WM-CBF.

4.4 Results

4.4.1 2D Dataset

Figure 4.2 shows the estimated regularization maps and corresponding PWIs for 4 exemplary slices of the in-vivo data. The strength of the regularization parameter is reciprocal related to the noise standard deviation. A clear variation is visible between slices and also within one slice i.e at large vessel locations, at the boarder of the head, or due to the different coil sensitivity.

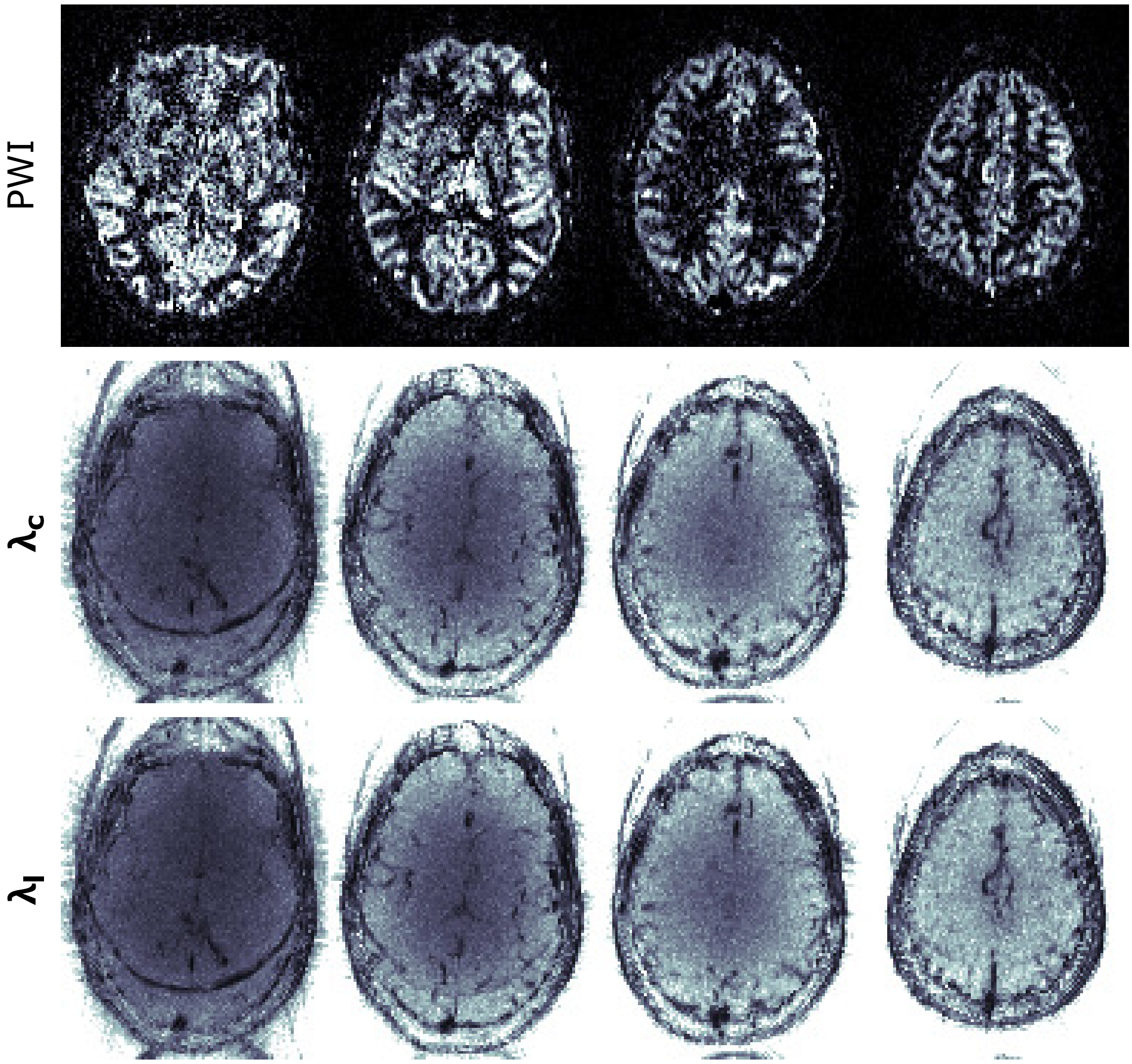

Figure 4.2: PWIs of 4 exemplary slices and corresponding estimated spatial dependent regularization parameter maps (λ_c and λ_l).

Figure 4.3 illustrates the noisy and denoised synthetic CBF-maps for a different number of averages. Compared with the simple mean filter all denoising approaches improve the visual quality and quantitative values. The improvement of the denoising approaches get smaller for higher SNR levels. The incorporation of a third dimension slightly increases the image quality for both approaches. The highest image enhancement could be achieved with the proposed spatial adaptive regularization method leading to continuously higher quantitative values, but the improvement is only small compared to the robust CL-T-L1 method.

Figure 4.4 shows the performance of the different denoising approaches on in-vivo data of subject 8. The gold standard CBF-map was generated from 500 C/L-pairs. Similar to the results of the synthetic datasets, the performance of the 3D denoising approaches is slightly better than the performance of the 2D approaches. The CBF-maps appear more natural with a lower number of over smoothed structures leading to an improved visual quality of the CBF-maps. This visual impression is confirmed by the two quantitative metrics showing continuously higher values for the 3D approaches. However, the performance gain of the spatial adaptive approach is minor and only visible in the quantitative metrics.

Figure 4.5 shows a quantitative evaluation of the denoising approaches with the mean SSIM and PSNR for the remaining 7 subjects. On average the 3D denoising approaches (SA-TGV/CL-T-L1) improves the SSIM of about 0.45/0.39 % and the PSNR of about 0.55/0.4 dB compared with the 2D approaches. For each subject, the highest performance increase is achieved with the 3D spatial adaptive approach.

4.4.2 3D Dataset

Figure 4.6 shows the performance of different denoising algorithms on the simulated synthetic ASL-dataset with spatial varying noise. Three different SNR levels were considered. An increase in SNR leads to a smaller performance difference between the individual approaches and a lower image enhancement compared with the simple mean. The isotropic voxel size shows a clear performance improvement of the two 3D approaches. The highest level of agreement with the noise free CBF-map is achieved with the proposed 3D-SA approach. The visual impression is confirmed by the two quantitative metrics showing an improvement of 0.88/0.87/0.67 % in SSIM and 0.4/0.23/0.13 dB in PSNR using 25/50/75 C/L-pairs compared with the second best method 3D CL-T-L1.

In Figure 4.7, 4.8, and 4.9 an exemplary CBF-map of the different high resolution in-vivo datasets is shown. The results are in accordance with the results from the synthetic dataset. A qualitative comparison of the different resolutions shows that the amount of noise increases with the resolution. Especially the CBF-map with the highest resolution is dominated by noise without no clear GM to WM contrast. The TGV based denoising methods were able to enhance the image quality of the CBF-maps. The proposed 3D-SA yields the highest image enhancement while preserving edges and structures very well.

A quantitative evaluation of all methods is shown in Figure 4.10. Boxplots of CBF-values in GM and WM for different resolutions are given. As expected, an increase in voxel

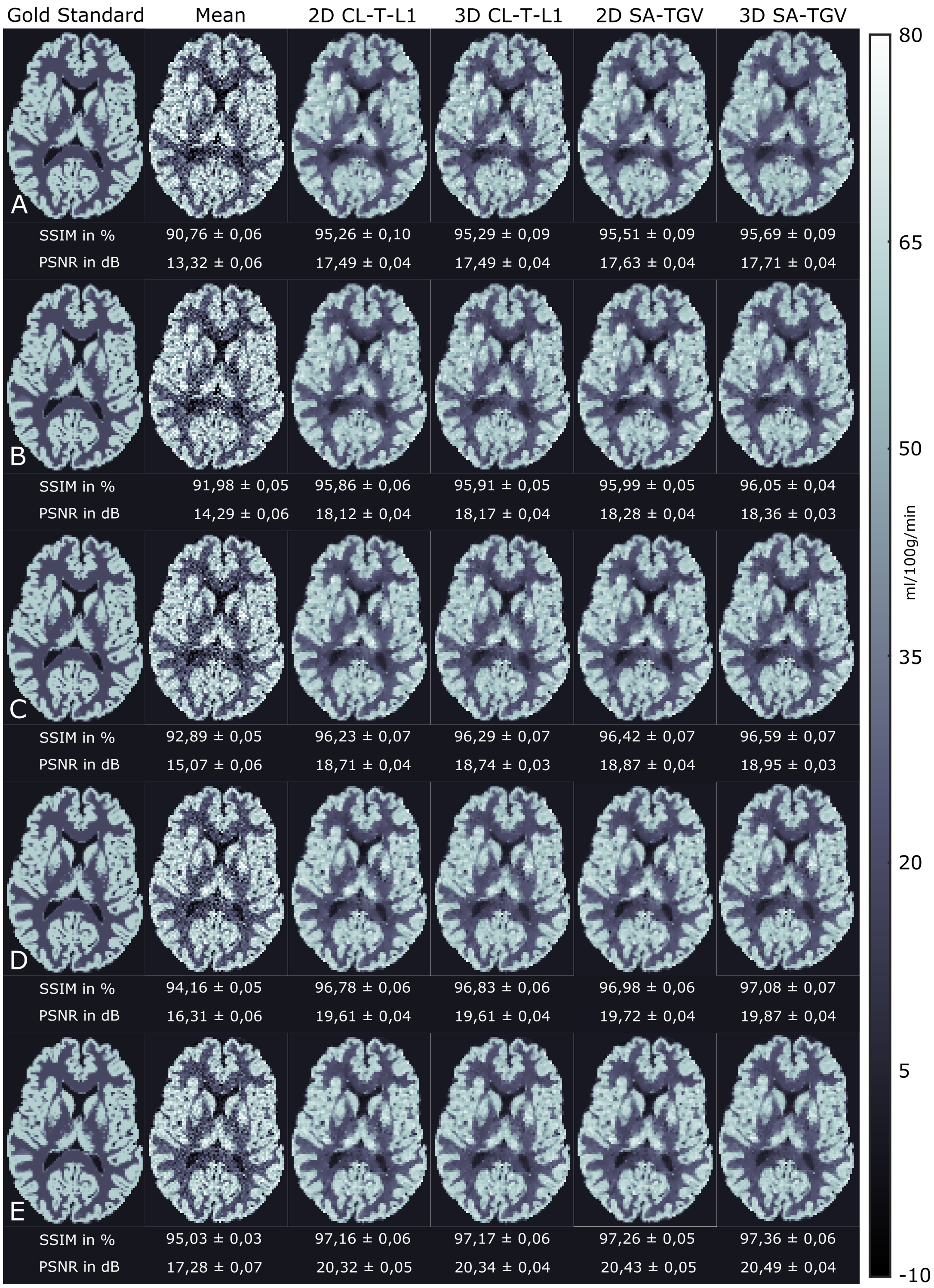

		Mean	2D CL-T-L1	3D CL-T-L1	2D SA-TGV	3D SA-TGV
A	SSIM in %	90,76 ± 0,06	95,26 ± 0,10	95,29 ± 0,09	95,51 ± 0,09	95,69 ± 0,09
	PSNR in dB	13,32 ± 0,06	17,49 ± 0,04	17,49 ± 0,04	17,63 ± 0,04	17,71 ± 0,04
B	SSIM in %	91,98 ± 0,05	95,86 ± 0,06	95,91 ± 0,05	95,99 ± 0,05	96,05 ± 0,04
	PSNR in dB	14,29 ± 0,06	18,12 ± 0,04	18,17 ± 0,04	18,28 ± 0,04	18,36 ± 0,03
C	SSIM in %	92,89 ± 0,05	96,23 ± 0,07	96,29 ± 0,07	96,42 ± 0,07	96,59 ± 0,07
	PSNR in dB	15,07 ± 0,06	18,71 ± 0,04	18,74 ± 0,03	18,87 ± 0,04	18,95 ± 0,03
D	SSIM in %	94,16 ± 0,05	96,78 ± 0,06	96,83 ± 0,06	96,98 ± 0,06	97,08 ± 0,07
	PSNR in dB	16,31 ± 0,06	19,61 ± 0,04	19,61 ± 0,04	19,72 ± 0,04	19,87 ± 0,04
E	SSIM in %	95,03 ± 0,03	97,16 ± 0,06	97,17 ± 0,06	97,26 ± 0,05	97,36 ± 0,06
	PSNR in dB	17,28 ± 0,07	20,32 ± 0,05	20,34 ± 0,04	20,43 ± 0,05	20,49 ± 0,04

Figure 4.3: Synthetic simulated gold standard CBF-map, noisy CBF-map and denoised CBF-maps for different number of C/L-pairs (40 (A), 50 (B), 60 (C), 80 (D) and 100 (E)). In addition, the SSIM and PSNR averaged over 50 trials are given.

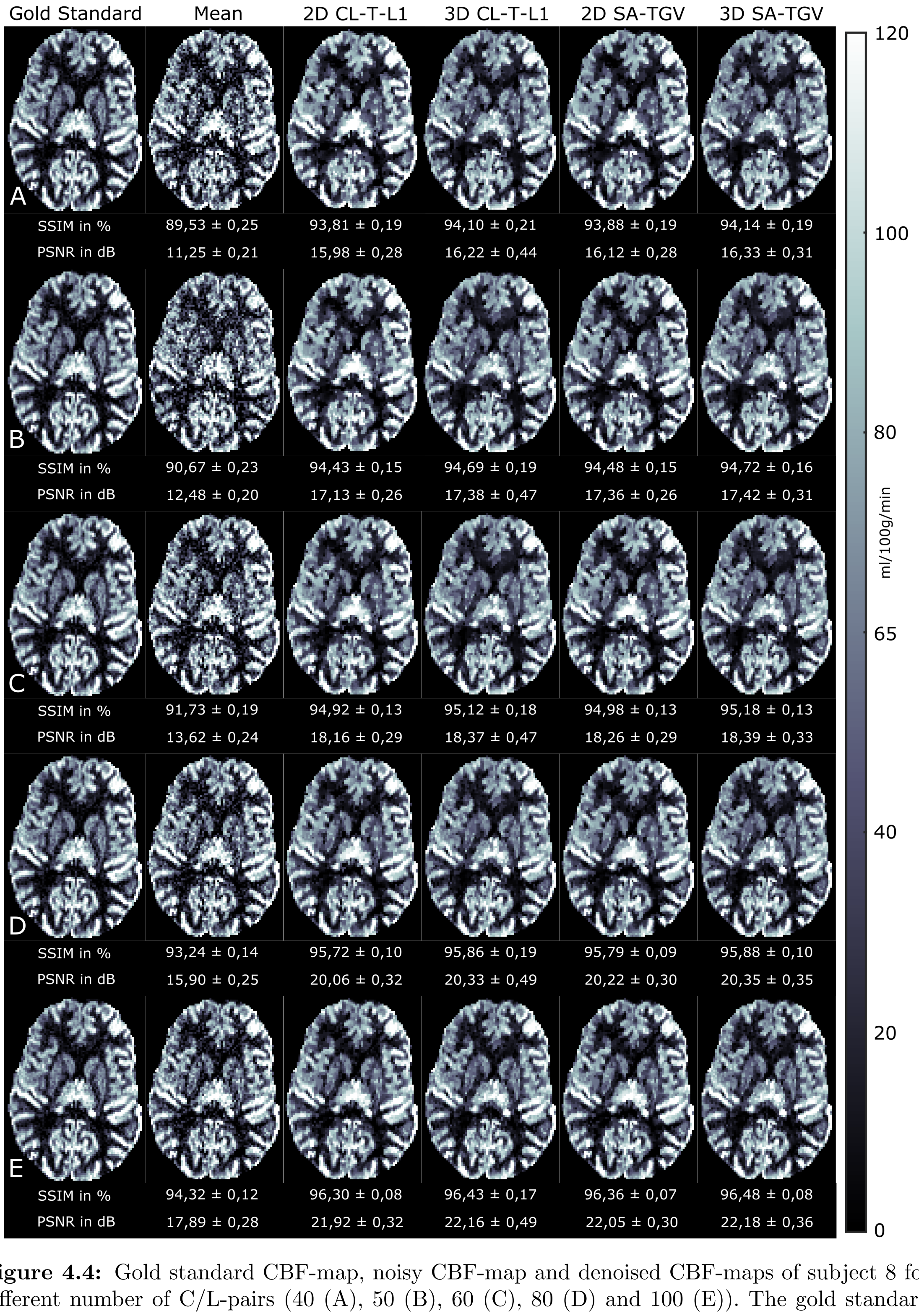

	Mean	2D CL-T-L1	3D CL-T-L1	2D SA-TGV	3D SA-TGV
SSIM in %	89,53 ± 0,25	93,81 ± 0,19	94,10 ± 0,21	93,88 ± 0,19	94,14 ± 0,19
PSNR in dB	11,25 ± 0,21	15,98 ± 0,28	16,22 ± 0,44	16,12 ± 0,28	16,33 ± 0,31
SSIM in %	90,67 ± 0,23	94,43 ± 0,15	94,69 ± 0,19	94,48 ± 0,15	94,72 ± 0,16
PSNR in dB	12,48 ± 0,20	17,13 ± 0,26	17,38 ± 0,47	17,36 ± 0,26	17,42 ± 0,31
SSIM in %	91,73 ± 0,19	94,92 ± 0,13	95,12 ± 0,18	94,98 ± 0,13	95,18 ± 0,13
PSNR in dB	13,62 ± 0,24	18,16 ± 0,29	18,37 ± 0,47	18,26 ± 0,29	18,39 ± 0,33
SSIM in %	93,24 ± 0,14	95,72 ± 0,10	95,86 ± 0,19	95,79 ± 0,09	95,88 ± 0,10
PSNR in dB	15,90 ± 0,25	20,06 ± 0,32	20,33 ± 0,49	20,22 ± 0,30	20,35 ± 0,35
SSIM in %	94,32 ± 0,12	96,30 ± 0,08	96,43 ± 0,17	96,36 ± 0,07	96,48 ± 0,08
PSNR in dB	17,89 ± 0,28	21,92 ± 0,32	22,16 ± 0,49	22,05 ± 0,30	22,18 ± 0,36

Figure 4.4: Gold standard CBF-map, noisy CBF-map and denoised CBF-maps of subject 8 for different number of C/L-pairs (40 (A), 50 (B), 60 (C), 80 (D) and 100 (E)). The gold standard CBF-map was calculated from the 500 C/L-pairs. In addition the SSIM and PSNR averaged over 50 trials are given.

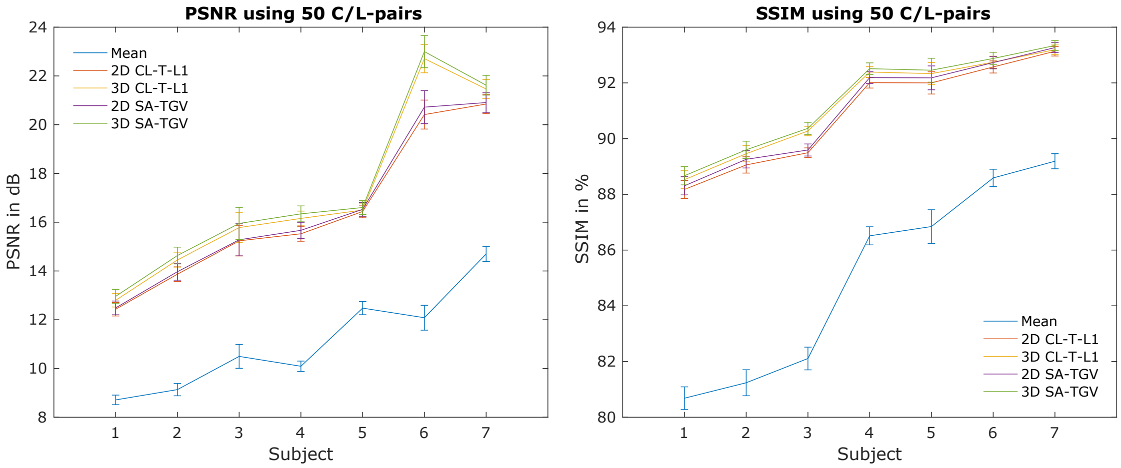

Figure 4.5: Quantitative performance comparison of the proposed methods using 50 C/L-pairs. The SSIM and PSNR averaged over 50 trials for the 7 subjctes are given. Error bars denote ±1 standard deviation.

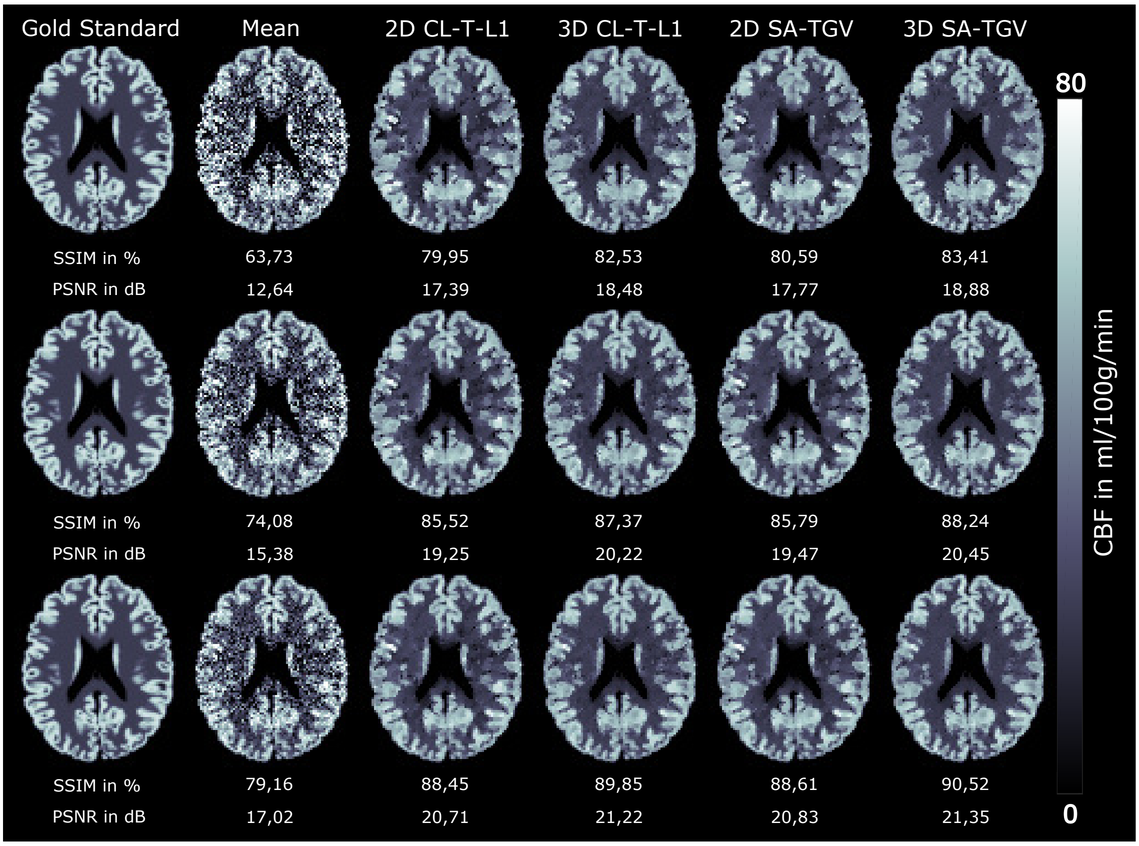

Figure 4.6: Synthetic simulated high resolution CBF-map, noisy CBF-map, and denoised CBF-maps using 4 different denoising approaches. Top row 25 averages, middle row 50 averages and bottom row 75 averages. In addition, the SSIM and PSNR are given.

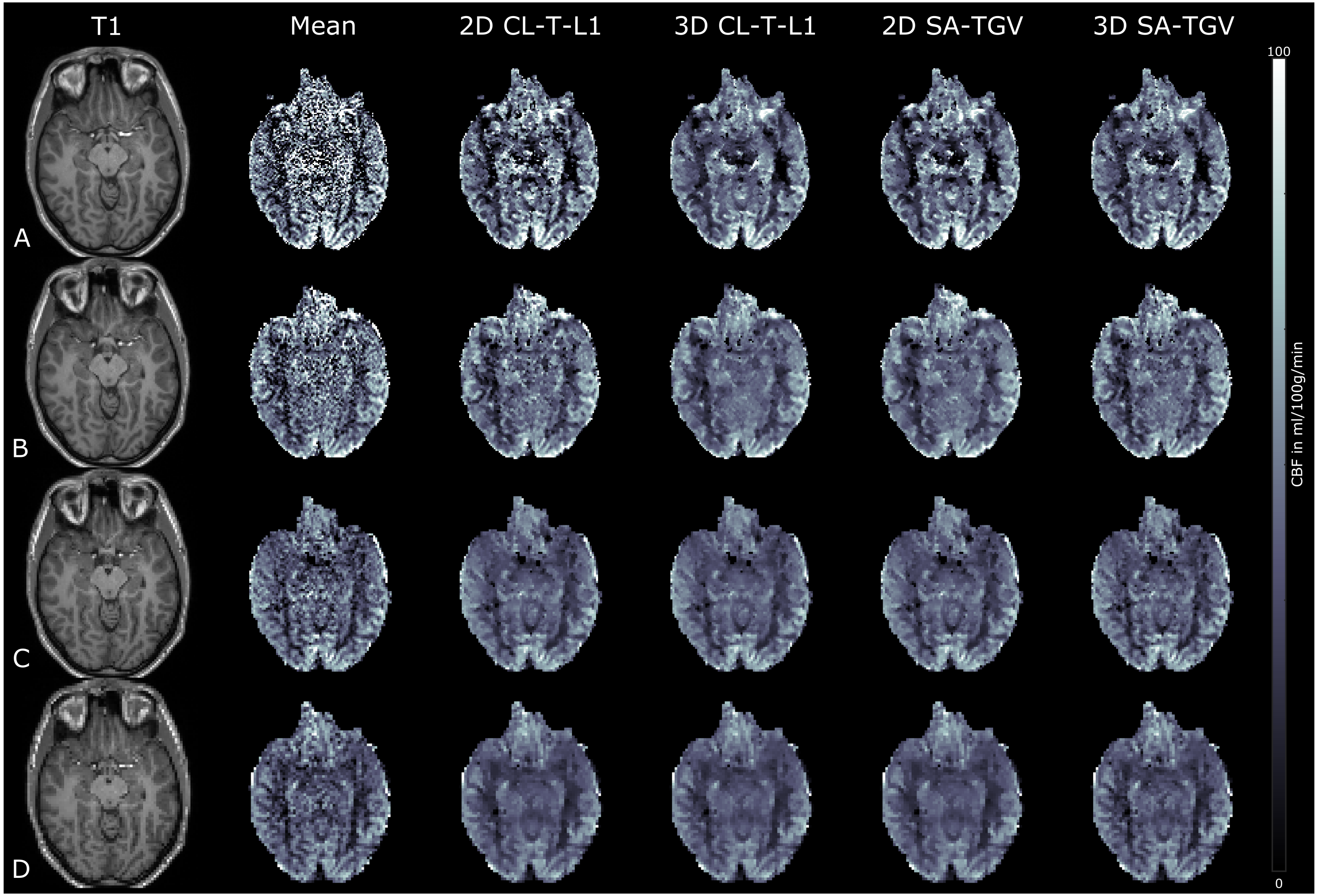

Figure 4.7: Performance comparison of the different denoising approaches for an exemplary in-vivo CBF-map at different spatial resolutions: (A) 1.3 mm iso, (B) 1.6 mm iso, (C) 2.0 mm iso, and (D) 2.5 mm iso. Note the different noise levels in the mean CBF images.

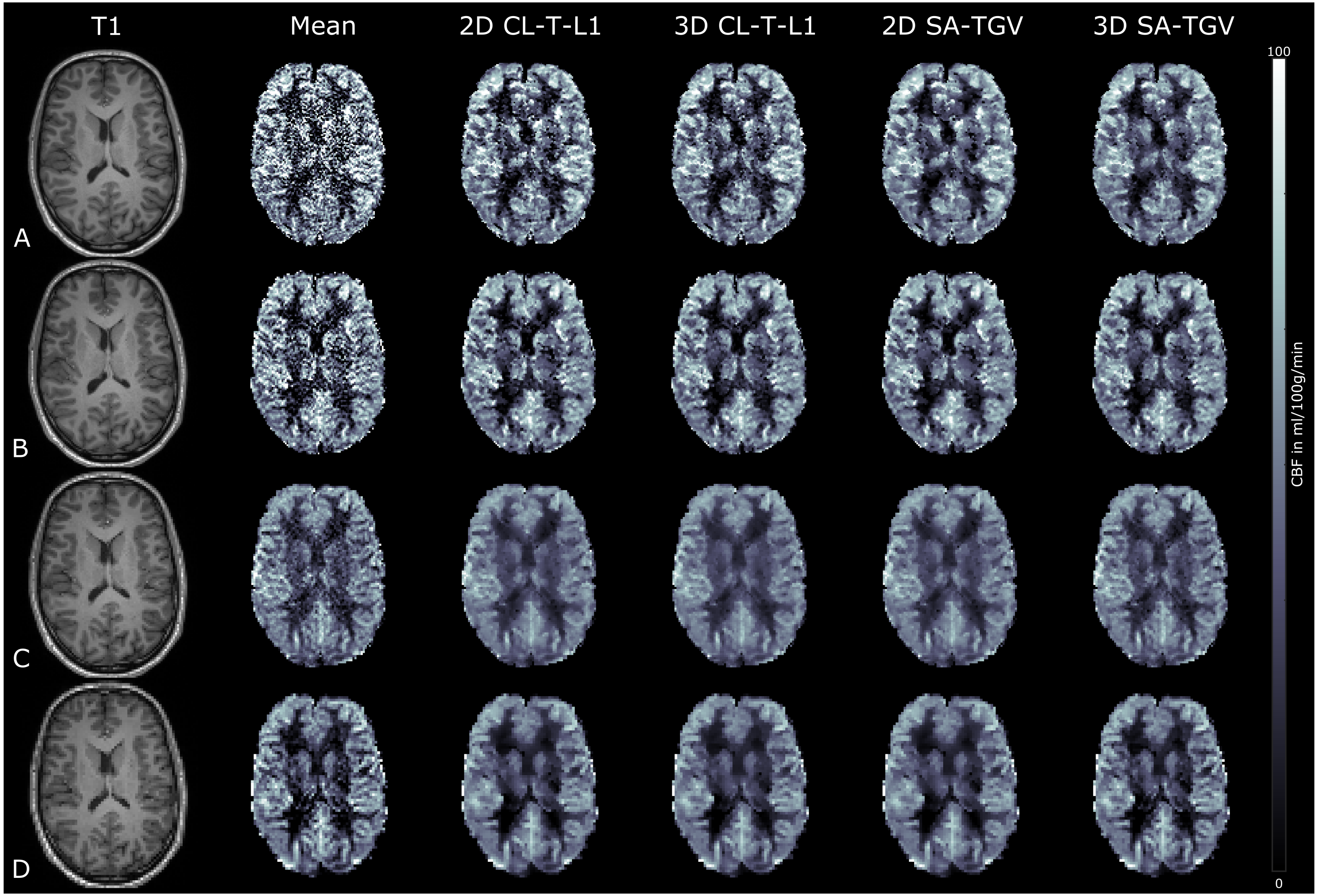

Figure 4.8: Performance comparison of the different denoising approaches for an exemplary in-vivo CBF-map at different spatial resolutions: (A) 1.3 *mm* iso, (B) 1.6 *mm* iso, (C) 2.0 *mm* iso, and (D) 2.5 *mm* iso. Note the different noise levels in the mean CBF images.

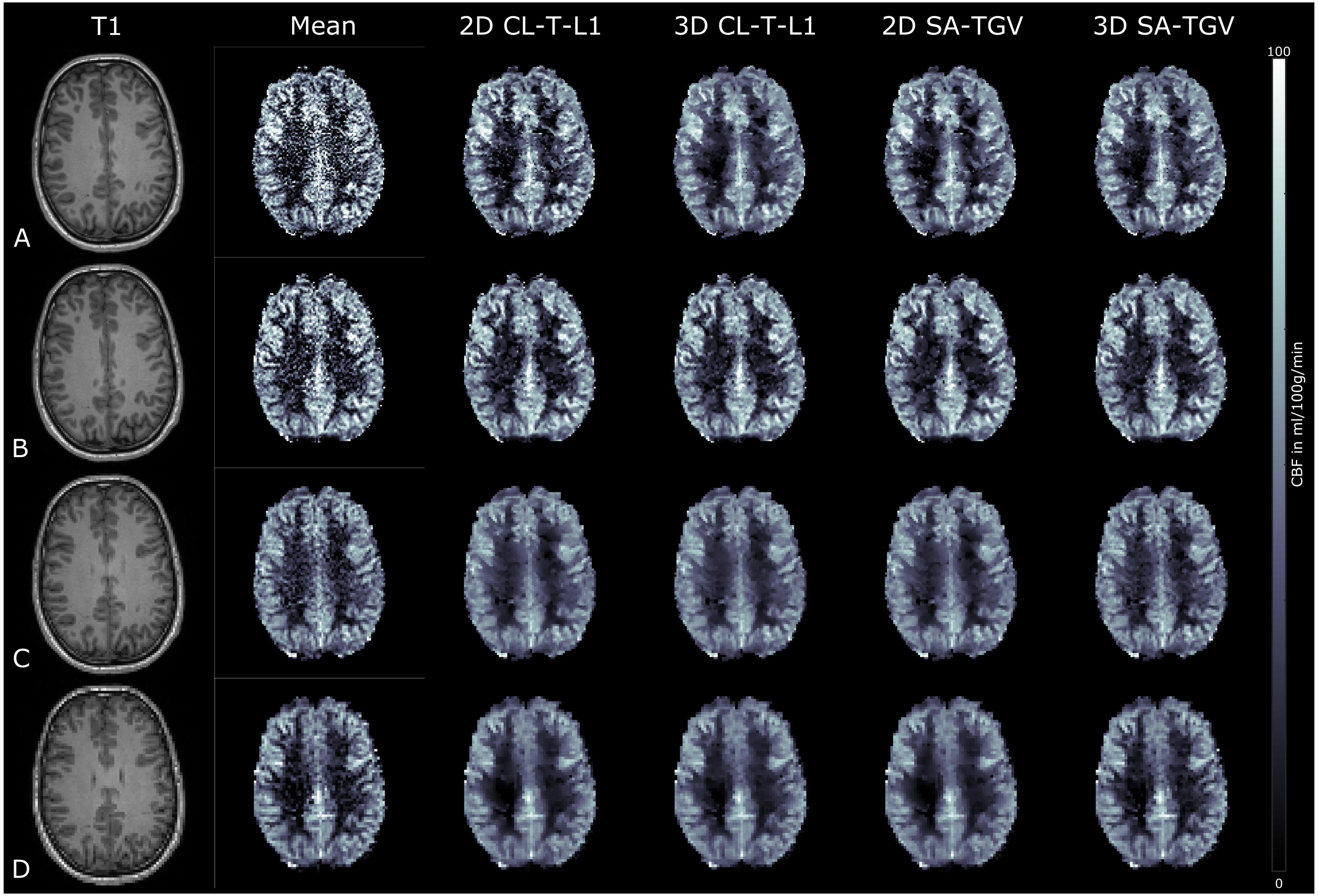

Figure 4.9: Performance comparison of the different denoising approaches for an exemplary in-vivo CBF-map at different spatial resolutions: (A) 1.3 mm iso, (B) 1.6 mm iso, (C) 2.0 mm iso, and (D) 2.5 mm iso. Note the different noise levels in the mean CBF images.

size decreases the inter-quartile range (IQR) and whiskers, indicating a higher SNR of the data. This is in accordance with the visual impression in Figure 4.9. For all TGV based denoising methods the median values for GM and WM are close to the mean CBF-maps, while the IQR could be reduced by approximately 50% for the high, and 30% for the low resolution data. The difference between the individual approaches is minor, however, the proposed 3D-SA approach shows the smallest IQR and the closest median to the noisy CBF-map.

4.5 Discussion

In this study we presented a TGV based denoising technique for ASL imaging, which takes into account spatial variations in noise level. Simulated low and high resolution as well as 2D and accelerated 3D in-vivo ASL datasets with different SNR-levels were considered. For all datasets the proposed method enhances the image quality and corresponding quantitative metrics compared with the robust CL-T-L1 approach proposed in chapter 3.

In ASL imaging the spatial regularization map can be easily calculated due to the nature of repeated measurements. The estimated maps (Figure 4.2) confirm previous findings that ASL datasets are often corrupted with local outliers due to changes in cardiac [159] or respiratory cycle [277], or due to the use of parallel imaging with multi-coil arrays leading to spatial dependent noise. Higher standard deviations are visible in regions of large vessels potentially leading to intravascular artifacts in the CBF images (Figure 4.4). In addition, boarder regions show a higher variation primary caused by motion as well as deep brain structures due to the reduced coil sensitivities. These variations are directly exploited in the proposed denoising approach resulting in improved image quality as well as higher quantitative metrics for the synthetic dataset. However, the improvement is small indicating that the robust CL-T-L1 approach is able to account for outliers and also to a certain extent for changes in noise level. The L^2 norm for the data-fidelity term penalizes higher deviations stronger than the L^1 norm. As a results, regions with high contrast changes get blurred, while the L^1 norm preserves edges and features well. Therefore, if an accurate estimation of spatial adaptive maps is not possible (e.g. the number of averages are too small) the CL-T-L1 approaches would deliver meaningful results.

Comparing the performance of the 2D denoising approaches with the 3D algorithm the improvement is only visible in quantitative metrics and is more or less negligible. This is not very intuitive because the information gained by the additional dimension should improve the results. However, the 2D datasets were simulated according to the in-vivo acquisition. The ascending multi-slice acquisition leads to an increased PLD and hence to a lower signal in the upper slices as illustrated in Figure 4.2. In case of 3D denoising this change in intensity is suboptimal because a change in contrast in the third dimension

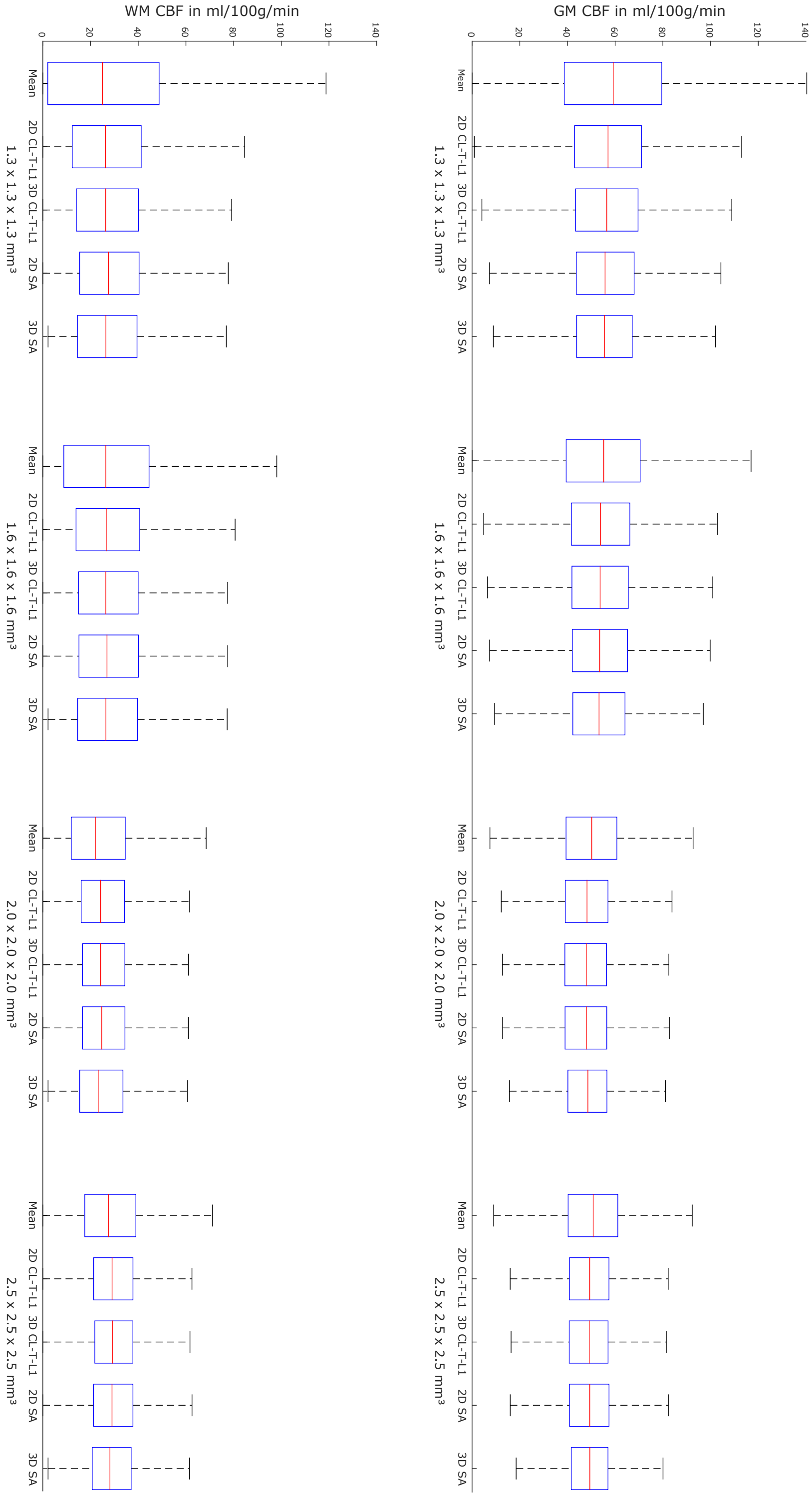

Figure 4.10: Mean CBF-values in GM and WM for 4 different resolutions.

leads to additional costs during the optimization process. In the 2D denoising approaches this change in contrast is accounted by normalization of the corresponding 2D images. Another reason could be the anisotropic voxel size. The slice thickness is 3.6 mm with an additional slice gap of 0.9 mm resulting in 4.5 mm in total. Since the structures in the GM are changing rapidly form slice to slice the low resolution hampers the performance of 3D approaches.

For the 2D in-vivo datasets a similar behavior is observable. However, the improvement for 3D approaches is higher as for the synthetic dataset. The 3D denoising methods provide more natural CBF-maps and additionally higher quantitative SSIM and PSNR values for all subjects. One reason could be the natural variation of the CBF in the GM and WM of the in-vivo dataset. In contrast, the synthetic dataset has more or less constant areas. In case of constant areas, a strong penalization can be used to remove the noise and achieve a low cost of the penalization functional. However, if natural variations exits this high penalization causes oversmoothing and thereby degrading the image quality. A trade-off between noise removal and oversmoothing has to be chosen for the 2D approaches. This may explain the weaker regularization parameter for the in-vivo dataset. In such cases, the use of additional information in the third dimension could help to remove noise.

The potential of the 3D denoising algorithms is reflected in the high resolution 3D synthetic datasets. Both approaches show a clear improvement in visual quality and quantitative metrics compared with the 2D approaches. Again, the highest improvement is achieved for the proposed 3D-SA-TGV approach, which directly exploits the uncertainties in the data fidelity term. For the in-vivo dataset, the higher resolutions clearly reduces the partial volume effects (PVE) leading to higher CBF values and better localization of structures. However, this is accompanied by a significant higher noise level. The denoising methods successfully suppress noise but introduce blurring, especially in the CBF-maps with very high noise levels. The blurring is accompanied with a loss in image quality and effective resolution. A good compromise between noise, resolution, smoothing, and acquisition time is achieved by the 3D dataset with 2 mm isotropic resolution.

The proposed spatial adaptive method has the advantages that the model and regularization parameters are very robust for a specific dataset i.e. the same parameters can be used for different SNR levels or subjects. In contrast, the robust L^1 method uses a different regularization parameter for a different number of averages. Nevertheless, if the readout or labeling schemes is changed both parameters of the SA-TGV has to be tuned accordingly. This can be explained by the high contrast change between non-background suppressed 2D and background suppressed 3D ASL data. In addition, the blurring in the 3D images leads to a lower contrast to noise ratio.

In summary, the results of this study highlights the potential of using a spatial adaptive regularization approach for image enhancement of ASL data. The regularization map takes into account local variations of noise. As a consequence, this approach reduces outliers, improves the image quality and accompanied quantitative values. It provides high resolution CBF-maps within a clinical acceptable measurement time. Further improvements are expected by considering the SNR in the voxels instead of the uncertainties. Thus, especially for 2D-multi slice imaging the signal change due to the longer PLDs can be considered. In addition, the different SNR levels in WM and GM can be included.

4.6 Conclusion

The incorporation of a spatial varying regularization parameter in the TGV denoising approach increases the SNR and image quality compared to a single regularization parameter. In addition the proposed method allows for automatic denoising of ASL data. The regularization parameter can be easily calculated by estimating the temporal standard deviation. This approach is capable of meeting highly clinical demands in terms of scan time reduction, accounting for local outliers and enhancing image quality.

5

Variational Denoising for Dynamic Arterial Spin Labeling Perfusion Data

This chapter is based on the following abstracts which were accepted for the ISMRM 2017 and 2018:

> M. Schloegl, S. M. Spann, C. S. Aigner, M. Holler, K. Bredies, and R. Stollberger. Improved Denoising of Dynamic Arterial Spin Labeling with Infimal Convolution of Total Generalized Variation. In *Proceedings of the 25th Annual Meeting of ISMRM*, Honolulu, 2017
>
> S. M. Spann, M. Schloegl, C. S. Aigner, K. Koschutnig, M. Holler, K. Bredies, and R. Stollberger. Improved functional Arterial Spin Labeling by spatio-temporal ICTGV denoising. In *Proceedings of the 26th Annual Meeting of ISMRM*, Paris, 2018

Contents

5.1 Introduction

So far we only considered static or steady state conditions in arterial spin labeling (ASL) i.e. acquiring the ASL signal at one specific post-labeling delay (PLD) and by assuming that the cerebral blood flow (CBF) does not change during the acquisition. All denoising methods proposed in chapter 3 and 4 are limited to these static ASL measurements. However, for many applications it is important to consider and maintain the ASL signal evolution through time. For example, in task based functional arterial spin labeling (fASL) the activity of the human brain in response to a specified task is investigated in space and time. This relies on the mechanism that increased neural activity is accomplished by an increase in metabolism and CBF [99]. During the rest state spontaneous fluctuations in CBF are observable over time due to time-varying neuronal activity. This fluctuations are synchronized in certain brain regions and used to study resting-state functional connectomics i.e. brain regions which shows a high correlation in fluctuations are likely connected to each other. [25] Another important application is pharmacological functional magnetic resonance imaging (phMRI). In these studies the change in CBF induced by medication or recreational drugs is evaluated for understanding their effect on the brain systems i.e. Gollub et al. [103] showed that cocain infusion decreases the CBF in gray matter (GM). A study by Cemeron et al. [37] showed that an intake of 250mg caffeine leads to a vasoconstriction of the cerebral vascular and hence reduces the whole brain CBF down to 30%. Dynamic ASL measurements are especially important for patients with cerebrovascular disease for whom the healthy and affected brain region might have a different arterial transit time (ATT) which is not known in advance. In this case the right choice of the PLD has a major impact on the quantification accuracy. The acquisition of the time evolution of ASL signal in each voxel can solve this transit time problem. However for all those applications a high temporal resolution is necessary which dramatically reduces the SNR compared to static measurements where tens of averages are acquired. This makes post-processing techniques for gaining SNR even more important. In this chapter the concept of infimal convolution of total generalized variation (ICTGV) denoising is presented which was proposed by Holler et al. [131] and applied in the context of 2D dynamic magnetic resonance imaging (MRI) data reconstruction [221]. The proposed method is validated on two exemplary ASL applications; First in a task based fASL study where the perfusion changes in local brain regions correlates with neural activation and second in a multi-PLD experiment where the evolution of the ASL signal in each voxel is investigated.

5.2 Theory

5.2.1 Spatio-Temporal TGV

The basic theory for variational models with spatial regularization was described in chapter 3.2.2 "Total Generalized Variation for ASL Denoising". Recapturing the definition of the spatial TGV-functional (equation 4.1) it is straightforward to extend this to spatio-temporal dimensions. Similar to the extension for the 3D anisotropic case, an additional dimension and a corresponding weight is introduced in the gradient ($\nabla : U \mapsto U^4$) and symmetrized gradient ($\epsilon : U^4 \mapsto U^{10}$) operator in the spatio-temporal domain ($U \in$

$\Re^{N_x \times N_y \times N_z \times N_t}$) leading to:

$$TGV^2_{\alpha_1,\alpha_0}(u) = \min_{v} \left\{ \alpha_1 \left|\left| \nabla u - v \right|\right|_1 + \alpha_0 \left|\left| \epsilon v \right|\right|_1 \right\} \tag{5.1}$$

with

$$(\nabla u)_{i,j,k,t} = \begin{pmatrix} s_x \left(\partial_x^+ u\right)_{i,j,k,t} \\ s_y \left(\partial_y^+ u\right)_{i,j,k,t} \\ s_z \left(\partial_z^+ u\right)_{i,j,k,t} \\ s_t \left(\partial_t^+ u\right)_{i,j,k,t} \end{pmatrix}, \tag{5.2}$$

and

$$(\epsilon v)_{i,j,k,t} = \begin{pmatrix} s_x \left(\partial_x^- v^1\right)_{i,j,k,t} \\ s_y \left(\partial_y^- v^2\right)_{i,j,k,t} \\ s_z \left(\partial_z^- v^3\right)_{i,j,k,t} \\ s_t \left(\partial_t^- v^3\right)_{i,j,k,t} \\ \frac{1}{2}\left(\left(s_x \partial_x^- v^2\right)_{i,j,k,t} + \left(s_y \partial_y^- v^1\right)_{i,j,k,t}\right) \\ \frac{1}{2}\left(\left(s_x \partial_x^- v^3\right)_{i,j,k,t} + \left(s_z \partial_z^- v^1\right)_{i,j,k,t}\right) \\ \frac{1}{2}\left(\left(s_x \partial_x^- v^4\right)_{i,j,k,t} + \left(s_t \partial_t^- v^1\right)_{i,j,k,t}\right) \\ \frac{1}{2}\left(\left(s_y \partial_y^- v^3\right)_{i,j,k,t} + \left(s_z \partial_z^- v^2\right)_{i,j,k,t}\right) \\ \frac{1}{2}\left(\left(s_y \partial_y^- v^4\right)_{i,j,k,t} + \left(s_t \partial_t^- v^2\right)_{i,j,k,t}\right) \\ \frac{1}{2}\left(\left(s_z \partial_z^- v^4\right)_{i,j,k,t} + \left(s_t \partial_t^- v^3\right)_{i,j,k,t}\right) \end{pmatrix} = \begin{pmatrix} w^1 \\ w^2 \\ w^3 \\ w^4 \\ w^5 \\ w^6 \\ w^7 \\ w^8 \\ w^9 \\ w^{10} \end{pmatrix}, \tag{5.3}$$

where $u \in U$ is the volume time series, $v \in U^4$ is a tensor field, α_0 and α_1 are positive weights, and $\partial_x^+ : U \mapsto U$ and $\partial_x^- : U \mapsto U$ are the discrete forward and backward differences defined in the Appendix C.1.1 and C.1.3. We denote by $N_x \times N_y \times N_z$ the dimensions of image space, and by N_t the number of time frames. The incorporation of an additional temporal dimension allows to exploit spatial and temporal redundancy of the dataset. By applying the proposed total generalized variation (TGV) functional (equation 5.1) we obtain a dynamic image series which is smooth in space and time. A crucial part is the choice of the right spatial and temporal weights. For the spatial dimensions the corresponding weights s_x, s_y, s_z are given by the voxel dimensions. However for the temporal dimension the weight s_t is not known in advance as the relation of frames or time-steps to spatial voxels is unclear. (Note that the weights in space and time can be reduced to a simple parameter $\beta = \frac{\beta_t}{\beta_s}$ controlling the relation between time and space which is defined in the Appendix C.1.6 and C.1.6 respectively.) By fixing this spatio-temporal ratio to one value we have to decide if we prefer a higher temporal or a higher spatial regularization. The first is favorable for regions where no or only slow signal changes occur over time since it strongly penalizes temporal variations. For areas with high dynamic changes a higher spatial regularization is beneficial. Since dynamic ASL data have locally different dynamic properties i.e. areas with no or slow dynamic changes as well as regions with high dynamic changes, a trade off between those two situations has to be chosen. To address this problem Holler et. al. [131] proposed the infimal convolution of two spatio-temporal TGV functions with different spatial and temporal weights.

5.2.2 Infimal Convolution of TGV

The infimal convolution of two spatio-temporal TGV functionals is defines as

$$ICTGV^2_{\alpha_1,\alpha_0,\beta_1,\beta_2}(u) = \min_v TGV^2_{\alpha_1,\alpha_0,\beta_1}(u-v) + TGV^2_{\alpha_1,\alpha_0,\beta_2}(v)\,. \tag{5.4}$$

By using two different spatio-temporal ratios i.e. $\beta_1 < 1$ and $\beta_2 > 1$ we can account for different dynamic properties. The first $TGV^2_{\alpha_1,\alpha_0,\beta_1}$ functional enforces pice-wise smoothness in space and time, but allows more model deviations in space. In contrast, the second $TGV^2_{\alpha_1,\alpha_0,\beta_2}$ functional allows more deviations in time. The infimal convolution of those two functionals separates the original volume sequence u in two volume sequences $u-v$ and v and balances the contribution of those two volumes locally. The defined ICTGV functional provides dynamic volumes, which are smooth in space and time and additionally takes into account rapidly changing contrasts as well as slow or stable contrast. [131]

For denoising of a dynamic ASL dataset equation 5.4 has to be extended with a data-fidelity term and a corresponding regularization parameter λ. This parameter balances the strength of data faithfulness versus regularization. This leads to the following final minimization problem:

$$u^* \in \arg\min_u \frac{\lambda}{2}\,||u-d_u||_2^2 + ICTGV^2_{\alpha_1,\alpha_0,\beta_1,\beta_2}(u)\,. \tag{5.5}$$

This minimization problem is non-smooth but convex and can be efficiently solved by Chambolle-Pocks primal dual algorithm. Therefore, the problem has to be reformulated as a saddle-point problem. This reformulation as well as the numerical solution is given in Appendix C.2.8.

5.3 Implementation

All necessary steps in the iterative primal dual algorithm reduce to simple arithmetic operations which can be highly parallelized on a graphics processing unit (GPU). Therefore, the ICTGV denoising algorithm was implemented in C++ with compute unified device architecture (CUDA) parallel processing using the AGILE [149] and accelerated variational dynamic MRI reconstruction (AVIONIC) [222] library. For all denoising applications the model parameters α_1 and α_0 for the TGV functionals were set to $\alpha_1/\alpha_0 = 1/\sqrt{3}$, which proved to be a reasonable choice for MRI images [148]. Further model parameters (β_1, β_2, and s) were optimized for each applications individually as this parameters depend on the dynamic properties of the dataset. The regularization parameter λ adjusts the balance between regularization and data consistency and depends on the signal-to-noise ratio (SNR) of the dataset. Hence, it is adjusted for the experiments according to the SNR. For all applications the number of iterations was set to 2000, which is enough to ensure convergence.

5.4 Application to Functional Arterial Spin Labeling

5.4.1 Short Introduction to fMRI

Since its introduction in 1990 functional magnetic resonance imaging (fMRI) has become the most widely used technique to study the activity of the living brain. Compared with positron emission tomography (PET) it is non-invasive, does not require a radioactive tracer, and is much cheaper. Furthermore, it has a much higher spatial resolution with well defined anatomic landmarks and includes whole brain coverage compared to electroencephalography (EEG). [67]

The basis for functional neuroimaging are complex physiological changes in the brain as a result of increased neural activity. The exact mechanism linking the complex cellular, metabolic, and vascular changes are still under investigation but can be summarized as follows. During activation several cellular processes of neurons require energy in form of adenosin triphosphate (ATP). Large amounts of ATP are produced by the oxidative glucose metabolism, which require oxygen and glucose. Since the brain has no locale energy storage, both substrates are continuously supplied by the CBF. Consequently, during neuronal activity the increase in metabolic rate (glucose and oxygen consumption) is accompanied by an increase in CBF and blood velocity. In addition, it leads to a vasodilatory response increasing the cerebral blood volume (CBV). [35, 199]

Fox and Raichle [89, 90] studied the relationship between neural activity and the physiological changes. They implied a linear coupling between neural activation and cerebral metabolic rate of oxygen (CMRO2) but a non-linear coupling, with a disproportional rise, in case of CBF as well as cerebral metabolic rate of glucose (CMRGlc). The fractional change in CBF and CMRGlc are similar [90, 99] and typically by a factor of 2-3 higher compared to CMRO2 [61, 129, 145]. This disproportional increase in CBF compared with CMRO2 results in a net increase in the amount of oxygenated blood. As consequence, the deoxygenation of venous blood drops [35]. Deoxygenated hemoglobin (dHb) is paramagnetic due to the unpaired electrons and produces a local susceptibility induced field shift leading to a reduction in T_2^* [265]. This measurable effect is known as blood oxygen level dependent (BOLD) effect [191] and leads to a drop in the MRI signal. Since in neural activity the ratio of oxygenated hemoglobin (oHb) to dHb increases an increase in T_2^* is observable. The typically BOLD response raises the baseline signal by a factor of 0.5-5% [67]. However, the signal changes are not quantifiable in physiological units. Since the BOLD response depends on the deoxygenation level of venous blood, the change in CBV

in response to neural activity directly affects the oxygenation level and hence the BOLD response. The BOLD signal is therefore only a indirect measure of neural activity without quantitative, physiological interpretation as it depends on changes in CBF, CMRO2 and CBV [120]. Other physiological variables such as heart rate variability [235], breathing rate [69] or respiration volume [23] can change the BOLD signal i.e. breath holding can change the BOLD signal up to 4% [264]. Furthermore, low-frequency drifts known as baseline drifts are present in BOLD fMRI data. The source of this drifts are systematic changes in the MRI hardware i.e. heating of shim as a result of gradient heating [80, 237].
An alternative fMRI method for studying the neural activity is ASL. In contrast to BOLD, fASL provides quantitative information of perfusion changes over time. It provides, therefore, a direct measure of the CBF induced signal change due to either an external stimulus (i.e. a flashing checkerboard) or due to spontaneous brain activity (i.e. resting-state fMRI). [166] A task-based fASL experiment was first demonstrated by Kwong [151] and the CBF increases 30-90% in the activation region depending on the performed task [316]. Whereas in BOLD the signal change is unit-less and always related in percentages to the baseline, in ASL the change in CBF can be quantified in absolute units. The additional insensitivity to baseline drifts in ASL, due to pair-wise subtraction of adjacent control and label images, makes ASL perfectly suited for applications with a slowly varying signal over time (long task block) and for longitudinal studies i.e. for studying long-term effects of working memory training [255], for studying disease progressions or for studying the effects of a given pharmacological agents on the baseline CBF [48].
Several studies reported that fASL has a higher spatial accuracy compared to BOLD fMRI [172, 207, 267]. The ASL signal is more located to the brain parenchyma and shows a better spatial correlation to anatomical landmarks since the measured CBF is primarily from small arterioles and capillaries. In contrast, the BOLD signal stems from the change in oxygenation of blood and shows a bias toward the venous side away from the activated brain region [278]. Another interesting feature of fASL is the higher intra-individual reproducibility [156, 216, 267] and the lower inter-subject variation [267] compared to BOLD. However fASL has two major challenges which restrains its application in clinical and research areas: first a low signal-to-noise ratio and second a low temporal resolution due to the additional labeling time and PLD.
In this work ICTGV is used to address the limitation of low SNR. ICTGV incorporates spatial and temporal information for denoising of the perfusion weighted image (PWI) time series. The denoising method is evaluated on task-based finger tapping experiments and compared to standard Gaussian denoising. The ICTGV denoising approach is validated on in-vivo data as well as on a synthetic generated dataset.

5.4.2 Methods

5.4.2.1 2D Data Acquisition

Four healthy volunteers were scanned at a 3T magnetic resonance (MR) system (Magnetom Skyra, Siemens Healthcare, Germany). Pulsed ASL measurements were performed using PICORE/Q2TIPS single shot echoplanar imaging (EPI) with a 20-channel head coil. The following imaging parameters were used: 15 slices with 6 mm thickness, distance factor 25%, 3x3 mm^2 in-plane resolution, 6/8 partial-Fourier, repetition time (TR)/echo time (TE) = 2500/13 ms, bolus or labeling duration (TI1)/inversion time (TI) = 800/1800 ms and labeling slice thickness 10 cm. A block design paradigm with seven interleaved 30-second periods of rest and finger tapping (right hand) was conducted resulting in an acquisition time of 7 min 10 s.

5.4.2.2 Anatomical Data Acquisition

For each subject an additionally T_1 weighted image was acquired using a 3D magnetization prepared - rapid gradient echo (MPRAGE) sequence with the following imaging parameters: resolution of 1x1x1 mm^3, 192 slices, phase oversampling = 15%, slice oversampling = 33%, TR/TE/TI = 1910/1.81/1000 ms, Grappa-factor = 4, flip-angle = 8°, acquisition time = 2 min 55 s.

5.4.2.3 Anatomical Data Processing

For each subject the T_1 weighted images were segmented into GM, white matter (WM), and cerebrospinal fluid (CSF) using statistical parameter mapping v 12 (SPM12)[1] (Wellcome Trust Centre for Neuroimaging, University College London, UK) [92] and coregistered to the native ASL image. From this coregisted tissue partial volume (PV) maps a brain mask was generated by summing up the corresponding maps and including voxels with a tissue content greater than 0.1.

5.4.2.4 Synthetic Dataset

In order to evaluate the proposed method, a synthetic CBF-map was generated based on the segmented T_1 weighted image of one subject as described in section 3.3.4 "Numerical Phantom". In this synthetic CBF-map, voxels corresponding to activations due to motor tasks (voxels in the primary sensorimotor area, supplementary motor area, and parietal and parietal associative area) are superimposed with a BOLD effect and ASL activation signal change (30s on/off, 7 runs) as shown in Figure 5.1 and described in [122]. Zero mean Gaussian noise was added to this synthetic ASL image time series.

---

[1] https://www.fil.ion.ucl.ac.uk/spm/software/spm12/

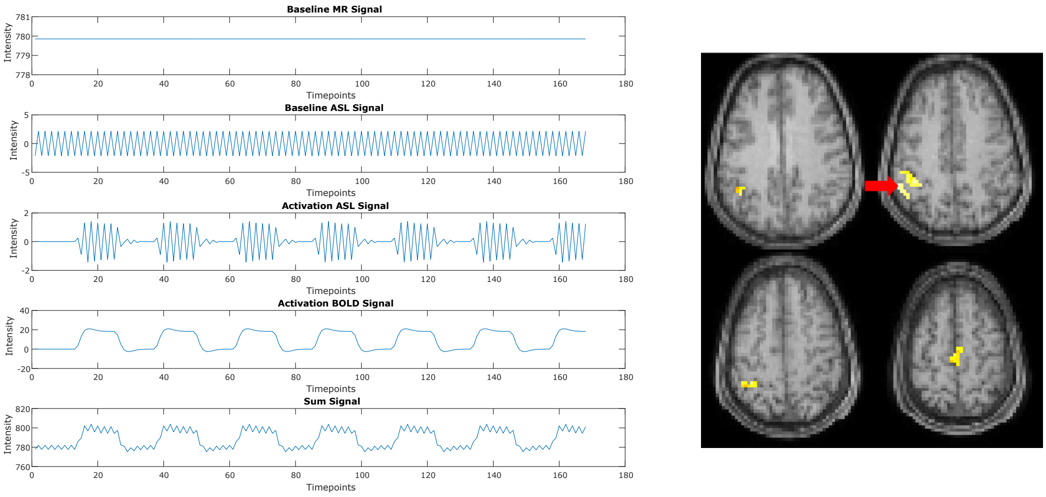

Figure 5.1: Simulated BOLD-effect and ASL signal change in one representative voxel. The time course of the selected voxel is marked with a red arrow in the T_1 weighted image. Gold standard activation map (FWE, $p < 0.05$) overlayed on a coregisted T_1 weighted image.

5.4.2.5 ASL Data Processing

ASL data processing and statistical analysis were conducted using MATLAB (Mathworks, Natick, Massachusetts), SPM12, ASL-toolbox [293, 294] and in-house developed MATLAB scripts. Prior to denoising the ASL time series were motion-corrected and global signal fluctuations were regressed out of the ASL image time series at each voxel [293, 294]. To eliminate the BOLD signal contamination in the ASL time series surround subtraction was applied [167, 307]. Afterwards, the perfusion weighted time series was denoised using the proposed spatio-temporal approach and for comparison using a conventional 3D-Gaussian kernel with 6 mm full width at half maximum (FWHM). From the noisy and denoised PWIs, the CBF-maps were quantified using a general kinetic model [34] for pulsed arterial spin labeling (PASL) as defined in section 4.3.4 "Quantification of CBF". Subsequent task-based fASL analysis was performed in SPM12 for each subject. A general linear model (GLM) was fitted in the CBF time series. The model was specified using a box-car function convolved with a canonical hemodynamic response function. The statistical maps were thresholded at $p < 0.05$ after family wise error (FWE) correction and overlayed on the coregistered T_1 weighted images.

5.4.2.6 Parameter Choice

The regularization parameter λ as well as the ICTGV model parameters, β_1, β_2, and s were optimized using the simulated dataset. A grid search was performed and the parameter values which achieved the most true and the least false activation voxels were used. This parameters are $\beta_1 = 7$, $\beta_2 = 1$, $s = 0.6$ and $\lambda = 0.1$.

5.4.3 Results

Figure 5.2 shows the activation-maps (FWE, $p < 0.05$) overlayed on a T_1 weighted image for the simulated dataset using no denoising, Gaussian denoising, and the proposed denoising method as preprocessing step. Compared with no denoising and Gaussian denoising, the incorporation of temporal information in the proposed denoising method results in detection of all activations for 4 as well as 7 runs. Since the time course of fASL data is highly redundant, the inclusion of the temporal information is very effective. This improvement in spatio-teporal denoising is illustrated in Figure 5.3, showing the acquired PWIs at 4 different time points for subject 4. During the finger tapping period (timepoint 14 and 17) a clear signal increase in the motor cortex (green arrow) of the perfusion weighted images is visible. Figure 5.4 shows the activation maps (FWE, $p < 0.05$) of subject 4 and the corresponding fitted CBF response in the voxel with the highest t-value. The ICTGV denoised time-series exhibits substantial improvement in noise suppression compared with standard spatial Gaussian denoising. This results in statistically significant activations in the motor areas (bottom row). Figure 5.5 shows exemplary the activation maps (FWE, $p < 0.05$) of the remaining three subjects.

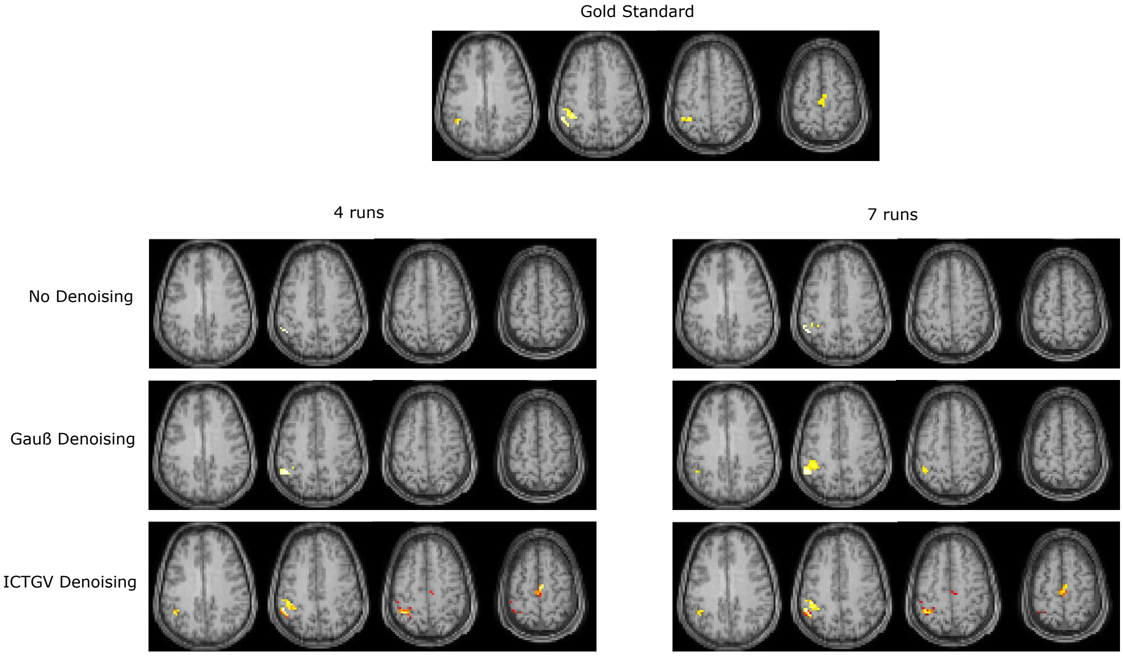

Figure 5.2: Activation map (FWE, $p < 0.05$) overlayed on a coregisted T_1 weighted image generated from the gold standard (noise free), noisy, Gaussian denoised, and ICTGV denoised CBF time series.

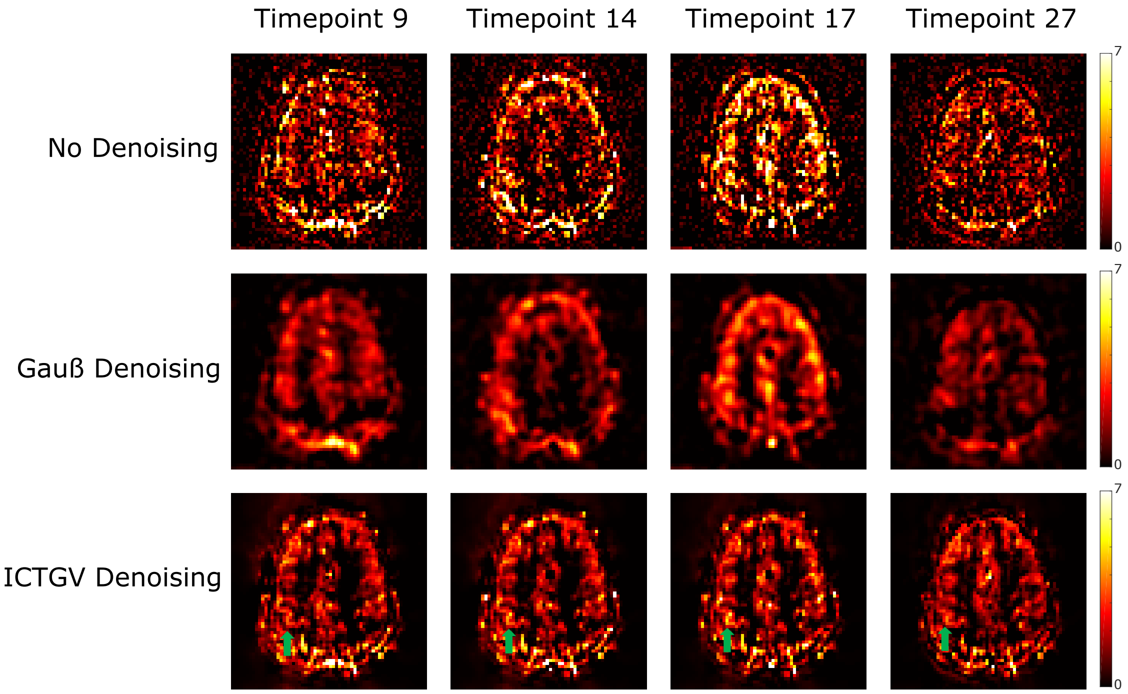

Figure 5.3: Perfusion weighted images at 4 different time points of one slice from subject 4 without denoising, using Gaussian denoising, and using the proposed method. The CBF-increase/neuronal activity in the motor cortex due to finger tapping is clearly visible in the ICTGV-denoised PWIs (green arrow). Timepoint 9 and 27 are PWIs acquired during rest and timepoint 14 and 17 are PWIs acquired during finger tapping.

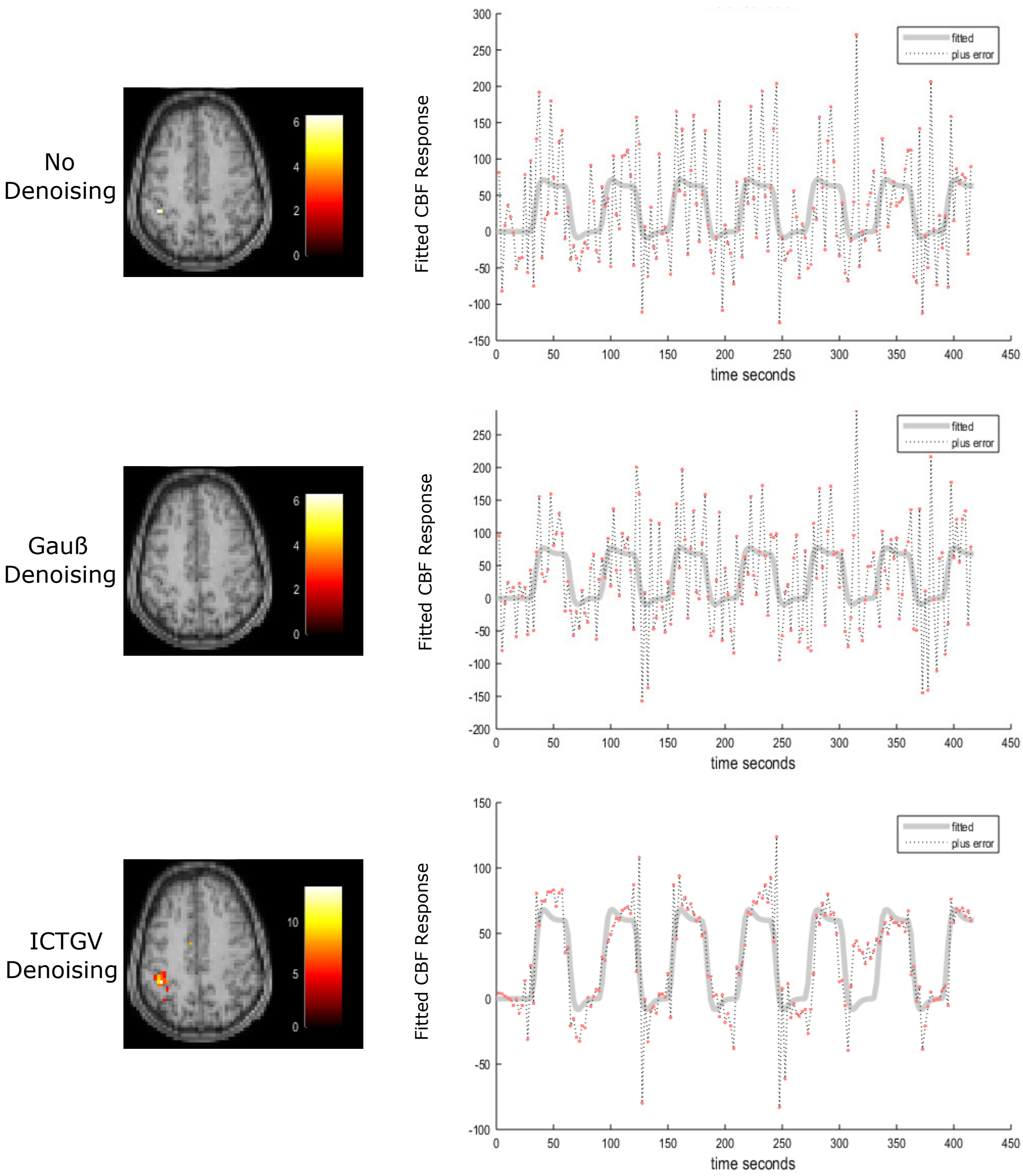

Figure 5.4: Activation maps (FWE, $p < 0.05$) of one representative subject (4) overlayed on a coregisted T_1 weighted image using noisy data, Gaussian denoised, and ICTGV denoised data. Fitted CBF response in one voxel of the motor cotex during the finger tapping experiment.

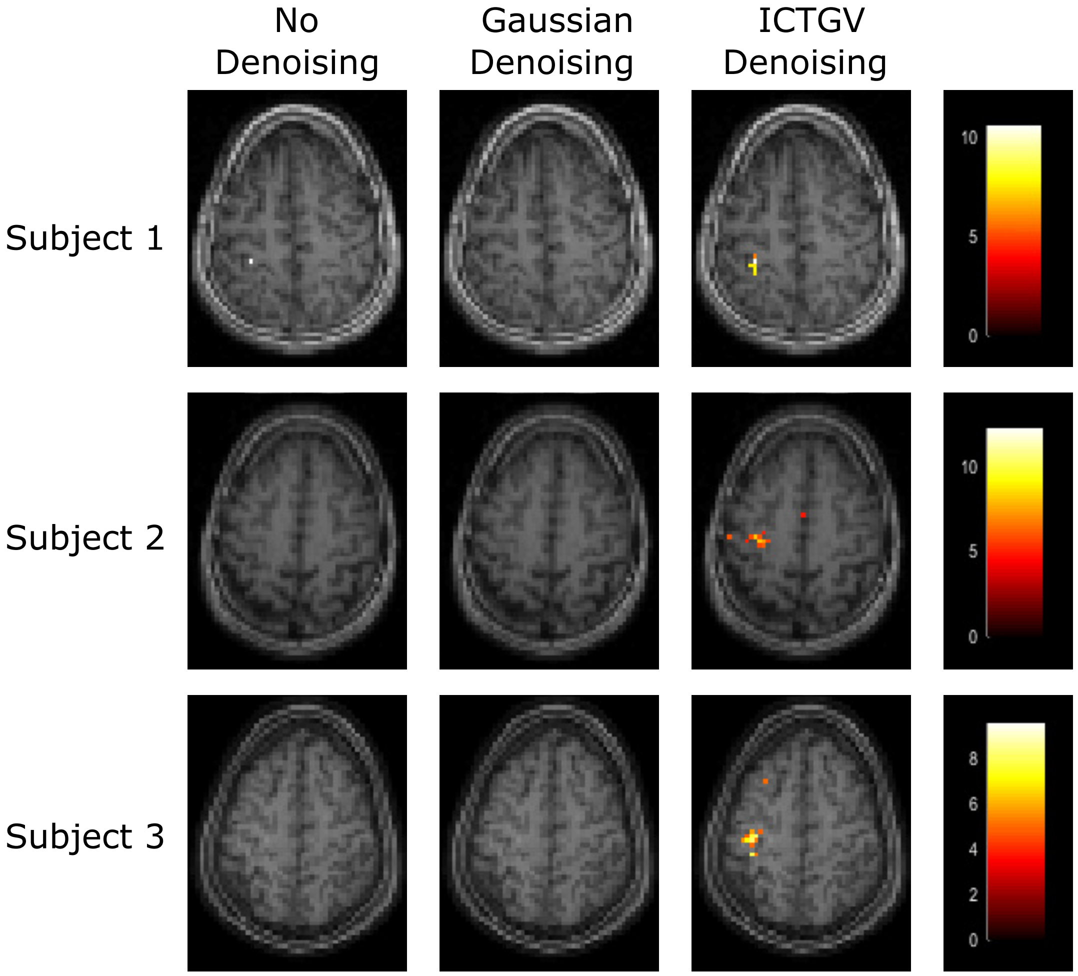

Figure 5.5: Activation maps (FWE, $p < 0.05$) overlayed on a coregisted T_1 weighted image of the remaining 3 subjects conducted form the noisy, Gaussian denoised, and ICTGV denoised time series.

5.4.4 Discussion

In this chapter the effect of spatio-temporal denoising based on infimal convolution of TGV functionals was assessed for fASL data. The proposed method combines two spatio-temporal weights, allowing for stronger temporal regularization in areas with low dynamic change and weaker temporal regularization in areas with high dynamic change. The incorporation of temporal information in the denoising procedure improves the image quality and accomplished statistics for both, simulations and in-vivo data compared with standard Gaussian denoising. This can be explained by exploiting the high temporal redundancy of fASL images directly in the denoising process.

For the synthetic dataset an increase in the number of runs from 4 to 7 improves the SNR leading to a higher number of detected activation voxels for the noisy time-series. A further improvement is visible in Figure 5.2 for the Gaussian denoising approach. The incorporation of spatial information of the neighborhood reduces the noise and improves the accompanied statistics. However, the spatial smoothing has a side-effect. It leads to statistically significant false-positive activations e.g. several activations in the white matter visible in Figure 5.2. In comparison the activation maps obtained from the ICTGV denoised time series are very similar to the ground truth maps. All voxels with activation were successfully detected for 4 as well as for 7 runs. Nevertheless, for this approach some false positive activations are visible (Figure 5.2). One option to reduce this false positive activation is by using spatial thresholding, which is commonly used in fMRI and relies on the assumption that neuronal activity induces signal changes over several voxels [88].

For the in-vivo dataset only subject 1 and 4 show an activation in the motor cortex using the noisy-time series as input. Surprisingly, for the Gaussian denoised time-series non of the 4 subjects shows an activation in the motor cortex. One reason could be, that the spatial resolution is very low (3x3x6 mm^3) compared to the cortical gray matter thickness, which is typically between 1.5 and 4.5 mm, and 2.5 mm on average [75, 87]. Spatial smoothing at this low resolution can increase the partial volume effect and thereby reducing the activation related change in CBF and hence the effect size. Furthermore, the Gaussian denoising is only effective in removing random noise with equal variance. Thus, outliers or artifacts due to physiological noise can not be effectively suppressed. In contrast to the simulated dataset, where only zero mean Gaussian noise was added, the in-vivo datasets are additionally corrupted with outliers and different artifacts due to physiological noise (clearly visible in the PWI timeseries in Figure 5.3). The outliers and artifacts can further reduce the effect size. An inclusion of a strong regularization along the time domain can suppress these artifacts to a certain degree (Figure 5.3). This results in a well recovering of the underlying signal and hence an improved detection of activation in the motor cortex.

For the proposed method several model parameters have to be set up correctly. This was achieved by simulating a synthetic fASL dataset. Since the model is very general the optimized model parameters can be directly transferred to the in-vivo dataset. However, for different number of runs or datasets the regularization parameter λ has to be adjusted to take into account different noise levels. The proposed method was implemented in CUDA to accelerate the computation time. The denoising of the whole 4D fASL dataset took approximately 4min.

In summary the presented study highlights the use of effective denoising methods for fASL data. The proposed ICTGV method with two spatio-temporal weights is well suited for task-based fASL as it accounts for both, the high dynamic change in response to neural activation as well as no dynamic change during the baseline condition. A further improvement in SNR or spatial resolution can be achieved by combing the proposed method with a background suppressed 3D readout. The use of background suppression in combination with 3D readouts increases the SNR and temporal stability by approximately a factor of 3, and thereby the reliability of activation maps [283]. In addition, the proposed method can be extended to a 4D reconstruction approach by including the MRI forward operator in the minimization problem. In combination with an accelerated 3D acquisitions, using a time-varying undersampling scheme, the spatial resolution or spatial coverage of the PWI time series can be pushed further.

5.5 Application to Multi-PLD Data

5.5.1 Introduction

In ASL the images are typically acquired using a single-PLD because it is easy to implement and allows boosting the SNR by repeating the measurements [8]. As discussed previously in chapter 2, for single-PLD acquisitions the selected PLD must be higher than the ATT of the blood to avoid miss-quantification of CBF. However, it is difficult to select the right PLD prospective because the ATT varies between healthy subjects and patients with vascular diseases i.e. patients with steno-occlusive disease [100]. One way to solve this transit time problem is by using a very long PLD, ensuring that the blood has sufficient time to reach the tissue. However, this leads to a longer acquisition time and additionally to a lower SNR due to the T_1-relaxation of the labeled blood. An alternative approach to solve this problem is by measuring the ATT in addition to the CBF. This is achieved by performing multiple ASL experiments at different PLD and fitting this measurements to a kinetic model [34]. ATT is a valuable physiological parameter for the characterization of collateral flow and hemodynamically impaired regions [27, 62].

However, for dynamic ASL data a trade-off between spatial and temporal resolution has to be chosen. For whole brain coverage with the recommended segmented 3D-acquisition [8] only a limited number of PLD can be acquired in a clinically acceptable time. To overcome this drawback, accelerated single-shot 3D acquisition strategies were implemented recently [28, 134, 253]. This acceleration comes at the cost of reduced SNR, making the estimation of CBF and ATT with a non-linear least squares (NLLSQ) fitting approach quite challenging. To improve the SNR and stabilize the fitting approach, we present a denoising approach based on infimal convolution of total generalized variations. The method is validated on a synthetic phantom dataset including simulated pathologies and on a healthy subject for a different number of averages.

5.5.2 Methods

5.5.2.1 Data Acquisition

One healthy subject was measured on a 3T Siemens Prisma (Siemens, Erlangen, Germany) system after giving written informed consent. ASL data were acquired using a pseudo continous arterial spin labeling (pCASL) sequence with a 2D controlled aliasing in parallel imaging results in higher acceleration (CAIPIRINHA) accelerated single-shot 3-D gradient and spin echo (GRASE) readout [134] with background suppression. The following imaging parameters were used: matrix size = 64x64x38, field of view (FoV) = 192x192x114 mm^3 resulting in 3 mm^3 isotropic resolution, 10% phase- and 17.5% slice oversampling, TR/TE = 5260/14.44 ms, 2x2$^{(1)}$ CAIPIRINHA pattern, phase-partial Fourier 6/8, refocusing flip angle = 180°, EPI-factor = 25, turbo factor (TF) = 22, segments = 1. In total 16 time-points with 4 averages were acquired using a labeling duration of $\{1.05, 1.3, 1.55, 1.8, \ldots, 1.8\}$ s and a PLD of $\{0, 0, 0, 0 : 0.25 : 3\}$ s within an acquisition time of 11 min 29 s. The ASL labeling plane was placed according to a time of flight (ToF) angiogram in the neck area above the bifurcation of the carotid artery and below the V3 segment [282].

Additionally, a T_1 weighted image was acquired using a 3D-MPRAGE sequence with the following imaging parameters: 1 mm isotropic resolution, 176 slices, TR = 1900 ms, TE = 2.7 ms, TI = 900 ms, flip angle = 9°, acquisition time = 5 min 58 s.

5.5.2.2 Synthetic Dataset

In order to validate the proposed denoising approach, a synthetic ASL dataset was created based on a high resolution (1 mm isotropic) T_1- and proton density (PD)-map (M_0) supplied by MRiLab [164] for MATLAB r2016b (The Mathworks, Natick, MA, USA). CBF-values of 65 $ml/100g/min$ and 20 $ml/100g/min$ with corresponding ATT values of 800 ms and 1500 ms were attributed to GM and WM tissue respectively [72, 155, 201, 325]. Additionally, a hyper perfusion area in frontal WM (40 $ml/100g/min$) and in the putamen (114 $ml/100g/min$) with corresponding reduced ATT of 750 ms and 400 ms were added. In a subsequent step, the high resolution images were downsampled to 3 mm isotropic resolution using tri-linear interpolation. This introduces additional PV effects and matches typical resolution of 3D-ASL acquisitions. From the downsampled CBF- and ATT-map a time series of 16 PWIs, using the same labeling duration (LD) and PLD as for the in-vivo acquisition, were simulated using the general kinetic model for pCASL [34] (see section 5.5.2.5 "Quantification of CBF and ATT"). The control images are assigned to $C = 0.1 \cdot M_0$, which models a background suppression of 90% applied to M_0. The label images are simply given by $L = C - \text{PWI}$. Afterwards, complex Gaussian noise was added to each control and label images separately with a SNR level similar to in-vivo measurements. An example of the ground truth and noisy PWI time series is given in Figure 5.6.

5.5.2.3 Anatomical Image Processing

The high resolution T_1 weighted image was segmented into GM and WM using SPM12 and computational anatomy toolbox v 12 (CAT12) [98] toolbox[2] (C. Gaser, Structural Brain Mapping Group, Jena University Hospital, Jena, Germany). The segmented GM and WM partial volume maps as well as the high resolution T_1 weighted image were coregistered to the mean PWI as suggested by Mutsaerts et al. [187]. A brain mask was generated by summing up the corresponding GM- and WM-PV-maps followed by a 3D dilation with a kernel element of size 3.

5.5.2.4 ASL Data Processing

Motion correction of the ASL time series was performed using SPM12 and ASL-Toolbox [294, 295]. In a subsequent step the perfusion weighted time series was calculated and denoised using the proposed ICTGV approach.

5.5.2.5 Quantification of CBF and ATT

The quantification of CBF and ATT from the perfusion weighted time series is based on the general kinetic model for pCASL [34]:

$$PWI(t_n) = \begin{cases} 0 & t_n < \Delta t \\ 2\alpha M_{0\lambda} \mathrm{f} T_{1_{app}} e^{-\frac{\Delta t}{T_{1,b}}} \left(1 - e^{\frac{-t_n + \Delta t}{T_{1_{app}}}}\right) & \Delta t \leq t_n < \Delta t + \tau \\ 2\alpha M_{0\lambda} \mathrm{f} T_{1_{app}} e^{-\frac{\Delta t}{T_{1,b}} - \frac{t_n - \tau - \Delta t}{T_{1_{app}}}} \left(1 - e^{\frac{-\tau}{T_{1_{app}}}}\right) & \Delta t + \tau \leq t_n, \end{cases} \tag{5.6}$$

where f is the CBF in $ml/100g/min$, Δt is the ATT in minutes, T_1 is the longitudinal relaxation decay constant of tissue, which is $1.33/60$ min for 3T, M_0 is the acquired proton density weighted image, and $T_{1,b}$ the longitudinal relaxation decay constant of blood, which is $1.65/60$ min at 3T [169], α is the labeling efficiency and set to 0.85 [56] for the synthetic dataset and to 0.7 [283] for the in-vivo data because of the used background suppression. τ is the labeling duration and is set to $\{1.05, 1.3, 1.55, 1.8, \ldots, 1.8\}$ s with the corresponding PLDs of $\{0, 0, 0, 0 : 0.25 : 3\}$ s, t_n is the acquisition time point, i.e. the sum of post labeling delay and labeling duration. Further, the blood-brain partition coefficient λ is assumed to be 90 ml/g [125], thus $M_{0\lambda} = M_0/\lambda$. The apparent longitudinal relaxation decay of tissue is give by $\frac{1}{T1_{app}} = 1/T_1 + \mathrm{f}/\lambda$.

5.5.2.6 Fitting Algorithm

The estimation of the CBF and ATT maps from the noisy and denoised perfusion weighted time series is performed using a NLLSQ fitting algorithm. The NLLSQ function *lsqnonlin*

---

[2] `http://www.neuro.uni-jena.de/cat/`

in MATLAB (The Mathworks, Natick, MA, USA) estimates the unknown (CBF and ATT) from equation 5.6 by means of a trust-region reflective method. Additional box constraints on CBF and ATT are used to limit their values to a physiologically meaningful range of [0, 300] $ml/100g/min$ for CBF and [0, 6] seconds for ATT, respectively.

5.5.2.7 Data Evaluation and Error Propagation

In order to show the benefit of the proposed method, we evaluated the stability and error propagation by performing a pseudo replica analysis. Therefore a set of 100 perfusion weighted time series with different noise realizations but equal standard deviation were computed. For each time series the CBF and ATT were estimated from the denoised and noisy perfusion weighted images. Afterwards, the voxel-wise median and inter-quartile range between the 25^{th} and 75^{th} quartile were calculated for evaluation. Additionally, for the simulated and in-vivo dataset median CBF and ATT values as well es inter-quartile range (IQR)-values of GM and WM tissues were reported to study systematic errors. For the simulated dataset tissue masks were created by assigning CBF values within [18, 22] $ml/100g/min$ to WM and CBF values within [60, 65] $ml/100g/min$ to GM. For the in-vivo dataset the co-registered GM- and WM-PV-maps were thresholded by a factor of 0.9 to generate the tissue masks.

5.5.3 Results

5.5.3.1 Synthetic ASL Data

Figure 5.6 shows the ground truth simulated, the noisy, and the denoised perfusion weighted time series at 6 different timepoints. Qualitative comparison of the PWIs shows a high noise suppression of the proposed method, especially at areas with low SNR while maintaining the dynamic contrast change. This is illustrated in four representative voxels in Figure 5.7. In the WM voxels the signal is dominated by noise and no clear signal change can be observed for the noisy image (red). In contrast, the proposed method recovers the signal change very well and shows a high correlation to the noise free ground truth time course. This improvement in signal recovery results in more accurate CBF and ATT maps, shown in Figure 5.8. Especially in the low SNR areas (WM), the nonlinear fitting leads to many outliers for the noisy input. The voxel wise fitting stability, with and without denoising, is presented in Figure 5.9. The median values are close to the ground truth values. However, the prior denoising of the time series leads to a lower IQR for the ATT as well as the CBF-map. This visual impression is confirmed by the box-plots in Figure 5.10 showing an IQR decrease in WM-ATT of 65% and WM-CBF of 48%, respectively for the proposed method compared with the noisy input.

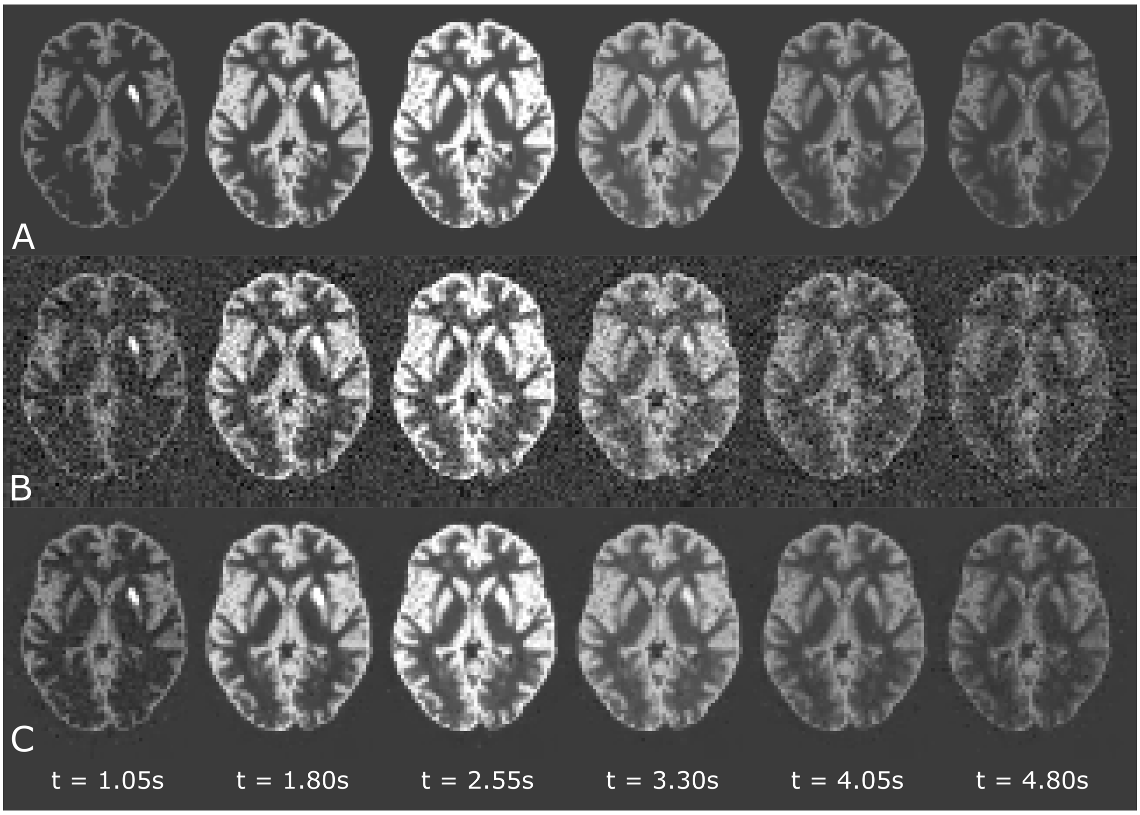

Figure 5.6: Simulated perfusion weighted time series for 6 different PLDs. Top row (A) shows the noise free, middle row (B) the noisy, and bottom row (C) the ICTGV denoised PWIs. The proposed method is able to remove noise but maintains the image contrast and edges.

5.5.3.2 In-vivo Data

Figure 5.11 shows the estimated CBF- and ATT-maps of the in-vivo subject using a different number of averages per PLD. For the highest number of averages both methods perform well resulting in a good image quality. However, the proposed method shows a lower number of outliers especially in the ATT-map. The effect of denoising is more pronounced for a lower number of averages. While the NLLSQ fitting of the noisy data results in an increased number of outliers and hence in a decreased image quality, the fitting of the ICTGV denoised data provides reasonable quantitative maps even for the lowest number of averages. This visual improvement is confirmed in the corresponding box-plots in Figure 5.12 showing a lower IQR range for the proposed method.

5.5.4 Discussion

In this study we presented a spatio-temporal denoising approach based on infimal convolution of TGV functionals for multi-PLD ASL data. The infimal convolution of two TGV functionals with different spatio-temporal weights ($\beta_1 < \beta_2$) allows the automatic

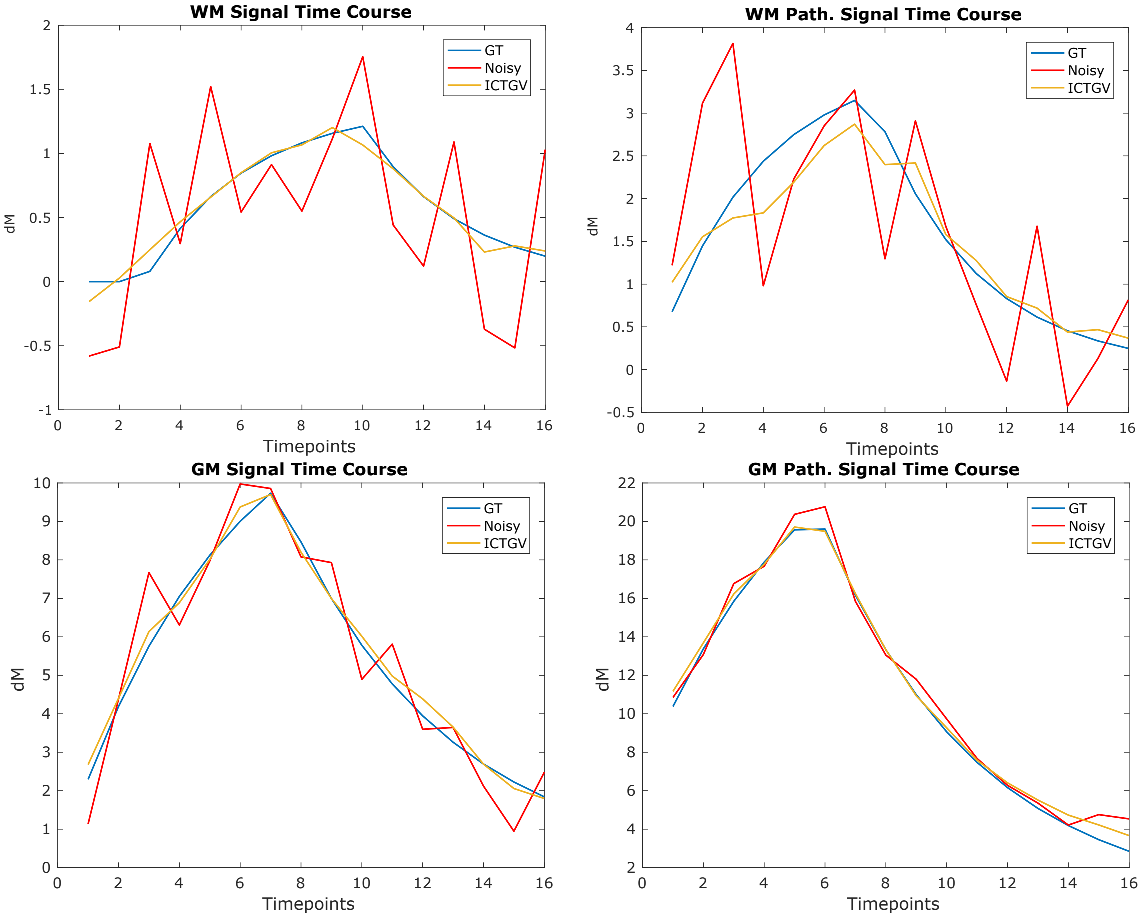

Figure 5.7: Comparison of the ground truth dynamic ASL signal (blue) with the noisy (red) and ICTGV denoised (yellow) ASL signal in four different voxels. The ICTGV denoising recovers the original signal time course very well for low (WM) as well as high (GM) SNR cases.

separation of the signal into two components: one with low signal change and a second with high dynamic changes. Hence, local different dynamic characteristics of the ASL signal are considered during the optimization approach. The proposed method was validated on simulated synthetic and in-vivo ASL datasets with a different number of averages per PLD. For all datasets a substantial improvement in noise suppression is observable for the proposed method and edges as well as small structures (pathologies) are well preserved. The improved noise suppression is especially visible in PWIs with a low SNR (very short or very long PLD) and additionally in the exemplary ASL signal time courses shown in Figure 5.7. For all four cases the proposed method reduces noise and successfully recovers the original noise free ground truth time course. This stabilize the non-linear fitting procedure resulting in more accurate quantitative maps. The visual improvement is confirmed with the results of the pseudo-replica method, showing a lower IQR range in WM for the ICTGV denoised (CBF 11% and ATT 9%) maps compared

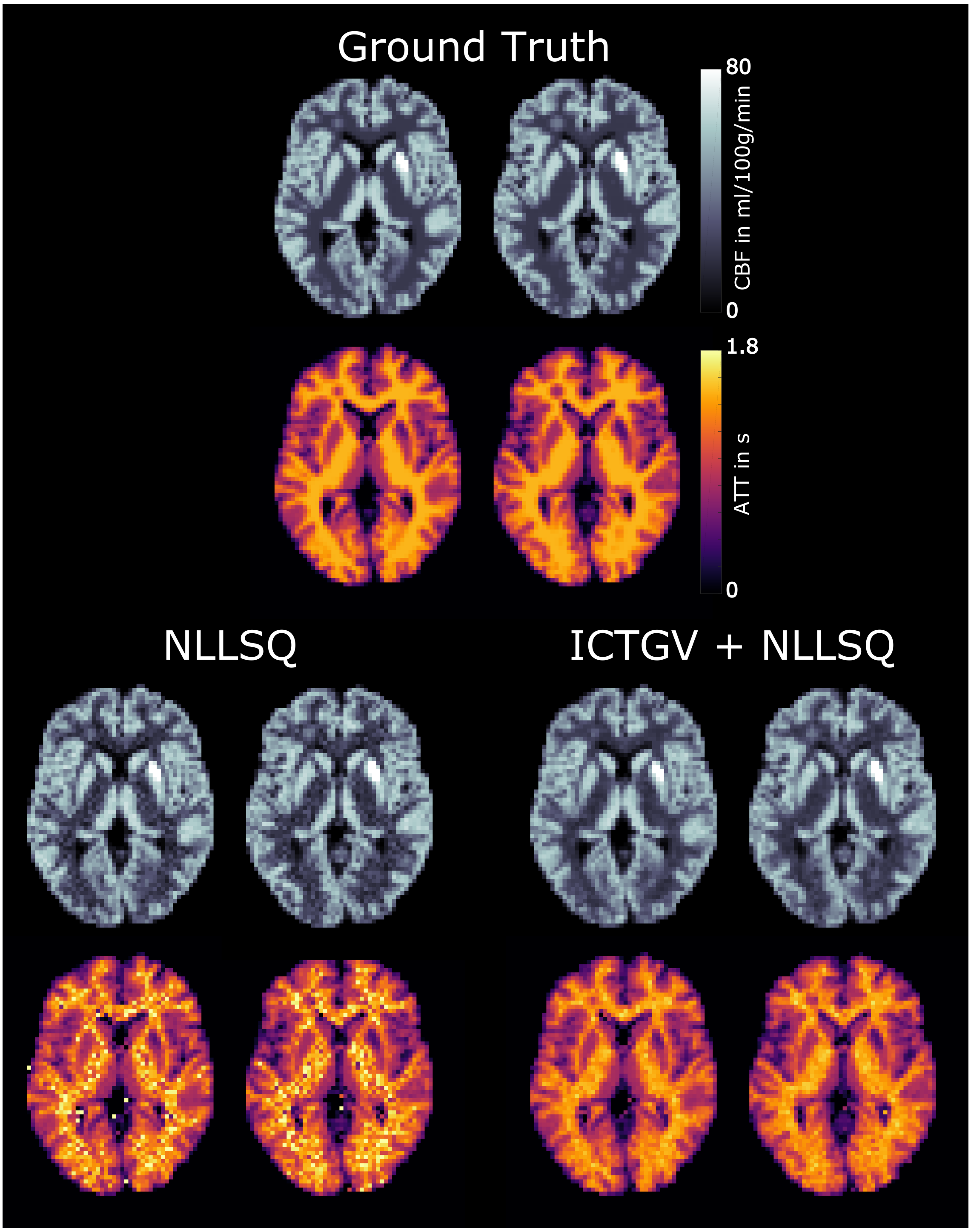

Figure 5.8: Comparison of two representative CBF- and ATT-maps estimated from the noisy and denoised perfusion weighted time series. The proposed method (ICTGV + NLLSQ) shows superior noise removal in CBF and ATT compared with the NLLSQ fitting approach.

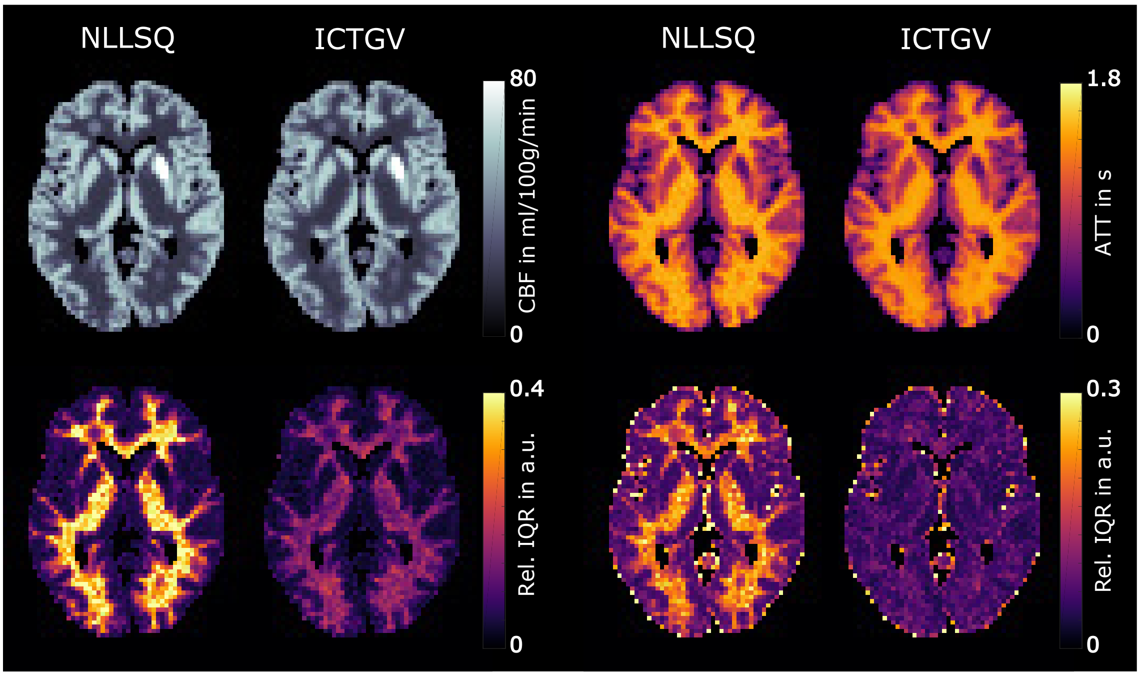

Figure 5.9: Fitting results for the pseudo replica method showing the voxel-wise median and IQR in CBF and ATT over 100 different noise realizations. For both methods the median CBF- and ATT-maps are visually close to the noise free maps showing no systematic error. The additional denoising of the PWI time series stabilizes the fitting procedure resulting in a lower IQR than without denoising.

to the standard NLLSQ approach (CBF 31% and ATT 21%). In general, the variation (IQR) is higher in WM compared with GM. This is caused by the approximately three times lower perfusion and additional longer ATT resulting in a lower SNR. However, the reduction of uncertainties by including prior information comes at the cost of a bias in the dynamic ASL signal leading to an overestimation of CBF in WM and an underestimation of CBF in GM. The amount of bias can be controlled by the regularization parameter and gets higher with stronger regularization. This bias can be accounted to a certain extend by using a debiasing methods [33, 64], which could be included in a further step.

The synthetic high resolution images were downsampled to 3 *mm* isotropic resolution matching the typical ASL resolution. This accounts for partial volume effects (PVE) and leads to transient tissue boundaries. Therefore, the reference CBF and ATT values in GM and WM shows a natural variation represented by the IQR in the box plots.

Similar to the synthetic dataset the proposed method reduces noise in the time series of the in-vivo dataset. This improves the non-linear estimation of CBF and ATT leading to a lower number of outliers especially in the WM. While for the NLLSQ approach, the number of outliers increases with a reduced number of averages per PLD, the proposed

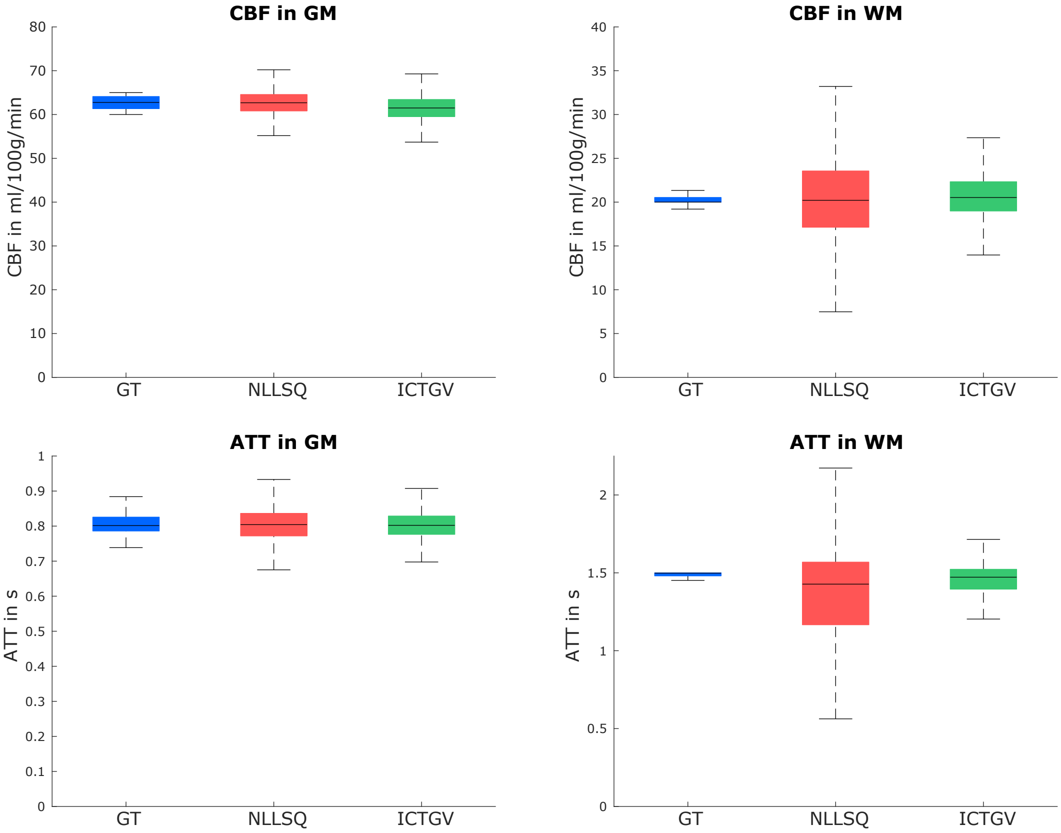

Figure 5.10: Boxplots of the CBF and ATT in GM- and WM-tissue over 100 runs. The median of the NLLSQ fitting approach shows a lower bias in GM- and WM-CBF compared to the denoised images but comes at the cost of higher uncertainties (higher IQR).

method provides a good image quality with only a minor visible degradation. This visual impression is confirmed by the quantitative boxplots in Figure 5.12 showing similar IQR- and median-values in GM and WM tissue independent of the number of averages. In contrast, and as expected, the IQR increases for the standard NLLSQ approach using a lower number of averages.

The utilized CAIPIRINHA accelerated GRASE sequence improves the temporal resolution of ASL data which is beneficial in two ways: First it reduces the sensitivity to motion artifacts, which can lead to uninterpretable quantitative maps in segmented acquisitions; And second it provides a more flexible approach for multi-PLD data, allowing to sample a broader range of the ASL signal.

In summary, the proposed ICTGV approach allows an essential reduction in acquisition time (from 11 min 29 s to 2 min 55 s) while maintaining the quality and quantification accuracy of CBF- and ATT-maps. This improvement potentially helps to enable the

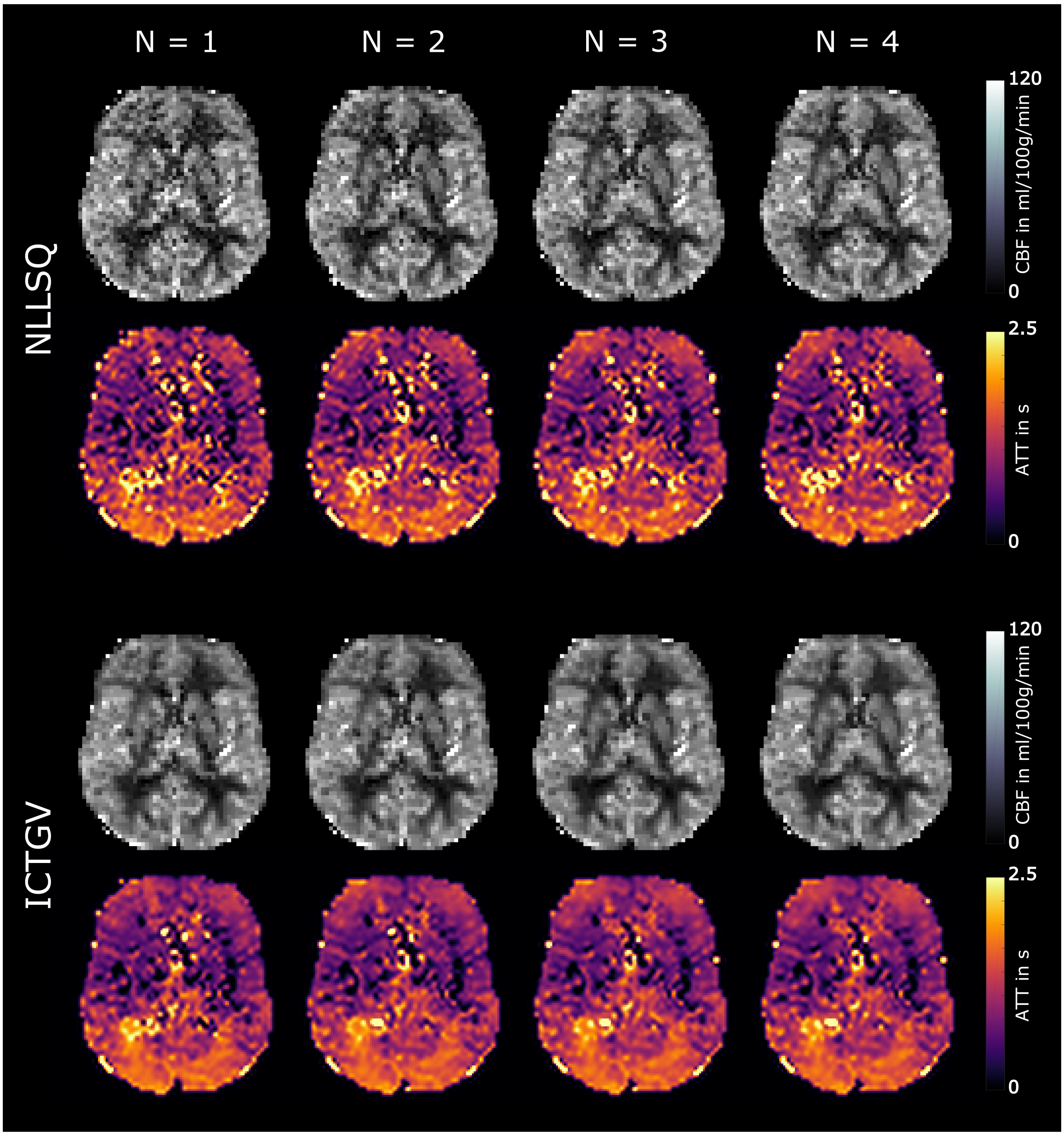

Figure 5.11: One representative CBF- and ATT-map estimated from a different number of averages (N). For the highest number of averages both methods produces meaningful CBF- and ATT-maps. However, the proposed denoising method stabilizes the non-linear fitting approach and leads to a lower number of outliers. Even for one average per PLD ($t_{acq} = 2\ min\ 55\ s$) meaningful CBF- and ATT-maps can be estimated from the ICTGV denoised time series.

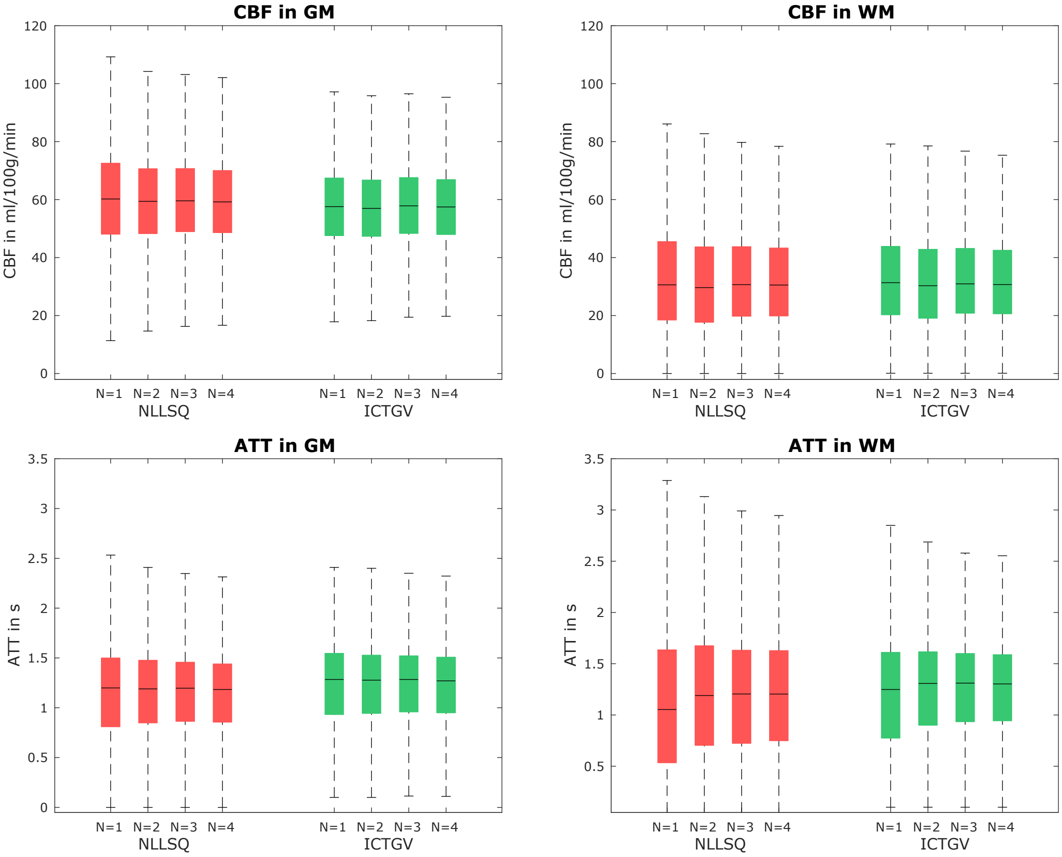

Figure 5.12: Boxplots of the CBF- and ATT-values in GM- and WM-tissue of the in-vivo data in dependence of the number of averages. The NLLSQ fitting approach shows a higher IQR in GM- and WM-tissue compared to the denoised images.

consolidation of clinical applicability and higher spatial resolutions. Further improvements are expected by extending the denoising approach to a reconstruction approach including coil-sensitivities and Fourier sampling. This provides additional information and matches the assumption of Gaussian noise in the raw data. In addition, this approach could be combined with a time-dependent CAIPIRINHA sampling pattern, allowing for higher acceleration factors, thereby reducing the through-plane blurring or increasing the spatial resolution.

5.5.5 Conclusion

The results of both studies (fASL and multi-PLD) demonstrate the potential of the proposed regularization approach for dynamic ASL data. With this general TGV model a substantial suppression of noise can be achieved and the signal can be successfully recovered from the noisy data by taking into account correlations of the varying signal intensity along the time series as well as inclusion of information of the spatial neighborhood. This stabilizes the fitting approach resulting in improved image quality and accomplished statistics. Consequently, the proposed method highly satisfies clinical and research demands.

6

Realt Time Functional Arterial Spin Labeling

This chapter is based on the following publication:

> D. Grössinger, S. E. Kober, S. M. Spann, R. Stollberger, and G. Wood. Real-Time Functional Magnetic Resonance Imaging as a Tool for Neurofeedback. *Lernen und Lernstörungen*, pages 1–12, apr 2020, doi: 10.1024/2235-0977/a000300

and on the following abstract which was accepted for ISMRM 2020:

> S. M. Spann, D. Grössinger, C. S. Aigner, J. Pfeuffer, G. Wood, and R. Stollberger. Self-Regulation of Brain Functions using Real-Time Neurofeedback Functional Arterial Spin Labeling. In *Proceedings of the 28th Annual Meeting of ISMRM*, 2020

Contents

6.1 Introduction

In chapter 5 the basic principles of functional magnetic resonance imaging (fMRI) to map the neuronal activity were presented. The underlying contrast mechanism are the blood oxygen level dependent (BOLD) contrast obtained with a $T2^*$ weighted sequence and the perfusion contrast obtained with arterial spin labeling (ASL). In conventional fMRI studies the images are acquired during a task-based paradigm (several interleaved blocks of task and rest) and the activation analysis is carried out in a subsequent step. Real time functional magnetic resonance imaging (RT-fMRI) is an extension to traditional fMRI and was first proposed by Cox et al. in 1995 [53]. In RT-fMRI the data acquisition keep pace with the reconstruction, analysis and visualization of functional data. This provides several advantages compared to the traditional fMRI studies [53]. First, it allows online monitoring of data quality. This improves the reliability of fMRI because of the possibility of detecting strong head movement or other physiological artifacts [287]. Second, functional activity maps are provided immediately, which allows the detection of poor task performance. In both cases, the acquisition can be repeated immediately. The online analysis is particular useful for pre-surgical functional localization and intra-operative guidance [126, 127, 185]. Third, new task and stimulus protocols can be easily developed [53]. And fourth, the fast processing and visualization enables the opportunity of providing a neurofeedback (NF) to the subject. This means that the individuals get acoustic or visual feedback how strong the activity in a certain brain region is related to a specific task or behavior. Hence, the subjects can learn to influence their own brain activation. This was first demonstrated for BOLD fMRI by Weiskopf et al. [297]. In their study a healthy volunteer was able to increase the BOLD signal of the anterior cingulate cortex (ACC) across feedback sessions indicating a learning or self-regulation effect [297]. With this study a new research area was born called RT-fMRI-NF, which has grown rapidly popularity. Several studies demonstrated the potential of RT-fMRI-NF as an effective intervention tool for different clinical domains i.e. depression [319], pain regulation [63, 79], tinnitus [112], Parkinson's disease [256], schizophrenia [193, 219], and auditory hallucinations [193].

Until now all RT-fMRI-NF studies were carried out using the BOLD effect. Besides BOLD-fMRI, functional arterial spin labeling (fASL) is a very promising approach for studying the neural activation due to its sensitivity to blood flow alterations. It has important advantages compared to BOLD fMRI, which makes fASL perfectly suited for NF studies: increased spatial accuracy [172, 207, 267], higher intra-individual reproducibility [156, 216, 267], a direct activation related absolute change in cerebral blood flow (CBF) [151], and a stable baseline signal.

So far only one study investigated the real-time processing of fASL data [121]. However, the study focused only on the online monitoring of the ASL signal without providing feedback to the subject. In this study we implemented a real-time solution for ASL data processing and feedback generation. This pipeline includes the acquisition of data, image reconstruction, post-processing, and neurofeedback presentation during a task to guide the subject's performance. The computation of all processing steps is done within the repetition time and allows guiding the subject's activation intermediately. The real-time pipeline is evaluated on 5 healthy subjects using a finger tapping paradigm with one baseline and two feedback runs.

6.2 Methods

6.2.1 Data Acquisition

5 subjects were measured on a 3T magnetic resonance (MR) system (Skyra, Siemens Healthcare, Germany) after giving written informed consent. A prototype pseudo continous arterial spin labeling (pCASL) sequence with 3D-gradient and spin echo (GRASE) readout and background suppression [283] was used with the following imaging parameters: FOV = 192x192x96 mm^3, 3x3x6 mm^3 resolution, 16 slices, phase-/slice-oversampling = 10/15%, slice-partial Fourier = 6/8, phase-partial Fourier = 6/8, echoplanar imaging (EPI)-factor = 51, turbo factor (TF) = 14, repetition time (TR)/echo time (TE) = 4000/23 ms, labeling duration (LD)/post-labeling delay (PLD) = 1800/1700 ms. A baseline (BL) finger tapping experiment was conducted using a block-wise paradigm with 6 interleaved blocks (32 s rest/task). The experiment consists of one BL run and two feedback (FB) runs (FB1 and FB2). The BL run was used to locate the activation area in the motor cortex and to create the activation mask of the motor cortex for each subject.

Additionally, from each subject a T_1 weighted image was acquired using a 3D-magnetization prepared - rapid gradient echo (MPRAGE) sequence with the following imaging parameters: resolution of 1x1x1 mm^3, 192 slices, phase oversampling = 15%, slice oversampling = 33%, TR/TE/inversion time (TI) = 1910/1.81/1000 ms, Grappa-factor = 4, flip-angle = 8°, acquisition time = 2 min 55 s.

6.2.2 Real Time Pipeline

Figure 6.1 provides an overview of the proposed real-time neurofeedback processing pipeline. After acquisition and reconstruction on the scanner site the ASL DICOM image is transferred to workstation (WS)1 . On WS1 the ASL preprocessing steps were preformed in MATLAB (MathWorks, Natick, MA, USA) using statistical parameter mapping v 12 (SPM12) and in-house developed MATLAB scripts. First motion-correction was performed by realigning the acquired ASL image to the first image of the time-series (control image). Afterwards, the perfusion weighted image (PWI) was calculated using surround subtraction, which eliminates the BOLD contamination in the perfusion weighted image [167, 307]. In a third step the PWI was spatial smoothed using 3D Gaussian filter with a full width at half maximum (FWHM) of 3 mm. From this denoised perfusion weighed image the corresponding CBF values were calculated for each voxel using a general kinetic model [34] for pCASL data [8]:

$$CBF(x,y,z) = \frac{6000 \cdot \lambda \cdot PWI(x,y,z) \cdot e^{\frac{PLD}{T_{1,b}}}}{2 \cdot \alpha \cdot M_0(x,y,z) \cdot T_{1,b} \cdot \left(1 - e^{\frac{-\tau}{T_{1,b}}}\right)} \tag{6.1}$$

where λ is the blood-brain partition coefficient and set to 0.9 ml/g [125],

$T_{1,b}$ is the longitudinal relaxation time of blood at 3T and set to 1.65 s [169], α is the labeling efficiency and set to 0.75 for pCASL due to 2 background-suppression pulses, τ is the labeling duration and set to 1.8 s, PLD is set to 1.7 s, $PWI(x,y,z)$ is the denoised difference image and M_0 is the acquired proton density image.

The whole procedure (from image reconstruction to presenting feedback) lasts approximately 2 s which is within the range of one TR (4 s). After each acquisition the calculated CBF-maps were updated on WS1 as shown in Figure 6.2 to allow monitoring the image quality and CBF-values during the experiment.

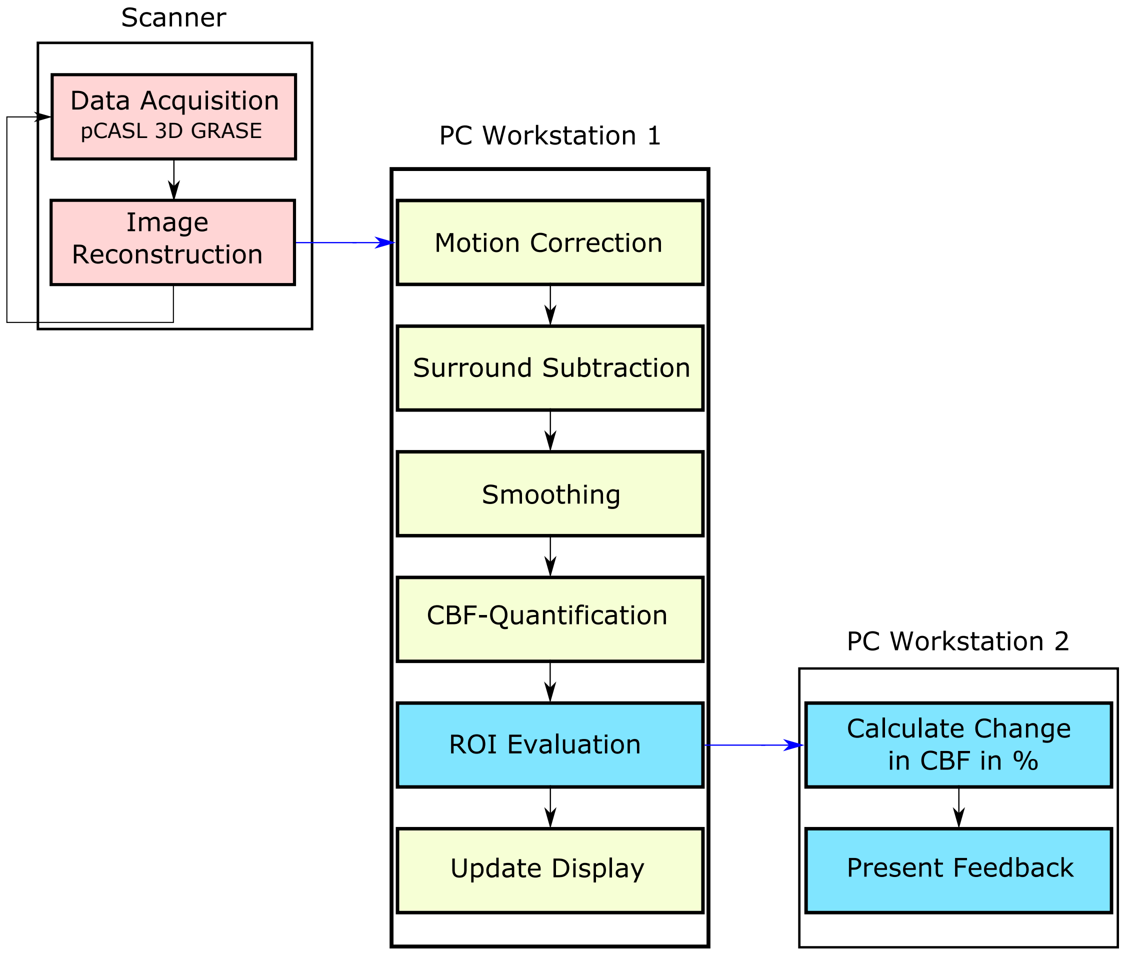

Figure 6.1: Processing pipeline for real time neurofeedback (RT-NF) fASL. After image acquisition and reconstruction the ASL data is transferred to WS1 for post-processing and CBF quantification. The blue rectangles were only performed in the FB runs because the region of interest (ROI) in the activation area is defined after the baseline run. In the FB runs the mean CBF is calculated in the activation region and transferred to WS2. In WS2 the change in CBF between baseline and task is calculated and presented on a monitor.

After the baseline run a general linear model (GLM) was fitted in the CBF-time

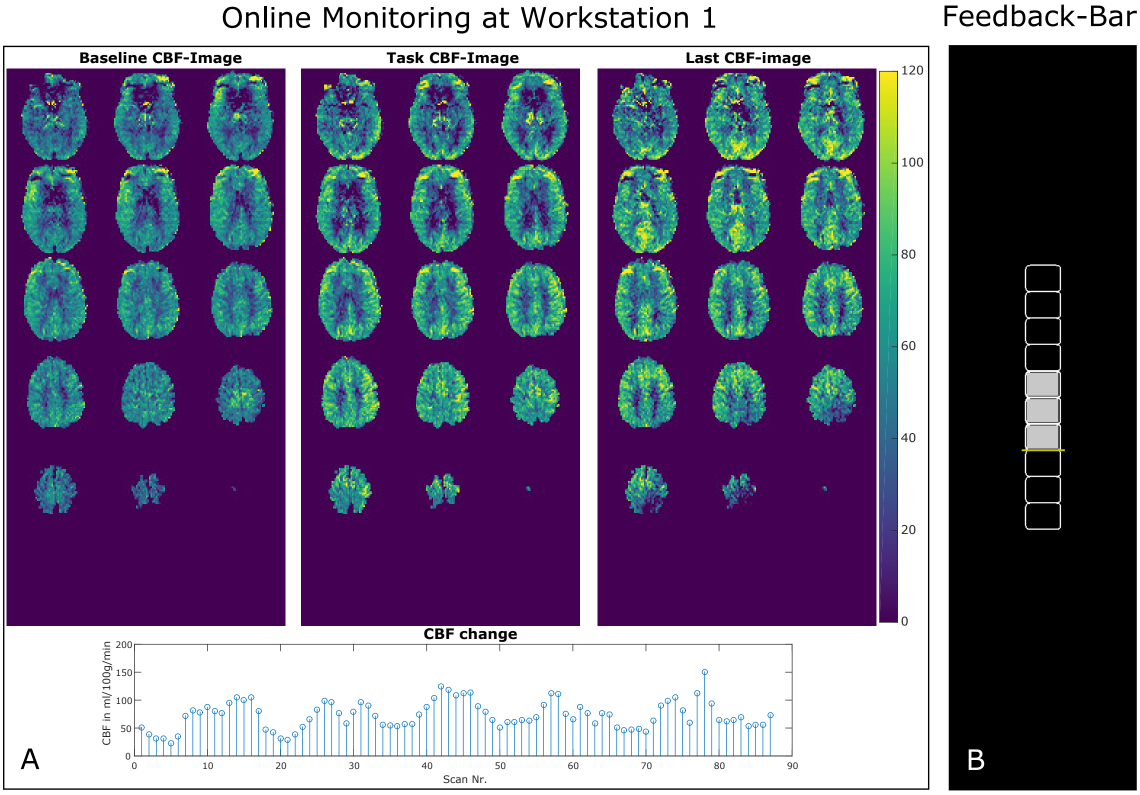

Figure 6.2: (A) Mean CBF-map during task, rest and the latest calculated CBF-map. The stem plot shows the mean CBF values calculated in the activation area, which was defined from the baseline run. This figure is updated after each acquisition and allows the user to online monitor the ASL signal. Subfigure (B) shows the presented NF bar to guide the subject's neuronal activity. The yellow line shows the baseline CBF and an increase or decrease of one rectangular corresponds to a change of 15% in CBF.

series for localization of the activation area in the motor cortex. The model was specified using a box-car function convolved with a canonical hemodynamic response function. The statistical maps were thresholded at $p < 0.05$ after family wise error (FWE) correction. The statistical maps (t-value maps) as well as the average CBF during baseline and task were used to define the activation area in the motor cortex. The created mask (ROI) serves as basis for FB1 and FB2. The mean CBF in the defined ROI was calculated at each time point t:

$$CBF_{ROI}[t] = \frac{1}{N} \sum_{x \in ROI} CBF[x,t] \tag{6.2}$$

where N is the number of CBF-values in the defined ROI. For each baseline condition the mean CBF in the ROI ($CBF_{ROI}[t]$) was averaged over the whole duration of the condition:

$$CBF_{BL} = \frac{1}{N} \sum_{t=BL_{start}}^{t=BL_{end}} CBF_{ROI}[t] \qquad (6.3)$$

This CBF was used as a reference for the feedback presentation. The relative change of CBF during the task condition was calculated using equation 6.4 and presented to the subject via a monitor to guide the subject's cognitive activation.

$$CBF_{change}[t] = 100 \times \frac{CBF_{ROI}[t]}{CBF_{BL}} \qquad (6.4)$$

With the provided feedback the subjects tried to modify the original finger tapping experiment, which was a continuous alternating finger tapping, by changing the frequency, using different finger wiggles etc. to increase the neural activity in the motor cortex. An increase in neural activity increases the CBF and hence the feedback-bar (Figure 6.2(B)). The feedback representation was implemented in PsychoPy software.

6.3 Results

Figure 6.4 lists the mean CBF-values in the defined activation region for all 3 runs. Except for subject 3, we observe a slight increase in CBF of FB1 compared with BL. It should be noted that different strategies such as changing the frequency or using different finger wiggles can lead to higher as well as lower CBF values in the activation area. In contrast, subject 3 was not able to find the right strategy in FB1. However, in the second feedback run the mean CBF clearly increased for all subjects in the activation area. This indicates that each subject was able to learn strategies to regulate their own neural activity. The CBF increase is also visible in the CBF-maps of each subject shown in Figure 6.3 (red arrows). Figure 6.5 shows the mean CBF time course of all subjects averaged over the 6 blocks. The same increase in CBF as for the individual subjects is observable with the highest increase during FB2.

6.4 Discussion

In this chapter we present a pipeline for processing ASL data in real time. This allows on the one hand to online monitor the ASL acquisition and on the other hand to perform RT-NF studies. The online-monitoring of the ASL signal is very helpful in identifying a low inversion-efficiency of pCASL data due to field inhomogeneities, changes in blood-velocity, or due to turbulent flow and thereby enables the operator the possibility to change the labeling parameters or to relocate the labeling plane. Since ASL is a subtraction technique it is very sensitive to subject motion. Head movement leads to strong artifacts, which can lead to poor activation maps. This artifacts are clearly visible in the updated CBF-maps. In such a case the

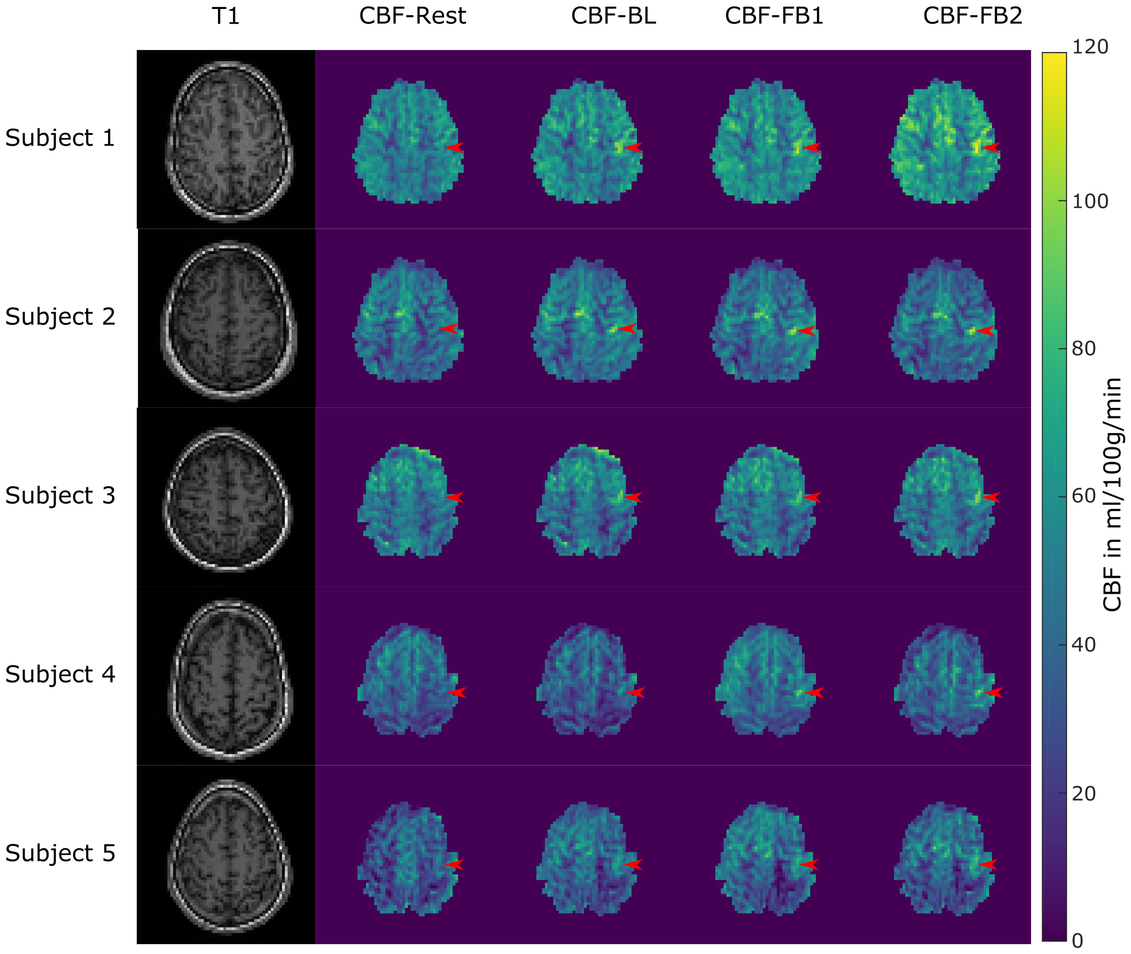

Figure 6.3: One representative CBF-map of each subject during rest and task in the BL, FB1 and FB2 run. Comparing the CBF-maps during BL and FB1 for all subjects except subject 3 an increase in the motor cortex is visible (red arrows). In FB2 an increase in the CBF is clearly visible for all subjects.

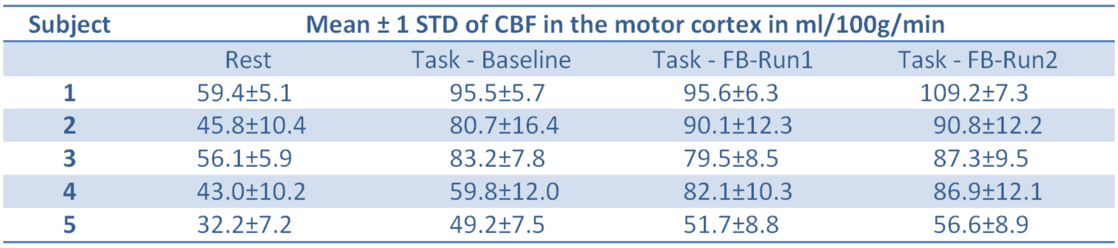

Subject	Mean ± 1 STD of CBF in the motor cortex in ml/100g/min			
	Rest	Task - Baseline	Task - FB-Run1	Task - FB-Run2
1	59.4±5.1	95.5±5.7	95.6±6.3	109.2±7.3
2	45.8±10.4	80.7±16.4	90.1±12.3	90.8±12.2
3	56.1±5.9	83.2±7.8	79.5±8.5	87.3±9.5
4	43.0±10.2	59.8±12.0	82.1±10.3	86.9±12.1
5	32.2±7.2	49.2±7.5	51.7±8.8	56.6±8.9

Figure 6.4: Mean ± 1 STD of CBF values in the activation area of the motor cortex for each subject

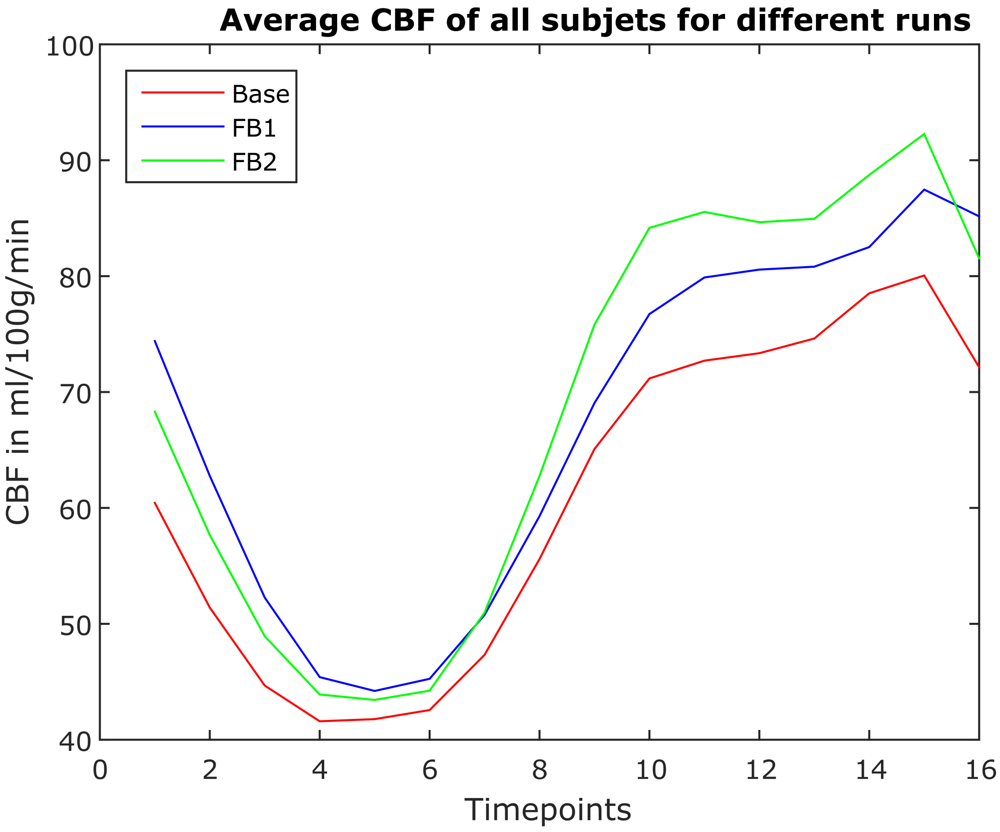

Figure 6.5: Averaged CBF time course over all subjects in the activation area of the motor cortex for baseline run (Base), FB run 1 and FB run 2. An increase in CBF during the task condition (timepoint 8-16) is visible for both feedback runs, which indicates that the subjects were able to learn to control their activation due to the provided neuro-feedback.

experiment can be repeated immediately and does not require a second session days apart.

The results of this study show that the subjects were able to learn to control their own brain activation and the mean CBF in the activation area increased from 73.7± 18.8 $ml/100g/min$ without feedback to 86.2 ± 18.9 $ml/100g/min$ with feedback presentation. Each subject was able to learn to influence their neural activations and successfully increased the CBF in the activation region. However, the amount of increase in CBF is different between subjects and runs, indicating that the learning progress was different for the subjects. For example subject 2 and 4 increased the CBF in the first FB run but the increase in the second feedback run was minor. One reason for this could be that the subjects were able to found a good strategy very fast in the first run. During the second run they used the same strategy or slight modifications leading to a similar strong activation increase as during the first run. In contrast, subject 3 performed worse in the first FB run compared to the BL run. This indicates that a change in the FB strategy could lead to a lower as well as to a higher CBF, depending on the way finger tapping is performed. Nevertheless, in the second feedback run the subject was able to increase the activation in the motor cortex, thereby indicating that the subject was able to learn from the first feedback run which finger tapping strategies are worse than the original one. In the second run the subject found some strategies which leads to a higher activation and hence an increased CBF.

In Figure 6.5 a general perfusion increase during the baseline condition is observable for both feedback runs compared with the baseline run. At the current time it is not clear if the CBF generally increases during the feedback procedure due to complex cognitive processes or if the increase in CBF is due to normal physiological variations. Additional studies are necessary to find out the origin of this CBF increase, for example several baseline and feedback runs could be performed on different sessions or days. The baseline runs could than be compared among each other and additionally with the feedback runs. This could provide insights into the root of the CBF change and provides additional information about the reproducibility of RT-NF studies.

One limitation of RT-NF based on ASL is the low temporal resolution and accompanied delay in feedback presentation. The whole feedback procedure takes at least 4 s, which is limited by the long TR due to the labeling period and the PLD. Additionally the hemodynamic response in fASL is a slow varying signal and has a delay of approximately 4-6 seconds until the peak is reached [317]. Hence, the total time until feedback is presented to the subject is approximately 8-10 s. This means that each new finger tapping strategy should be performed at least 10 s to see an influence. Hence, only two to three different strategies can be performed by the subject during an activation period. In our study we informed the subjects about this effect and the corresponding delay time. This delay in feedback presentation is suboptimal because the subjects had to be aware of the feedback also in the first 10 s of the baseline condition to see the behavior of their last used strategy which might be confusing. For example subject 3 reported after the scan session that it was very hard to change the strategy and at the same time keep in mind that the current presented change in CBF is from a previous strategy. The subject also reported that the change in strategy was maybe too fast which could explain the fact that for subject 3 no gain in feedback run 1 was found.

Since this was the first RT-NF experiment based on ASL many additional optimization and evaluation steps are necessary to find the best study design. A better block design may be preferable, e.g. a lower total number of interleaved blocks with an increased duration of 64 s compared to the used of 32 s. This has a few advantages: First the subjects can try several strategies within one run. Second, for every new block the delay time due to the hemodynamic response affect the CBF quantification in the first 4 seconds. A lower number of blocks would reduced this effect. Third, a more accurate estimation of the baseline CBF during rest can be achieved with a longer baseline block. Taking into account the provided feedback of subject 3 a better feedback design might be helpful i.e a discrete feedback after 12 *s* would be more appropriate than a feedback every 4 *s*. With this feedback change the subject would be informed how well the last performance was and even when they can switch to a new strategy. This might avoid confusing and a too fast change to a new strategy.

In this proof of principle study only 5 subjects were investigated. An evaluation on more subjects with additional statistical analysis would be of high interest to validate this first findings.

6.5 Conclusion

We proposed a real-time solution for fASL RT-NF studies where all necessary acquisition and processing steps were executed within a single TR. This allows to monitor the ASL signal and to guide the subjects' cognitive process. The results of this study demonstrate that subjects can learn to regulate their brain activity during a finger tapping experiment based on the provided neurofeedback. This can be used to promote rehabilitation of different symptoms e.g. in stroke patients were motor and cognitive processes are often impaired.

7

Variational Reconstruction for 4D Arterial Spin Labeling Perfusion Data

This chapter is based on the following publication:

> S. M. Spann, X. Shao, D. J. Wang, C. S. Aigner, M. Schloegl, K. Bredies, and R. Stollberger. Robust single-shot acquisition of high resolution whole brain ASL images by combining time-dependent 2D CAPIRINHA sampling with spatio-temporal TGV reconstruction. *NeuroImage*, page 116337, nov 2019, doi: 10.1016/J.NEUROIMAGE.2019.116337

and on the following abstract which was accepted for ISMRM 2019:

> S. M. Spann, X. Shao, D. J. Wang, C. S. Aigner, M. Schloegl, K. Bredies, and R. Stollberger. Improving temporal resolution of 3D Arterial Spin Labeling perfusion imaging by combining CAIPIRINHA encoding and spatio-temporal TGV reconstruction. In *Proceedings of the 27th Annual Meeting of ISMRM*, Montreal, 2019

Contents

7.1 Introduction

Since the introduction of arterial spin labeling (ASL) in 1992 [66], many different acquisition and labeling approaches have been proposed to improve the signal-to-noise ratio (SNR) and robustness of ASL images. This led to a recent consensus paper from the International Society for Magnetic Resonance in Medicine (ISMRM) perfusion study group [8]. The recommended way to acquire ASL data in clinical settings is using a fast 3D acquisition technique such as turbo spin echo (TSE) stack of spirals (SoSP) [283, 318] or gradient and spin echo (GRASE) [85, 86, 109] in combination with pseudo continous arterial spin labeling (pCASL) [56]. Besides the advantage of higher SNR and the incorporation of efficient background suppression [179, 318] to reduce physiological noise, 3D-acquisitions suffer from the drawback that the echo train length is much longer than the T2-relaxation of blood. This leads to a exponential filtering of the k-space along the second phase encoding direction. This undesirable k-space filtering is described by the modulation transfer function (MTF) and depends on the k-space acquisition order and echo train length. A longer echo-train leads to a narrower MTF which results in a broadened point spread function (PSF) in the image space leading to strong blurring along the second phase encoding direction. Accompanied by the blurring is a lower effective resolution in the phase encoding direction which leads to partial volume effects and quantification errors. In addition, detailed structures are degraded and the detection of small lesions is reduced. Different strategies were proposed to reduce the amount of blurring to a certain extent. For example Liang et al. [162] and Zhao et al. [328] proposed a variable flip angle approach to broaden the MTF leading to sharper PSF and hence reduced blurring. Galazzo et al. [94] proposed a retrospective deconvolution method in image space to deblure the acquired images. Another more intuitive approach is to reduce the echo train length by acquiring the full 3D k-space in several shots or segments, as recommended by the consensus paper [8]. A shorter echo-train leads to a lower filtering effect of the k-space and and hence less blurred images. However, this comes at the cost of a decreased temporal resolution and therefore increased sensitivity to inter-segment motion, which is problematic for uncooperative subjects and patients. Improvements in motion robustness were achieved by using prospective motion correction strategies e.g. motion sensitive navigator echoes [228, 334] or optical tracker systems [5]. Besides the advantage of improved motion robustness, the drawback of a lower temporal resolution still remains, which limits its applications to perfusion based functional magnetic resonance imaging (fMRI) or multi-post-labeling delay (PLD) ASL [34].

Another way to improve the temporal resolution is to undersample the k-space and use parallel imaging methods such as SENSE or GRAPPA to reconstruct the images [73, 282, 295]. However, only moderate acceleration factors of 2-3 are recommended by the consensus paper, because the SNR of the perfusion weighted image (PWI) is inherently low and decreases further with higher acceleration factors, due to the g-factor penalty. Recently, a 2D-controlled aliasing in parallel imaging results in higher acceleration (CAIPIRINHA) accelerated 3D-GRASE readout [28] and a 3D-accelerated TSE-SoSP readout [43] were employed for pCASL scanning with conventional reconstructions. These approaches allow the acquisition of whole brain ASL images with decent spatial and temporal resolutions, and provide an improvement in SNR compared with standard parallel imaging (e.g. GRAPPA) based reconstructions. This increase in temporal resolution improves the robustness against motion. However, compared to the fully sampled acquisitions, the temporal signal to noise ratio (TSNR) is still reduced for both (accelerated 3D GRASE and TSE-SoSP) approaches due to the g-factor penalty. As an alternative approach, we proposed a total generalized variation (TGV)-based reconstruction approach and showed improved image quality using retrospective undersampled data [245]. This TGV-based reconstruction incorporated the averaging of ASL signals directly in the reconstruction of single PLD images by using all raw data in one reconstruction process.

This study combines now CAIPIRINHA accelerated 3D-GRASE acquisition and an enhanced ASL-TGV framework allowing the reconstruction of the whole 3D time series in one compact procedure. Firstly, an accelerated 3D-GRASE sequence with a time-dependent 2D-CAIPIRINHA sampling pattern was implemented as a single-shot acquisition to improve the temporal resolution and robustness against motion. The time-dependent sampling pattern has the advantage that the temporal incoherence between control/label (C/L)-pairs is increased, and additionally allows the estimation of the coil sensitivities without an additional pre-scan. Secondly, the reconstruction algorithm was adapted to incorporate additional temporal regularization on the whole C/L-time series. The result of the reconstruction method is a 4D C/L-series, which allows performing motion correction retrospectively in image space, and is capable of handling 4D ASL data. The purpose of this study is to present and evaluate the proposed acquisition and reconstruction approach by comparison with a standard segmented approach on numerical and in-vivo data.

7.2 Theory

7.2.1 Acceleration of 3D ASL Data Acquisition

A pCASL sequence with background suppressed 3D-GRASE readout was developed and the pulse sequence diagram is shown in Figure 7.1A. Background suppression was achieved by one pre-saturation pulse and two inversion pulses, and the timing for inversion pulses was optimized by numerical simulations [230]. Parameters for the balanced pCASL scheme were: Hanning window-shaped RF pulse with duration of 500 μs and spacing of 360 μs, flip angle = 25°, slice-selective labeling gradient = 6 mT/m and the average labeling gradient amplitude was 0.6 mT/m [312]. To reduce the echo-train length of the 3D-GRASE readout 2D-CAIPIRINHA sampling [32] was implemented. More precisely, time-dependent 2D-CAIPIRINHA acceleration with an acceleration factor from 1 to 3 is supported along phase encoding (PE1) and partition encoding (PE2) directions respectively. For all acceleration factors a center out acquisition is used (Figure 1B). The time-dependent 2D-CAIPIRINHA pattern is shifted between subsequent C/L-pairs in the phase encoding (PE)1 and PE2 direction as exemplary shown in Figure 1C. This shift in acquisition pattern increases the temporal incoherence between subsequent acquisitions and over time each point in k-space is sampled. Therefore, the coil sensitivity maps can be estimated directly from the averaged k-space. For comparison of the proposed 2D-CAIPIRINHA acquisition scheme the standard segmented 3D GRASE acquisition is shown in Figure 1D.

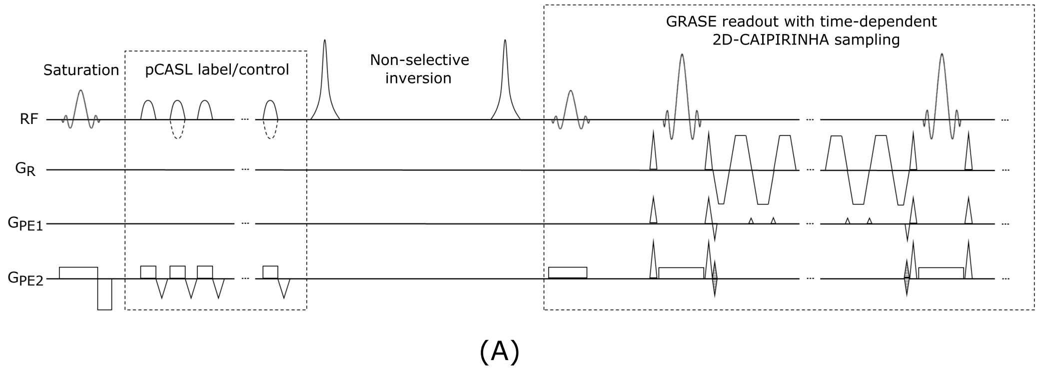

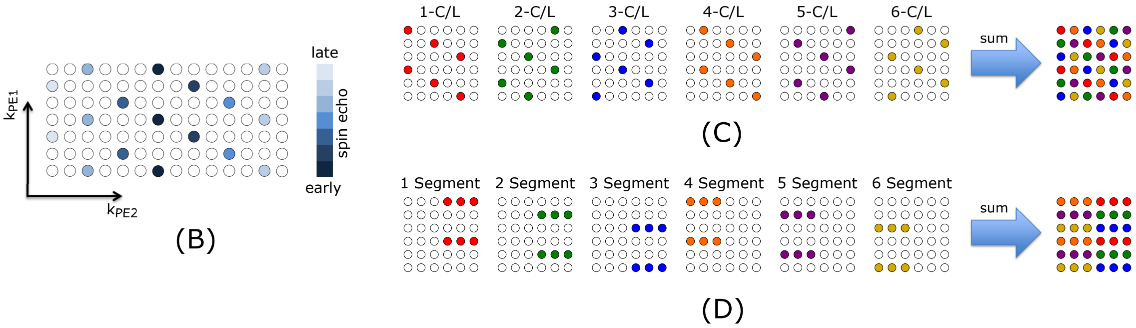

Figure 7.1: (A) Sequence diagram for accelerated 3D-GRASE acquisition with variable 2D-CAIPIRINHA pattern and balanced pCASL labeling (dotted lines are modification in control condition). The background suppression consists of a pre-saturation and 2 non-selective inversion pulses. The acquisition strategy is shown for a CAIPIRINHA 1x6$^{(2)}$ pattern. A center out acquisition is used as illustrated in (B). For one C/L-pair the same 2D-CAIPIRINHA pattern is used. Between subsequent C/L-pairs the pattern is shifted in PE1 or PE2 direction as exemplary shown in (C). This variation increases the temporal incoherence between the C/L-pairs and additionally allows the estimation of the coil sensitivity maps directly from the summed data. Subfigure (D) shows for comparison the acquisition scheme of the fully sampled but segmented approach for the used settings.

7.2.2 Reconstruction of ASL Data

7.2.2.1 Variational Reconstruction

In variational magnetic resonance imaging (MRI) reconstruction the unknown image u is estimated from measured noisy data d by a regularized optimization procedure formulated in a general way as

$$u^* \in \arg\min_u D(u,d) + R(u), \tag{7.1}$$

where $D(u,d)$ represents the data-fidelity term and $R(u)$ the regularization term. The data-fidelity term connects the measured data $d \in C^{N_x \times N_y \times N_z \times N_s \times N_t}$ with the estimated image $u \in C^{N_x \times N_y \times N_z \times N_t}$ via a linear forward operator K. We denote by $N_x \times N_y \times N_z$ the dimensions of image space, N_s the number of coils and by N_t the number of time frames. Here for the data-fidelity term, the L^2-norm is an appropriate choice, due to the theoretical expectation of Gaussian noise statistics of the complex data:

$$D(u,d) = \frac{1}{2} \left|\left|K(u) - d\right|\right|_2^2 \tag{7.2}$$

The forward operator K includes the coil sensitivity profiles, the Fourier operator and the sampling pattern. For reconstruction of 3D-time dependent data with variable sampling pattern in the time-domain, the operator K is defined as follows:

$$K : u = (u_t)_{\{t=1\ldots N\}} \rightarrow (F_t \left\{b_s u_t\right\}_{(s,t)}), \tag{7.3}$$

where F_t defines the Fourier operator for each time-frame including the varying undersampling pattern over time [222], $b_s \in C^{N_x \times N_y \times N_z}$ describes the coil sensitivities for each coil s, and u_t the 3D volume at each time frame t. The regularization term $R(u)$ contains a-priori information about the structure of the estimated volume. Different spatio-temporal constraints exist like total variation [218] or wavelets [186]. The choice of the regularization term is crucial and for MRI image it was shown that TGV [31] is well suited [149]. TGV enforces piece-wise smooth images and is defined for spatio-temporal data as follows:

$$R(u) = TGV^2_{\alpha_1,\alpha_0,\beta}(u), \tag{7.4}$$

$$TGV^2_{\alpha_1,\alpha_0,\beta}(u) = \min_v \left\{\alpha_1 \left|\left|\nabla_\beta u - v\right|\right|_1 + \alpha_0 \left|\left|\epsilon_\beta v\right|\right|_1\right\}, \tag{7.5}$$

where $\nabla_\beta u$ and $\epsilon_\beta v$ are the gradient and the symmetrized gradient respectively as defined in equation C.15 and equation C.19 in the Appendix. In case of a spatio-temporal regularization an additional parameter $\beta = \frac{\beta_2}{\beta_1}$ is necessary to define the relation between spatial and temporal grid size as described in chapter 5.2 "Theory".

7.2.2.2 Reconstruction Setup

With the defined data-fidelity and regularization term in equation 7.2 and 7.5 respectively, the control volume time series can be reconstructed as follows:

$$c^* \in \arg\min_c \frac{\lambda_c}{2} \left|\left|Kc - d_c\right|\right|_2^2 + TGV^2_{\alpha_1,\alpha_0,\beta}(c). \tag{7.6}$$

Since in ASL imaging always two different types of images are acquired the control and the label, the reconstruction approach for the control images formulated in equation 7.6 can be extended by including the label image time-series:

$$(c^*, l^*) \in \underset{c,l}{\arg\min}\ \frac{\lambda_c}{2}\, ||Kc - d_c||_2^2 + \frac{\lambda_l}{2}\, ||Kl - d_l||_2^2 + TGV^2_{\alpha_1,\alpha_0,\beta}\,(l) + TGV^2_{\alpha_1,\alpha_0,\beta}\,(c)\,. \quad (7.7)$$

However in ASL, the key quantity is the perfusion weighted image which is obtained by subtracting the label from the control image. Therefore, the goal of our reconstruction approach is to achieve a PWI with a good SNR and image quality. To this end an additional spatio-temporal constraint on the perfusion weighted image [332] is set which results in the final minimization problem:

$$\begin{aligned}(c^*, l^*) \in \underset{c,l}{\arg\min}\ & \frac{\lambda_c}{2}\, ||Kc - d_c||_2^2 + \frac{\lambda_l}{2}\, ||Kl - d_l||_2^2 + \gamma_1\,(w)\, TGV^2_{\alpha_1,\alpha_0,\beta}\,(l) + \\ & \gamma_1\,(w)\, TGV^2_{\alpha_1,\alpha_0,\beta}\,(c) + \gamma_2\,(w)\, TGV^2_{\alpha_1,\alpha_0,\beta}\,(c - l)\,.\end{aligned} \quad (7.8)$$

Additionally a weight function $\gamma(w)$ was introduced in the functional to balance between the TGV terms as suggested in [222, 247],

$$\gamma_1(w) = \frac{w}{\min(w, 1-w)}, \qquad \gamma_2(w) = \frac{(1-w)}{\min(w, 1-w)}, \quad (7.9)$$

where $w \in (0, 1)$.

The minimization problem defined in equation 7.8 is non-smooth but convex and can be solved using a first-order primal-dual algorithm [41]. This algorithm needs to reformulate the problem in equation 7.8 as a saddle point problem. Details of the implementation can be found in the Appendix C.2. The proposed reconstruction method is from now on referred as "ASL-TGV" approach.

7.2.2.3 Implementation

The reconstruction algorithm was implemented in C++ with CUDA parallel processing using the AGILE [149] and AVIONIC [222] library. The model parameters for the TGV functional were set to $\alpha_1/\alpha_0 = 1/\sqrt{3}$, which proved to be a reasonable choice for MRI images. The number of iterations was set to 1000, and the following model parameters were used: w = 0.9 and $\beta = 7$. Despite the set of fixed model parameters, the proposed method requires the choice of the right regularization parameter λ. This parameter was set to 7/8/9/10 for 12/18/24/30 C/L-pairs and was optimized as described in section 7.3.3.4 "Parameter Optimization".

7.3 Methods

7.3.1 Data Acquisition

Five healthy volunteers (four men and one woman, age range: 28 - 34 years) were scanned on a 3T MR system (Prisma, Siemens Healthcare, Germany) using a 32 channel head coil and pCASL with 3D-GRASE readout after informed consent was obtained. For the standard fully sampled and segmented acquisition the following imaging parameters were used: field of view (FoV) = 200 x 200 mm^2, matrix = 64 x 64 x 38, 20% slice oversampling, 3.1 x 3.1 x 3 mm^3 resolution, TE = 15 ms, TR = 4100 ms, refocusing FA = 180°, EPI-factor = 21, turbo factor (TF) = 23, 6 segments, labeling duration (LD) = 1800 ms, PLD = 1800 ms, resulting in an acquisition time of 4 min 30 s for five C/L-pairs and one M_0 image. Furthermore, a 2D-CAIPIRINHA accelerated single-shot 3D-GRASE pCASL acquisition was performed with the same imaging parameters and LD/PLD as those for the segmented acquisition, but with a 6-fold acceleration using an adapted time dependent CAIPIRINHA $1\text{x}6^{(2)}$ pattern as shown in Figure 7.1. For the accelerated acquisition, the M_0 image was acquired with a two-shot acquisition using pattern 1 and 5 as illustrated in Figure 7.1. The acquisition time for the C/L-pairs between the fully sampled with segmented acquisition and the single-shot acquisition were matched to 4 min 6 s. Additionally, for the accelerated and non-accelerated acquisitions, a repeated scan was performed in 2 subjects, during which the subjects were asked to move the head in a consistent manner using acoustic cues which were presented every 4 seconds. The movement pattern was as follows: right-left-center followed by nodding up - nodding down - center. The movement pattern was repeated until the acquisition was finished.

One multi-delay ASL dataset was acquired using the same imaging parameters used for the single PLD data. Five PLDs were used: 500/1000/1500/2000/2500 ms. For the fully sampled acquisition 1 average per PLD was acquired and for the proposed single-shot method 6 averages per PLD were acquired within an acquisition time of 4 min 6 s.

Additionally from each subject, T_1 weighted images were acquired using a 3D-magnetization prepared - rapid gradient echo (MPRAGE) sequence with the following imaging parameters: 1 mm isotropic resolution, FoV = 256 x 224 mm^2, 176 slices, TR/TE/TI = 1900/2.7/900 ms, flip angle = 9°, acquisition time = 5 min 58 s.

7.3.2 Synthetic Dataset

For validation of the proposed reconstruction method, a synthetic dataset was created in MATLAB (MathWorks, Natick, MA, USA) based on a high resolution (1 mm isotropic) T_1-weighted and an acquired fully sampled ASL dataset. In a first step, the high-resolution T_1-weighted image was segmented into gray matter (GM) and white matter (WM) using Statistical Parameter Mapping (SPM) 12[1] (Wellcome Trust Centre for Neuroimaging, Uni-

---

[1] https://www.fil.ion.ucl.ac.uk/spm/software/spm12/

versity College London, UK) [92] and CAT12 [98] software[2] (C. Gaser, Structural Brain Mapping Group, Jena University Hospital, Jena, Germany). The results of the segmentation process were tissue partial volume (PV)-maps. The high resolution T_1 weighted image and the GM- and WM-PV-maps were coregistered to the mean PWI as suggested by Mutsaerts et al. [187]. Subsequently GM and WM values of 65 $ml/100g/min$ and 20 $ml/100g/min$, reported for the normal human brain [155, 325] were assigned to the GM and WM-PV-maps as described in [247]. This leads to a more realistic cerebral blood flow (CBF)-map with partial volume effects and is illustrated in Figure 7.2. Additionally, a hyperperfusion (120 $ml/100g/min$) and a hypoperfusion (0 $ml/100g/min$) area which exactly match the ASL voxel space were added in the simulated CBF-map. These areas are displayed in Figure 7.2. From the CBF-map a perfusion weighted image was calculated using the ASL model recommended by the consensus paper [8]:

$$CBF(x,y,z) = \frac{6000 \cdot \lambda \cdot \mathrm{PWI}(x,y,z) \cdot e^{\frac{\mathrm{PLD}}{T_{1,b}}}}{2 \cdot \alpha \cdot M_0(x,y,z) \cdot T_{1,b} \cdot \left(1 - e^{\frac{-\tau}{T_{1,b}}}\right)} \tag{7.10}$$

where α is the labeling efficiency and set to 0.85 [56], τ is the labeling duration and set to 1.8 s, and the PLD is set to 1.8 s [8]. M_0 is the acquired proton density weighted image, λ is the blood-brain partition coefficient and set to 0.9 ml/g [125], $T_{1,b}$ is the longitudinal relaxation time of blood at 3T and set to 1.65 s [169] and CBF(x,y,z) is the generated synthetic CBF-map. Afterwards the PWI was blurred using a Lorentzian-PSF by simulating the MTF as described in [282], assuming a TE of 15 ms and a T2 of blood of 186 ms [47]. From the blurred PWI image, the label (L) image was calculated by simple subtraction from the control (C) image.

A time-series of 30 C/L-images were simulated. 3-D coil sensitivity maps, consisting of 32 coils equally spaced on a spherical surface, were computed using Biot-Savart's law. The C/L-images were multiplied by the coil sensitivity profiles. Afterwards coil images were transformed in k-space and complex Gaussian noise was added.

7.3.3 Data Processing

7.3.3.1 Structural Data

For each subject the T_1 weighted images were segmented into GM and WM and coregistered to the native ASL image as described in section 7.3.2 ”Synthetic Dataset”. A brain mask was generated by summing up the corresponding GM- and WM-PV-maps followed by a 3D dilation with a kernel element of size 3.

---

[2] http://www.neuro.uni-jena.de/cat/

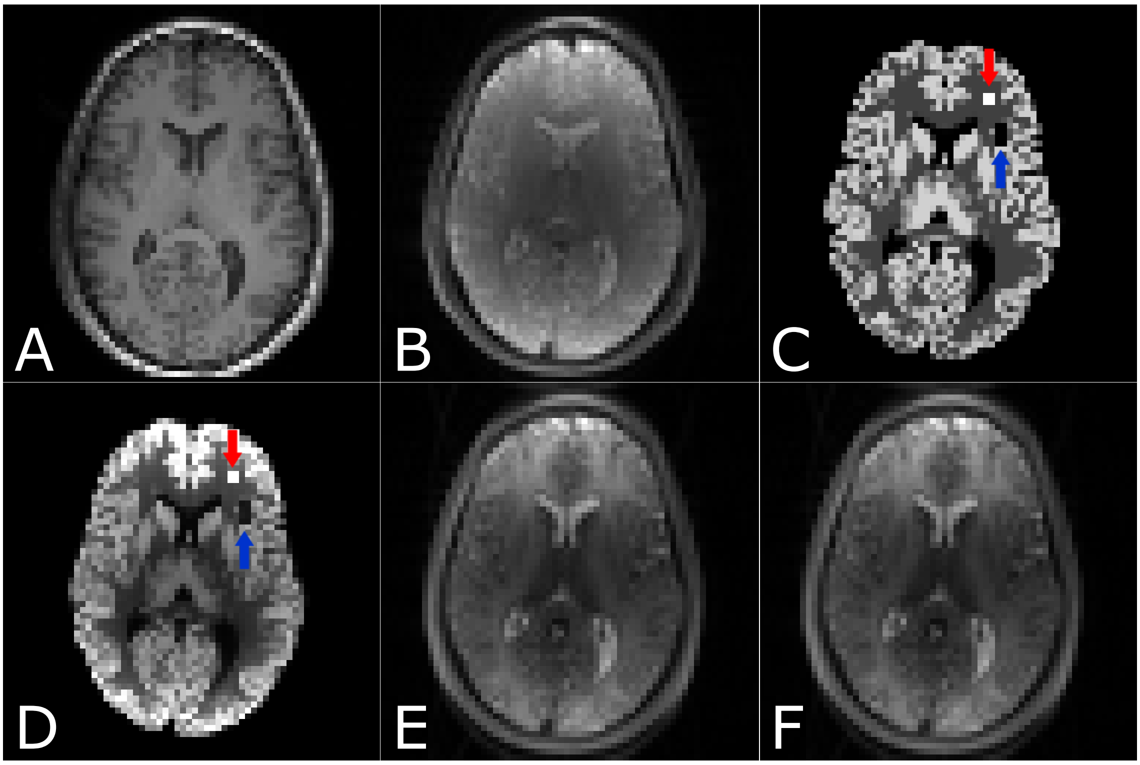

Figure 7.2: Simulated ASL dataset in ASL space. (A) Co-registered T_1 weighted image, (B) proton-density weighted image (M_0), (C) synthetic simulated noise-free CBF-map with a hyperperfusion area (120 $ml/100g/min$) indicated with a red arrow and the hypoperfusion area (0 $ml/100g/min$) indicated with a blue arrow, (D) PWI after blurring using a simulated MTF, (E) control image, and (F) label image.

7.3.3.2 Raw Data Processing of in-vivo Data

The raw k-space data files were loaded into Matlab using MapVBVD software[3]. Subsequent raw data preprocessing included: removing the readout-oversampling, echoplanar imaging (EPI) phase correction using the 3 reference line approach [115], ramp sampling correction, and coil compression.

7.3.3.3 Image Reconstruction and Processing

In addition to the proposed reconstruction algorithm, further data processing steps were performed with statistical parameter mapping v 12 (SPM12), ASL-Toolbox [293, 294] and Matlab. First, a coil compression was performed to reduce graphics processing unit (GPU)-memory and reconstruction time using singular value decomposition (SVD) with a cut-off of 0.1. Afterwards, the coil sensitivity profiles were estimated from the averaged k-space data using eigenvector-based iterative self-consistent parallel imaging reconstruction

---

[3] https://github.com/CIC-methods/FID-A/tree/master/inputOutput/mapVBVD

(ESPIRIT) from the BART toolbox [270]. For comparison of our proposed reconstruction algorithm the ESPIRIT reconstruction with L2 regularization (ESP-L2) [269] from the BART toolbox [270], and additionally a single TGV reconstruction [149] was used, which has previously shown to outperform standard SENSE reconstruction. The single TGV reconstruction (spatial total generalized variation (sTGV)) refers to an individual 3D reconstruction of the C and L images. The reconstructed images were motion-corrected using SPM and ASL-toolbox. Afterwards, the averaged perfusion weighted image was calculated from the motion corrected time series. From this temporal averaged perfusion weighted image the CBF-maps were calculated using the recommended ASL model (equation 7.10) with the parameters defined in section 7.3.2 ”Synthetic Dataset”. For the multi-delay approach the CBF and arterial transit time (ATT) were estimated by fitting the general kinetic model [34] to the perfusion weighted time series using Bayesian inference for arterial spin labeling (BASIL)[4] [44, 106] from the FSL [137] toolbox.

7.3.3.4 Parameter Optimization

The reconstruction parameters for the individual methods were optimized by maximizing the structural similarity index (SSIM) [292] between the ground-truth CBF-map and the calculated CBF-map for the simulated dataset. For the in-vivo dataset the same parameters employed for the simulated dataset were used due to the lack of noise free ground-truth.

7.3.3.5 Data Evaluation

For the simulated dataset and in-vivo data a comparison between fully sampled but segmented acquisition and the proposed single-shot acquisition with different reconstruction algorithms was carried out. Additionally, for the proposed single-shot acquisition the corresponding C and L images were summed up to get a fully sampled k-space, e.g. control acquisition 1 to 6 gives the first fully sampled control k-space, control acquisition 7 to 12 the second fully sampled k-space for the control image, et cetera. This is now referred to as ”accelerated sum”. For the simulated dataset the mean SSIM and peak signal-to-noise ratio (PSNR) were calculated between the noise free ground truth and the processed CBF-map. Furthermore, mean GM and WM CBF-values were calculated. For the single-PLD in-vivo data only mean GM and WM CBF as well as mean TSNR were reported due to the lack of noise free ground-truth. The TSNR for the reconstructed PWIs was calculated in the gray-, white-matter and whole brain respectively using equation 7.11. For the multi-PLD dataset mean GM and WM CBF as well as ATT were reported.

$$TSNR_{PWI} = \frac{Mean(PWI)}{SD(PWI)} \tag{7.11}$$

---

[4] https://github.com/ibme-qubic/oxford_asl

7.4 Results

7.4.1 Synthetic Dataset

The reconstruction results of the fully sampled and accelerated synthetic dataset for a different number of C/L-pairs are shown in Figure 7.3. Qualitative comparison of the CBF-maps shows a lower level of noise for the accelerated-dataset reconstructed with the proposed ASL-TGV algorithm compared with the CBF-maps generated from the fully sampled as well as from the sTGV and ESP-L2 reconstruction. Further, as expected the quality of the CBF-maps decreases with decreasing number of C/L-pairs. The proposed method yields high fidelity CBF-maps for the lowest number of 12 C/L-pairs, whereas for the sTGV and ESP-L2 method the noise is still dominant. This leads to the result that the hypoperfusion area, indicated with a blue arrow in Figure 7.3, is only visible in the fully sampled as well as in the ASL-TGV images. However, the hyperperfusion area is clearly visible for all approaches due to the high SNR signal. This improvement in image quality is in accordance with the quantitative metrics of SSIM and PSNR, which were calculated over the whole brain. For 30 C/L-pairs the improvement is about 1% in SSIM and 1dB in PSNR for the proposed method compared to the fully sampled but segmented approach, although the scan time for one PWI is reduced by a factor of 6. Furthermore, for a lower number of C/L-pairs (12) and hence a lower SNR, the improvement of the proposed method is about 4% (SSIM) and 3dB (PSNR) compared with the fully sampled approach. In addition, the proposed method improves the SSIM by about 12% using 30 C/L-pairs and by 18% using 12 C/L-pairs, compared with the two separate reconstruction approaches (ESP-L2 and sTGV).

The mean CBF values for GM, WM, hyper- and hypoperfusion area are shown in Figure 7.4. For all 4 methods the estimated CBF-values are close to the noise free ground truth (GT). The estimated CBF-values in the GM for fully sampled (Full), ASL-TGV, sTGV, and ESP-L2 are 48.42 ± 6.9, 45.93 ± 6.2, 42.11 ± 8.9, 41.47 ± 8.6 ml/100g/min respectively compared to the ground truth of 48.66 ± 5.4 ml/100g/min. The ASL-TGV reconstruction approach shows a lower bias than the CBF-maps reconstructed using ESP-L2 or sTGV. As expected reducing the number of C/L-pairs increases the standard deviation due to the lower SNR but the mean values in GM and WM are still the same. The ASL-TGV has the lowest standard deviation and the increase is only slightly, from 6.2 $ml/100g/min$ using 30 C/L-pairs to 6.9 $ml/100g/min$ using 12 C/L-pairs.

7.4.2 In-vivo Data

7.4.2.1 Single-Delay ASL Data

The mean $TSNR_{PWI}$ values for GM, WM, and whole brain averaged over all subjects shows an improvement of roughly 20%, 25%, and 16% respectively for the accelerated ASL-TGV reconstruction results compared with the fully sampled but segmented approach. In

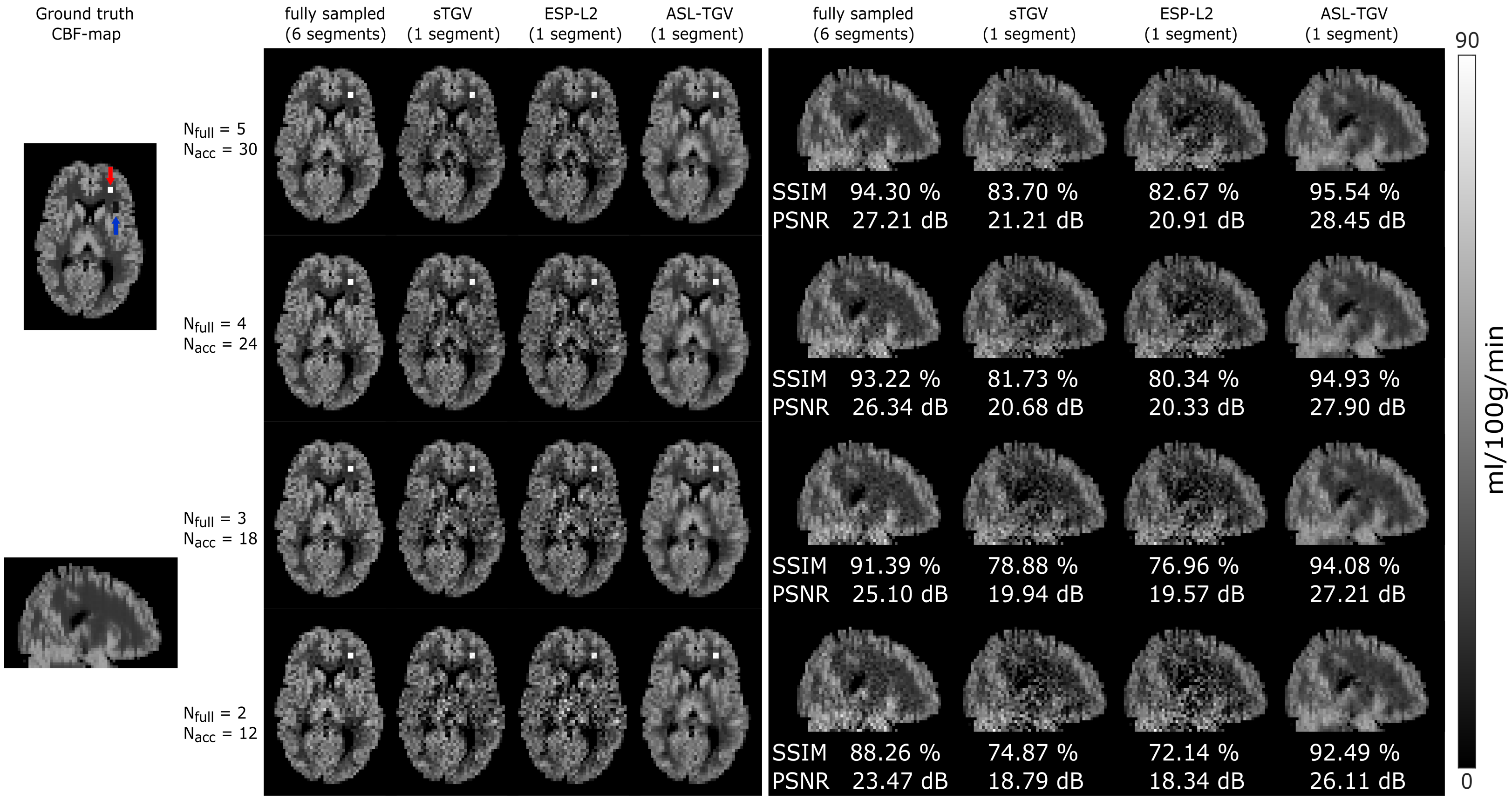

Figure 7.3: Transversal and sagittal view of one representative slice of CBF-map from the simulated synthetic dataset. Performance comparison of the fully sampled CBF-maps and the proposed accelerated 2D-time CAIPIRINHA acquisition using different reconstruction approaches and a different number of averages. In the transversal views the hyperperfusion (indicated with a red arrow) and hypoperfusion area (indicated with a blue arrow) are clearly visible in the segmented as well as in the CBF-maps using the proposed ASL-TGV method. The qualitative improvement in image quality and noise suppression is in concordance with the quantitative metrics SSIM and PSNR. Note that the SSIM and PSNR values in the sagittal views are calculated over the whole brain.

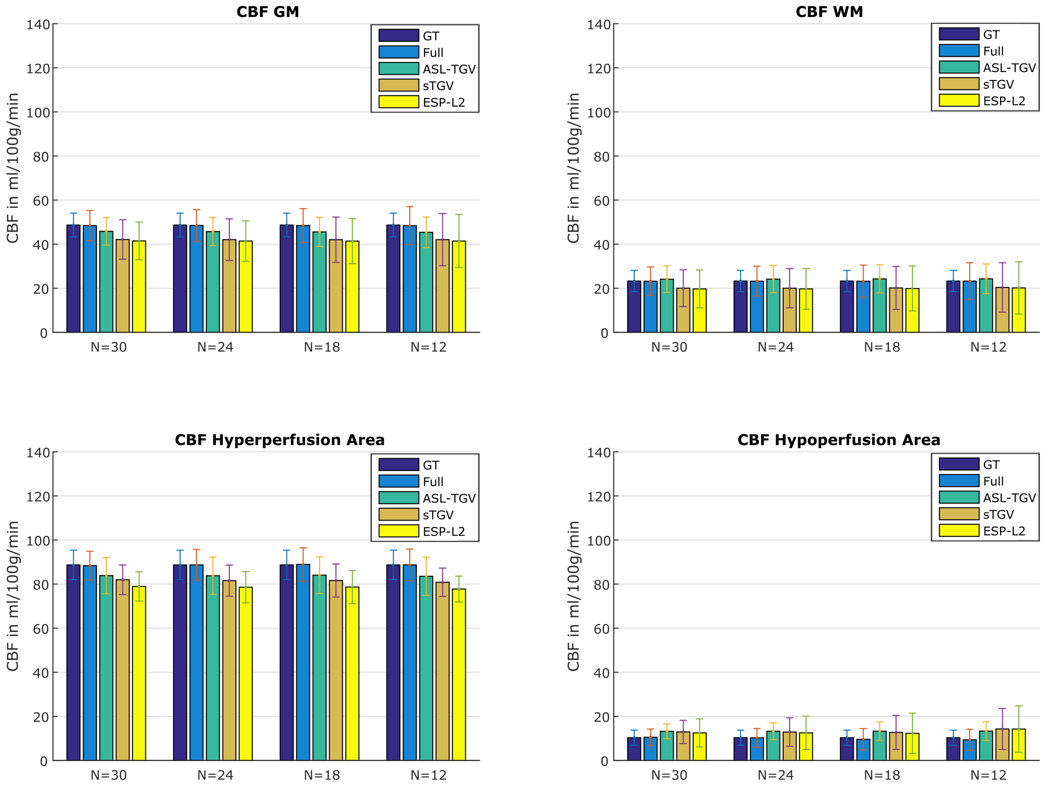

Figure 7.4: Mean and standard deviation of CBF-values in four different areas of the synthetic CBF-map for the fully sampled (Full) and accelerated approach in dependence of different numbers of C/L-pairs. Note that the standard deviation in the noise free GT is due to blurring and incorporation of GM and WM values with a probability higher than 90%. Additionally, a N of 30 corresponds to 5 C/L-pairs for the fully sampled approach due to a 6-fold lower temporal resolution.

contrast, the standard single TGV reconstruction approach shows a TSNR decrease of 66% for GM, 69% for WM and 67% for the whole brain compared to the fully sampled data.

Compared with the fully sampled image, the TSNR is improved although the temporal resolution is increased by a factor of 6. This increase in TSNR is visualized in Figure 7.5(B), which shows the single perfusion weighted image from subject 5 for the different methods. The improvement in image quality is confirmed for the CBF-maps visible in Figure 7.6, which shows results from the motionless data on the left side and the CBF-maps reconstructed form the motion-corrupted dataset on the right side. For the fully sampled data, the motion between segments leads to aliasing artifacts and low quality CBF-maps compared to the CBF-maps generated form the accelerated single-shot data. The proposed acquisition strategy shows an improved robustness to motion for the accel-

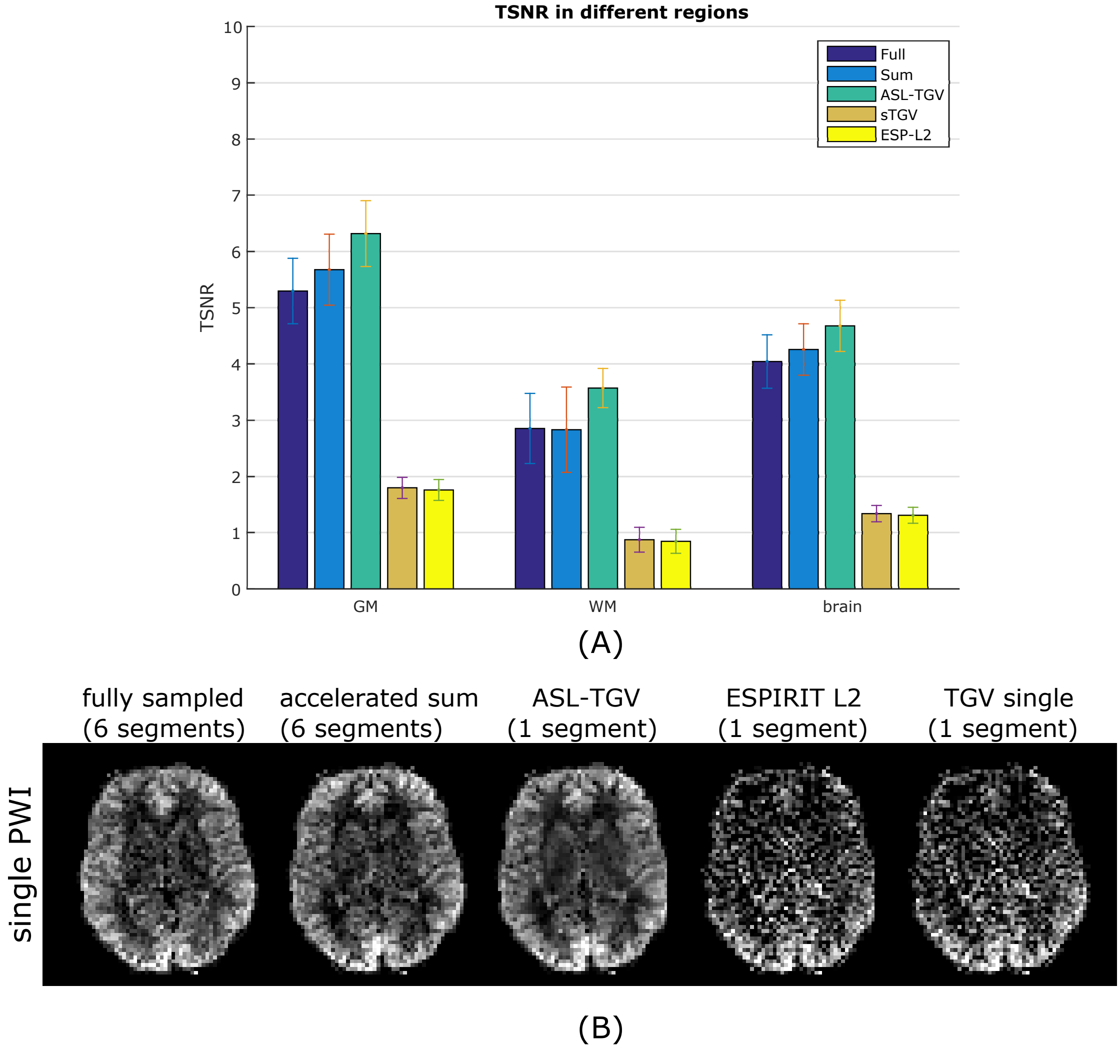

Figure 7.5: (A) Comparison of the TSNR of the PWIs averaged over all subjects for GM, WM, and whole brain between different acquisition and reconstruction methods. The error bars shows the standard deviation. (B) Single perfusion weighted image from subject 5 for the segmented approaches (fully and accelerated sum) and the proposed single-shot method reconstructed with different algorithms.

erated sum, however many residual motion-related artifacts remain (illustrated by the red arrow in Figure 7.6). These motion-related artifacts can be suppressed by using a sTGV or ESP-L2 reconstruction but at the cost of decreased TSNR due to the g-factor penalty. Overall, the combination of the time-dependent 2D-CAIPIRINHA acquisition with the proposed spatio-temporal TGV reconstruction algorithm shows the best image quality for the motionless as well as motion-corrupted ASL data. Furthermore, for the single-shot acquisition the CBF-maps of the ASL-TGV are the most similar to the CBF-maps of the accelerated sum.

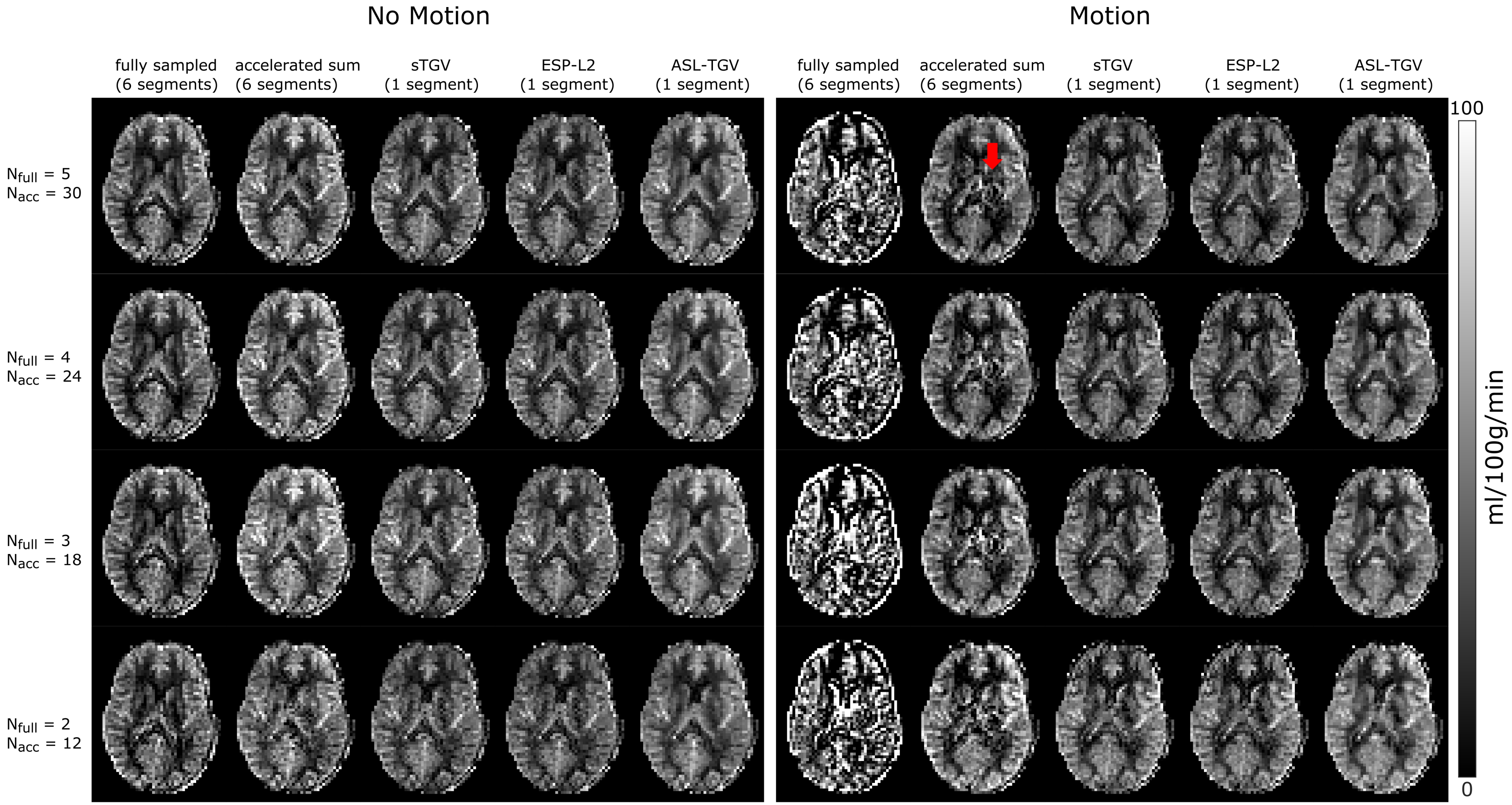

Figure 7.6: One representative slice of CBF-map in dependence of different number of C/L-pairs of example subject 1. N_{full} is the number of C/L-pairs acquired for the fully sampled data and N_{acc} is the number of C/L-pairs acquired for the proposed accelerated single-shot data ($N_{full} = 5/4/3/2$; $t_{acq} = 4\ min\ 30\ s/\ 3\ min\ 41\ s/\ 2\ min\ 52\ s/\ 2\ min\ 3\ s$, $N_{acc} = 30/24/18/12$; $t_{acq} = 4\ min\ 14\ s/\ 3\ min\ 25\ s/\ 2\ min\ 36\ s/\ 1\ min\ 46\ s$). On the left side are the CBF-maps where the subject was asked to lie as still as possible, whereas on the right side are the results from the subject moving his head during the acquisition. As expected the results of the segmented acquisition show lots of artifacts for the motion case whereas the single-shot methods perform well and delivers CBF-maps with good image quality. The highest improvement in image quality is achieved with the proposed ASL-TGV approach. The red arrow indicates remaining motion artifacts for the accelerated sum approach.

The CBF values in GM and WM for the motion-less and motion-corrupted data as a function of different numbers of C/L-pairs are shown in Figure 7.7. In addition to visual improvements the proposed method yields accurate quantitative CBF-values. In case of the fully sampled approach the motion leads to severe artifacts which result in a higher standard deviation and an additional bias in mean CBF values compared to the single-shot approaches. An increase in the standard deviations is also visible for the accelerated sum approach, whereas for the single-shot approaches the CBF-values are in high accordance between motion-less and motion-corrupted datasets.

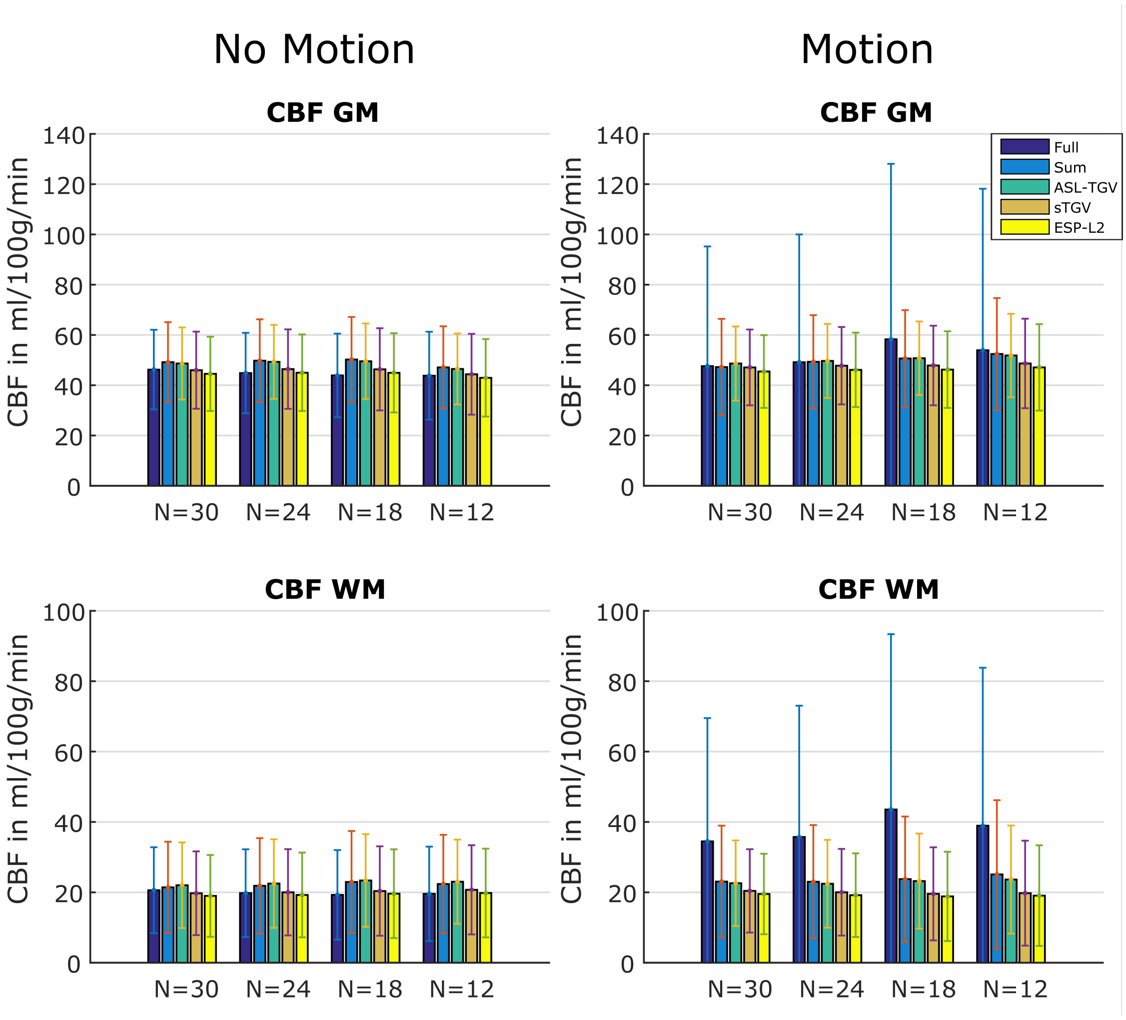

Figure 7.7: Mean and standard deviation of CBF-values in GM and WM of subject 1 for the fully sampled approach (Full) and the proposed accelerated acquisition combined with different reconstruction methods using a different number of C/L-pairs. The error bars denote ±1 standard deviation.

Figure 7.8 shows the CBF-maps of subject 2 for the different acquisition and reconstruction approaches respectively. The reconstruction results are in accordance with those of subject 1. The motion during the acquisition leads to artifacts in the CBF-maps, which are corrected in the proposed single-shot acquisition due to the retrospective motion correction. The corresponding mean GM and WM values of subject 2 are plotted in Figure 7.9.

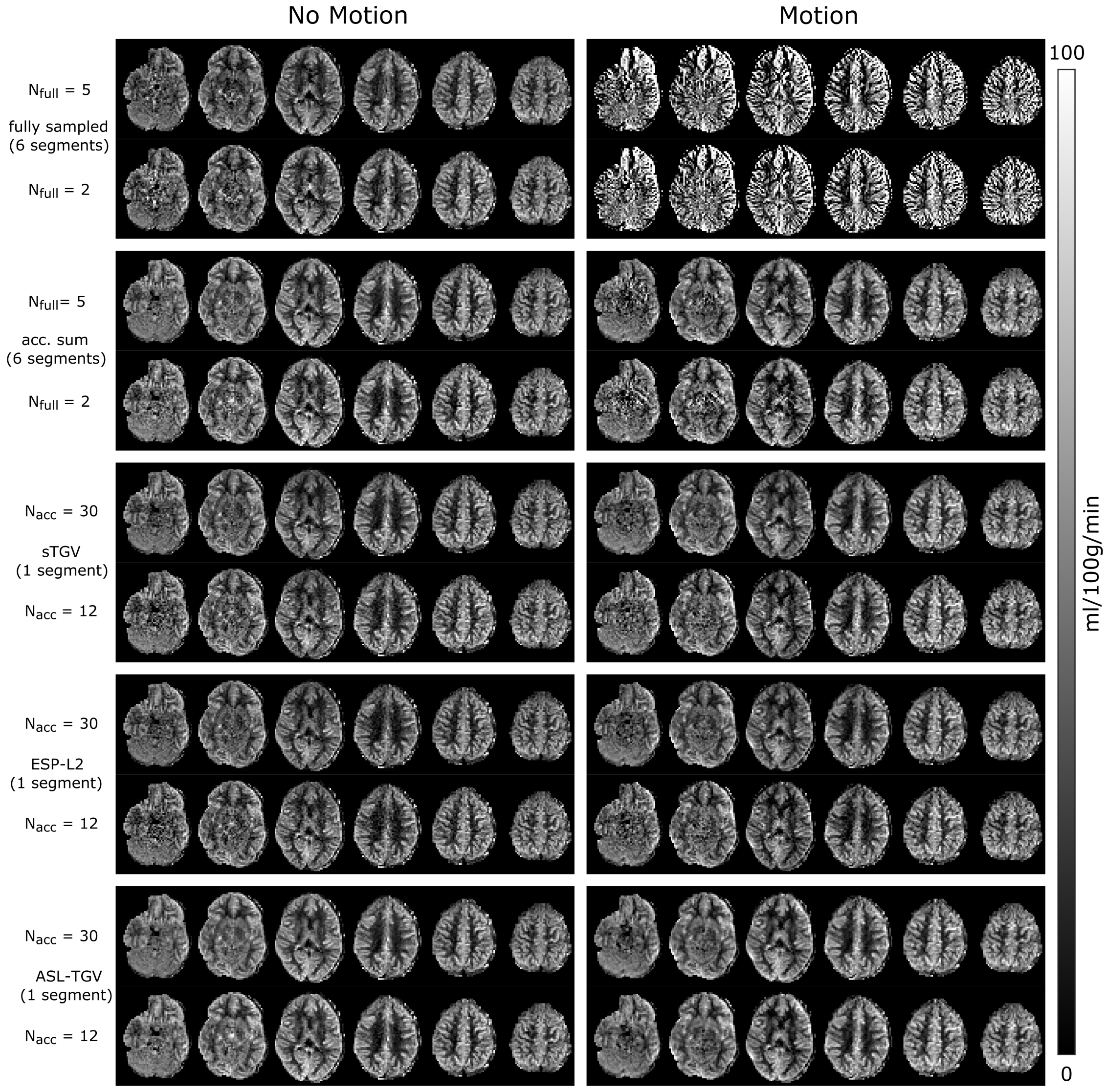

Figure 7.8: Different slices of CBF-maps for the highest and lowest number of averages ($N_{full} = 5/2$; $t_{acq} = 4\ min\ 30\ s/2\ min\ 3\ s$, $N_{acc} = 30/12$; $t_{acq} = 4\ min\ 14\ s/1\ min\ 46\ s$) of subject 2. The single-shot CBF-maps reconstructed with the ASL-TGV approach shows an improved image quality compared to fully sampled but segmented acquisition for the motionless acquisition. In case of subject movement, the CBF-maps of the segmented approach are not interpretable whereas for the single-shot method the motion can be corrected retrospectively, which results in CBF-maps with a good image quality.

Figure 7.10 shows one representative CBF-map in transversal and sagittal plane of the

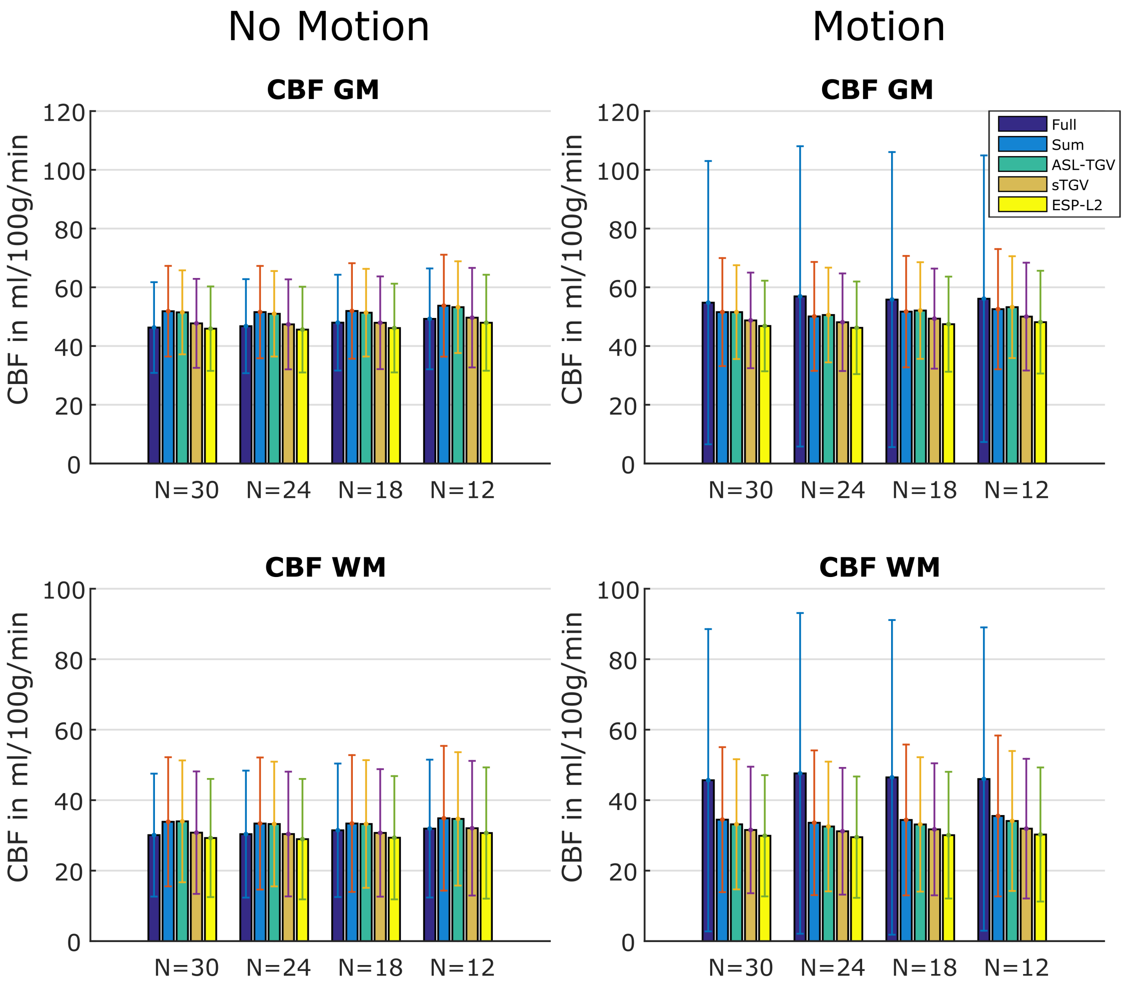

Figure 7.9: Mean CBF-values in GM and WM of subject 2 for the fully sampled but segmented approach and the proposed accelerated single-shot acquisition in combination with different reconstruction approaches. The error bars denote ±1 standard deviation.

remaining three subjects (subject 3 to subject 5) for the 5 acquisition and reconstruction approaches respectively. The results are in accordance with the results of subject 1 and 2 with an improved image quality for the proposed single-shot approach combined with the proposed ASL-TGV reconstruction compared with the rest approaches. This visual improvement is confirmed by the quantitative mean CBF values in the GM and WM which show the most accurate results for the proposed ASL-TGV approach as illustrated in Figure 7.11.

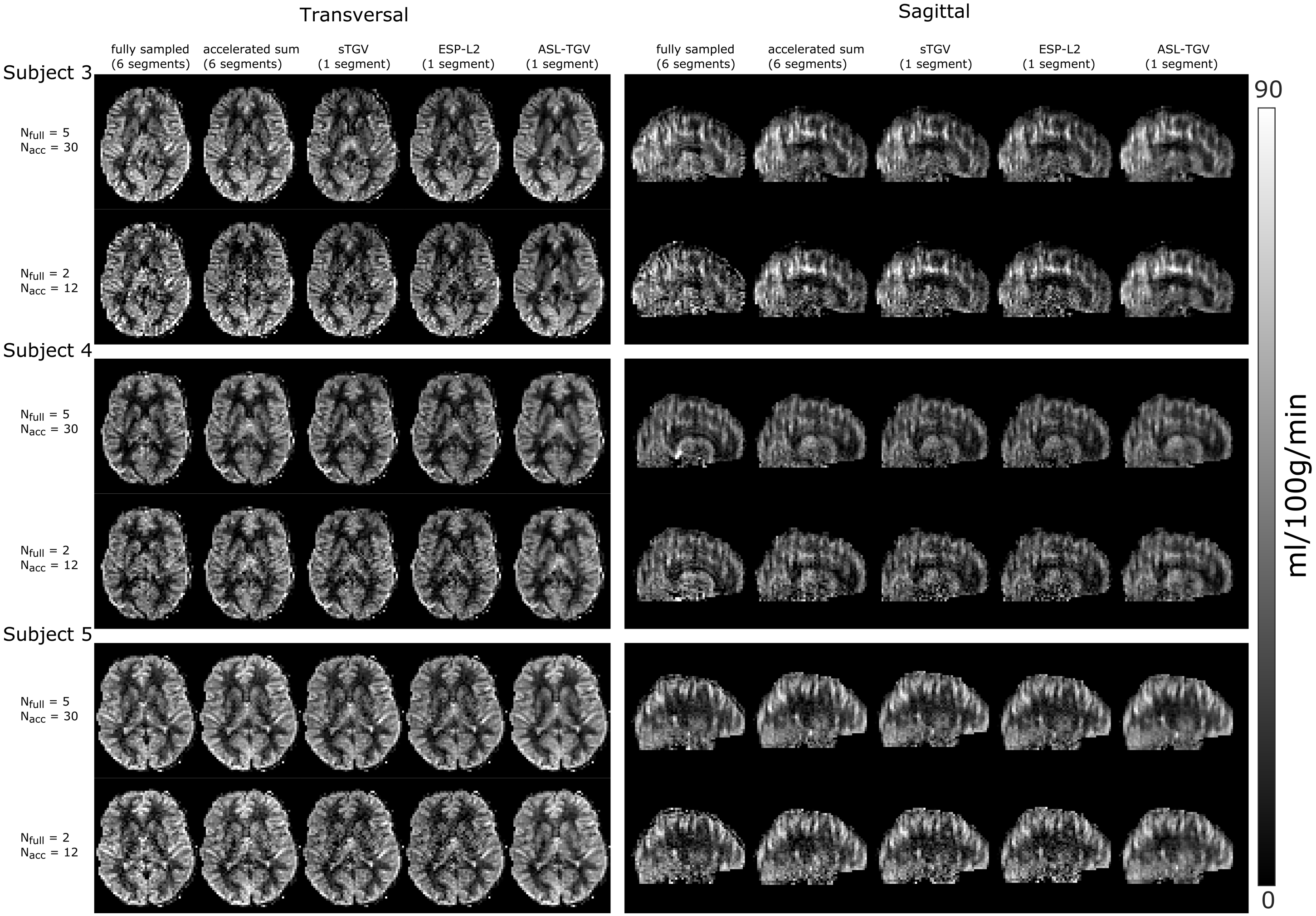

Figure 7.10: Transversal and sagittal view of one representative CBF-map of subject 3, 4 and 5 for different acquisition and reconstruction techniques using the highest and lowest number of C/L-pairs. ($N_{full} = 5/2$; $t_{acq} = 4\ min\ 30\ s/2\ min\ 3\ s$, $N_{acc} = 30/12$; $t_{acq} = 4\ min\ 14\ s/1\ min\ 46\ s$). The proposed single-shot acquisition in combination with the ASL-TGV reconstruction approach shows an improved noise suppression and image quality, despite the high acceleration factor of 6, compared to the fully sampled but segmented acquisition.

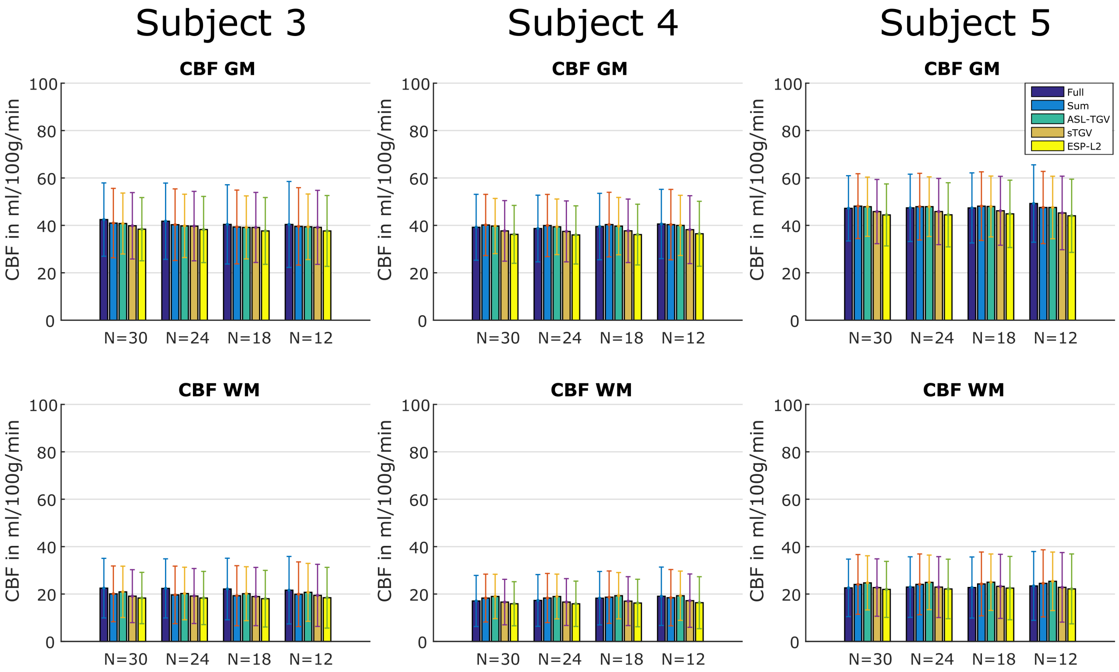

Figure 7.11: Mean GM and WM CBF-values of subjects 3 to 5 for different acquisition and reconstruction approaches in dependence of the number N of C/L-pairs. The error bars denote ±1 standard deviation.

7.4.2.2 Multi-Delay ASL Data

Figure 7.12 shows the perfusion weighted images at different PLDs and the corresponding estimated CBF and ATT maps respectively. The perfusion weighted images reconstructed with the proposed ASL-TGV algorithm shows the highest quality. This improvement in SNR leads to sharper and more detailed CBF- and ATT-maps for the proposed method compared to the other methods (illustrated by the red arrow in Figure 7.12). The corresponding mean CBF and ATT values in GM and WM are shown in Figure 7.13.

7.5 Discussion

In this study we present a novel single-shot 3D-GRASE acquisition with a time-dependent 2D-CAIPIRINHA sampling combined with a spatio-temporal reconstruction approach for pCASL scanning. Simulated synthetic and in-vivo single-PLD ASL datasets with a different number of C/L-pairs were considered. Both synthetic and in-vivo datasets show an improvement in noise-suppression and image-quality for ASL data compared to standard fully-sampled but segmented acquisition. The use of a time-dependent CAIPIRINHA sampling pattern allows the estimation of the coil-sensitivity maps directly from the averaged k-space data without the use of an additional pre-scan. Furthermore, the temporal incoherence is increased between each C/L-pair which is directly exploited in the proposed

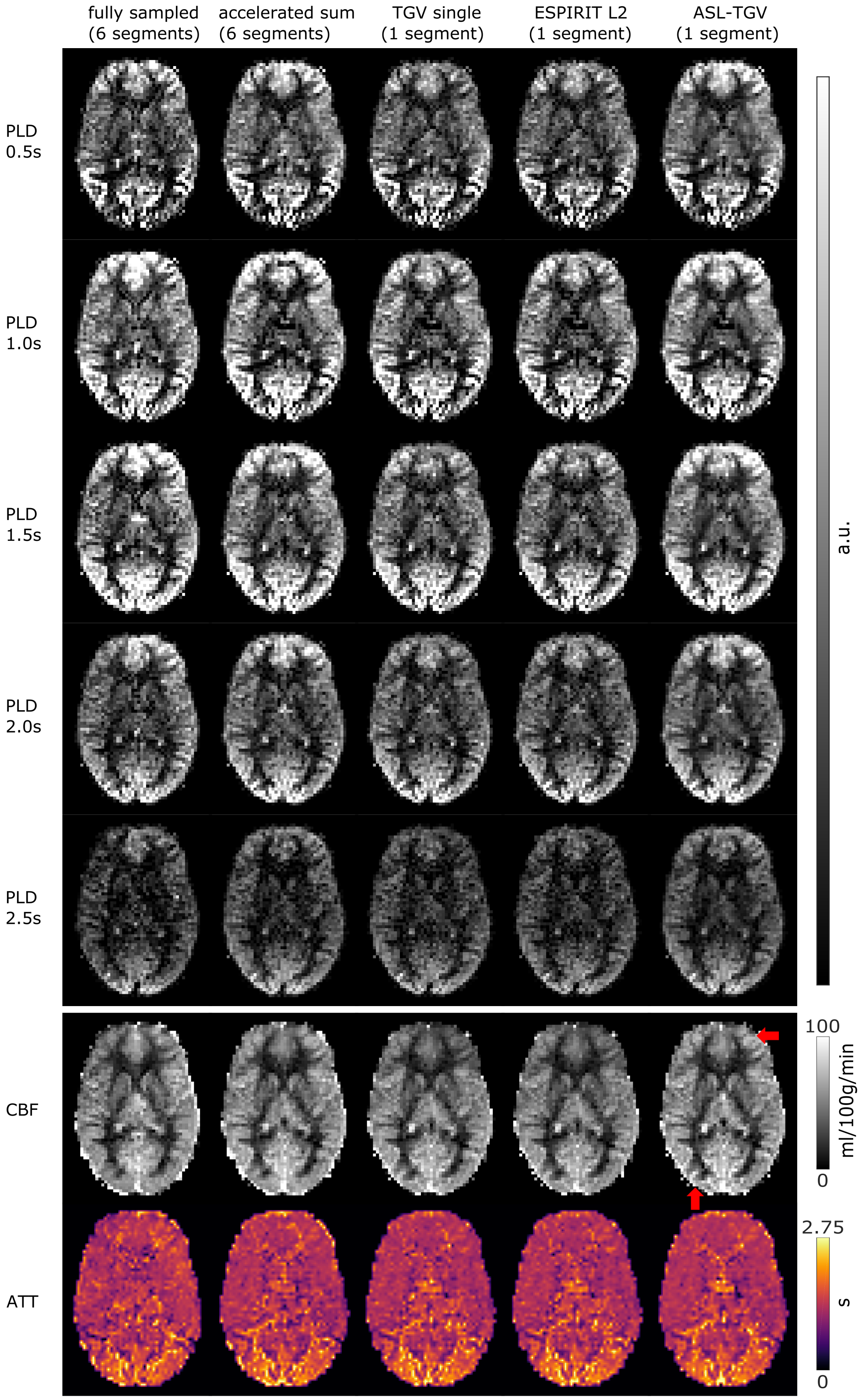

Figure 7.12: One representative slice of PWI at different PLDs and the corresponding estimated CBF- and ATT-maps. The red arrow indicates areas where the ASL-TGV method provides more details in the CBF-map.

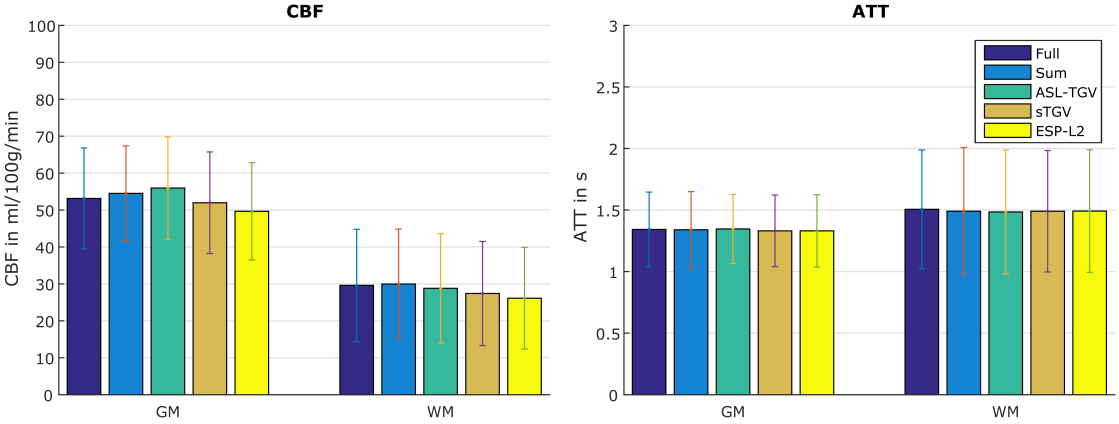

Figure 7.13: Mean CBF- and ATT-values in GM and WM for the fully sampled but segmented approach and the proposed accelerated single-shot acquisition in combination with different reconstruction approaches. The error bars denote ±1 standard deviation.

joint spatio-temporal reconstruction approach. This leads to a higher TSNR compared to the fully-sampled but segmented acquisition and also compared to the two single reconstruction methods. These results are in accordance with the results of [28], which reported a decrease of TSNR for accelerated 2D-CAIPIRINHA sequences with a fixed acquisition pattern compared to the fully sampled but segmented 3D-GRASE approach in combination with SENSE reconstruction. Similar results were reported by [43] for accelerated stack-of-spirals acquisitions with 3D-SPIRIT reconstruction. It should be noted that in our study the TSNR was not calculated in a time-equivalent manner between the fully sampled and accelerated acquisition. An additional incorporation of the number of averages in the TSNR calculation would result in a higher TSNR for the single as well as for the proposed ASL-TGV reconstruction method. In contrast to the aforementioned studies, the proposed acquisition and reconstruction method increases the TSNR, which results in an improved image quality. The increase in temporal resolution by a factor of 6 allows single-shot acquisition of the whole volume and hence improves the robustness to motion. Furthermore, the improved temporal resolution and TSNR could be very beneficial for perfusion based functional MRI [290]. However, the potential and evaluation of the current approach for perfusion based fMRI is out of scope of this study and will be part of future work.

For the proposed reconstruction approach the used model parameters are very robust and yield accurate results for simulated and in-vivo datasets with and without motion as well as for different number of C/L-pairs. However, the regularization parameter has to be adapted according to the noise level, but this is also the case for the sTGV or ESP-L2 approach where the regularization parameter has to be chosen accordingly. Compared to these single reconstruction approaches, our proposed method exploits the structural redundancy in the C/L-images as well as in the PWIs. This leads to a higher SNR, better image quality as well as more accurate CBF-values compared to these two single reconstruction approaches. The accuracy of CBF-quantification is of high importance for quantitative analysis. Furthermore, the use of a spatio-temporal constraint on the PWI reduces noise and leads to a better detection of the hypoperfusion area, which vanishes for the two single reference reconstruction algorithms (Figure 7.3). However, all three constrained reconstruction methods have a tendency to reduce the perfusion differences between adjacent regions with increasing regularization strength. The procedure for optimizing the regularization parameter with the SSIM is also sensitive to this effect and some bias remains. The present study, nevertheless, shows that for the proposed ASL-TGV method this bias is smaller than that of reconstruction approaches using only spatial regularization. For instance, the bias for the three methods ASL-TGV / sTGV / ESP-L2 is 5.5 / 7.6 / 11 % respectively in the small hyperperfusion area for 30 C/L-pairs and 5.8 / 8.9 / 12.3 % for 12 C/L-pairs. The remaining bias can be further reduced by using a debiasing method [33, 64] which could be performed in a future step. The additional incorporation of time information directly into the reconstruction approach strongly increases the TSNR and leads to CBF-maps with a higher image-quality. The fully sampled but segmented acquisition yields the lowest bias for the synthetic images. However, one should note that motion or physiological artifacts between segments are not simulated. Hence, the results for the accelerated sum approach are not shown for the synthetic data, because the difference between fully sampled and accelerated sum is only due to different Gaussian noise which is negligible. Physiological artifacts and motion can lead to misalignments in k-space which directly affects the reconstruction quality of the PWI and cannot be corrected retrospectively. This is exemplary illustrated in Figure 7.6 and 7.7 where the subject moves the head during the acquisition with a maximum rotation of 3° and translation of 2 mm. As expected, the fully sampled but segmented approach results in CBF-maps with severe artifacts which are not interpretable. In contrast, the proposed accelerated single-shot acquisition provides high quality CBF-maps which are in high accordance with the "motionless" CBF-maps. This is important for clinical as well as research settings, where otherwise a rescan is necessary. Additionally, the quantitative CBF-values are in high accordance between motionless and motion corrupted data, which highlights the potential of the proposed approach for uncooperative subjects such as children and elderly.

In our study we additionally compared the fully sampled k-space of the accelerated acquisition, obtained by summing up the corresponding C/L-k-spaces, with the fully sampled standard GRASE acquisition. In Figure 7.6 and 7.7 it is clearly visible that the proposed acquisition strategy is inherently more robust against motion than the standard segmented approach. This is due to the way how the 3D k-space is sampled. For the proposed method the whole k-space (PE1 and PE2) is sampled in an interleaved manner as illustrated in Figure 7.1C. In contrast the standard segmented approach acquires the k-space points only interleaved along PE1 (Figure 7.1D). In PE2 direction the first half of k-space (partition 24-46) is sampled with segments 1-3 and the second half (partition

1-23) is sampled with segments 4-6. In case of motion this leads to a higher inconsistency in the k-space symmetry along PE2 and hence to more severe motion artifacts. This result in lower TSNR values for the standard segmented GRASE acquisition compared to the accelerated sum method. The variability in CBF-values between those two acquisitions could be due to brain metabolism or physiological noise, e.g. motion, respiration or differences in cardiac cycle which can affect the mean CBF-values [280]. For example in Figure 7.6 some intravascular artifacts are clearly visible in the CBF-maps obtained from the accelerated sum. This explains the higher mean CBF-values in Figure 7.7 compared to the fully sampled approach. In contrast, the mean CBF-values of subject 4 and 5 show higher CBF values for the fully sampled approach compared to the accelerated sum method. However, the variations in CBF between those two acquisitions are small and comparable to reported inter-scan variations in CBF [116, 315]. By comparing the CBF-values of the accelerated sum with the single reconstruction approaches (ESP-L2 and sTGV) a clear bias with an underestimation of the CBF-values for GM as well as WM is observable. This bias can be reduced by using the proposed ASL-TGV reconstruction method which uses spatio-temporal constraints on control, label and perfusion weighted images simultaneously. This leads to more accurate reconstruction results and hence in a high agreement of the CBF-values with the accelerated sum acquisition for all subjects.

The proposed single-shot acquisition has in comparison to the fully sampled approach the advantage that more PWIs can be acquired for one PLD and in combination with the ASL-TGV reconstruction the SNR can be improved (Figure 7.12). A higher number of averages per PLD provides a better estimation of the noise and leads therefore to a more accurate setting of the spatial regularization of BASIL. This leads to improved perfusion images with sharper edges for the single-shot methods compared to the fully sampled approach (Figure 7.12). The improved SNR of ASL-TGV allows additionally a weaker regularization of BASIL that further reduces smoothing and provides higher CBF-values (Figure 7.13) for GM and lower CBF values for WM.

An improvement in temporal resolution provides a more flexible approach for multi-PLD ASL data and could be either used to increase the number of total sampling points (PLDs), which was recently shown to improve the accuracy of the quantification [311], or to shift the number of averages form high SNR acquisitions (short PLD) to low SNR acquisitions (long PLD), which will be investigated in a future work.

An additional benefit of the proposed single-shot method is the increased temporal resolution which results in a 6 fold increase in acquired C/L-pairs. This could be very beneficial in case of outliers. The elimination of a small number of C/L-pairs due to outliers has a negligible effect on the overall SNR, whereas for the fully sampled approach with only a few averages the exclusion of 1 or 2 images would have a big effect on the overall SNR.

The computation time for the sTGV reconstruction is approximately 13 seconds for one image which results in total in 780 seconds for 30 C/L-pairs using a Titan XP graphics card. In comparison for the proposed ASL-TGV method the reconstruction time of a whole 4D ASL dataset is approximately 250 seconds for 30 C/L-pairs. This is a decrease in computational time of 312% over the sTGV reconstruction method. However, one limitation of the reconstruction framework is the available GPU-memory and therefore the limited number of C/L-pairs. For the current dataset 36 C/L-pairs can be reconstructed simultaneously. Different strategies can be used to overcome this problem, e.g. using (mutli-threading) data streaming to multiple GPUs concurrently [175] or by reconstructing the 4D ASL-dataset in blocks.

The mean background suppression efficiency of the proposed method is 91.05 ± 1.2 % in GM and 88.8 ± 1.5 % in WM respectively. This leads to a TSNR improvement of approximately 365/338 % in GM/WM compared to non-background suppressed ASL imaging (data not shown). Whereas a higher improvement in background suppression would lead to lower subtraction artifacts due to motion or temporal fluctuations this could lead to a loss in performance of all used reconstruction methods. This is due to a lower SNR in the C/L-images. However, we expected that our proposed ASL-TGV outperforms the other reconstruction algorithm because it incorporates information of the C/L-image as well as the PWI simultaneously. Additionally, an even higher background suppression needs more background suppression pulses which would affect the labeling efficiency due to imperfections of the inversion pulse. Furthermore, the lower SNR in the C/L-images would affect additionally the quality of motion correction [45]. Hence, a strong background suppression with two pulses is recommended by the consensus paper [8].

One limitation of the generated synthetic dataset is the shape of the hypo- and hyperperfusion ROI. They fit exactly in the voxels of the ASL images. A more realistic ROI would be a spherical region drawn in high resolution space which is than down sampled to ASL space. This would lead to more realistic hyper- and hypoperfusion areas with boards across the voxels.

In summary, the results of this study highlights that the proposed accelerated time-dependent 2D-CAIPIRINHA sampling strategy combined with the proposed ASL-TGV reconstruction approach, which exploits spatial and temporal information of the C/L-images simultaneously, allows single-shot ASL acquisition of the whole brain. As a consequence, this method improves the robustness of ASL images against motion. Additionally, due to the spatial and temporal constrains, it improves the SNR and image quality for simulation and in-vivo data with and without motion. Furthermore, it yields high quality quantitative CBF-maps from single-PLD data with only 12 C/L-pairs ($t_{acq} = 1\ min\ 36\ s$) and high quality CBF and ATT-maps from multi-PLD ASL data. This improvement addresses urgent clinical demands. A further improvement in the image quality could be expected by combining the proposed approach with a prospective motion correction strategy [5, 228]. Additionally, to reduce the amount of blurring in the final CBF images, which leads to an underestimation of the GM and an overestimation of WM-values, a variable-flip angle readout scheme [162] or a deblurring method [94] could be used. An additional improvement of the proposed acquisition method could be the use of a Hadamard encoding scheme [107] to increase the number of sampling points of the kinetic curve.

7.6 Conclusion

The proposed time-dependent CAIPIRINHA sampling in combination with a spatio-temporal reconstruction approach adapted for ASL data provides high-quality CBF-maps from the whole brain with a single-shot 3D acquisition. It addresses important clinical demands in terms of scan-time reduction and motion-robustness compared to standard segmented 3D readouts. Furthermore, it increases the TSNR and reduces the acquisition time of one PWI by a factor of 6 compared to fully sampled but segmented 3D-GRASE pCASL acquisition. This makes this approach very promising for perfusion fMRI, multi-delay ASL data as well as for uncooperative subjects, patients or children.

8

Conclusion and Outlook

Arterial spin labeling (ASL) is a very promising approach with distinct advantages compared to other perfusion measurements. The non-invasiveness and possibility of absolute quantification of the cerebral blood flow (CBF) opens a broad range of applications in the clinical and scientific area. However, today many challenges still remain to bring ASL perfusion imaging into clinical routine. The aim of this thesis was to improve the acquisition efficiency of ASL imaging and thereby improving the robustness, quality, and reliability of ASL imaging. Several methodological improvements for ASL imaging were proposed. Variational denoising methods for static (chapter 3 and 4) and dynamic (chapter 5) ASL imaging were developed with a significant reduction in acquisition time and an improved robustness against artifacts and outliers in the data. In chapter 6 we introduced a pipeline for processing and monitoring ASL data in real-time. The pipeline also offers the possibility for neurofeedback studies. In the last chapter a new accelerated 3D-gradient and spin echo (GRASE) acquisition in combination with a ASL-total generalized variation (TGV) reconstruction approach was proposed to solve the inter-segment motion problem of current recommended segmented acquisitions. In the following subsection the main findings will be discussed and an corresponding outlook will be presented.

Static Denoising of ASL

In chapter 3 and 4 different spatio-temporal variational denoising approaches for ASL imaging were investigated and compared with recent published denoising methods. The first implementation uses the mean perfusion weighted image (PWI) as input, which is so far the standard input for denoising of ASL images. A successive extension of this approach by including more information in the denoising procedure was assessed. This extensions include in the first step the perfusion weighted time series as input, in the next step the whole 4D dataset, and in the last step additionally the spatial-dependent regularization map. The main findings can be summarized as follows: (1) Denoising generally improves the quality of CBF-maps and allows a significant reduction in acquisition time. (2) Including successive more information in the denoising procedure leads to an further improvement in image quality and the best results can be achieved by exploiting temporal and spatial similarities of all images to jointly denoise the control and label images. (3) For the data-fidelity term a L^1 norm is preferable over the L^2 norm, as it is more robust against outliers and provides sharper edges. (4) 3D denoising approaches are preferable over 2D approaches and the improvement increases with higher resolutions. (5) The spatial adaptive regularization approach takes into account the varying noise level in the images and thereby increases the image quality slightly over the robust L^1 norm TGV approach. In addition, it allows for automatic denoising of the ASL data independent of the number of averages, as the change in the signal-to-noise ratio (SNR) is directly exploited in the regularization parameter maps. (6) Compared with the reference denoising approaches our proposed method shows improved noise removal while maintaining structures and edges and an improved robustness against outliers. This results in an enhanced image quality and quantitative accuracy. (7) The model parameters of the developed methods are very stable over subjects for a specific image acquisition. In contrast, for the reference denoising approaches different parameters has to be used for different subjects. (8) Although most approaches accounts for the change in SNR by using noise dependent filter parameters, the estimation and characterization of noise with one single parameter is often inaccurate and the degree of smoothing depends additionally on the voxel size and image contrast.

Although ASL is an inherently low SNR technique, it is interesting that neither in the recommendation paper of the International Society for Magnetic Resonance in Medicine (ISMRM) perfusion study group [8] nor the recently published software package "ExploreASL", developed through the cost action "ASL in Dementia", suggests denoising of ASL images. The results of our study clearly shows that the image quality and quantitative metrics such as structural similarity index (SSIM) and peak signal-to-noise ratio (PSNR) can be improved using image denoising. However, two potential problems for denoising in the clinical and scientific research exists. First, depending on the readout and labeling approach, ASL images have a different contrast and SNR level. To achieve optimal results the denoising parameters had to be set up accordingly i.e the regularization parameter λ. The proposed spatial adaptive approach inherently accounts for different noise levels and is very robust for a specific type of image acquisition but nevertheless a change in image contrast (going from 2D echoplanar imaging (EPI) to 3D GRASE) leads to a change in the parameters. Second, inclusion of prior information leads to a reduction of the standard deviation but comes at the cost of a bias. ASL is a quantitative method and therefore the bias produced by the denoising method should be ideally zero. This is especially important in group studies or pharmokenetic studies where CBF changes between individual brain regions are investigated. The proposed method delivers meaningful results, which are in high accordance to the ground truth images, nevertheless a small bias exists. A combination of the proposed method with a debiasing method [33] can reduce the systematic error and thereby increase the accuracy of the quantitative values. This should be implemented in a next step. In addition, most of the denoising studies validate their approach on a synthetic dataset or on a small population of healthy subjects. A systematic study of ASL denoising methods on numerical data with different contrasts and SNR levels as well as an application and validation on a large cohort, including data from different sequences, healthy and patient datasets, and data from different scanners could be helpful for bringing the denoising algorithm into a standard ASL processing pipeline.

Another still open question for variational methods is the use of an optimal image prior. The second order TGV enforces pice-wise smoothness of the images and allows for jumps between tissue boarders. For many natural and magnetic resonance imaging (MRI) applications this was shown to be a reasonable image prior. Also the results of our studies shows that TGV_α^2 is very well suited for denoising ASL images. However, Schwarzbach et al. [225] recently implemented a variational network for ASL imaging, which maintains data-fidelity but learns the image prior on a small subset (4 datasets). This approach performed on par with the proposed CL-T-L1 TGV method showing the potential of including a higher number and more complex image priors. In Schwarzbach's network only the mean perfusion weighted image was used as input. An inclusion of additional temporal information of the PWI or including the whole available data similar to the proposed approach might improve the results further and may a potential next step to enhance the image quality of ASL data. However, we should keep in mind that for different datasets a new model and prior has to be learned, whereas the proposed spatial adaptive approach uses the same parameters for different resolutions. As previous mentioned ASL images have a different contrast, noise level, and corruption with outliers, depending on the used acquisition and labeling scheme. Currently, it is not clear which model or prior might be best suited for which image contrast. In a potential next step the variational network might give insights into the right choice of image priors. This information could be used for forming a new classes of image priors, specific for ASL images. In addition, a combination with non-local operators would be a potential next step. The non-local operators take into account global information, based on data-similarity, which might be more suited due to the high redundancy in MRI images [215].

During the last years deep neuronal networks have gained increased popularity for denoising of ASL images. These approaches show first promising results, however, several training datasets are necessary to estimate the parameters of the complex network structure following long training times [111, 195, 314]. For example Xie et al. used 200 [314], Halles et al. used 131 [111], and Owen et al. used 20 datasets but for each dataset 10 different samples [195]. Furthermore, the learned network is somehow limited to the used acquisition parameters such as voxel size, matrix size, and SNR. A change in one of those parameters requires to learn the whole network once again in a complex training. This potentially poor transfer and complex learning, limits its applicability in clinical and scientific day life and may struggle the use in a standardized ASL pipeline. However, for this very new approaches more validations on healthy and pathological cases are necessary and more studies regarding the stability of the approaches must be performed.

Dynamic Denoising of ASL

In chapter 5 the concept of infimal convolution of total generalized variation (ICTGV) was introduced for denoising of dynamic ASL data. This general approach uses two spatio-temporal weights, which are automatically balanced in the optimization procedure. This takes into account locally different dynamic properties allowing for stronger temporal regularization in areas with slow dynamic changes and weaker temporal regularization in areas with high dynamic changes. As consequence, the original ASL signal is well recovered from noisy and artifact corrupted data. Accompanied with the increase in SNR is the improved parameter estimation from multi-post-labeling delay (PLD) data as well as the detection of activation related areas in functional arterial spin labeling (fASL).

Our studies highlight the importance of denoising ASL data for dynamic applications. In case of multi-PLD data the improvement in noise suppression stabilize the non-linear fitting approach showing a lower inter-quartile range (IQR) over different noise-realization. Accompanied with the noise suppression is a more accurate estimation of CBF and arterial transit time (ATT), with less outliers in the corresponding maps. Similar results were observed for the perfusion based functional magnetic resonance imaging (fMRI) dataset. Compared with standard Gaussian denoising the proposed method removes outlier, suppresses noise while maintains high data-fidelity with a well preservation of small details and edges. This results in recovery of all activation areas in the synthetic generated map. For both applications a second order ICTGV regularization functional is used as a-priori model. It might be possible to further improve the image quality by using higher number of components or higher order TGV functionals. Especially for the multi-PLD dataset a third order ICTGV functional would be more suited as the kinetic curve shows primary a smooth behavior. In addition, this approach can be extended to control-label time series similar as for the proposed static denoising approaches. However, both extensions come at the cost of additional model complexity and computational burden and the benefit has to be validated in a future study.

The proposed denoising technique might be especially beneficial for white matter regions where the SNR is much lower due to prolonged ATT and lower perfusion. Due to the low SNR white matter perfusion is often neglected or overlooked [123], although it can provide useful information in various diseases [146, 180].

For dynamic datasets a trade-off between spatial and temporal resolution has to be chosen. A high temporal resolution provides a good sampling of the kinetic curve, or the activation related signal change in CBF, which is sought to increase the quantification accuracy. Similar a high spatial resolution leads to lower partial volume (PV) effects potentially increasing the statistical power of fASL data. For both methods we focused on a high temporal resolution in our study. The combination of the proposed method with more sophisticated acquisition and labeling strategies will allow a higher spatial resolution while maintaining the temporal resolution. An evaluation of the proposed method on higher spatial resolution would be of great interest to benefit form the accurate localization of neuronal activity using fASL. Current studies, including also ours, uses 3 *mm* in-plane and 3-6 *mm* through plane resolution. This is a very low resolution since the cortex structures are between 1.5 and 4.5 *mm* depending on the location and 2.5 *mm* on average [75, 87]. Accompanied with this coarse spatial resolution are partial volume effects (PVE). This reduces the change in CBF during the activation period potentially reducing the statistical power. In addition, a higher resolution provides the option to investigation the CBF-changes in the different cortical layers as suggested by Jin et al. [139]. In blood oxygen level dependent (BOLD) based fMRI a study regarding layer dependent activation was recently proposed by Beckett et al. [17]. This might give new insights in understanding metabolic changes due to neural activation and to draw observations in which layer the CBF increases. A first promising work in this direction was proposed by Shao et al. [229] showing a correlation of CBF with gray matter (GM) density.

For both applications the model and regularization parameters were tuned on a synthetic generated dataset with known ground truth. The results of the parameter tuning clearly shows that different dynamic properties of data sets lead to different model parameters. However, for one application the parameters are very robust and can be directly transferred to the in-vivo dataset. This good generalization greatly improves the usability for clinical and research applications. Nevertheless, a big change in SNR levels requires a adjustment of the regularization parameter. The influence of different SNR levels was not considered during this thesis, which is currently one limitation. This influence should be considered in a next step.

A current limitation of the proposed method is the implementation using a single graphics processing unit (GPU). This constraints the size of the dynamic time series. One workaround could be to divide the whole dataset into sub-blocks which are then denoised separately. However, this can lead to a performance loss because some information is neglected during the minimization process. A more appropriate solution would be to use data-streaming onto multiple GPUs concurrently [175].

In case of multi-PLD dataset the proposed method can be combined with a Hadamard encoding labeling strategies to improve either the spatial resolution of the ASL data or to improve the temporal resolution. Further improvements are expected by extending the denoising approach to a reconstruction approach and combine this with the time-depended controlled aliasing in parallel imaging results in higher acceleration (CAIPIRINHA) accelerated 3D-GRASE acquisition proposed in chapter 7.

RT-NF ASL

In chapter 6 we presented an interesting alternative to BOLD fMRI for neurofeedback studies. We investigated the proof-of-principle concept for controlling neuronal activation during a finger tapping experiment using fASL. The results demonstrates that all subjects were able to learn to control their brain activity and increased the CBF of about 10% in the first, and of about 16% in the second feedback run compared with no feedback. The first results are very promising and show the potential of this method for real-time applications. Problems occurring in BOLD based fMRI like baseline drifts, or relative changes without quantitative reference can be solved with this technique. This might be helpful in gaining insights into processes involved during neurofeedback. Currently the specificity of neurofeedback effects is still not completely clear, and serves as a topic of ongoing research in BOLD based fMRI. Additional reproducibility and comparison studies with BOLD based MRI would be highly interesting to validate the first results and see the potential and advantages of the proposed method.

The proposed real time pipeline provides an important tool for ASL imaging in general. The online monitoring shows potential artifacts arising form successive head motion or poor labeling efficiency due to B_0 inhomogeneities, or turbulent flow. In such cases the patient's head can be fixed or the labeling plane can be reallocated immediately. Beside the application on healthy subjects, the proposed concept could be applied to stroke patients in form of rehabilitation. The online monitoring gives the user insights in the performance of the patients during this process.

There are still a lot of open questions and future directions to go in this new field. For example the right design of the paradigm, the right form of the presented feedback, and also the mechanism involved during the feedback session remains unclear. In real time neurofeedback (RT-NF) studies based on the BOLD signal a short block duration is used to omit the effect of baseline drifts. This can hamper the accuracy of the neurofeedback signal. The absolute quantification of ASL data provides the possibility to increase the block duration resulting in a more accurate baseline signal. In addition, the hemodynamic response in fASL is a slow varying signal and has a delay of approximately 4-6 seconds until the peak is reached. Accompanied with this delay is an inaccurate feedback at the beginning of each activation block. Longer block durations would reduces this influence.

The feedback design is another open topic. In the current study the subjects received a feedback every 4 seconds. However, due to the post-processing steps and the hemodynamic response the total delay time of the feedback is 8-10 seconds. This might confuse the subject during the task and an intermittent feedback after 12 *s* or after a whole activation block might be more suited [141].

Although the first results are very promising, the contrast to noise ratio of fASL is very low and approximately 1 for the used finger tapping experiment. Other cognitive functions such as emotion have an even lower contrast to noise ration, which might hamper the advantages of the method. Especially on a single subject basis, the provided feedback might be not reliable enough to gain accurate results. However, this has to be validated in further steps.

One current limitation of real time ASL is the limited number of slices, and the limited spatial and temporal resolution. In our study we used a slice thickness of 6 *mm* to achieve a reasonable brain coverage. The low temporal resolution and inherent blurring of the GRASE sequences causes PVE. This leads to underestimation of GM CBF, potentially dampening the effect of activation related CBF increase. The low temporal resolution is caused by the long labeling period and the additional PLD. Velocity selective arterial spin labeling (VSASL) might reduce the repetition time since moving spins are labeled independent of their position. This eliminates the ATT form pulsed arterial spin labeling (PASL)/pseudo continous arterial spin labeling (pCASL) sequences. Higher spatial resolutions can be gained with accelerated acquisitions in combination with fast reconstruction methods. The handling of the huge amount of raw-data with iterative reconstruction is quite challenging within the repetition time of 3-4 seconds. One potential solution can be provided by recent developed deep learning based methods. The learned neuronal networks provide meaningful results in a few tens of milliseconds [113, 225]. This feature makes them perfectly suited for real time application and should be integrated into the developed pipeline.

Accelerated 3D data acquisition

So far moderate acceleration factors of 2-3 were recommended from the ISMRM consensus due to the inherently low SNR of ASL images. In chapter 6 we proposed a new acquisition strategy for accelerated ASL imaging in combination with a 4D variational reconstruction approach that exploits the whole ASL data simultaneously. With this approach acceleration factors of 6 can be achieved allowing the acquisition of high resolution whole brain data within a single shot. This significantly improves the motion robustness compared with recommended segmented acquisitions and might be of great interest for a variety of clinical applications, especially those were involuntary spontaneous movement can occur such as stroke imaging or in uncooperative patients. In addition, it provides a higher flexibility for multi-PLD acquisitions or can be used for the investigation of neuronal activity with a high spatial and temporal resolution.

The implemented time-depended CAIPIRINHA pattern has two advantages compared with the static pattern. First, the time depended acquisition strategy allows the estimation of the coil sensitivity maps without the use of an additional pre-scan. Second, the shift from measurement to measurement increases the temporal incoherence, which is directly utilized in the 4D reconstruction approach. This results in a slightly higher temporal signal to noise ratio (TSNR) compared with the fully sampled acquisition. In contrast to standard spatial variational reconstruction approaches the image quality and quantitative metrics are significantly higher. The coupling of the control, label, and perfusion weighted image during the reconstruction reduces the bias compared with the separate reconstructions. A further reduction of the bias is expected by applying a de-biasing method after the reconstruction [33].
Although the proposed accelerated single-shot acquisition addresses the demands of motion-robustness the challenge of blurring along the second phase encoding direction still remains. Our acquisition used an echo train length $< 300\ ms$ as recommended by the consensus paper [8]. However, the results showed that the bias due to the T2-relaxation of blood is much higher than the bias caused by one of the reconstruction approaches. One can argue that for clinical diagnosis the bias in absolute value is not so important than motion insensitivity because both, the healthy and diseased tissue are equally affected. In addition, the quality of the images may be sufficient for clinical diagnosis. However, for group studies a robust and reliable absolute quantification is necessary. A potential solution might be to incorporate a de-blurring operator directly in the reconstruction approach. The side effect of de-blurring is the noise amplification, which could be hold low with the spatio-temporal constraints. A further reduction is expected by combining the de-blurring operator with a variable flip-angle scheme [162, 328]. A more intuitive approach would be to implemented the same $1x6^{(2)}$ pattern as a two shot acquisition. This could significantly reduce the echo-train length and accompanied bias but comes at the cost of a decreased temporal resolution. Hence, it might be only suited if no or only slight head motion is expected.

The proposed single-shot method is only validated on a few healthy subject. A fully validation including patients with cerebrovascular diseases would be a possible next step to investigate the potential of the method, especially the motion robustness. Beside perfusion measurement, ASL provides the possibility to obtain a dynamic angiogramm of the brain vessels [258]. Recent promising studies show that the feeding arteries in AVM can be successfully detected [93]. To locate such small vessels high spatial and temporal resolutions are necessary. Both requirements are fulfilled with the proposed method showing another potential application area.

The motion correction is currently performed after reconstruction. This may introduce some blurring due to the incooperation of temporal information. Superior results are expected if the the motion-correction is directly integrated in the reconstruction approach. The motion information can be either gained from a tracking systems or by performing a two step procedure.

The regularization and model parameters were optimized using a grid search on a numerical generated dataset. The optimized parameters were then directly used for the in-vivo data and provide reasonable results. The robustness of the model parameters for different kind of data is of high importance for the general applicability. Similar to the spatial adaptive denoising approaches the regularization parameter could be replaced by an estimated g-factor map taking into account the spatial varying noise directly in the reconstruction process.

In our study we limited the acceleration by a factor of 6. Higher acceleration factors would be of great interest and can be either used to reduce the total echo train length and hence the blurring, or to increase the spatial resolution of the ASL images. For the latter, first promising results were recently published in form of an abstract [227] suggesting acceleration-factors of up to 12 on a 7T MRI scanner. With this high resolution (2 mm isotropic) whole brain images were obtained. In a potentially next step the performance of higher acceleration factors will be evaluated.

The proposed reconstruction method is not limited to a specific sampling pattern. In general, arbitrary Cartesian sampling strategies such as pseudo-random or pseudo spiral could be used. In addition, the reconstruction approach can be adjusted for non-Cartesian sampling strategies. Several studies indicate that non-Cartesian sampling strategies are preferable over Cartesian sampling [282]. Therefore, an even higher acceleration factor is expected by using more sophisticated patterns. A potential next step could be to test different sampling schemes on the generated phantom and compare their performance. Instead of simulated coil sensitivity maps, the original profiles can be taken into account in the simulation study. In general the variations of the coil sensitivities might be lower from inferior to superior direction. Hence, sampling pattern with lower acceleration factors in the inferior-superior direction and higher acceleration factors along the other directions might be more suited.

A

List of Acronyms

ACC	anterior cingulate cortex 138
AccASL	acceleration selective arterial spin labeling 42
ACPC	anterior commissure posterior commissure 51
AIF	arterial input function 36, 37
ASL	arterial spin labeling iii, v, xvii, xix, xx, xxii–xxvii, xxix, 2, 3, 8–11, 13, 22–29, 33–37, 39–43, 45–49, 51–56, 61, 62, 67–70, 74, 81, 84, 86–89, 91–96, 100, 107, 109–112, 114, 116–118, 124–126, 128, 129, 131, 132, 134, 138–142, 145, 146, 148, 149, 151–158, 160, 161, 163–176, 178–181, 210, 212, 213, 215
ATP	adenosin triphosphate 115
ATT	arterial transit time xxiv, xxvii, 24–27, 41, 45, 112, 124–128, 130–134, 156, 166–168, 171, 176, 179
AVIONIC	accelerated variational dynamic MRI reconstruction 114
BASE	unprepared basis and selective inversion 15
BASIL	Bayesian inference for arterial spin labeling 156, 170
BL	baseline xxv, 139, 142–144
BOLD	blood oxygen level dependent xxiii, 115–118, 137, 138, 177, 178
BS	background suppression xix, 34, 35, 48, 49, 52–54
bSSFP	balanced steady state free precession 20
CAIPIRINHA	controlled aliasing in parallel imaging results in higher acceleration xxv, xxvi, 95, 125, 132, 134, 148–150, 153, 158, 160, 166, 168, 171, 172, 178, 180
CASL	continous arterial spin labeling xviii, 10–15, 18–20, 23, 37, 39, 40, 50, 51

CAT12	computational anatomy toolbox v 12 126
CBF	cerebral blood flow iii, xvii, xix–xxvii, 2, 6–8, 10, 13, 18, 23–26, 31, 33, 34, 37, 39, 41, 45, 47, 48, 50–54, 56, 61, 67–69, 73–77, 79–81, 83, 85–89, 95–110, 112, 115–121, 123–128, 130–134, 138–145, 154–174, 176–179
CBV	cerebral blood volume 6, 115, 116
CMRGlc	cerebral metabolic rate of glucose 115
CMRO2	cerebral metabolic rate of oxygen 6, 115, 116
CSF	cerebrospinal fluid 53, 68, 92, 117
CUDA	compute unified device architecture 114, 123
dHb	deoxygenated hemoglobin 115
DIPLOMA	double inversions with proximal labeling of both tag and control images 15
DSA	digital subtraction angiography 43
DSC	dynamic susceptibility contrast 8
EEG	electroencephalography 115
EPI	echoplanar imaging xviii, xix, 18, 26–31, 33, 68, 74, 93, 98, 117, 125, 139, 155, 174
EPISTAR	echoplanar imaging and signal targeting with alternating radio frequency 18
ESPIRIT	eigenvector-based iterative self-consistent parallel imaging reconstruction 155, 156
FAIR	flow-sensitive alternating inversion recovery 15, 18, 19
FAIRER1	flow-sensitive alternation inversion recovery excluding radiation damping 15
FAIRER2	flow-sensitive alternation inversion recovery with an extra radio frequency pulse 15
fASL	functional arterial spin labeling xxiv, 3, 112, 116, 118, 119, 122–124, 134, 138, 140, 145, 146, 176–179
FB	feedback xxiv, xxv, 139–144
FID	free induction decay xix, 26, 29–32
fMRI	functional magnetic resonance imaging 26, 115, 116, 123, 137, 138, 148, 168, 172, 176–178
FoV	field of view 27, 67, 68, 95, 125, 153
FWE	family wise error xxiii, 118, 119, 121, 122, 141
FWHM	full width at half maximum 74, 98, 118, 139
GLM	general linear model 118, 140
GM	gray matter xix, xxi, xxiii, xxiv, xxvi, xxvii, 6, 34, 38, 47, 53, 68, 69, 79, 82, 87, 95, 98, 100, 107–110, 112, 117, 125–127, 129, 131, 132, 134, 153, 154, 156, 157, 159, 160, 162–164, 166, 168, 170, 171, 177, 179

GPU	graphics processing unit 114, 155, 171, 177
GRAPPA	generalized autocalibrating partial parallel acquisition 67, 68
GRASE	gradient and spin echo xix, xxv, 3, 29–31, 33, 35, 49, 88, 93, 95, 125, 132, 139, 148–150, 153, 166, 168–170, 172–174, 178, 179
GT	ground truth xxvi, 157, 159
ICA	independent component analysis 88
ICA	internal carotid artery xx, 43, 44, 51, 52
ICTGV	infimal convolution of total generalized variation xxiii, xxiv, 112, 114, 116, 119–123, 126, 128–130, 132, 133, 176, 215
IDFT	inverse discrete Fourier transformation 92
IQR	inter-quartile range xxiv, 107, 127–129, 131, 132, 134, 176
ISMRM	International Society for Magnetic Resonance in Medicine xviii, 22, 148, 174, 179
LD	labeling duration 23, 24, 44, 45, 95, 125, 139, 153
MAP	Maximum-a-Posteriori 57
MPRAGE	magnetization prepared - rapid gradient echo 68, 117, 125, 139, 153
MR	magnetic resonance 67, 95, 117, 139
MRF	Markov random fields 58
MRI	magnetic resonance imaging iii, 1, 2, 8, 14, 19, 26, 49, 55–57, 59–61, 92, 112, 114–116, 124, 150–152, 168, 175, 178, 181
MT	magnetization transfer xviii, 13–15, 18, 20, 21
MTF	modulation transfer function xxv, 148, 154, 155
NF	neurofeedback xxv, 3, 138, 141
NLLSQ	non-linear least squares xxiv, 124, 126, 128, 130–132, 134
OEF	oxygen extraction fraction 6
oHb	oxygenated hemoglobin 115
PASL	pulsed arterial spin labeling xviii–xx, 14–19, 22, 23, 37–40, 43, 50–52, 56, 88, 93, 97, 98, 118, 179
PCA	principle component analysis 88
pCASL	pseudo continous arterial spin labeling xviii–xx, xxv, 19–23, 25, 37–41, 43, 50–52, 88, 93, 95, 97, 98, 125, 126, 139, 142, 148–150, 153, 166, 172, 179
PCT	perfusion computed tomography 8
PD	proton density 95, 125

PE	phase encoding xxv, 150, 169, 170
PET	positron emission tomography 1, 8, 24, 36, 115
phMRI	pharmacological functional magnetic resonance imaging 112
PI	parallel imaging 3, 92
PICORE	proximal inversion with a control for offresonance effects 15, 18
PLD	post-labeling delay xviii, xx, xxiii, xxiv, xxvii, 3, 9, 23–27, 41, 43–45, 49, 51, 52, 54, 95, 107, 110–112, 116, 124–126, 128, 129, 131–134, 139, 145, 148, 149, 153, 154, 156, 166, 167, 170, 171, 176, 178–180
PROPELLER	periodically rotated overlapping parallel lines with enhanced reconstruction 49
PSF	point spread function xix, 31, 148, 154
PSNR	peak signal-to-noise ratio xx–xxii, xxvi, 74–77, 79–82, 84, 86–88, 98, 100–103, 109, 156–158, 174
PULSAR	pulsed star labeling of arterial regions 15
PV	partial volume xx, 53, 68, 69, 95, 117, 125–127, 154, 177
PVE	partial volume effects iii, v, 47, 109, 131, 177, 179
PWI	perfusion weighted image xvii, xxii–xxvii, 10, 18, 19, 41, 44, 45, 56, 61, 62, 95, 99, 116, 118–120, 123–129, 131, 139, 148, 152, 154–157, 160, 167–173, 175
Q2TIPS	QUIPSS II with thin-slice TI1 periodic saturation 15
QUASAR	quantitative star labeling of arterial regions 15
QUIPSS	quantitative imaging of perfusion using a single subtraction 15
QUIPSS II	quantitative imaging of perfusion using a single subtraction version II xviii, 15, 16, 23, 41
RARE	rapid acquisition with relaxation enhancement xix, 29, 31–33, 92
RF	radio frequency xvii–xix, 9–12, 14, 15, 18–23, 30, 32, 41, 42, 50–52, 92
RMSE	root mean squared error 71, 74
ROI	region of interest xxiv, 140, 141
RT-fMRI	real time functional magnetic resonance imaging 138
RT-NF	real time neurofeedback xxiv, 140, 142, 145, 146, 178
SAR	specific absorption rate 14, 15, 19, 50

SNR	signal-to-noise ratio iii, v, xx, xxiv, 2, 9, 19, 22, 23, 25, 26, 29, 31–33, 40, 45, 47, 48, 50, 52, 55, 56, 61, 75, 81, 86–89, 92, 100, 107, 109, 110, 115, 116, 123–125, 127, 129, 131, 148, 149, 152, 157, 166, 168, 170, 171, 174–177, 179
SoSP	stack of spirals xix, 31–33, 148, 149
SPECT	single-photon emission computer tomography 8
SPM12	statistical parameter mapping v 12 68, 70, 96, 117, 118, 126, 139, 155
SSIM	structural similarity index xx–xxii, xxvi, 71, 72, 74–77, 79–82, 84, 86–88, 96, 98, 100–103, 109, 156–158, 169, 174
STAR	signal targeting with alternating radio frequency 15, 18
sTGV	spatial total generalized variation 156, 157, 160, 168–171
SVD	singular value decomposition 155
TE	echo time 68, 117, 125, 139
TF	turbo factor 125, 139, 153
TGV	total generalized variation xxi, xxvi, xxvii, xxix, 2, 56, 60, 61, 64, 65, 70, 71, 74, 75, 80, 81, 83, 84, 87–89, 93, 94, 96, 97, 100, 107, 110, 113, 114, 122, 128, 134, 149, 151, 152, 156–161, 163–171, 173–176, 210, 212, 215
TI	inversion time 9, 68, 88, 117, 125, 139
TI1	bolus or labeling duration 68, 117
TILT	transfer insensitive labeling technique 15
ToF	time of flight 95, 125
TR	repetition time 53, 68, 117, 125, 139, 145, 146
TSE	turbo spin echo 148, 149
TSNR	temporal signal to noise ratio xix, xxvi, 33, 35, 149, 156, 159, 160, 168–172, 180
TV	total variation 59–61
UNFAIR	un-inverted flow-sensitive alternating inversion recovery 15
VE-ASL	vessel encoded arterial spin labeling 43
VSASL	velocity selective arterial spin labeling 40–42, 179
WHO	World Health Organization 1
WM	white matter xix, xxi, xxiii, xxiv, xxvi, xxvii, 6, 34, 47, 53, 68, 69, 75, 79, 82, 87, 95, 98, 100, 107–110, 117, 125–127, 129, 131, 132, 134, 153, 154, 156, 157, 159, 160, 162–164, 166, 168, 170, 171

WS	workstation xxiv, 139, 140
XeCT	xenon-enhanced computed tomography 8

B

List of Publications

Journal Publications

S. M. Spann, K. S. Kazimierski, C. S. Aigner, M. Kraiger, K. Bredies, and R. Stollberger. Spatio-temporal TGV denoising for ASL perfusion imaging. *NeuroImage*, 157:81–96, aug 2017, doi: 10.1016/j.neuroimage.2017.05.054

S. M. Spann, X. Shao, D. J. Wang, C. S. Aigner, M. Schloegl, K. Bredies, and R. Stollberger. Robust single-shot acquisition of high resolution whole brain ASL images by combining time-dependent 2D CAPIRINHA sampling with spatio-temporal TGV reconstruction. *NeuroImage*, page 116337, nov 2019, doi: 10.1016/J.NEUROIMAGE.2019.116337

D. Grössinger, S. E. Kober, S. M. Spann, R. Stollberger, and G. Wood. Real-Time Functional Magnetic Resonance Imaging as a Tool for Neurofeedback. *Lernen und Lernstörungen*, pages 1–12, apr 2020, doi: 10.1024/2235-0977/a000300

O. Maier, S. M. Spann, D. Pinter, T. Gattringer, N. Hinteregger, C. Enzinger, J. Pfeuffer, K. Bredies, and R. Stollberger. Non-linear fitting with joint spatial regularization in Arterial Spin Labeling. *submitted to Medical Image Analysis*

Magazine Publications

S. M. Spann. New Horizons for Arterial Spin Labeling. *TU Graz research*, pages 27–29, 2020

Conference Proceedings

S. M. Spann, D. Grössinger, C. S. Aigner, J. Pfeuffer, G. Wood, and R. Stollberger. Self-Regulation of Brain Functions using Real-Time Neurofeedback Functional Arterial Spin Labeling. In *Proceedings of the 28th Annual Meeting of ISMRM*, 2020

O. Maier, S. M. Spann, L. Bogensperger, and R. Stollberger. Fast Simultaneous Multi-Slice Multi-Shell Diffusion Tensor Imaging with Model-based Reconstruction. In *Proceedings of the 28th Annual Meeting of ISMRM*, 2020

O. Maier, S. M. Spann, D. Pinter, T. Gattringer, L. Pirpamer, C. Enzinger, J. Pfeuffer, and R. Stollberger. Robust Perfusion Parameter Quantification from 3D Single- Shot Multi-Delay ASL measurements. In *Proceedings of the 28th Annual Meeting of ISMRM*, 2020

X. Shao, S. M. Spann, K. Wang, L. Yan, R. Stollberger, and D. J. Wang. High-resolution whole brain ASL perfusion imaging at 7T with 12-fold acceleration and spatial-temporal regularized reconstruction. In *Proceedings of the 28th Annual Meeting of ISMRM*, 2020

M. A. Schwarzbach, S. M. Spann, C. S. Aigner, K. Hammernik, T. Pock, and R. Stollberger. Combining Variational Optimization and Deep Learning for efficient ASL image quality enhancement. In *Magnetic Resonance Materials in Physics, Biology and Medicine*, Rotterdam, 2019

S. M. Spann, X. Shao, D. J. Wang, C. S. Aigner, M. Schloegl, K. Bredies, and R. Stollberger. Improving temporal resolution of 3D Arterial Spin Labeling perfusion imaging by combining CAIPIRINHA encoding and spatio-temporal TGV reconstruction. In *Proceedings of the 27th Annual Meeting of ISMRM*, Montreal, 2019

A. Lesch, C. S. Aigner, S. M. Spann, M. Schloegl, and R. Stollberger. 3D Bloch-Siegert EPI B1+-mapping. In *Proceedings of the 27th Annual Meeting of ISMRM*, Montreal, 2019

S. M. Spann, M. Schloegl, C. S. Aigner, K. Koschutnig, M. Holler, K. Bredies, and R. Stollberger. Improved functional Arterial Spin Labeling by spatio-temporal ICTGV denoising. In *Proceedings of the 26th Annual Meeting of ISMRM*, Paris, 2018

S. M. Spann, C. S. Aigner, M. Schloegl, A. Lesch, K. Bredies, S. Ropele, D. Pinter, L. Pirpamer, and R. Stollberger. Acceleration of ASL data acquisition using spatio-temporal TGV Reconstruction. In *Proceedings of the 26th Annual Meeting of*

ISMRM, Paris, 2018

S. M. Spann, K. S. Kazimierski, C. S. Aigner, and R. Stollberger. A denoising method for arterial spin labeling data based on total generalized variation (TGV) with a spatial varying regularization parameter. In *Proceedings of the 25th Annual Meeting of ISMRM*, Honolulu, 2017

M. Schloegl, S. M. Spann, C. S. Aigner, M. Holler, K. Bredies, and R. Stollberger. Improved Denoising of Dynamic Arterial Spin Labeling with Infimal Convolution of Total Generalized Variation. In *Proceedings of the 25th Annual Meeting of ISMRM*, Honolulu, 2017

S. M. Spann, C. S. Aigner, K. S. Kazimierski, M. Kraiger, and R. Stollberger. Total generalized variation (TGV) for spatio-temporal denoising of high resolution ASL perfusion data. In *Magnetic Resonance Materials in Physics, Biology and Medicine*, Vienna, 2016

S. M. Spann, K. S. Kazimierski, C. S. Aigner, M. Kraiger, and R. Stollberger. Influence of denoising techniques on the absolute CBF quantification of ASL perfusion data. In *BMT 2016 "Dreilaendertagung" Swiss, Austrian and German Societies of Biomedical Engineerin*, Basel, 2016

S. M. Spann, K. S. Kazimierski, C. S. Aigner, M. Kraiger, and R. Stollberger. Total generalized variation (TGV) for spatio-temporal denoising of high resolution ASL perfusion data. In *Imaging with Modulated/Incomplete Data 2016*, Graz, 2016

Oral Presentations

S. M. Spann, D. Grössinger, C. S. Aigner, J. Pfeuffer, G. Wood, and R. Stollberger. Self-Regulation of Brain Functions using Real-Time Neurofeedback Functional Arterial Spin Labeling. In *Proceedings of the 28th Annual Meeting of ISMRM*, 2020

S. M. Spann. New Horizons for Arterial Spin Labeling - MRI Encoding Meets Information Technology. In *4th Human- and Biotechnology FoE Day*, Graz, Austria, 2019

S. M. Spann. Robust 3D Brain Perfusion Imaging using Arterial Spin Labeling. In *INGE ST Netzwerktreffen*, Graz, Austria, 2019

S. M. Spann, X. Shao, D. J. Wang, C. S. Aigner, M. Schloegl, K. Bredies, and R. Stollberger. Improving temporal resolution of 3D Arterial Spin Labeling perfusion imaging by combining CAIPIRINHA encoding and spatio-temporal TGV reconstruction. In *Proceedings of the 27th Annual Meeting of ISMRM*, Montreal, 2019

S. M. Spann. Spatio-Temporal TGV denoising for ASL perfusion imaging. In *INGE ST Forschungspreisverleihung*, Graz, Austria, 2018

S. M. Spann, C. S. Aigner, M. Schloegl, A. Lesch, K. Bredies, S. Ropele, D. Pinter, L. Pirpamer, and R. Stollberger. Acceleration of ASL data acquisition using spatio-temporal TGV Reconstruction. In *Proceedings of the 26th Annual Meeting of ISMRM*, Paris, 2018

S. M. Spann, K. S. Kazimierski, C. S. Aigner, and R. Stollberger. Variational Denoising for Arterial Spin Labeling. In *SFB Statusseminar*, Admont, Austria, 2016

S. M. Spann, C. S. Aigner, K. S. Kazimierski, M. Kraiger, and R. Stollberger. Total generalized variation (TGV) for spatio-temporal denoising of high resolution ASL perfusion data. In *Magnetic Resonance Materials in Physics, Biology and Medicine*, Vienna, 2016

Prices and Awards

ISMRM Magna Cum Laude Merit Award
in the category "Perfusion and Permeability"
ISMRM 2020 Virtual Meeting

ISMRM Magna Cum Laude Merit Award
in the category "Perfusion and Permeability"
ISMRM 2019 in Paris, France

ISMRM Summa Cum Laude Merit Award
in the category "Perfusion and Permeability"
ISMRM 2018 in Paris, France

ISMRM Magna Cum Laude Merit Award
in the category "Perfusion and Permeability"
ISMRM 2018 in Paris, France

INGE-St. Research Price

1. Place in the category "Publications"
Graz 2018, Austria

C

Appendix

C.1 Definitions

Throughout this chapter we denote by N_x, N_y and N_z the image space dimensions, and by N_t the number of time frames.

C.1.1 Discrete Forward Differences

2D Discrete Forward Differences

The discrete forward differences for an image $u \in \Re^{N_x \times N_y}$ with Dirichlet boundary conditions are given by:

$$
\begin{aligned}
\left(\partial_x^+ u\right)_{i,j} &= \begin{cases} \frac{u_{i+1,j} - u_{i,j}}{h_x} & 1 \leq i < N_x, \\ 0 & i = N_x, \end{cases} \\
\left(\partial_y^+ u\right)_{i,j} &= \begin{cases} \frac{u_{i,j+1} - u_{i,j}}{h_y} & 1 \leq j < N_y, \\ 0 & j = N_y, \end{cases}
\end{aligned}
\tag{C.1}
$$

where h_x and h_y are the grid size of the image.

3D Discrete Forward Differences

The discrete forward differences for a volume $u \in \Re^{N_x \times N_y \times N_z}$ with Dirichlet boundary conditions are given by:

$$
\begin{aligned}
\left(\partial_x^+ u\right)_{i,j,k} &= \begin{cases} \frac{u_{i+1,j,k}-u_{i,j,k}}{h_x} & 1 \leq i < N_x, \\ 0 & i = N_x, \end{cases} \\
\left(\partial_y^+ u\right)_{i,j,k} &= \begin{cases} \frac{u_{i,j+1,k}-u_{i,j,k}}{h_y} & 1 \leq j < N_y, \\ 0 & j = N_y, \end{cases} \\
\left(\partial_z^+ u\right)_{i,j,k} &= \begin{cases} \frac{u_{i,j,k+1}-u_{i,j,k}}{h_z} & 1 \leq k < N_z, \\ 0 & k = N_z, \end{cases}
\end{aligned}
\tag{C.2}
$$

where h_x, h_y and h_z are the grid size of the volume.

4D Discrete Forward Differences

The discrete forward differences for a volume time series $u \in \Re^{N_x \times N_y \times N_z \times N_t}$ with Dirichlet boundary conditions are given by:

$$
\begin{aligned}
\left(\partial_x^+ u\right)_{i,j,k,t} &= \begin{cases} \frac{u_{i+1,j,k,t}-u_{i,j,k,t}}{h_x} & 1 \leq i < N_x, \\ 0 & i = N_x, \end{cases} \\
\left(\partial_y^+ u\right)_{i,j,k,t} &= \begin{cases} \frac{u_{i,j+1,k,t}-u_{i,j,k,t}}{h_y} & 1 \leq j < N_y, \\ 0 & j = N_y, \end{cases} \\
\left(\partial_z^+ u\right)_{i,j,k,t} &= \begin{cases} \frac{u_{i,j,k+1,t}-u_{i,j,k,t}}{h_z} & 1 \leq k < N_z, \\ 0 & k = N_z, \end{cases} \\
\left(\partial_t^+ u\right)_{i,j,k,t} &= \begin{cases} \frac{u_{i,j,k,t+1}-u_{i,j,k,t}}{h_t} & 1 \leq t < N_t, \\ 0 & t = N_t, \end{cases}
\end{aligned}
\tag{C.3}
$$

where h_x, h_y and h_z are the grid size of the volume and h_t is the grid size of the time domain.

C.1.2 Adjoint of Discrete Forward Differences

Adjoint of 2D Discrete Forward Differences

The adjoint of 2D discrete forward differences for an image $u \in \Re^{N_x \times N_y}$ with Dirichlet boundary conditions are given by:

$$\begin{aligned}
\left(\partial_x^{*+}u\right)_{i,j} &= \begin{cases} \frac{-u_{i,j}}{h_x} & i=1, \\ \frac{u_{i-1,j}-u_{i,j}}{h_x} & 1<i<N_x, \\ \frac{u_{i-1,j}}{h_x} & i=N_x, \end{cases} \\
\left(\partial_y^{*+}u\right)_{i,j} &= \begin{cases} \frac{-u_{i,j}}{h_y} & j=1, \\ \frac{u_{i,j-1}-u_{i,j}}{h_y} & 1<j<N_y, \\ \frac{u_{i,j-1}}{h_y} & j=N_y, \end{cases}
\end{aligned} \tag{C.4}$$

where h_x and h_y are the grid size of the image.

Adjoint of 3D Discrete Forward Differences

The adjoint of 3D discrete forward differences for a volume $u \in \Re^{N_x \times N_y \times N_z}$ with Dirichlet boundary conditions are given by:

$$\begin{aligned}
\left(\partial_x^{*+}u\right)_{i,j,k} &= \begin{cases} \frac{-u_{i,j,k}}{h_x} & i=1, \\ \frac{u_{i-1,j,k}-u_{i,j,k}}{h_x} & 1<i<N_x, \\ \frac{u_{i-1,j,k}}{h_x} & i=N_x, \end{cases} \\
\left(\partial_y^{*+}u\right)_{i,j,k} &= \begin{cases} \frac{-u_{i,j,k}}{h_y} & j=1, \\ \frac{u_{i,j-1,k}-u_{i,j,k}}{h_y} & 1<j<N_y, \\ \frac{u_{i,j-1,k}}{h_y} & j=N_y, \end{cases} \\
\left(\partial_z^{*+}u\right)_{i,j,k} &= \begin{cases} \frac{-u_{i,j,k}}{h_z} & k=1, \\ \frac{u_{i,j,k-1}-u_{i,j,k}}{h_z} & 1<k<N_z, \\ \frac{u_{i,j,k-1}}{h_z} & k=N_z, \end{cases}
\end{aligned} \tag{C.5}$$

where h_x, h_y and h_z are the grid size of the volume.

Adjoint of 4D Discrete Forward Differences

The adjoint of 4D discrete forward differences for a volume time series $u \in \Re^{N_x \times N_y \times N_z \times N_t}$ with Dirichlet boundary conditions are given by:

$$
\begin{aligned}
\left(\partial_x^{*+} u\right)_{i,j,k} &= \begin{cases} \frac{-u_{i,j,k,t}}{h_x} & i = 1, \\ \frac{u_{i-1,j,k,t} - u_{i,j,k,t}}{h_x} & 1 < i < N_x, \\ \frac{u_{i-1,j,k,t}}{h_x} & i = N_x, \end{cases} \\
\left(\partial_y^{*+} u\right)_{i,j,k} &= \begin{cases} \frac{-u_{i,j,k,t}}{h_y} & j = 1, \\ \frac{u_{i,j-1k,t} - u_{i,j,k,t}}{h_y} & 1 < j < N_y, \\ \frac{u_{i,j-1,k,t}}{h_y} & j = N_y, \end{cases} \\
\left(\partial_z^{*+} u\right)_{i,j,k,t} &= \begin{cases} \frac{-u_{i,j,k,t}}{h_z} & k = 1, \\ \frac{u_{i,j,k-1,t} - u_{i,j,k,t}}{h_z} & 1 < k < N_z, \\ \frac{u_{i,j,k-1,t}}{h_z} & k = N_z, \end{cases} \\
\left(\partial_t^{*+} u\right)_{i,j,k,t} &= \begin{cases} \frac{-u_{i,j,k,t}}{h_t} & t = 1, \\ \frac{u_{i,j,k,t-1} - u_{i,j,k,t}}{h_t} & 1 < t < N_t, \\ \frac{u_{i,j,k,t-1}}{h_t} & t = N_t, \end{cases}
\end{aligned}
\tag{C.6}
$$

where h_x, h_y and h_z are the grid size of the volume and h_t is the grid size of the time domain.

C.1.3 Discrete Backward Differences

2D Discrete Backward Differences

The discrete backward differences for an image $u \in \Re^{N_x \times N_y}$ with Dirichlet boundary conditions are given by:

$$
\begin{aligned}
\left(\partial_x^{-} u\right)_{i,j} &= \begin{cases} \frac{u_{i,j} - u_{i-1,j}}{h_x} & 1 < i \leq N_x, \\ 0 & i = 1, \end{cases} \\
\left(\partial_y^{-} u\right)_{i,j} &= \begin{cases} \frac{u_{i,j} - u_{i,j-1}}{h_y} & 1 < j \leq N_y, \\ 0 & j = 1, \end{cases}
\end{aligned}
\tag{C.7}
$$

where h_x and h_y are the grid size of the image.

3D Discrete Backward Differences

The discrete backward differences for a volume $u \in \Re^{N_x \times N_y \times N_z}$ with Dirichlet boundary conditions are given by:

$$
\begin{aligned}
\left(\partial_x^- u\right)_{i,j,k} &= \begin{cases} \frac{u_{i,j,k}-u_{i-1,j,k}}{h_x} & 1 < i \leq N_x, \\ 0 & i = 1, \end{cases} \\
\left(\partial_y^- u\right)_{i,j,k} &= \begin{cases} \frac{u_{i,j,k}-u_{i,j-1,k}}{h_y} & 1 < j \leq N_y, \\ 0 & j = 1, \end{cases} \\
\left(\partial_z^- u\right)_{i,j,k} &= \begin{cases} \frac{u_{i,j,k}-u_{i,j,k-1}}{h_z} & 1 < k \leq N_z, \\ 0 & k = 1, \end{cases}
\end{aligned}
\tag{C.8}
$$

where h_x, h_y and h_z are the grid size of the volume.

4D Discrete Backward Differences

The discrete backward differences for a volume time series $u \in \Re^{N_x \times N_y \times N_z \times N_t}$ with Dirichlet boundary conditions are given by:

$$
\begin{aligned}
\left(\partial_x^- u\right)_{i,j,k,t} &= \begin{cases} \frac{u_{i,j,k,t}-u_{i-1,j,k,t}}{h_x} & 1 < i \leq N_x, \\ 0 & i = 1, \end{cases} \\
\left(\partial_y^- u\right)_{i,j,k,t} &= \begin{cases} \frac{u_{i,j,k,t}-u_{i,j-1,k,t}}{h_y} & 1 < j \leq N_y, \\ 0 & j = 1, \end{cases} \\
\left(\partial_z^- u\right)_{i,j,k,t} &= \begin{cases} \frac{u_{i,j,k,t}-u_{i,j,k-1,t}}{h_z} & 1 < k \leq N_z, \\ 0 & k = 1, \end{cases} \\
\left(\partial_t^- u\right)_{i,j,k,t} &= \begin{cases} \frac{u_{i,j,k,t}-u_{i,j,k,t-1}}{h_t} & 1 < t \leq N_t, \\ 0 & t = 1, \end{cases}
\end{aligned}
\tag{C.9}
$$

where h_x, h_y and h_z are the grid size of the volume and h_t is the grid size of the time domain.

C.1.4 Adjoint of Discrete Backward Differences

Adjoint of 2D Discrete Backward Differences

The adjoint of discrete backward differences for an image $u \in \Re^{N_x \times N_y}$ with Dirichlet boundary conditions are given by:

$$\begin{aligned}
\left(\partial_x^{*-} u\right)_{i,j} &= \begin{cases} \frac{-u_{i+1,j}}{h_x} & i = 1, \\ \frac{u_{i,j} - u_{i+1,j}}{h_x} & 1 < i < N_x, \\ \frac{u_{i,j}}{h_x} & i = N_x, \end{cases} \\
\left(\partial_y^{*-} u\right)_{i,j} &= \begin{cases} \frac{-u_{i,j+1}}{h_y} & j = 1, \\ \frac{u_{i,j} - u_{i,j+1}}{h_y} & 1 < j < N_y, \\ \frac{u_{i,j}}{h_y} & j = N_y, \end{cases}
\end{aligned} \tag{C.10}$$

where h_x and h_y are the grid size of the image.

Adjoint 3D Discrete Backward Differences

The adjoint of discrete backward differences for a volume $u \in \Re^{N_x \times N_y \times N_z}$ with Dirichlet boundary conditions are given by:

$$\begin{aligned}
\left(\partial_x^{*-} u\right)_{i,j,k} &= \begin{cases} \frac{-u_{i+1,j,k}}{h_x} & i = 1, \\ \frac{u_{i,j,k} - u_{i+1,j,k}}{h_x} & 1 < i < N_x, \\ \frac{u_{i,j,k}}{h_x} & i = N_x, \end{cases} \\
\left(\partial_y^{*-} u\right)_{i,j,k} &= \begin{cases} \frac{-u_{i,j+1,k}}{h_y} & j = 1, \\ \frac{u_{i,j,k} - u_{i,j+1,k}}{h_y} & 1 < j < N_y, \\ \frac{u_{i,j,k}}{h_y} & j = N_y, \end{cases} \\
\left(\partial_z^{*-} u\right)_{i,j,k} &= \begin{cases} \frac{-u_{i,j,k+1}}{h_z} & k = 1, \\ \frac{u_{i,j,k} - u_{i,j,k+1}}{h_z} & 1 < k < N_z, \\ \frac{u_{i,j,k}}{h_z} & k = N_z, \end{cases}
\end{aligned} \tag{C.11}$$

where h_x, h_y and h_z are the grid size of the volume.

Adjoint 4D Discrete Backward Differences

The adjoint of discrete backward differences for a volume time series $u \in \Re^{N_x \times N_y \times N_z \times N_t}$ with Dirichlet boundary conditions are given by:

$$
\begin{aligned}
\left(\partial_x^{*-} u\right)_{i,j,k,t} &= \begin{cases} \frac{-u_{i+1,j,k,t}}{h_x} & i = 1, \\ \frac{u_{i,j,k,t} - u_{i+1,j,k,t}}{h_x} & 1 < i < N_x, \\ \frac{u_{i,j,k,t}}{h_x} & i = N_x, \end{cases} \\
\left(\partial_y^{*-} u\right)_{i,j,k,t} &= \begin{cases} \frac{-u_{i,j+1,k,t}}{h_y} & j = 1, \\ \frac{u_{i,j,k,t} - u_{i,j+1,k,t}}{h_y} & 1 < j < N_y, \\ \frac{u_{i,j,k,t}}{h_y} & j = N_y, \end{cases} \\
\left(\partial_z^{*-} u\right)_{i,j,k,t} &= \begin{cases} \frac{-u_{i,j,k+1,t}}{h_z} & k = 1, \\ \frac{u_{i,j,k,t} - u_{i,j,k+1,t}}{h_z} & 1 < k < N_z, \\ \frac{u_{i,j,k,t}}{h_z} & k = N_z, \end{cases} \\
\left(\partial_t^{*-} u\right)_{i,j,k,t} &= \begin{cases} \frac{-u_{i,j,k,t+1}}{h_t} & t = 1, \\ \frac{u_{i,j,k,t} - u_{i,j,k,t+1}}{h_t} & 1 < t < N_t, \\ \frac{u_{i,j,k,t}}{h_t} & t = N_t, \end{cases}
\end{aligned}
\tag{C.12}
$$

where h_x, h_y and h_z are the grid size of the volume and h_t is the grid size of the time domain.

C.1.5 Discrete Gradient Operator

2D Discrete Gradient Operator

The discrete gradient operator for a given image $u \in \Re^{N_x \times N_y}$ is a mapping $\nabla : u \to v$, where $v \in \Re^{N_x \times N_y \times 2}$, defined as

$$
(\nabla u)_{i,j} = \begin{pmatrix} (\partial_x^+ u)_{i,j} \\ \left(\partial_y^+ u\right)_{i,j} \end{pmatrix} = \begin{pmatrix} v^1 \\ v^2 \end{pmatrix}. \tag{C.13}
$$

3D Discrete Gradient Operator

The discrete gradient operator for a given volume $u \in \Re^{N_x \times N_y \times N_z}$ is a mapping $\nabla : u \to v$, where $v \in \Re^{N_x \times N_y \times N_z \times 3}$, defined as

$$
(\nabla u)_{i,j,k} = \begin{pmatrix} (\partial_x^+ u)_{i,j,k} \\ \left(\partial_y^+ u\right)_{i,j,k} \\ (\partial_z^+ u)_{i,j,k} \end{pmatrix} = \begin{pmatrix} v^1 \\ v^2 \\ v^3 \end{pmatrix}. \tag{C.14}
$$

4D Discrete Gradient Operator

The discrete gradient operator for a given volume time series $u \in \Re^{N_x \times N_y \times N_z \times N_t}$ is a mapping $\nabla : u \to v$, where $v \in \Re^{N_x \times N_y \times N_z \times N_t \times 4}$, defined as

$$(\nabla_\beta u)_{i,j,k,t} = \begin{pmatrix} (\beta_1 \partial_x^+ u)_{i,j,k,t} \\ \left(\beta_1 \partial_y^+ u\right)_{i,j,k,t} \\ (\beta_1 \partial_z^+ u)_{i,j,k,t} \\ \left(\beta_2 \partial_t^+ u\right)_{i,j,k,t} \end{pmatrix} = \begin{pmatrix} v^1 \\ v^2 \\ v^3 \\ v^4 \end{pmatrix}. \tag{C.15}$$

The additional parameter $\beta = \beta_1/\beta_2$ defines the relation between temporal and spatial grid size.

C.1.6 Discrete Symmetrized Gradient Operator

2D Discrete Symmetrized Gradient Operator

The discrete symmetrized gradient operator for a given vector $v \in \Re^{N_x \times N_y \times 2}$ is a mapping $\epsilon : v \to w$, where $w \in \Re^{N_x \times N_y \times 4}$, defined as

$$\begin{aligned}(\epsilon v)_{i,j} &= \frac{1}{2}\left((\nabla v)_{i,j} + (\nabla v)_{i,j}^T\right) = \\ &= \begin{pmatrix} \left(\partial_x^- v^1\right)_{i,j} & \frac{1}{2}\left(\left(\partial_x^- v^2\right)_{i,j} + \left(\partial_y^- v^1\right)_{i,j}\right) \\ \frac{1}{2}\left(\left(\partial_x^- v^2\right)_{i,j} + \left(\partial_y^- v^1\right)_{i,j}\right) & \left(\partial_y^- v^2\right)_{i,j} \end{pmatrix} = \\ &= \begin{pmatrix} w^1 & w^2 \\ w^3 & w^4 \end{pmatrix}.\end{aligned} \tag{C.16}$$

Since $w^2 = w^3$ equation C.16 can be rearranged:

$$(\epsilon v)_{i,j} = \begin{pmatrix} \left(\partial_x^- v^1\right)_{i,j} \\ \frac{1}{2}\left(\left(\partial_x^- v^2\right)_{i,j} + \left(\partial_y^- v^1\right)_{i,j}\right) \\ \left(\partial_y^- v^2\right)_{i,j} \end{pmatrix} = \begin{pmatrix} w^1 \\ w^2 \\ w^3 \end{pmatrix}. \tag{C.17}$$

3D Discrete Symmetrized Gradient Operator

The discrete symmetrized gradient operator for a given vector $v \in \Re^{N_x \times N_y \times N_z \times 3}$ is a mapping $\epsilon : v \to w$, where $w \in \Re^{N_x \times N_y \times N_z \times 6}$, defined as

$$\begin{aligned}(\epsilon v)_{i,j,k} &= \frac{1}{2}\left((\nabla v)_{i,j,k} + (\nabla v)_{i,j,k}^T\right) = \\ &= \begin{pmatrix} \left(\partial_x^- v^1\right)_{i,j,k} \\ \left(\partial_y^- v^2\right)_{i,j,k} \\ \left(\partial_z^- v^3\right)_{i,j,k} \\ \frac{1}{2}\left(\left(\partial_x^- v^2\right)_{i,j,k} + \left(\partial_y^- v^1\right)_{i,j,k}\right) \\ \frac{1}{2}\left(\left(\partial_x^- v^3\right)_{i,j,k} + \left(\partial_z^- v^1\right)_{i,j,k}\right) \\ \frac{1}{2}\left(\left(\partial_y^- v^3\right)_{i,j,k} + \left(\partial_z^- v^2\right)_{i,j,k}\right) \end{pmatrix} = \begin{pmatrix} w^1 \\ w^2 \\ w^3 \\ w^4 \\ w^5 \\ w^6 \end{pmatrix}.\end{aligned} \tag{C.18}$$

4D Discrete Symmetrized Gradient Operator

The discrete symmetrized gradient operator for a given vector $v \in \Re^{N_x \times N_y \times N_z \times N_t \times 4}$ is a mapping $\epsilon : v \to w$, where $w \in \Re^{N_x \times N_y \times N_z \times N_t \times 10}$, defined as

$$(\epsilon_\beta v)_{i,j,k,t} = \frac{1}{2}\left((\nabla v)_{i,j,k,t} + (\nabla v)^T_{i,j,k,t}\right) =$$
$$= \begin{pmatrix} \left(\beta_1 \partial_x^- v^1\right)_{i,j,k,t} \\ \left(\beta_1 \partial_y^- v^2\right)_{i,j,k,t} \\ \left(\beta_1 \partial_z^- v^3\right)_{i,j,k,t} \\ \left(\beta_2 \partial_t^- v^4\right)_{i,j,k,t} \\ \frac{1}{2}\left(\left(\beta_1 \partial_x^- v^2\right)_{i,j,k,t} + \left(\beta_1 \partial_y^- v^1\right)_{i,j,k,t}\right) \\ \frac{1}{2}\left(\left(\beta_1 \partial_x^- v^3\right)_{i,j,k,t} + \left(\beta_1 \partial_z^- v^1\right)_{i,j,k,t}\right) \\ \frac{1}{2}\left(\left(\beta_1 \partial_x^- v^4\right)_{i,j,k,t} + \left(\beta_2 \partial_t^- v^1\right)_{i,j,k,t}\right) \\ \frac{1}{2}\left(\left(\beta_1 \partial_y^- v^3\right)_{i,j,k,t} + \left(\beta_1 \partial_z^- v^2\right)_{i,j,k,t}\right) \\ \frac{1}{2}\left(\left(\beta_1 \partial_y^- v^4\right)_{i,j,k,t} + \left(\beta_2 \partial_t^- v^2\right)_{i,j,k,t}\right) \\ \frac{1}{2}\left(\left(\beta_1 \partial_z^- v^4\right)_{i,j,k,t} + \left(\beta_2 \partial_t^- v^3\right)_{i,j,k,t}\right) \end{pmatrix} = \begin{pmatrix} w^1 \\ w^2 \\ w^3 \\ w^4 \\ w^5 \\ w^6 \\ w^7 \\ w^8 \\ w^9 \\ w^{10} \end{pmatrix}. \tag{C.19}$$

C.1.7 Discrete Divergence Operator

2D Discrete Divergence Operator

The adjoint operation of the gradient operator is the negative divergence $\nabla^* = -\text{div}^1$. The 2D divergence operator ($\text{div}^1 : v \to u$) is defined as

$$\left(\text{div}^1 v\right)_{i,j} = \left(\left(\partial_x^{*+} v^1\right)_{i,j} + \left(\partial_y^{*+} v^2\right)_{i,j}\right), \tag{C.20}$$

with $v \in \Re^{N_x \times N_y \times 2}$ and $u \in \Re^{N_x \times N_y}$.

3D Discrete Divergence Operator

The adjoint operation of the gradient operator is the negative divergence $\nabla^* = -\text{div}^1$. The 3D divergence operator ($\text{div}^1 : v \to u$) is defined as

$$\left(\text{div}^1 v\right)_{i,j,k} = \left(\left(\partial_x^{*+} v^1\right)_{i,j,k} + \left(\partial_y^{*+} v^2\right)_{i,j,k} + \left(\partial_z^{*+} v^3\right)_{i,j,k}\right), \tag{C.21}$$

with $v \in \Re^{N_x \times N_y \times N_z \times 3}$ and $u \in \Re^{N_x \times N_y \times N_z}$.

4D Discrete Divergence Operator

The adjoint operation of the gradient operator is the negative divergence $\nabla^* = -\text{div}^1$. The 4D divergence operator ($\text{div}^1 : v \to u$) is defined as

$$\begin{aligned}\left(\mathrm{div}_\beta^1 v\right)_{i,j,k,t} = \Big(&\beta_1 \left(\partial_x^{*+} v^1\right)_{i,j,k,t} + \beta_1 \left(\partial_y^{*+} v^2\right)_{i,j,k,t} + \\ &\beta_1 \left(\partial_z^{*+} v^3\right)_{i,j,k,t} + \beta_2 \left(\partial_t^{*+} v^1\right)_{i,j,k,t}\Big),\end{aligned} \tag{C.22}$$

with $v \in \Re^{N_x \times N_y \times N_z \times N_t \times 4}$ and $u \in \Re^{N_x \times N_y \times N_z \times N_t}$. The additional parameter $\beta = \beta_1/\beta_2$ defines the relation between spatial and temporal grid size.

C.1.8 Discrete Symmetrized Divergence Operator

2D Discrete Symmetrized Divergence Operator

The discrete symmetrized divergence operator is chosen to be adjoint to the symmetrized gradient operator, that is $\epsilon^* = -\mathrm{div}^2$. The 2D symmetrized divergence operator ($\mathrm{div}^2 : w \to v$) is defined as

$$\left(\mathrm{div}^2 w\right)_{i,j} = \begin{pmatrix} \left(\partial_x^{*-} w_1\right)_{i,j} + \left(\partial_y^{*-} w_3\right)_{i,j} \\ \left(\partial_x^{*-} w_3\right)_{i,j} + \left(\partial_y^{*-} w_2\right)_{i,j} \end{pmatrix}, \tag{C.23}$$

with $w \in \Re^{N_x \times N_y \times 3}$ and $v \in \Re^{N_x \times N_y \times 2}$.

3D Discrete Symmetrized Divergence Operator

The discrete symmetrized divergence operator is chosen to be adjoint to the symmetrized gradient operator, that is $\epsilon^* = -\mathrm{div}^2$. The 3D symmetrized divergence operator ($\mathrm{div}^2 : w \to v$) is defined as

$$\left(\mathrm{div}^2 w\right)_{i,j,k} = \begin{pmatrix} \left(\partial_x^{*-} w_1\right)_{i,j,k} + \left(\partial_y^{*-} w_4\right)_{i,j,k} + \left(\partial_z^{*-} w_5\right)_{i,j,k} \\ \left(\partial_x^{*-} w_4\right)_{i,j,k} + \left(\partial_y^{*-} w_2\right)_{i,j,k} + \left(\partial_z^{*-} w_6\right)_{i,j,k} \\ \left(\partial_x^{*-} w_5\right)_{i,j,k} + \left(\partial_y^{*-} w_6\right)_{i,j,k} + \left(\partial_z^{*-} w_3\right)_{i,j,k} \end{pmatrix}, \tag{C.24}$$

with $w \in \Re^{N_x \times N_y \times N_z \times 6}$ and $v \in \Re^{N_x \times N_y \times N_z \times 3}$.

4D Discrete Symmetrized Divergence Operator

The discrete symmetrized divergence operator is chosen to be adjoint to the symmetrized gradient operator, that is $\epsilon^* = -\mathrm{div}^2$. The 4D symmetrized divergence operator ($\mathrm{div}^2 : w \to v$) is defined as

$$\left(\mathrm{div}_\beta^2 w\right)_{i,j,k,t} = \begin{pmatrix} \beta_1 \left(\partial_x^{*-} w_1\right)_{i,j,k,t} + \beta_1 \left(\partial_y^{*-} w_5\right)_{i,j,k,t} + \beta_1 \left(\partial_z^{*-} w_6\right)_{i,j,k,t} + \beta_2 \left(\partial_t^{*-} w_7\right)_{i,j,k,t} \\ \beta_1 \left(\partial_x^{*-} w_5\right)_{i,j,k,t} + \beta_1 \left(\partial_y^{*-} w_2\right)_{i,j,k,t} + \beta_1 \left(\partial_z^{*-} w_8\right)_{i,j,k,t} + \beta_2 \left(\partial_t^{*-} w_9\right)_{i,j,k,t} \\ \beta_1 \left(\partial_x^{*-} w_6\right)_{i,j,k,t} + \beta_1 \left(\partial_y^{*-} w_8\right)_{i,j,k,t} + \beta_1 \left(\partial_z^{*-} w_3\right)_{i,j,k,t} + \beta_2 \left(\partial_t^{*-} w_{10}\right)_{i,j,k,t} \\ \beta_1 \left(\partial_x^{*-} w_7\right)_{i,j,k,t} + \beta_1 \left(\partial_y^{*-} w_9\right)_{i,j,k,t} + \beta_1 \left(\partial_z^{*-} w_{10}\right)_{i,j,k,t} + \beta_2 \left(\partial_t^{*-} w_4\right)_{i,j,k,t} \end{pmatrix}, \tag{C.25}$$

with $w \in \Re^{N_x \times N_y \times N_z \times N_t \times 10}$ and $v \in \Re^{N_x \times N_y \times N_z \times N_t \times 4}$.

C.1.9 Indicator Function

The convex indicator function is defined as follows

$$I_{||\cdot||_\infty \leq 1}(y) = \begin{cases} 0 & ||y||_\infty \leq 1 \\ +\infty & ||y||_\infty > 1 \end{cases} \tag{C.26}$$

C.1.10 Convex Conjugate

The convex or Fenchel conjugate of a function $f : \Re^N \mapsto \Re$ is defined as

$$f^*(y) = \sup_x \langle x, y \rangle - f(x). \tag{C.27}$$

The Fenchel conjugate of any kind of norm $f(x) = ||\cdot||$ is given by the indicator function

$$f^*(y) = I_{||\cdot||_\infty \leq 1}(y), \tag{C.28}$$

and the Fenchel conjugate of a squared norm $f(x) = \frac{1}{2}||\cdot||^2$ is defined as

$$f^*(y) = \frac{1}{2}||y||_*^2, \tag{C.29}$$

where $||y||_*$ is the corresponding dual norm of $f(x)$.

C.1.11 Proximal Mapping

Given a convex function f, the proximal mapping of f is the operator given by

$$x^* = (I + \sigma f)^{-1}(\chi) = P_{\sigma,f}(\chi) = \arg\max_x \frac{1}{2}||x - \chi||_2^2 + \sigma f(x). \tag{C.30}$$

In this thesis several proximal mappings were used. For $f^*(y) = I_{||\cdot||_\infty \leq \alpha}(y)$ the proximal mapping is defined as

$$\begin{aligned} P_{\sigma f^*}(\chi) = P_\alpha(\chi) = & \arg\max_y \frac{1}{2}||y - \chi||_2^2 + I_{||\cdot||_\infty \leq 1}(y) = \\ & \frac{\chi}{\max\left(1, \frac{|\chi|}{\alpha}\right)}. \end{aligned} \tag{C.31}$$

The proximal mapping for $f^*(y) = \frac{1}{2\lambda}||y||_2^2$ is given by

$$\begin{aligned} P_{\lambda,\sigma f^*}(\chi) = P^2_{\lambda,\sigma}(\chi) = \; & \arg\max_y \frac{1}{2}\left|\left|y-\chi\right|\right|_2^2 + \frac{1}{2\lambda}\left|\left|y\right|\right|_2^2 = \\ & \frac{\chi}{1+\frac{\sigma}{\lambda}}. \end{aligned} \tag{C.32}$$

The proximal mapping for $f^*(y) = \frac{\lambda}{2}\left|\left|y-z\right|\right|_2^2$ is given by

$$\begin{aligned} P_{\lambda,\tau f^*}(\chi) = P^2_{\lambda,\tau}(\chi) = \; & \arg\max_y \frac{1}{2}\left|\left|y-\chi\right|\right|_2^2 + \frac{1}{2\lambda}\left|\left|y-z\right|\right|_2^2 = \\ & \frac{\chi+\lambda\tau z}{1+\tau\lambda}. \end{aligned} \tag{C.33}$$

The proximal mapping for $f^*(y) = \frac{\lambda}{2}\left|\left|\varsigma y-z\right|\right|_2^2$ is given by

$$\begin{aligned} P_{\lambda,\varsigma,\tau,f^*}(\chi) = P^2_{\lambda,\varsigma,\tau}(\chi) = \; & \arg\max_y \frac{1}{2}\left|\left|y-\chi\right|\right|_2^2 + \frac{1}{2\lambda}\left|\left|\varsigma y-z\right|\right|_2^2 = \\ & \frac{\chi+\lambda\tau\varsigma^* z}{1+\varsigma^*\varsigma\tau\lambda}. \end{aligned} \tag{C.34}$$

C.2 Algorithm

C.2.1 Variational Denoising - L^2 Norm

The total generalized variational denoising of a perfusion weighted image $dM \in \Re^{N_x \times N_y}$ is defined as

$$dM^* \in \arg\min_{dM} \frac{\lambda}{2}\left|\left|dM - d_{dM}\right|\right|_2^2 + TGV^2_{\alpha_1,\alpha_0}(dM) \ , \tag{C.35}$$

where $d_{dM} \in \Re^{N_x \times N_y}$ is the given noisy image. The full minimization problem reads as follows

$$\min_{dM,p_1} \frac{\lambda}{2}\left|\left|dM - d_{dM}\right|\right|_2^2 + \alpha_1\left|\left|\nabla dM - p_1\right|\right|_1 + \alpha_0\left|\left|\epsilon p_1\right|\right|_1 . \tag{C.36}$$

For solving this problem with the primal dual splitting algorithm, it has to be reformulated as a saddle point problem. This is achieved by calculating the convex conjugates of the functions using definition C.27 .

$$\begin{aligned} \min_{dM,p_1} \max_{p_2,p_3} \; & \frac{\lambda}{2}\left|\left|dM - d_{dM}\right|\right|_2^2 + \langle \nabla dM - p_1, p_2 \rangle - \\ & I_{\left|\left|\cdot\right|\right|_\infty \le \alpha_1\gamma_1}(p_2) + \langle \epsilon p_1, p_3 \rangle - I_{\left|\left|\cdot\right|\right|_\infty \le \alpha_0\gamma_1}(p_3) . \end{aligned} \tag{C.37}$$

The full iterative update scheme is given in algorithm 3.

```
Algorithm 3 Primal dual algorithm for TGV denoising using a $L^2$-norm data fidelity term
Input: $d_{dM}$
Output: $dM$
Initialize: $p_1^0$, $p_2^0$, $p_3^0$, $dM^0$, $\overline{dM}^0$, $\overline{p}_1^0$, choose $\tau$, $\sigma > 0$

for $n = 0$ until maxIter
    Dual Update:
    $p_2^{n+1} = P_{\alpha_1}\left(p_2^n + \sigma\left(\nabla\overline{dM}^n - \overline{p}_1^n\right)\right)$
    $p_3^{n+1} = P_{\alpha_0}\left(p_3^n + \sigma\epsilon\overline{p}_1^n\right)$
    Primal Update:
    $dM^{n+1} = P^2_{\lambda,\tau}\left(dM^n - \tau\left(\nabla^* p_2^{n+1}\right)\right)$
    $p_1^{n+1} = p_1^n - \tau\left(-p_2^{n+1} + \epsilon^* p_3^{n+1}\right)$
    Extrapolation step:
    $\overline{dM}^{n+1} = 2dM^{n+1} - dM^n$
    $\overline{p}_1^{n+1} = 2p_1^{n+1} - p_1^n$
```

C.2.2 Variational Denoising - L^1 Norm

The total generalized variational denoising of a perfusion weighted image $dM \in \Re^{N_x \times N_y}$ using the L^1-norm for the data-fidelity term is defined as

$$dM^* \in \underset{dM,p_1}{\arg\min}\ \lambda \left|\left|dM - d_{dM}\right|\right|_1 + \alpha_1 \left|\left|\nabla dM - p_1\right|\right|_1 + \alpha_0 \left|\left|\epsilon p_1\right|\right|_1, \tag{C.38}$$

where $d_{dM} \in \Re^{N_x \times N_y}$ is the given noisy image. The solution of this problem is given by the primal dual splitting problem. Therefore, the problem has to be reformulated as a convex-concave saddle point problem. This is achieved by using the definition of the Fenchel conjugate C.27 leading to

$$\begin{aligned}\min_{dM,p_1}\ \max_{dM_2,p_2,p_3}\ & \langle dM - d_{dM}, dM_2\rangle - I_{||\cdot||_\infty \leq \lambda}\left(dM_2\right) + \\ & \langle \nabla dM - p_1, p_2\rangle - I_{||\cdot||_\infty \leq \alpha_1\gamma_1}\left(p_2\right) + \\ & \langle \epsilon p_1, p_3\rangle - I_{||\cdot||_\infty \leq \alpha_0\gamma_1}\left(p_3\right).\end{aligned} \tag{C.39}$$

The implementation of the L^1-norm TGV denoising is given in algorithm 4.

Algorithm 4 Primal dual algorithm for TGV denoising using a L^1-norm data fidelity term

```
Input: $d_{dM}$
Output: $dM$
Initialize: $p_1^0$, $p_2^0$, $p_3^0$, $dM^0$, $dM_2^0$, $\overline{dM}^0$, $\overline{p}_1^0$, choose $\tau$, $\sigma > 0$

  for $n = 0$ until maxIter

    Dual Update:
    $dM_2^{n+1} = P_\lambda\left(dM_2^n + \sigma\overline{dM}^n\right)$
    $p_2^{n+1} = P_{\alpha_1}\left(p_2^n + \sigma\left(\nabla\overline{dM}^n - \overline{p}_1^n\right)\right)$
    $p_3^{n+1} = P_{\alpha_0}\left(p_3^n + \sigma\epsilon\overline{p}_1^n\right)$

    Primal Update:
    $dM^{n+1} = dM^n - \tau\left(dM_2^{n+1} + \nabla^* p_2^{n+1}\right)$
    $p_1^{n+1} = p_1^n - \tau\left(-p_2^{n+1} + \epsilon^* p_3^{n+1}\right)$

    Extrapolation step:
    $\overline{dM}^{n+1} = 2dM^{n+1} - dM^n$
    $\overline{p}_1^{n+1} = 2p_1^{n+1} - p_1^n$
```

C.2.3 Variational ASL Denoising Including Time Series Information - L^2 Norm

The total generalized variational denoising of a perfusion weighted image ($dM \in \Re^{N_x \times N_y}$) including temporal information in the L^2-norm data fidelity term is defined as

$$dM^* \in \underset{dM}{\arg\min}\ \frac{\lambda}{2}\left|\left|\varsigma dM - d_{dM}\right|\right|_2^2 + TGV_{\alpha_1,\alpha_0}^2\left(dM\right)\ , \tag{C.40}$$

where $d_{dM} \in \Re^{N_x \times N_y \times N_t}$ is the given noisy image time series. For solving this problem with the primal dual splitting algorithm, it has to be reformulated as a saddle point problem. This is achieved by calculating the convex conjugates of the functions using definition C.27 .

$$\begin{aligned} \min_{dM,p_1}\ \max_{p_2,p_3}\ & \frac{\lambda}{2}\left|\left|\varsigma dM - d_{dM}\right|\right|_2^2 + \left\langle \nabla dM - p_1, p_2\right\rangle - \\ & I_{\left|\left|\cdot\right|\right|_\infty \le \alpha_1\gamma_1}\left(p_2\right) + \left\langle \epsilon p_1, p_3\right\rangle - I_{\left|\left|\cdot\right|\right|_\infty \le \alpha_0\gamma_1}\left(p_3\right) \end{aligned} \tag{C.41}$$

The full iterative update scheme is given in algorithm 5.

Algorithm 5 Primal dual algorithm for TGV denoising including time series information in the L^2-norm data fidelity term

```
Input: $d_{dM}$
Output: $dM$
Initialize: $p_1^0$, $p_2^0$, $p_3^0$, $dM^0$, $\overline{dM}^0$, $\overline{p}_1^0$, choose $\tau$, $\sigma > 0$

  for $n = 0$ until maxIter

    Dual Update:
    $p_2^{n+1} = P_{\alpha_1}\left(p_2^n + \sigma\left(\nabla\overline{dM}^n - \overline{p}_1^n\right)\right)$
    $p_3^{n+1} = P_{\alpha_0}\left(p_3^n + \sigma\epsilon\overline{p}_1^n\right)$

    Primal Update:
    $dM^{n+1} = P^2_{\lambda,\varsigma,\tau}\left(dM^n - \tau\left(\nabla^* p_2^{n+1}\right)\right)$
    $p_1^{n+1} = p_1^n - \tau\left(-p_2^{n+1} + \epsilon^* p_3^{n+1}\right)$

    Extrapolation step:
    $\overline{dM}^{n+1} = 2dM^{n+1} - dM^n$
    $\overline{p}_1^{n+1} = 2p_1^{n+1} - p_1^n$
```

C.2.4 Variational ASL Denoising Including Time Series Information - L^1 Norm

The total generalized variational denoising of a perfusion weighted image ($dM \in \Re^{N_x \times N_y}$) including temporal information in the L^1-norm data fidelity term is defined as

$$dM^* \in \underset{dM,p_1}{\arg\min}\ \lambda \left|\left|\varsigma dM - d_{dM}\right|\right|_1 + \alpha_1 \left|\left|\nabla dM - p_1\right|\right|_1 + \alpha_0 \left|\left|\epsilon p_1\right|\right|_1 \tag{C.42}$$

where $d_{dM} \in \Re^{N_x \times N_y \times N_t}$ is the given noisy image time series. The solution of this problem is given by the primal dual splitting problem. Therefore, the problem has to be reformulated as a convex-concave saddle point problem. This is achieved by using the definition of the Fenchel conjugate C.27 leading to

$$\begin{aligned} \min_{dM,p_1} \ \max_{dM_2,p_2,p_3} \ & \langle \varsigma dM - d_{dM}, dM_2 \rangle - I_{||\cdot||_\infty \leq \lambda}\left(dM_2\right) + \\ & \langle \nabla dM - p_1, p_2 \rangle - I_{||\cdot||_\infty \leq \alpha_1\gamma_1}\left(p_2\right) + \\ & \langle \epsilon p_1, p_3 \rangle - I_{||\cdot||_\infty \leq \alpha_0\gamma_1}\left(p_3\right). \end{aligned} \tag{C.43}$$

The implementation of the full denoising problem is given in algorithm 6.

Algorithm 6 Primal dual algorithm for TGV denoising including time series information in the L^1-norm data fidelity term

```
Input: $d_{dM}$
Output: $dM$
Initialize: $p_1^0$, $p_2^0$, $p_3^0$, $dM^0$, $dM_2^0$, $\overline{dM}^0$, $\overline{p}_1^0$, choose $\tau$, $\sigma > 0$

for $n = 0$ until maxIter
    Dual Update:
    $dM_2^{n+1} = P_\lambda\left(dM_2^n + \sigma\varsigma\overline{dM}^n\right)$
    $p_2^{n+1} = P_{\alpha_1}\left(p_2^n + \sigma\left(\nabla\overline{dM}^n - \overline{p}_1^n\right)\right)$
    $p_3^{n+1} = P_{\alpha_0}\left(p_3^n + \sigma\epsilon\overline{p}_1^n\right)$

    Primal Update:
    $dM^{n+1} = dM^n - \tau\left(\varsigma^* dM_2^{n+1} + \nabla^* p_2^{n+1}\right)$
    $p_1^{n+1} = p_1^n - \tau\left(-p_2^{n+1} + \epsilon^* p_3^{n+1}\right)$

    Extrapolation step:
    $\overline{dM}^{n+1} = 2dM^{n+1} - dM^n$
    $\overline{p}_1^{n+1} = 2p_1^{n+1} - p_1^n$
```

C.2.5 Full Variational ASL Denoising Model - L^2 Norm

The full ASL-TGV denoising approach with L^2-norm for the data fidelity term is defined as

$$
\begin{aligned}
(c^*, l^*) \in \underset{c,l}{\arg\min}\ & \frac{\lambda}{2}\,||\varsigma c - d_c||_2^2 + \frac{\lambda}{2}\,||\varsigma l - d_l||_2^2 + \\
& \gamma_1(w)\,TGV^2_{\alpha_1,\alpha_0}(l) + \gamma_2(w)\,TGV^2_{\alpha_1,\alpha_0}(c - l)\,.
\end{aligned}
\tag{C.44}
$$

The solution of this problem is given by the primal dual splitting problem. Therefore, the problem has to be reformulated as a convex-concave saddle point problem. This is achieved by using the definition of the Fenchel conjugate C.27 leading to

$$
\begin{aligned}
\min_{c,l,p_1,q_1}\quad \max_{p_2,p_3,q_2,q_3}\ & \frac{\lambda}{2}\,||\varsigma c - d_c||_2^2 + \frac{\lambda}{2}\,||\varsigma l - d_l||_2^2 \\
& \langle\nabla(c - l) - p_1, p_2\rangle - I_{||\cdot||_\infty \le \alpha_1\gamma_2}(p_2) + \\
& \langle\epsilon p_1, p_3\rangle - I_{||\cdot||_\infty \le \alpha_0\gamma_2}(p_3) + \\
& \langle\nabla(l) - q_1, q_2\rangle - I_{||\cdot||_\infty \le \alpha_1\gamma_1}(q_2) + \\
& \langle\epsilon q_1, q_3\rangle - I_{||\cdot||_\infty \le \alpha_0\gamma_1}(q_3)\,.
\end{aligned}
\tag{C.45}
$$

The final update scheme for the primal dual algorithm of the saddle point problem C.45 is defined in Algorithm 7.

Algorithm 7 Primal Dual Algorithm for L^2 ASL-TGV denoising

```
Input: $d_c$, $d_l$
Output: $c$, $l$
Initialize: $p_1^0, p_2^0, p_3^0, q_1^0, q_2^0, q_3^0, c^0, l^0, \overline{c}^0, \overline{l}^0, \overline{p}_1^0, \overline{q}_1^0$, choose $\tau, \sigma > 0$
  for $n = 0$ until maxIter
    Dual Update:
    $p_2^{n+1} = P_{\alpha_1,\gamma_1}\left(p_2^n + \sigma\left(\nabla\overline{c}^n - \nabla\overline{l}^n - \overline{p}_1^n\right)\right)$
    $p_3^{n+1} = P_{\alpha_0,\gamma_1}\left(p_3^n + \sigma\epsilon\overline{p}_1^n\right)$
    $q_2^{n+1} = P_{\alpha_1,\gamma_2}\left(q_2^n + \sigma\left(\nabla\overline{l}^n - \overline{q}_1^n\right)\right)$
    $q_3^{n+1} = P_{\alpha_0,\gamma_2}\left(q_3^n + \sigma\epsilon\overline{q}_1^n\right)$
    Primal Update:
    $c^{n+1} = P^2_{\lambda,\varsigma,\tau}\left(c^n - \tau\left(\nabla^* p_2^{n+1} + \varsigma^* c_2^{n+1}\right)\right)$
    $l^{n+1} = P^2_{\lambda,\varsigma,\tau}\left(l^n - \tau\left(-\nabla^* p_2^{n+1} + \nabla^* q_2^{n+1} + \varsigma^* l_2^{n+1}\right)\right)$
    $p_1^{n+1} = p_1^n - \tau\left(-p_2^{n+1} + \epsilon^* p_3^{n+1}\right)$
    $q_1^{n+1} = q_1^n - \tau\left(-q_2^{n+1} + \epsilon^* q_3^{n+1}\right)$
    Extrapolation step:
    $\overline{c}^{n+1} = 2c^{n+1} - c^n$
    $\overline{l}^{n+1} = 2l^{n+1} - l^n$
    $\overline{p}_1^{n+1} = 2p_1^{n+1} - p_1^n$
    $\overline{q}_1^{n+1} = 2q_1^{n+1} - q_1^n$
```

C.2.6 Full Variational ASL Denoising Model - L^1 Norm

The full ASL-TGV denoising approach with L^1-norm for the data fidelity term is defined as

$$\begin{aligned}(c^*, l^*) \in \arg\min_{c,l} \frac{\lambda}{2} ||\varsigma c - d_c||_1 + \frac{\lambda}{2} ||\varsigma l - d_l||_1 + \\ \gamma_1 (w)\, TGV^2_{\alpha_1,\alpha_0} (l) + \gamma_2 (w)\, TGV^2_{\alpha_1,\alpha_0} (c - l) .\end{aligned} \tag{C.46}$$

The solution of this problem is given by the primal dual splitting problem. Therefore, the problem has to be reformulated as a convex-concave saddle point problem. This is achieved by using the definition of the Fenchel conjugate C.27 leading to

$$\begin{aligned}\min_{c,l,p_1,q_1} \quad \max_{c_2,l_2,p_2,p_3,q_2,q_3} &\langle \varsigma c - d_c, c_2 \rangle - I_{||\cdot||_\infty \leq \lambda} (c_2) + \langle \varsigma l - d_l, l_2 \rangle - I_{||\cdot||_\infty \leq \lambda} (l_2) + \\ &\langle \nabla (c - l) - p_1, p_2 \rangle - I_{||\cdot||_\infty \leq \alpha_1 \gamma_2} (p_2) + \\ &\langle \epsilon p_1, p_3 \rangle - I_{||\cdot||_\infty \leq \alpha_0 \gamma_2} (p_3) + \\ &\langle \nabla (l) - q_1, q_2 \rangle - I_{||\cdot||_\infty \leq \alpha_1 \gamma_1} (q_2) + \\ &\langle \epsilon q_1, q_3 \rangle - I_{||\cdot||_\infty \leq \alpha_0 \gamma_1} (q_3) .\end{aligned} \tag{C.47}$$

The final update scheme for the primal dual algorithm of the saddle point problem C.47 is defined in Algorithm 8.

Algorithm 8 Primal Dual Algorithm for L^1 ASL-TGV denoising

```
Input: $d_c$, $d_l$
Output: $c$, $l$
Initialize: $p_1^0$, $p_2^0$, $p_3^0$, $q_1^0$, $q_2^0$, $q_3^0$, $c^0$, $c_2^0$, $l^0$, $l_2^0$, $\bar{c}^0$, $\bar{l}^0$, $\bar{p}_1^0$, $\bar{q}_1^0$, choose $\tau$, $\sigma > 0$
  for $n = 0$ until maxIter
    Dual Update:
    $p_2^{n+1} = P_{\alpha_1,\gamma_1}\left(p_2^n + \sigma\left(\nabla\bar{c}^n - \nabla\bar{l}^n - \bar{p}_1^n\right)\right)$
    $p_3^{n+1} = P_{\alpha_0,\gamma_1}\left(p_3^n + \sigma\epsilon\bar{p}_1^n\right)$
    $q_2^{n+1} = P_{\alpha_1,\gamma_2}\left(q_2^n + \sigma\left(\nabla\bar{l}^n - \bar{q}_1^n\right)\right)$
    $q_3^{n+1} = P_{\alpha_0,\gamma_2}\left(q_3^n + \sigma\epsilon\bar{q}_1^n\right)$
    $c_2^{n+1} = P_\lambda\left(c_2^n + \sigma\left(\varsigma\bar{c}^n - d_c\right)\right)$
    $l_2^{n+1} = P_\lambda\left(l_2^n + \sigma\left(\varsigma\bar{l}^n - d_l\right)\right)$
    Primal Update:
    $c^{n+1} = c^n - \tau\left(\nabla^* p_2^{n+1} + \varsigma^* c_2^{n+1}\right)$
    $l^{n+1} = l^n - \tau\left(-\nabla^* p_2^{n+1} + \nabla^* q_2^{n+1} + \varsigma^* l_2^{n+1}\right)$
    $p_1^{n+1} = p_1^n - \tau\left(-p_2^{n+1} + \epsilon^* p_3^{n+1}\right)$
    $q_1^{n+1} = q_1^n - \tau\left(-q_2^{n+1} + \epsilon^* q_3^{n+1}\right)$
    Extrapolation step:
    $\bar{c}^{n+1} = 2c^{n+1} - c^n$
    $\bar{l}^{n+1} = 2l^{n+1} - l^n$
    $\bar{p}_1^{n+1} = 2p_1^{n+1} - p_1^n$
    $\bar{q}_1^{n+1} = 2q_1^{n+1} - q_1^n$
```

C.2.7 Spatial Adaptive Variational ASL Denoising - L^2 Norm

The variational denoising method for ASL imaging with spatial adaptive regularization maps is given by

$$\begin{aligned}(c^*, l^*) \in \underset{c,l}{\arg\min}\ & \frac{1}{2}\left|\left|\lambda_c\left(\varsigma c - d_c\right)\right|\right|_2^2 + \frac{1}{2}\left|\left|\lambda_l\left(\varsigma l - d_l\right)\right|\right|_2^2 + \\ & \gamma_1\left(w\right) TGV_{\alpha_1,\alpha_0}^2\left(l\right) + \gamma_2\left(w\right) TGV_{\alpha_1,\alpha_0}^2\left(c - l\right).\end{aligned} \tag{C.48}$$

The solution of this problem is given by the primal dual splitting problem. Therefore, the problem has to be reformulated as a convex-concave saddle point problem. This is achieved by using the definition of the Fenchel conjugate C.27 leading to

$$
\begin{aligned}
\min_{c,l,p_1,q_1} \quad \max_{p_2,p_3,q_2,q_3} \frac{1}{2}\left|\left|\lambda_c\left(\varsigma c - d_c\right)\right|\right|_2^2 + \frac{1}{2}\left|\left|\lambda_l\left(\varsigma l - d_l\right)\right|\right|_2^2 \\
\left\langle \nabla\left(c-l\right) - p_1, p_2\right\rangle - I_{||\cdot||_\infty \leq \alpha_1\gamma_2}\left(p_2\right) + \\
\left\langle \epsilon p_1, p_3\right\rangle - I_{||\cdot||_\infty \leq \alpha_0\gamma_2}\left(p_3\right) + \\
\left\langle \nabla\left(l\right) - q_1, q_2\right\rangle - I_{||\cdot||_\infty \leq \alpha_1\gamma_1}\left(q_2\right) + \\
\left\langle \epsilon q_1, q_3\right\rangle - I_{||\cdot||_\infty \leq \alpha_0\gamma_1}\left(q_3\right).
\end{aligned}
\tag{C.49}
$$

The final update scheme for the primal dual algorithm of the saddle point problem C.49 is defined in Algorithm 9.

Algorithm 9 Primal Dual Algorithm for spatial adaptive ASL-TGV denoising

```
Input: $d_c$, $d_l$
Output: $c$, $l$
Initialize: $p_1^0$, $p_2^0$, $p_3^0$, $q_1^0$, $q_2^0$, $q_3^0$, $c^0$, $l^0$, $\overline{c}^0$, $\overline{l}^0$, $\overline{p}_1^0$, $\overline{q}_1^0$, choose $\tau$,$\sigma > 0$

  for $n = 0$ until maxIter

    Dual Update:
    $p_2^{n+1} = P_{\alpha_1,\gamma_1}\left(p_2^n + \sigma\left(\nabla\overline{c}^n - \nabla\overline{l}^n - \overline{p}_1^n\right)\right)$
    $p_3^{n+1} = P_{\alpha_0,\gamma_1}\left(p_3^n + \sigma\epsilon\overline{p}_1^n\right)$
    $q_2^{n+1} = P_{\alpha_1,\gamma_2}\left(q_2^n + \sigma\left(\nabla\overline{l}^n - \overline{q}_1^n\right)\right)$
    $q_3^{n+1} = P_{\alpha_0,\gamma_2}\left(q_3^n + \sigma\epsilon\overline{q}_1^n\right)$

    Primal Update:
    $c^{n+1} = P^2_{\lambda_c,\varsigma,\tau}\left(c^n - \tau\left(\nabla^* p_2^{n+1} + \varsigma^* c_2^{n+1}\right)\right)$
    $l^{n+1} = P^2_{\lambda_l,\varsigma,\tau}\left(l^n - \tau\left(-\nabla^* p_2^{n+1} + \nabla^* q_2^{n+1} + \varsigma^* l_2^{n+1}\right)\right)$
    $p_1^{n+1} = p_1^n - \tau\left(-p_2^{n+1} + \epsilon^* p_3^{n+1}\right)$
    $q_1^{n+1} = q_1^n - \tau\left(-q_2^{n+1} + \epsilon^* q_3^{n+1}\right)$

    Extrapolation step:
    $\overline{c}^{n+1} = 2c^{n+1} - c^n$
    $\overline{l}^{n+1} = 2l^{n+1} - l^n$
    $\overline{p}_1^{n+1} = 2p_1^{n+1} - p_1^n$
    $\overline{q}_1^{n+1} = 2q_1^{n+1} - q_1^n$
```

Note that in the above algorithm the regularization maps (λ_c and λ_l) are applied point wise in the operator $P^2_{\lambda,\varsigma,\tau}(\chi)$.

C.2.8 Spatio-Temporal ICTGV Denoising

The ICTGV denoising approach for dynamic ASL imaging is given by

$$\begin{aligned} dM^* \in \arg\min_{dM} \frac{\lambda}{2} \|dM - d_{dM}\|_2^2 + \gamma_1(w)\, TGV^2_{\alpha_1,\alpha_0,\beta}(dM - v) + \\ \gamma_2(w)\, TGV^2_{\alpha_1,\alpha_0,\beta}(v), \end{aligned} \tag{C.50}$$

where $d_{dM} \in \Re^{N_x \times N_y \times N_z \times N_t}$ is the acquired noisy image time series and $dM \in \Re^{N_x \times N_y \times N_z \times N_t}$ the denoised image time series. The solution of this problem is given by the primal dual splitting problem. Therefore, the problem has to be reformulated as a convex-concave saddle point problem. This is achieved by using the definition of the Fenchel conjugate C.27 leading to

$$\begin{aligned} \min_{dM,p_1,q_1,v} \max_{p_2,p_3,q_2,q_3} \frac{\lambda}{2} \|dM - d_{dM}\|_2^2 + \langle \nabla_\beta(dM - v) - p_1, p_2\rangle + \\ \langle \epsilon_\beta p_1, p_3\rangle + \langle \nabla_\beta(v) - q_1, q_2\rangle + \langle \epsilon_\beta q_1, q_3\rangle - \\ I_{\alpha_1,\gamma_1}(p_2) - I_{\alpha_0,\gamma_1}(p_3) - I_{\alpha_1,\gamma_2}(q_2) - I_{\alpha_0,\gamma_2}(q_3). \end{aligned} \tag{C.51}$$

The final update scheme for the primal dual algorithm of the saddle point problem C.51 is defined in Algorithm 10.

C.2.9 4D Variational ASL Reconstruction

The full ASL-TGV reconstruction approach for accelerated ASL data is defined as

$$\begin{aligned} (c^*, l^*) \in \arg\min_{c,l} \frac{\lambda_c}{2} \|Kc - d_c\|_2^2 + \frac{\lambda_l}{2} \|Kl - d_l\|_2^2 + \gamma_1(w)\, TGV_{\alpha_1,\alpha_0,\beta}(l) + \\ \gamma_1(w)\, TGV_{\alpha_1,\alpha_0,\beta}(c) + \gamma_2(w)\, TGV_{\alpha_1,\alpha_0,\beta}(c - l). \end{aligned} \tag{C.52}$$

The solution of this problem is given by the primal dual splitting problem. Therefore, the problem has to be reformulated as a convex-concave saddle point problem. This is achieved by using the definition of the Fenchel conjugate C.27 leading to

$$\begin{aligned} \min_{c,l,p_1,q_1,r_1} \max_{p_2,p_3,q_2,q_3,r_2,r_3,y,z} \langle Kc - d_c, y\rangle - \frac{1}{2\lambda_c} \|y\|_2^2 + \langle Kl - d_l, z\rangle - \frac{1}{2\lambda_l} \|z\|_2^2 + \\ \langle \nabla_\beta(c - l) - p_1, p_2\rangle + \langle \epsilon_\beta p_1, p_3\rangle + \langle \nabla_\beta l - q_1, q_2\rangle + \\ \langle \epsilon_\beta q_1, q_3\rangle + \langle \nabla_\beta c - r_1, r_2\rangle + \langle \epsilon_\beta r_1, r_3\rangle - \\ I_{\alpha_1,\gamma_2}(p_2) - I_{\alpha_0,\gamma_2}(p_3) - I_{\alpha_1,\gamma_1}(q_2) - \\ I_{\alpha_0,\gamma_1}(q_3) - I_{\alpha_1,\gamma_1}(r_2) - I_{\alpha_0,\gamma_1}(r_3). \end{aligned} \tag{C.53}$$

Algorithm 10 Primal Dual Algorithm for 4D ICTGV denoising

```
Input: $d_{dM}$
Output: $dM$
Initialize: $p_1^0, p_2^0, p_3^0, q_1^0, q_2^0, q_3^0, dM^0, v^0, \overline{dM}^0, \overline{v}^0, \overline{p}_1^0, \overline{q}_1^0$, choose $\tau, \sigma > 0$

  for $n = 0$ until maxIter

      Dual Update:
      $p_2^{n+1} = P_{\alpha_1,\gamma_1}\left(p_2^n + \sigma\left(\nabla_\beta \overline{dM}^n - \nabla_\beta \overline{v}^n - \overline{p}_1^n\right)\right)$
      $p_3^{n+1} = P_{\alpha_0,\gamma_1}\left(p_3^n + \sigma \epsilon_\beta \overline{p}_1^n\right)$
      $q_2^{n+1} = P_{\alpha_1,\gamma_2}\left(q_2^n + \sigma\left(\nabla_\beta \overline{v}^n - \overline{q}_1^n\right)\right)$
      $q_3^{n+1} = P_{\alpha_0,\gamma_2}\left(q_3^n + \sigma \epsilon_\beta \overline{q}_1^n\right)$

      Primal Update:
      $dM^{n+1} = P^2_{\lambda,\tau}\left(dM^n - \tau\left(\nabla^*_\beta p_2^{n+1}\right)\right)$
      $v^{n+1} = v^n - \tau\left(-\nabla^*_\beta p_2^{n+1} + \nabla^*_\beta q_2^{n+1}\right)$
      $p_1^{n+1} = p_1^n - \tau\left(-p_2^{n+1} + \epsilon^*_\beta p_3^{n+1}\right)$
      $q_1^{n+1} = q_1^n - \tau\left(-q_2^{n+1} + \epsilon^*_\beta q_3^{n+1}\right)$

      Extrapolation step:
      $\overline{dM}^{n+1} = 2dM^{n+1} - dM^n$
      $\overline{v}^{n+1} = 2v^{n+1} - v^n$
      $\overline{p}_1^{n+1} = 2p_1^{n+1} - p_1^n$
      $\overline{q}_1^{n+1} = 2q_1^{n+1} - q_1^n$
```

The final update scheme for the primal dual algorithm of the saddle point problem C.53 is defined in Algorithm 11.

Algorithm 11 Primal Dual Algorithm for 4D ASL-TGV reconstruction

```
Input: $d_c$, $d_l$
Output: $c$, $l$
Initialize: $p_1^0$,$p_2^0$,$p_3^0$,$q_1^0$,$q_2^0$,$q_3^0$,$r_1^0$,$r_2^0$,$r_3^0$,$c^0$,$l^0$,$y^0$,$z^0$,$\bar{c}^0$,$\bar{l}^0$,$\bar{p}_1^0$,$\bar{q}_1^0$,$\bar{r}_1^0$ choose $\tau$,$\sigma > 0$
  for $n = 0$ until maxIter
    Dual Update:
    $p_2^{n+1} = P_{\alpha_1,\gamma_2}\left(p_2^n + \sigma\left(\nabla_\beta \bar{c}^n - \nabla_\beta \bar{l}^n - \bar{p}_1^n\right)\right)$
    $p_3^{n+1} = P_{\alpha_0,\gamma_2}\left(p_3^n + \sigma\epsilon_\beta \bar{p}_1^n\right)$
    $q_2^{n+1} = P_{\alpha_1,\gamma_1}\left(q_2^n + \sigma\left(\nabla_\beta \bar{l}^n - \bar{q}_1^n\right)\right)$
    $q_3^{n+1} = P_{\alpha_0,\gamma_1}\left(q_3^n + \sigma\epsilon_\beta \bar{q}_1^n\right)$
    $r_2^{n+1} = P_{\alpha_1,\gamma_1}\left(r_2^n + \sigma\left(\nabla_\beta \bar{c}^n - \bar{r}_1^n\right)\right)$
    $r_3^{n+1} = P_{\alpha_0,\gamma_1}\left(r_3^n + \sigma\epsilon_\beta \bar{r}_1^n\right)$
    $y^{n+1} = P^2_{\lambda_c,\sigma}\left(y^n + \sigma\left(K\bar{c}^n - d_c\right)\right)$
    $z^{n+1} = P^2_{\lambda_l,\sigma}\left(z^n + \sigma\left(K\bar{l}^n - d_l\right)\right)$

    Primal Update:
    $c^{n+1} = c^n - \tau\left(\nabla_\beta^* p_2^{n+1} + \nabla_\beta^* r_2^{n+1} + K^* y^{n+1}\right)$
    $l^{n+1} = l^n - \tau\left(-\nabla_\beta^* p_2^{n+1} + \nabla_\beta^* q_2^{n+1} + K^* z^{n+1}\right)$
    $p_1^{n+1} = p_1^n - \tau\left(-p_2^{n+1} + \epsilon_\beta^* p_3^{n+1}\right)$
    $q_1^{n+1} = q_1^n - \tau\left(-q_2^{n+1} + \epsilon_\beta^* q_3^{n+1}\right)$
    $r_1^{n+1} = r_1^n - \tau\left(-r_2^{n+1} + \epsilon_\beta^* r_3^{n+1}\right)$

    Extrapolation step:
    $\bar{c}^{n+1} = 2c^{n+1} - c^n$
    $\bar{l}^{n+1} = 2l^{n+1} - l^n$
    $\bar{p}_1^{n+1} = 2p_1^{n+1} - p_1^n$
    $\bar{q}_1^{n+1} = 2q_1^{n+1} - q_1^n$
    $\bar{r}_1^{n+1} = 2r_1^{n+1} - r_1^n$
```

Bibliography

[1] S. Achard. The Statistical Analysis of Functional MRI Data. *Journal of Statistical Software*, 29(Book Review 3), 2009, doi: 10.18637/jss.v029.b03. (page 92)

[2] M. A. Addicott, L. L. Yang, A. M. Peiffer, L. R. Burnett, J. H. Burdette, M. Y. Chen, S. Hayasaka, R. A. Kraft, J. A. Maldjian, and P. J. Laurienti. The effect of daily caffeine use on cerebral blood flow: How much caffeine can we tolerate? *Human Brain Mapping*, 30(10):3102–3114, oct 2009, doi: 10.1002/hbm.20732. (page 6, 67)

[3] S. Aja-Fernandez and A. Tristan-Vega. A review on statistical noise models for Magnetic. *Tech Report of the LPI*, (TECH-LPI2013-01):1–23, 2013. (page 92)

[4] S. Aja-Fernández, A. Tristán-Vega, and W. S. Hoge. Statistical noise analysis in GRAPPA using a parametrized noncentral Chi approximation model. *Magnetic Resonance in Medicine*, 65(4):1195–1206, apr 2011, doi: 10.1002/mrm.22701. (page 92)

[5] M. Aksoy, J. Maclaren, and R. Bammer. Prospective motion correction for 3D pseudo-continuous arterial spin labeling using an external optical tracking system. *Magnetic Resonance Imaging*, 39:44–52, jun 2017, doi: 10.1016/j.mri.2017.01.018. (page 49, 148, 171)

[6] A. Alsaedi, D. Thomas, S. Bisdas, and X. Golay. Overview and Critical Appraisal of Arterial Spin Labelling Technique in Brain Perfusion Imaging, 2018, doi: 10.1155/2018/5360375. (page 15, 19, 20, 22)

[7] D. C. Alsop and J. A. Detre. Multisection cerebral blood flow MRI imaging with continuous arterial spin labeling. *Radiology*, 208(2):410–416, 1998, doi: 10.1148/radiology.208.2.9680569. (page 14)

[8] D. C. Alsop, J. A. Detre, X. Golay, M. Günther, J. Hendrikse, L. Hernandez-Garcia, H. Lu, B. J. MacIntosh, L. M. Parkes, M. Smits, M. J. P. van Osch, D. J. J. Wang, E. C. Wong, and G. Zaharchuk. Recommended implementation of arterial spin-labeled perfusion MRI for clinical applications: A consensus of the ISMRM perfusion study group and the European consortium for ASL in dementia. *Magnetic Resonance in Medicine*, 73(1):102–116, jan 2015, doi: 10.1002/mrm.25197. (page xviii, 2, 9, 20, 22, 23, 24, 25, 26, 27, 29, 32, 33, 34, 35, 37, 39, 45, 47, 49, 50, 53, 54, 69, 74, 92, 97, 98, 124, 139, 148, 154, 171, 174, 180)

[9] S. A. Amukotuwa, C. Yu, and G. Zaharchuk. 3D Pseudocontinuous arterial spin labeling in routine clinical practice: A review of clinically significant artifacts, jan 2016, doi: 10.1002/jmri.24873. (page 51)

[10] S. Aslan, F. Xu, P. L. Wang, J. Uh, U. S. Yezhuvath, M. Van Osch, and H. Lu. Estimation of labeling efficiency in pseudocontinuous arterial spin labeling. *Mag-*

netic Resonance in Medicine, 63(3):765–771, mar 2010, doi: 10.1002/mrm.22245. (page 51)

[11] I. Asllani, A. Borogovac, and T. R. Brown. Regression algorithm correcting for partial volume effects in arterial spin labeling MRI. *Magnetic Resonance in Medicine*, 60(6):1362–1371, dec 2008, doi: 10.1002/mrm.21670. (page 47)

[12] I. Asllani, C. Habeck, A. Borogovac, T. R. Brown, A. M. Brickman, and Y. Stern. Separating function from structure in perfusion imaging of the aging brain. *Human Brain Mapping*, 30(9):2927–2935, sep 2009, doi: 10.1002/hbm.20719. (page 47)

[13] G. Aubert and P. Kornprobst. Image restoration. In *Applied Mathematical Sciences (Switzerland)*, volume 147, pages 65–147. Springer, 2006, doi: 10.1007/978-0-387-44588-5_3. (page 59)

[14] R. Bammer. *MR & CT Perfusion Imaging: Clinical Applications and Theoretical Principles.* Wolters Kluwer Health, 2016. (page 12, 15, 18, 20, 31, 34, 36, 40, 41, 43, 47, 50, 51, 52, 54)

[15] E. L. Barbier, L. Lamalle, and M. Décorps. Methodology of brain perfusion imaging. *Journal of Magnetic Resonance Imaging*, 13(4):496–520, apr 2001, doi: 10.1002/jmri.1073. (page 15)

[16] J. Bause, P. Ehses, C. Mirkes, G. Shajan, K. Scheffler, and R. Pohmann. Quantitative and functional pulsed arterial spin labeling in the human brain at 9.4 t. *Magnetic Resonance in Medicine*, 75(3):1054–1063, mar 2016, doi: 10.1002/mrm.25671. (page 55)

[17] A. J. S. Beckett, T. Dadakova, J. Townsend, L. Huber, S. Park, and D. A. Feinberg. Comparison of BOLD and CBV using 3D EPI and 3D GRASE for cortical layer functional MRI at 7 T. *Magnetic Resonance in Medicine*, page mrm.28347, jun 2020, doi: 10.1002/mrm.28347. (page 177)

[18] Y. Behzadi, K. Restom, J. Liau, and T. T. Liu. A component based noise correction method (CompCor) for BOLD and perfusion based fMRI. *NeuroImage*, 37(1):90–101, aug 2007, doi: 10.1016/j.neuroimage.2007.04.042. (page 56)

[19] M. Bentourkia, A. Bol, A. Ivanoiu, D. Labar, M. Sibomana, A. Coppens, C. Michel, G. Cosnard, and A. G. De Volder. Comparison of regional cerebral blood flow and glucose metabolism in the normal brain: Effect of aging. *Journal of the Neurological Sciences*, 181(1-2):19–28, dec 2000, doi: 10.1016/S0022-510X(00)00396-8. (page 6)

[20] M. A. Bernstein, K. F. King, and X. J. Zhou. *Handbook of MRI Pulse Sequences.* Elsevier Inc., sep 2004, doi: 10.1016/B978-0-12-092861-3.X5000-6. (page 26, 27, 29, 31)

[21] E. S. Berry, P. Jezzard, and T. W. Okell. Off-resonance correction for pseudo-continuous arterial spin labeling using the optimized encoding scheme. *NeuroImage*, 199:304–312, oct 2019, doi: 10.1016/j.neuroimage.2019.05.083. (page 51)

[22] A. Bibic, L. Knutsson, F. Ståhlberg, and R. Wirestam. Denoising of arterial spin labeling data: wavelet-domain filtering compared with Gaussian smoothing. *Magma (New York, N.Y.)*, 23(3):125–37, jun 2010, doi: 10.1007/s10334-010-0209-8. (page 56, 68, 71, 73)

[23] R. M. Birn, M. A. Smith, T. B. Jones, and P. A. Bandettini. The respiration response function: The temporal dynamics of fMRI signal fluctuations related to changes in respiration. *NeuroImage*, 40(2):644–654, apr 2008, doi: 10.1016/j.neuroimage.2007.11.059. (page 116)

[24] B. Biswal, F. Zerrin Yetkin, V. M. Haughton, and J. S. Hyde. Functional connectivity in the motor cortex of resting human brain using echo-planar mri. *Magnetic Resonance in Medicine*, 34(4):537–541, 1995, doi: 10.1002/mrm.1910340409. (page 92)

[25] B. B. Biswal, J. Van Kylen, and J. S. Hyde. Simultaneous assessment of flow and BOLD signals in resting-state functional connectivity maps. *NMR in Biomedicine*, 10(4-5):165–170, jun 1997, doi: 10.1002/(SICI)1099-1492(199706/08)10:4/5⟨165::AID-NBM454⟩3.0.CO;2-7. (page 112)

[26] P. Bladt, M. J. van Osch, P. Clement, E. Achten, J. Sijbers, and A. J. den Dekker. Supporting measurements or more averages? How to quantify cerebral blood flow most reliably in 5 minutes by arterial spin labeling. *Magnetic Resonance in Medicine*, page mrm.28314, may 2020, doi: 10.1002/mrm.28314. (page 52)

[27] R. P. Bokkers, P. J. Van Laar, K. C. Van De Ven, L. J. Kapelle, C. J. Klijn, and J. Hendrikse. Arterial spin-labeling MR imaging measurements of timing parameters in patients with a carotid artery occlusion. *American Journal of Neuroradiology*, 29(9):1698–1703, oct 2008, doi: 10.3174/ajnr.A1232. (page 124)

[28] M. Boland, R. Stirnberg, E. D. Pracht, J. Kramme, R. Viviani, J. Stingl, and T. Stöcker. Accelerated 3D-GRASE imaging improves quantitative multiple post labeling delay arterial spin labeling. *Magnetic Resonance in Medicine*, 80(6):2475–2484, dec 2018, doi: 10.1002/mrm.27226. (page 124, 149, 168)

[29] A. Borogovac, C. Habeck, S. A. Small, and I. Asllani. Mapping brain function using a 30-day interval between baseline and activation: a novel arterial spin labeling fMRI approach. *Journal of cerebral blood flow and metabolism : official journal of the International Society of Cerebral Blood Flow and Metabolism*, 30(10):1721–1733, oct 2010, doi: 10.1038/jcbfm.2010.89. (page 47)

[30] K. Bredies and M. Holler. A TGV-Based Framework for Variational Image Decompression, Zooming, and Reconstruction. Part I: Analytics. *SIAM Journal on Imaging Sciences*, 8(4):2814–2850, jan 2015, doi: 10.1137/15M1023865. (page 70)

[31] K. Bredies, K. Kunisch, and T. Pock. Total Generalized Variation. *SIAM Journal on Imaging Sciences*, 3(3):492–526, 2010, doi: 10.1137/090769521. (page 56, 60, 151)

[32] F. A. Breuer, M. Blaimer, M. F. Mueller, N. Seiberlich, R. M. Heidemann, M. A. Griswold, and P. M. Jakob. Controlled aliasing in volumetric parallel imaging (2D CAIPIRINHA). *Magnetic Resonance in Medicine*, 55(3):549–556, mar 2006, doi: 10.1002/mrm.20787. (page 149)

[33] E.-M. Brinkmann, M. Burger, J. Rasch, and C. Sutour. Bias Reduction in Variational Regularization. *Journal of Mathematical Imaging and Vision*, 59(3):534–566, nov 2017, doi: 10.1007/s10851-017-0747-z. (page 131, 169, 175, 180)

[34] R. B. Buxton, L. R. Frank, E. C. Wong, B. Siewert, S. Warach, and R. R. Edelman. A general kinetic model for quantitative perfusion imaging with arterial spin labeling. *Magnetic resonance in medicine*, 40(3):383–96, sep 1998. (page 9, 26, 35, 36, 37, 38, 49, 53, 69, 73, 95, 97, 118, 124, 125, 126, 139, 148, 156)

[35] R. B. Buxton. *Introduction to functional magnetic resonance imaging: Principles and techniques*, volume 9780521899. Cambridge University Press, jan 2009, doi: 10.1017/CBO9780511605505. (page 18, 19, 27, 35, 115)

[36] F. Calamante, D. L. Thomas, G. S. Pell, J. Wiersma, and R. Turner. Measuring cerebral blood flow using magnetic resonance imaging techniques, 1999, doi: 10.1097/00004647-199907000-00001. (page 11, 14)

[37] O. G. Cameron, J. G. Modell, and M. Hariharan. Caffeine and human cerebral blood flow: A positron emission tomography study. *Life Sciences*, 47(13):1141–1146, jan 1990, doi: 10.1016/0024-3205(90)90174-P. (page 112)

[38] J. A. Chalela, D. C. Alsop, J. B. Gonzalez-Atavales, J. A. Maldjian, S. E. Kasner, and J. A. Detre. Magnetic resonance perfusion imaging in acute ischemic stroke using continuous arterial spin labeling. *Stroke*, 31(3):680–687, 2000, doi: 10.1161/01.STR.31.3.680. (page 8)

[39] A. Chambolle, V. Caselles, M. Novaga, D. Cremers, and T. Pock. An Introduction to Total Variation for Image Analysis. In *Theoretical Foundations and Numerical Methods for Sparse Recovery. Radon Series Comp. Appl. Math*, pages 263–340. de Gruyter, 2010, doi: 10.1515/9783110226157.263. (page 59)

[40] A. Chambolle and P. L. Lions. Image recovery via total variation minimization and related problems. *Numerische Mathematik*, 76(2):167–188, 1997, doi: 10.1007/s002110050258. (page 60)

[41] A. Chambolle and T. Pock. A First-Order Primal-Dual Algorithm for Convex Problems withÂ Applications to Imaging. *Journal of Mathematical Imaging and Vision*, 40(1):120–145, may 2011, doi: 10.1007/s10851-010-0251-1. (page 63, 64, 152)

[42] T. F. Chan, S. Esedoglu, and F. Park. A fourth order dual method for staircase reduction in texture extraction and image restoration problems. In *Proceedings - International Conference on Image Processing, ICIP*, pages 4137–4140, 2010, doi: 10.1109/ICIP.2010.5653199. (page 60)

[43] Y. V. Chang, M. Vidorreta, Z. Wang, and J. A. Detre. 3D-accelerated, stack-of-spirals acquisitions and reconstruction of arterial spin labeling MRI. *Magnetic Resonance in Medicine*, 78(4):1405–1419, oct 2017, doi: 10.1002/mrm.26549. (page 32, 149, 168)

[44] M. Chappell, A. Groves, B. Whitcher, and M. Woolrich. Variational Bayesian Inference for a Nonlinear Forward Model. *IEEE Transactions on Signal Processing*, 57(1):223–236, jan 2009, doi: 10.1109/TSP.2008.2005752. (page 156)

[45] M. Chappell, B. MacIntosh, and T. Okell. *Introduction to Perfusion Quantification using Arterial Spin Labelling*, volume 1. Oxford University Press, dec 2017, doi: 10.1093/oso/9780198793816.001.0001. (page 23, 25, 28, 31, 40, 49, 50, 53, 171)

[46] M. A. Chappell, M. W. Woolrich, S. Kazan, P. Jezzard, S. J. Payne, and B. J. MacIntosh. Modeling dispersion in arterial spin labeling: Validation using dynamic angiographic measurements. *Magnetic Resonance in Medicine*, 69(2):563–570, feb 2013, doi: 10.1002/mrm.24260. (page 40)

[47] J. J. Chen and G. B. Pike. Human whole blood <i>T</i> ₂ relaxometry at 3 Tesla. *Magnetic Resonance in Medicine*, 61(2):249–254, feb 2009, doi: 10.1002/mrm.21858. (page 154)

[48] Y. Chen, H. I. Wan, J. P. O'Reardon, D. J. Wang, Z. Wang, M. Korczykowski, and J. A. Detre. Quantification of cerebral blood flow as biomarker of drug effect: Arterial spin labeling phMRI after a single dose of oral citalopram. *Clinical Pharmacology and Therapeutics*, 89(2):251–258, feb 2011, doi: 10.1038/clpt.2010.296. (page 22, 116)

[49] Z. Chen, X. Zhang, C. Yuan, X. Zhao, and M. J. van Osch. Measuring the labeling efficiency of pseudocontinuous arterial spin labeling. *Magnetic Resonance in Medicine*, 77(5):1841–1852, may 2017, doi: 10.1002/mrm.26266. (page 51)

[50] Z. Chen, X. Zhao, X. Zhang, R. Guo, W. M. Teeuwisse, B. Zhang, P. Koken, J. Smink, C. Yuan, and M. J. van Osch. Simultaneous measurement of brain perfusion and labeling efficiency in a single pseudo-continuous arterial spin labeling scan. *Magnetic Resonance in Medicine*, 79(4):1922–1930, apr 2018, doi: 10.1002/mrm.26842. (page 51)

[51] D. A. Chesler and K. K. Kwong. An intuitive guide to the T1 based perfusion model. *International Journal of Imaging Systems and Technology*, 6(2-3):171–174, 1995, doi: 10.1002/ima.1850060206. (page 36)

[52] C. Constantinides. *Magnetic resonance imaging: The basics.* Taylor & Francis Ltd, 2016. (page 92)

[53] R. W. Cox, A. Jesmanowicz, and J. S. Hyde. Real-Time Functional Magnetic Resonance Imaging. *Magnetic Resonance in Medicine*, 33(2):230–236, feb 1995, doi: 10.1002/mrm.1910330213. (page 138)

[54] K. Dabov, A. Foi, V. Katkovnik, and K. Egiazarian. Image Denoising by Sparse 3-D Transform-Domain Collaborative Filtering. *IEEE Transactions on Image Processing*, 16(8):2080–2095, aug 2007, doi: 10.1109/TIP.2007.901238. (page 71, 73)

[55] M. S. Dagli, J. E. Ingeholm, and J. V. Haxby. Localization of cardiac-induced signal change in fMRI. *NeuroImage*, 9(4):407–415, 1999, doi: 10.1006/nimg.1998.0424. (page 92)

[56] W. Dai, D. Garcia, C. de Bazelaire, and D. C. Alsop. Continuous flow-driven inversion for arterial spin labeling using pulsed radio frequency and gradient fields. *Magnetic Resonance in Medicine*, 60(6):1488–1497, dec 2008, doi: 10.1002/mrm.21790. (page 9, 19, 20, 47, 50, 51, 55, 88, 98, 126, 148, 154)

[57] W. Dai, P. M. Robson, A. Shankaranarayanan, and D. C. Alsop. Modified pulsed continuous arterial spin labeling for labeling of a single artery. *Magnetic Resonance in Medicine*, 64(4):975–982, oct 2010, doi: 10.1002/mrm.22363. (page 43)

[58] W. Dai, P. M. Robson, A. Shankaranarayanan, and D. C. Alsop. Reduced resolution transit delay prescan for quantitative continuous arterial spin labeling perfusion imaging. *Magnetic Resonance in Medicine*, 67(5):1252–1265, may 2012, doi: 10.1002/mrm.23103. (page 26)

[59] W. Dai, A. Shankaranarayanan, and D. C. Alsop. Volumetric measurement of perfusion and arterial transit delay using hadamard encoded continuous arterial spin labeling. *Magnetic Resonance in Medicine*, 69(4):1014–1022, apr 2013, doi: 10.1002/mrm.24335. (page 45)

[60] I. Daubechies, M. Defrise, and C. De Mol. An iterative thresholding algorithm for linear inverse problems with a sparsity constraint. *Communications on Pure and Applied Mathematics*, 57(11):1413–1457, jul 2004, doi: 10.1002/cpa.20042. (page 71, 73)

[61] T. L. Davis, K. K. Kwong, R. M. Weisskoff, and B. R. Rosen. Calibrated functional MRI: Mapping the dynamics of oxidative metabolism. *Proceedings of the National Academy of Sciences of the United States of America*, 95(4):1834–1839, feb 1998, doi: 10.1073/pnas.95.4.1834. (page 115)

[62] A. De Havenon, D. R. Haynor, D. L. Tirschwell, J. J. Majersik, G. Smith, W. Cohen, and J. B. Andre. Association of collateral blood vessels detected by arterial spin labeling magnetic resonance imaging with neurological outcome after ischemic stroke. *JAMA Neurology*, 74(4):453–458, apr 2017, doi: 10.1001/jamaneurol.2016.4491. (page 124)

[63] R. C. DeCharms, F. Maeda, G. H. Glover, D. Ludlow, J. M. Pauly, D. Soneji, J. D. Gabrieli, and S. C. Mackey. Control over brain activation and pain learned by using real-time functional MRI. *Proceedings of the National Academy of Sciences of the United States of America*, 102(51):18626–18631, dec 2005, doi: 10.1073/pnas.0505210102. (page 138)

[64] C.-A. Deledalle, N. Papadakis, J. Salmon, and S. Vaiter. CLEAR: Covariant LEAst-Square Refitting with Applications to Image Restoration. *SIAM Journal on Imaging Sciences*, 10(1):243–284, jan 2017, doi: 10.1137/16M1080318. (page 131, 169)

[65] C. P. Derdeyn, T. O. Videen, K. D. Yundt, S. M. Fritsch, D. A. Carpenter, R. L. Grubb, and W. J. Powers. Variability of cerebral blood volume and oxygen extraction: stages of cerebral haemodynamic impairment revisited. *Brain*, 125(3):595–607, mar 2002, doi: 10.1093/brain/awf047. (page 6)

[66] J. A. Detre, J. S. Leigh, D. S. Williams, and A. P. Koretsky. Perfusion imaging. *Magnetic resonance in medicine*, 23(1):37–45, jan 1992. (page 2, 8, 9, 10, 13, 26, 35, 36, 148)

[67] J. A. Detre and J. Wang. Technical aspects and utility of fMRI using BOLD and ASL, may 2002, doi: 10.1016/S1388-2457(02)00038-X. (page 115)

[68] J. A. Detre, W. Zhang, D. A. Roberts, A. C. Silva, D. S. Williams, D. J. Grandis, A. P. Koretsky, and J. S. Leigh. Tissue specific perfusion imaging using arterial spin labeling. *NMR in Biomedicine*, 7(1-2):75–82, mar 1994, doi: 10.1002/nbm.1940070112. (page 8, 13)

[69] X. Di, S. S. Kannurpatti, B. Rypma, and B. B. Biswal. Calibrating BOLD fMRI activations with neurovascular and anatomical constraints. *Cerebral Cortex*, 23(2):255–263, 2013, doi: 10.1093/cercor/bhs001. (page 116)

[70] D. C. Dobson and F. Santosa. Recovery of Blocky Images from Noisy and Blurred Data. *SIAM Journal on Applied Mathematics*, 56(4):1181–1198, 1996, doi: 10.1137/S003613999427560X. (page 60)

[71] E. F. Domino, L. Ni, Y. Xu, R. A. Koeppe, S. Guthrie, and J. K. Zubieta. Regional cerebral blood flow and plasma nicotine after smoking tobacco cigarettes. *Progress in Neuro-Psychopharmacology and Biological Psychiatry*, 28(2):319–327, 2004, doi: 10.1016/j.pnpbp.2003.10.011. (page 6, 67)

[72] M. J. Donahue, C. C. Faraco, M. K. Strother, M. A. Chappell, S. Rane, L. M. Dethrage, J. Hendrikse, and J. C. Siero. Bolus arrival time and cerebral blood flow responses to hypercarbia. *Journal of Cerebral Blood Flow and Metabolism*, 34(7):1243–1252, 2014, doi: 10.1038/jcbfm.2014.81. (page 95, 125)

[73] G. Duhamel and D. C. Alsop. Single-Shot Susceptibility Insensitive Whole Brain 3D fMRI with ASL. In *Proceedings of the 12th Annual Meeting of ISMRM*, page 518, 2004. (page 29, 148)

[74] G. Duhamel, C. De Bazelaire, and D. C. Alsop. Evaluation of systematic quantification errors in velocity-selective arterial spin labeling of the brain. *Magnetic Resonance in Medicine*, 50(1):145–153, jul 2003, doi: 10.1002/mrm.10510. (page 9)

[75] C. Economo. The Cytoarchitectonics of the Human Cerebral Cortex. *Journal of the American Medical Association*, 93(10):794, sep 1929, doi: 10.1001/jama.1929.02710100056050. (page 123, 177)

[76] R. R. Edelman and Q. Chen. EPISTAR MRI: Multislice mapping of cerebral blood flow. *Magnetic Resonance in Medicine*, 40(6):800–805, 1998, doi: 10.1002/mrm.1910400603. (page 18)

[77] R. R. Edelman, B. Siewert, D. G. Darby, V. Thangaraj, A. C. Nobre, M. M. Mesulam, and S. Warach. Qualitative mapping of cerebral blood flow and functional localization with echo-planar MR imaging and signal targeting with alternating radio frequency. *Radiology*, 192(2):513–520, aug 1994, doi: 10.1148/radiology.192.2.8029425. (page 9, 14, 15, 18, 26)

[78] A. A. El-Dash. *Origin Of The Universe And Life On Earth.* Xlibris, 2012. (page 5)

[79] K. Emmert, M. Breimhorst, T. Bauermann, F. Birklein, D. Van De Ville, and S. Haller. Comparison of anterior cingulate vs. insular cortex as targets for real-time fMRI regulation during pain stimulation. *Frontiers in Behavioral Neuroscience*, 8(OCT):350, oct 2014, doi: 10.3389/fnbeh.2014.00350. (page 138)

[80] J. W. Evans, P. Kundu, S. G. Horovitz, and P. A. Bandettini. Separating slow BOLD from non-BOLD baseline drifts using multi-echo fMRI. *NeuroImage*, 105:189–197, jan 2015, doi: 10.1016/j.neuroimage.2014.10.051. (page 116)

[81] A. P. Fan, J. Guo, M. M. Khalighi, P. K. Gulaka, B. Shen, J. H. Park, H. Gandhi, D. Holley, O. Rutledge, P. Singh, T. Haywood, G. K. Steinberg, F. T. Chin, and G. Zaharchuk. Long-Delay Arterial Spin Labeling Provides More Accurate Cerebral Blood Flow Measurements in Moyamoya Patients: A Simultaneous Positron Emission Tomography/MRI Study. *Stroke*, 48(9):2441–2449, sep 2017, doi: 10.1161/STROKEAHA.117.017773. (page 24)

[82] L. Fan, F. Zhang, H. Fan, and C. Zhang. Brief review of image denoising techniques. *Visual Computing for Industry, Biomedicine, and Art*, 2(1):1–12, dec 2019, doi: 10.1186/s42492-019-0016-7. (page 57)

[83] R. Fang, J. Huang, and W.-M. Luh. A spatio-temporal low-rank total variation approach for denoising arterial spin labeling MRI data. In *2015 IEEE 12th International Symposium on Biomedical Imaging (ISBI)*, pages 498–502. IEEE, apr 2015, doi: 10.1109/ISBI.2015.7163920. (page 56, 71, 73, 74, 98)

[84] A. Fazlollahi, P. Bourgeat, X. Liang, F. Meriaudeau, A. Connelly, O. Salvado, and F. Calamante. Reproducibility of multiphase pseudo-continuous arterial spin labeling and the effect of post-processing analysis methods. *NeuroImage*, 117:191–201, aug 2015, doi: 10.1016/j.neuroimage.2015.05.048. (page 47, 56, 70)

[85] D. A. Feinberg, S. Ramanna, and M. Guenther. Evaluation of new ASL 3D GRASE Sequences using parallel imaging, segmented and interleaved k- Space at 3T with 12- and 32- channel coils. In *Proceedings of the 10th Annual Meeting of ISMRM*, page 623, 2002. (page 148)

[86] M. A. Fernández-Seara, Z. Wang, J. Wang, H.-Y. Rao, M. Guenther, D. A. Feinberg, and J. A. Detre. Continuous arterial spin labeling perfusion measurements using single shot 3D GRASE at 3 T. *Magnetic Resonance in Medicine*, 54(5):1241–1247, nov 2005, doi: 10.1002/mrm.20674. (page 148)

[87] B. Fischl and A. M. Dale. Measuring the thickness of the human cerebral cortex from magnetic resonance images. *Proceedings of the National Academy of Sciences of the United States of America*, 97(20):11050–11055, sep 2000, doi: 10.1073/pnas.200033797. (page 123, 177)

[88] S. D. Forman, J. D. Cohen, M. Fitzgerald, W. F. Eddy, M. A. Mintun, and D. C. Noll. Improved Assessment of Significant Activation in Functional Magnetic Resonance Imaging (fMRI): Use of a Cluster-Size Threshold. *Magnetic Resonance in Medicine*, 33(5):636–647, may 1995, doi: 10.1002/mrm.1910330508. (page 123)

[89] P. T. Fox and M. E. Raichle. Focal physiological uncoupling of cerebral blood flow and oxidative metabolism during somatosensory stimulation in human subjects. *Proceedings of the National Academy of Sciences of the United States of America*, 83(4):1140–1144, feb 1986, doi: 10.1073/pnas.83.4.1140. (page 115)

[90] P. T. Fox, M. E. Raichle, M. A. Mintun, and C. Dence. Nonoxidative glucose consumption during focal physiologic neural activity. *Science*, 241(4864):462–464, 1988, doi: 10.1126/science.3260686. (page 115)

[91] S. L. Franklin, S. Schmid, C. Bos, and M. J. van Osch. Influence of the cardiac cycle on velocity selective and acceleration selective arterial spin labeling. *Magnetic Resonance in Medicine*, 83(3):872–882, mar 2020, doi: 10.1002/mrm.27973. (page 50)

[92] K. J. K. J. Friston, J. Ashburner, S. Kiebel, T. Nichols, and W. D. Penny. *Statistical parametric mapping : the analysis of funtional brain images.* Elsevier/Academic Press, 2007. (page 117, 154)

[93] N. Fujima, T. Osanai, Y. Shimizu, A. Yoshida, T. Harada, N. Nakayama, K. Kudo, K. Houkin, and H. Shirato. Utility of noncontrast-enhanced time-resolved four-dimensional MR angiography with a vessel-selective technique for intracranial arteriovenous malformations. *Journal of Magnetic Resonance Imaging*, 44(4):834–845, oct 2016, doi: 10.1002/jmri.25222. (page 180)

[94] I. B. Galazzo, M. A. Chappell, D. L. Thomas, X. Golay, P. Manganotti, and E. De Vita. Reducing blurring artifacts in 3D-GRASE ASL by integrating new acquisition and analysis strategies. In *Proceedings of the 22th Annual Meeting of ISMRM*, page 2704, 2014. (page 29, 148, 171)

[95] D. Gallichan and P. Jezzard. Modeling the effects of dispersion and pulsatility of blood flow in pulsed arterial spin labeling. *Magnetic Resonance in Medicine*, 60(1):53–63, jul 2008, doi: 10.1002/mrm.21654. (page 40)

[96] D. M. Garcia, G. Duhamel, and D. C. Alsop. Efficiency of inversion pulses for background suppressed arterial spin labeling. *Magnetic Resonance in Medicine*, 54(2):366–372, aug 2005, doi: 10.1002/mrm.20556. (page 34)

[97] A. G. Gardener, P. A. Gowland, and S. T. Francis. Implementation of quantitative perfusion imaging using pulsed arterial spin labeling at ultra-high field. *Magnetic resonance in medicine*, 61(4):874–82, apr 2009, doi: 10.1002/mrm.21796. (page 55)

[98] C. Gaser and R. Dahnke. CAT - A Computational Anatomy Toolbox for the Analysis of Structural MRI Data. In *HBM*, 2016. (page 126, 154)

[99] M. D. Ginsberg, J. Y. Chang, R. E. Kelley, F. Yoshii, W. W. Barker, G. Ingenito, and T. E. Boothe. Increases in both cerebral glucose utilization and blood flow during execution of a somatosensory task. *Annals of Neurology*, 23(2):152–160, 1988, doi: 10.1002/ana.410230208. (page 112, 115)

[100] X. Golay, J. Hendrikse, and T. C. Lim. Perfusion Imaging Using Arterial Spin Labeling, feb 2004, doi: 10.1097/00002142-200402000-00003. (page 11, 12, 13, 124)

[101] X. Golay, E. T. Petersen, and F. Hui. Pulsed Star Labeling of Arterial Regions (PULSAR): A robust regional perfusion technique for high field imaging. *Magnetic Resonance in Medicine*, 53(1):15–21, jan 2005, doi: 10.1002/mrm.20338. (page 15)

[102] X. Golay, M. Stuber, K. P. Pruessmann, D. Meier, and P. Boesiger. Transfer insensitive labeling technique (TILT): Application to multislice functional perfusion imaging. *Journal of Magnetic Resonance Imaging*, 9(3):454–461, 1999, doi: 10.1002/(SICI)1522-2586(199903)9:3⟨454::AID-JMRI14⟩3.0.CO;2-B. (page 15)

[103] R. L. Gollub, H. C. Breiter, H. Kantor, D. Kennedy, D. Gastfriend, R. T. Mathew, N. Makris, A. Guimaraes, J. Riorden, T. Campbell, M. Foley, S. E. Hyman, B. Rosen, and R. Weisskoff. Cocaine decreases cortical cerebral blood flow but does not obscure regional activation in functional magnetic resonance imaging in human subjects. *Journal of Cerebral Blood Flow and Metabolism*, 18(7):724–734, jul 1998, doi: 10.1097/00004647-199807000-00003. (page 112)

[104] M. A. Griswold, P. M. Jakob, R. M. Heidemann, M. Nittka, V. Jellus, J. Wang, B. Kiefer, and A. Haase. Generalized Autocalibrating Partially Parallel Acquisitions (GRAPPA). *Magnetic Resonance in Medicine*, 47(6):1202–1210, 2002, doi: 10.1002/mrm.10171. (page 92)

[105] D. Grössinger, S. E. Kober, S. M. Spann, R. Stollberger, and G. Wood. Real-Time Functional Magnetic Resonance Imaging as a Tool for Neurofeedback. *Lernen und Lernstörungen*, pages 1–12, apr 2020, doi: 10.1024/2235-0977/a000300. (page)

[106] A. R. Groves, M. A. Chappell, and M. W. Woolrich. Combined spatial and non-spatial prior for inference on MRI time-series. *NeuroImage*, 45(3):795–809, apr 2009, doi: 10.1016/j.neuroimage.2008.12.027. (page 156)

[107] M. Guenther. Highly efficient accelerated acquisition of perfusion inflow series by Cycled Arterial Spin Labeling. In *Proceedings of the 15th Annual Meeting of ISMRM*, page 380, 2007. (page 171)

[108] M. Günther. Highly efficient accelerated acquisition of perfusion inflow series by Cycled Arterial Spin Labeling. *Proc. Intl. Soc. Mag. Reson. Med.*, 15:380, 2007. (page 26, 43, 45)

[109] M. Günther, K. Oshio, and D. A. Feinberg. Single-shot 3D imaging techniques improve arterial spin labeling perfusion measurements. *Magnetic Resonance in Medicine*, 54(2):491–498, aug 2005, doi: 10.1002/mrm.20580. (page 29, 47, 55, 88, 148)

[110] J. Guo, S. J. Holdsworth, A. P. Fan, M. R. Lebel, Z. Zun, A. Shankaranarayanan, and G. Zaharchuk. Comparing accuracy and reproducibility of sequential and Hadamard-encoded multidelay pseudocontinuous arterial spin labeling for measuring cerebral blood flow and arterial transit time in healthy subjects: A simulation and in vivo study. *Journal of Magnetic Resonance Imaging*, 47(4):1119–1132, apr 2018, doi: 10.1002/jmri.25834. (page 45)

[111] P. W. Hales, J. Pfeuffer, and C. A. Clark. Combined Denoising and Suppression of Transient Artifacts in Arterial Spin Labeling MRI Using Deep Learning. *Journal of Magnetic Resonance Imaging*, page jmri.27255, jun 2020, doi: 10.1002/jmri.27255. (page 175)

[112] S. Haller, N. Birbaumer, and R. Veit. Real-time fMRI feedback training may improve chronic tinnitus. *European Radiology*, 20(3):696–703, mar 2010, doi: 10.1007/s00330-009-1595-z. (page 138)

[113] K. Hammernik, T. Klatzer, E. Kobler, M. P. Recht, D. K. Sodickson, T. Pock, and F. Knoll. Learning a variational network for reconstruction of accelerated MRI data. *Magnetic Resonance in Medicine*, 79(6):3055–3071, jun 2018, doi: 10.1002/mrm.26977. (page 179)

[114] C. E. Hayes and P. B. Roemer. Noise correlations in data simultaneously acquired from multiple surface coil arrays. *Magnetic Resonance in Medicine*, 16(2):181–191, 1990, doi: 10.1002/mrm.1910160202. (page 92)

[115] O. Heid. Robust EPI Phase Correction. In *Proceedings of the 5th Annual Meeting of ISMRM*, page 2014, 1997. (page 27, 155)

[116] D. Heijtel, H. Mutsaerts, E. Bakker, P. Schober, M. Stevens, E. Petersen, B. van Berckel, C. Majoie, J. Booij, M. van Osch, E. VanBavel, R. Boellaard, A. Lammertsma, and A. Nederveen. Accuracy and precision of pseudo-continuous arterial spin labeling perfusion during baseline and hypercapnia: A head-to-head comparison with 15O H2O positron emission tomography. *NeuroImage*, 92:182–192, may 2014, doi: 10.1016/J.NEUROIMAGE.2014.02.011. (page 170)

[117] M. Helle, D. G. Norris, S. Rüfer, K. Alfke, O. Jansen, and M. J. Van Osch. Superselective pseudocontinuous arterial spin labeling. *Magnetic Resonance in Medicine*, 64(3):777–786, sep 2010, doi: 10.1002/mrm.22451. (page 43)

[118] J. A. Helpern, C. A. Branch, M. N. Yongbi, and N. C. Huang. Perfusion imaging by un-inverted flow-sensitive alternating inversion recovery (UNFAIR). *Magnetic Resonance Imaging*, 15(2):135–139, jan 1997, doi: 10.1016/S0730-725X(96)00353-0. (page 15)

[119] J. Hendrikse, J. Van Der Grond, H. Lu, P. C. Van Zijl, and X. Golay. Flow Territory Mapping of the Cerebral Arteries with Regional Perfusion MRI. *Stroke*, 35(4):882–887, apr 2004, doi: 10.1161/01.STR.0000120312.26163.EC. (page 42, 43)

[120] L. Hernandez-Garcia and H. Jahanian. Perfusion Based Functional MRI. In *Advanced Brain Neuroimaging Topics in Health and Disease - Methods and Applications*. InTech, may 2014, doi: 10.5772/58259. (page 1, 11, 14, 116)

[121] L. Hernandez-Garcia, H. Jahanian, M. K. Greenwald, J. K. Zubieta, and S. J. Peltier. Real-time functional MRI using pseudo-continuous arterial spin labeling. *Magnetic Resonance in Medicine*, 65(6):1570–1577, jun 2011, doi: 10.1002/mrm.22922. (page 138)

[122] L. Hernandez-Garcia, H. Jahanian, and D. B. Rowe. Quantitative analysis of arterial spin labeling FMRI data using a general linear model. *Magnetic Resonance Imaging*, 28(7):919–927, sep 2010, doi: 10.1016/j.mri.2010.03.035. (page 117)

[123] L. Hernandez-Garcia, A. Lahiri, and J. Schollenberger. Recent progress in ASL, feb 2019, doi: 10.1016/j.neuroimage.2017.12.095. (page 39, 40, 41, 42, 176)

[124] L. Hernandez-Garcia, G. R. Lee, A. L. Vazquez, and D. C. Noll. Fast Pseudo-Continuous Arterial Spin Labeling for Functional Imaging Using a Two-Coil System. *Magnetic Resonance in Medicine*, 51(3):577–585, mar 2004, doi: 10.1002/mrm.10733. (page 14)

[125] P. Herscovitch and M. E. Raichle. What is the correct value for the brain–blood partition coefficient for water? *Journal of cerebral blood flow and metabolism : official journal of the International Society of Cerebral Blood Flow and Metabolism*, 5(1):65–9, mar 1985, doi: 10.1038/jcbfm.1985.9. (page 69, 98, 126, 139, 154)

[126] S. Heunis, R. Besseling, R. Lamerichs, A. de Louw, M. Breeuwer, B. Aldenkamp, and J. Bergmans. Neu3CA-RT: A framework for real-time fMRI analysis. *Psychiatry Research - Neuroimaging*, 282:90–102, dec 2018, doi: 10.1016/j.pscychresns.2018.09.008. (page 138)

[127] J. Hirsch, M. I. Ruge, K. H. S. Kim, D. D. Correa, J. D. Victor, N. R. Relkin, D. R. Labar, G. Krol, M. H. Bilsky, M. M. Souweidane, L. M. DeAngelis, and P. H. Gutin. An Integrated Functional Magnetic Resonance Imaging Procedure for Preoperative Mapping of Cortical Areas Associated with Tactile, Mo-

tor, Language, and Visual Functions. *Neurosurgery*, 47(3):711–722, sep 2000, doi: 10.1097/00006123-200009000-00037. (page 138)

[128] M. L. Ho. Arterial spin labeling: Clinical applications, sep 2018, doi: 10.1016/j.neurad.2018.06.003. (page 1, 2, 8)

[129] R. D. Hoge, J. Atkinson, B. Gill, G. R. Crelier, S. Marrett, and G. B. Pike. Linear coupling between cerebral blood flow and oxygen consumption in activated human cortex. *Proceedings of the National Academy of Sciences of the United States of America*, 96(16):9403–9408, aug 1999, doi: 10.1073/pnas.96.16.9403. (page 115)

[130] M. Holler. *Higher Order Regularization for Model Based Data Decompression Dissertation*. PhD thesis, University of Graz, 2013. (page 64)

[131] M. Holler and K. Kunisch. On infimal convolution of TV-type functionals and applications to video and image reconstruction. *SIAM Journal on Imaging Sciences*, 7(4):2258–2300, nov 2014, doi: 10.1137/130948793. (page 112, 114)

[132] J. Hrabe and D. P. Lewis. Two analytical solutions for a model of pulsed arterial spin labeling with randomized blood arrival times. *Journal of Magnetic Resonance*, 167(1):49–55, mar 2004, doi: 10.1016/j.jmr.2003.11.002. (page 40)

[133] P. Irarrazabal and D. G. Nishimura. Fast Three Dimensional Magnetic Resonance Imaging. *Magnetic Resonance in Medicine*, 33(5):656–662, 1995, doi: 10.1002/mrm.1910330510. (page 31)

[134] D. Ivanov, J. Pfeuffer, A. Gardumi, K. Uludag, and B. A. Poser. 2D CAIPIRINHA improves accelerated 3D GRASE ASL. In *Proceedings of the 25th Annual Meeting of ISMRM*, page 3630, Honolulu, 2017. (page 95, 124, 125)

[135] H. Jahanian, D. C. Noll, and L. Hernandez-Garcia. B0 field inhomogeneity considerations in pseudo-continuous arterial spin labeling (pCASL): Effects on tagging efficiency and correction strategy. *NMR in Biomedicine*, 24(10):1202–1209, dec 2011, doi: 10.1002/nbm.1675. (page 51)

[136] G. H. Jahng, X. P. Zhu, G. B. Matson, M. W. Weiner, and N. Schuff. Improved perfusion-weighted MRI by a novel double inversion with proximal labeling of both tagged and control acquisitions. *Magnetic Resonance in Medicine*, 49(2):307–314, feb 2003, doi: 10.1002/mrm.10339. (page 15)

[137] M. Jenkinson, C. F. Beckmann, T. E. Behrens, M. W. Woolrich, and S. M. Smith. FSL. *NeuroImage*, 62(2):782–790, aug 2012, doi: 10.1016/j.neuroimage.2011.09.015. (page 156)

[138] B. Jian and B. C. Vemuri. Multi-fiber Reconstruction from Diffusion MRI Using Mixture of Wisharts and Sparse Deconvolution. In *Information Processing in Medical Imaging*, volume 4584 LNCS, pages 384–395. Springer Berlin Heidelberg, Berlin, Heidelberg, 2007, doi: 10.1007/978-3-540-73273-0_32. (page 58)

[139] T. Jin and S. G. Kim. Cortical layer-dependent dynamic blood oxygenation, cerebral blood flow and cerebral blood volume responses during visual stimulation. *NeuroImage*, 43(1):1–9, oct 2008, doi: 10.1016/j.neuroimage.2008.06.029. (page 177)

[140] J. B. Johnson. Thermal agitation of electricity in conductors. *Physical Review*, 32(1):97–109, 1928, doi: 10.1103/PhysRev.32.97. (page 92)

[141] K. A. Johnson, K. Hartwell, T. Lematty, J. Borckardt, P. S. Morgan, K. Govindarajan, K. Brady, and M. S. George. Intermittent "Real-time" fMRI Feedback Is Superior to Continuous Presentation for a Motor Imagery Task: A Pilot Study. *Journal of Neuroimaging*, 22(1):58–66, jan 2012, doi: 10.1111/j.1552-6569.2010.00529.x. (page 179)

[142] Y. Jung, E. C. Wong, and T. T. Liu. Multiphase pseudocontinuous arterial spin labeling (MP-PCASL) for robust quantification of cerebral blood flow. *Magnetic Resonance in Medicine*, 64(3):799–810, sep 2010, doi: 10.1002/mrm.22465. (page 51)

[143] S. S. Kety and C. F. Schmidt. The determination of cerebral blood flow in man by the use of nitrous oxide in low concentrations. *American Journal of Physiology-Legacy Content*, 143(1):53–66, 1945, doi: 10.1152/ajplegacy.1945.143.1.53. (page 1)

[144] S.-G. Kim. Quantification of relative cerebral blood flow change by flow-sensitive alternating inversion recovery (FAIR) technique: Application to functional mapping. *Magnetic Resonance in Medicine*, 34(3):293–301, sep 1995, doi: 10.1002/mrm.1910340303. (page 15, 18, 19)

[145] S. G. Kim, E. Rostrup, H. B. Larsson, S. Ogawa, and O. B. Paulson. Determination of relative CMRO2 from CBF and BOLD changes: Significant increase of oxygen consumption rate during visual stimulation. *Magnetic Resonance in Medicine*, 41(6):1152–1161, 1999, doi: 10.1002/(SICI)1522-2594(199906)41:6⟨1152::AID-MRM11⟩3.0.CO;2-T. (page 115)

[146] N. Kimura, H. Nakama, K. Nakamura, Y. Aso, and T. Kumamoto. Effect of white matter lesions on brain perfusion in alzheimer's disease. *Dementia and Geriatric Cognitive Disorders*, 34(3-4):256–261, dec 2012, doi: 10.1159/000345184. (page 176)

[147] F. Knoll, K. Bredies, T. Pock, and R. Stollberger. Second order total generalized variation (TGV) for MRI. *Magnetic Resonance in Medicine*, 65(2):480–491, feb 2011, doi: 10.1002/mrm.22595. (page 60, 61)

[148] F. Knoll, K. Bredies, T. Pock, and R. Stollberger. Second order total generalized variation (TGV) for MRI. *Magnetic Resonance in Medicine*, 65(2):480–491, feb 2011, doi: 10.1002/mrm.22595. (page 70, 114)

[149] F. Knoll, M. Freiberger, K. Bredies, and R. Stollberger. AGILE: An open source library for image reconstruction using graphics card hardware acceleration. In *Proceedings of the 19th Annual Meeting of ISMRM*, page 2554, 2011. (page 114, 151, 152, 156)

[150] G. Krüger and G. H. Glover. Physiological noise in oxygenation-sensitive magnetic resonance imaging. *Magnetic Resonance in Medicine*, 46(4):631–637, oct 2001, doi: 10.1002/mrm.1240. (page 92)

[151] K. K. Kwong, J. W. Belliveau, D. A. Chesler, I. E. Goldberg, R. M. Weisskoff, B. P. Poncelet, D. N. Kennedy, B. E. Hoppel, M. S. Cohen, R. Turner, H. M. Cheng -, T. J. Brady, and B. R. Rosen. Dynamic magnetic resonance imaging of human brain activity during primary sensory stimulation. *Proceedings of the National Academy of Sciences of the United States of America*, 89(12):5675–5679, jun 1992, doi: 10.1073/pnas.89.12.5675. (page 2, 6, 14, 116, 138)

[152] K. K. Kwong, D. A. Chesler, R. M. Weisskoff, K. M. Donahue, T. L. Davis, L. Ostergaard, T. A. Campbell, and B. R. Rosen. MR perfusion studies with t1-weighted echo planar imaging. *Magnetic Resonance in Medicine*, 34(6):878–887, 1995, doi: 10.1002/mrm.1910340613. (page 15, 18)

[153] N. Lazar. The Statistical Analysis of Functional MRI Data. *Journal of Statistical Software*, 29(Book Review 3), 2009, doi: 10.18637/jss.v029.b03. (page 93)

[154] D. Le Gall and A. Tabatabai. Sub-band coding of digital images using symmetric short kernel filters and arithmetic coding techniques. In *ICASSP-88., International Conference on Acoustics, Speech, and Signal Processing*, pages 761–764 vol.2. IEEE, 1988, doi: 10.1109/ICASSP.1988.196696. (page 73)

[155] K. L. Leenders, D. Perani, A. A. Lammertsma, J. D. Heather, P. Buckingham, M. J. Healy, J. M. Gibbs, R. J. Wise, J. Hatazawa, and S. Herold. Cerebral blood flow, blood volume and oxygen utilization. Normal values and effect of age. *Brain:a journal of neurology*, 113(1):27–47, feb 1990. (page 6, 68, 95, 125, 154)

[156] O. Leontiev and R. B. Buxton. Reproducibility of BOLD, perfusion, and CMRO2 measurements with calibrated-BOLD fMRI. *NeuroImage*, 35(1):175–184, mar 2007, doi: 10.1016/j.neuroimage.2006.10.044. (page 116, 138)

[157] A. Lesch, C. S. Aigner, S. M. Spann, M. Schloegl, and R. Stollberger. 3D Bloch-Siegert EPI B1+-mapping. In *Proceedings of the 27th Annual Meeting of ISMRM*, Montreal, 2019. (page)

[158] W. Li, P. Liu, H. Lu, J. J. Strouse, P. C. van Zijl, and Q. Qin. Fast measurement of blood T1 in the human carotid artery at 3T: Accuracy, precision, and reproducibility. *Magnetic Resonance in Medicine*, 77(6):2296–2302, jun 2017, doi: 10.1002/mrm.26325. (page 54)

[159] Y. Li, D. Mao, Z. Li, M. Schär, J. J. Pillai, J. G. Pipe, and H. Lu. Cardiac-triggered pseudo-continuous arterial-spin-labeling: A cost-effective scheme to further enhance the reliability of arterial-spin-labeling MRI. *Magnetic Resonance in Medicine*, 80(3):969–975, sep 2018, doi: 10.1002/mrm.27090. (page 92, 107)

[160] X. Liang, A. Connelly, and F. Calamante. Improved partial volume correction for single inversion time arterial spin labeling data. *Magnetic resonance in medicine*, 69(2):531–7, feb 2013, doi: 10.1002/mrm.24279. (page 47)

[161] X. Liang, A. Connelly, and F. Calamante. Voxel-Wise Functional Connectomics Using Arterial Spin Labeling Functional Magnetic Resonance Imaging: The Role of Denoising. *Brain connectivity*, 5(9):543–53, nov 2015, doi: 10.1089/brain.2014.0290. (page 56, 71, 73, 74, 98)

[162] X. Liang, A. Connelly, J.-D. Tournier, and F. Calamante. A variable flip angle-based method for reducing blurring in 3D GRASE ASL. *Physics in Medicine and Biology*, 59(18):5559–5573, sep 2014, doi: 10.1088/0031-9155/59/18/5559. (page 29, 148, 171, 180)

[163] T. Lindner, M. Helle, and O. Jansen. A Short Introduction to Arterial Spin Labeling and its Application to Flow Territory Mapping. *Clinical Neuroradiology*, 25(2):211–218, oct 2015, doi: 10.1007/s00062-015-0450-7. (page 43)

[164] F. Liu, J. V. Velikina, W. F. Block, R. Kijowski, and A. A. Samsonov. Fast Realistic MRI Simulations Based on Generalized Multi-Pool Exchange Tissue Model. *IEEE Transactions on Medical Imaging*, 36(2):527–537, feb 2017, doi: 10.1109/TMI.2016.2620961. (page 95, 125)

[165] P. Liu, J. Uh, and H. Lu. Determination of spin compartment in arterial spin labeling MRI. *Magnetic Resonance in Medicine*, 65(1):120–127, jan 2011, doi: 10.1002/mrm.22601. (page 24)

[166] T. T. Liu. Arterial Spin Labeling for functional Neuroimaging. In *MR an CT Perfusion and Pharmacokinetic Imaging*, pages 1136–1147. Wolters Kluwer, 2016. (page 116)

[167] T. T. Liu and E. C. Wong. A signal processing model for arterial spin labeling functional MRI. *NeuroImage*, 24(1):207–215, jan 2005, doi: 10.1016/j.neuroimage.2004.09.047. (page 118, 139)

[168] Y. Liu, X. Zhu, D. Feinberg, M. Guenther, J. Gregori, M. W. Weiner, and N. Schuff. Arterial spin labeling MRI study of age and gender effects on brain perfusion hemodynamics. *Magnetic Resonance in Medicine*, 68(3):912–922, sep 2012, doi: 10.1002/mrm.23286. (page 88)

[169] H. Lu, C. Clingman, X. Golay, and P. C. M. van Zijl. Determining the longitudinal relaxation time (T1) of blood at 3.0 Tesla. *Magnetic resonance in medicine*, 52(3):679–82, sep 2004, doi: 10.1002/mrm.20178. (page 23, 24, 69, 98, 126, 140, 154)

[170] W. M. Luh, E. C. Wong, P. A. Bandettini, and J. S. Hyde. QUIPSS II with thin-slice TI1 periodic saturation: a method for improving accuracy of quantitative perfusion imaging using pulsed arterial spin labeling. *Magnetic resonance in medicine*, 41(6):1246–54, jun 1999. (page 15, 67)

[171] W. M. Luh, S. L. Talagala, T. Q. Li, and P. A. Bandettini. Pseudo-continuous arterial spin labeling at 7 T for human brain: Estimation and correction for off-resonance effects using a Prescan. *Magnetic Resonance in Medicine*, 69(2):402–410, feb 2013, doi: 10.1002/mrm.24266. (page 51)

[172] W. M. Luh, E. C. Wong, P. A. Bandettini, B. D. Ward, and J. S. Hyde. Comparison of simultaneously measured perfusion and bold signal increases during brain activation with T1-based tissue identification. *Magnetic Resonance in Medicine*, 44(1):137–143, jul 2000, doi: 10.1002/1522-2594(200007)44:1⟨137::AID-MRM20⟩3.0.CO;2-R. (page 116, 138)

[173] W. M. Luh, E. C. Wong, S. L. Talagala, and P. A. Bandettini. Tagging Efficiency Improvement Using Velocity-matched Pseudo-continuous Arterial Spin Labeling and VERSE. In *Proceedings of the 16th Annual Meeting of ISMRM*, page 3341, 2008. (page 51)

[174] V. M. Mai, K. D. Hagspiel, J. M. Christopher, H. M. Do, T. Altes, J. Knight-Scott, A. L. Stith, T. Maier, and S. S. Berr. Perfusion imaging of the human lung using flow-sensitive Alternating Inversion Recovery with an Extra Radiofrequency pulse (FAIRER). *Magnetic Resonance Imaging*, 17(3):355–361, apr 1999, doi: 10.1016/S0730-725X(98)00190-8. (page 15)

[175] O. Maier, M. Schloegl, K. Bredies, and R. Stollberger. 3D Model-Based Parameter Quantification on Resource Constrained Hardware using Double-Buffering. In *Proceedings of the 27th Annual Meeting of ISMRM*, page 4839, 2019. (page 171, 177)

[176] O. Maier, S. M. Spann, L. Bogensperger, and R. Stollberger. Fast Simultaneous Multi-Slice Multi-Shell Diffusion Tensor Imaging with Model-based Reconstruction. In *Proceedings of the 28th Annual Meeting of ISMRM*, 2020. (page)

[177] O. Maier, S. M. Spann, D. Pinter, T. Gattringer, N. Hinteregger, C. Enzinger, J. Pfeuffer, K. Bredies, and R. Stollberger. Non-linear fitting with joint spatial regularization in Arterial Spin Labeling. *submitted to Medical Image Analysis.* (page)

[178] O. Maier, S. M. Spann, D. Pinter, T. Gattringer, L. Pirpamer, C. Enzinger, J. Pfeuffer, and R. Stollberger. Robust Perfusion Parameter Quantification from 3D Single-Shot Multi-Delay ASL measurements. In *Proceedings of the 28th Annual Meeting of ISMRM*, 2020. (page)

[179] N. Maleki, W. Dai, and D. C. Alsop. Optimization of background suppression for arterial spin labeling perfusion imaging. *Magnetic Resonance Materials in Physics, Biology and Medicine*, 25(2):127–133, apr 2012, doi: 10.1007/s10334-011-0286-3. (page 34, 47, 49, 148)

[180] D. M. Mandell, J. S. Han, J. Poublanc, A. P. Crawley, A. Kassner, J. A. Fisher, and D. J. Mikulis. Selective reduction of blood flow to white matter during hypercapnia corresponds with leukoaraiosis. *Stroke*, 39(7):1993–1998, jul 2008, doi: 10.1161/STROKEAHA.107.501692. (page 176)

[181] P. Mansfield. Multi-planar image formation using NMR spin echoes. *Journal of Physics C: Solid State Physics*, 10(3):L55—-L58, 1977, doi: 10.1088/0022-3719/10/3/004. (page 26)

[182] H. S. Markus. Cerebral perfusion and stroke. *Journal of Neurology, Neurosurgery and Psychiatry*, 75(3):353–361, mar 2004, doi: 10.1136/jnnp.2003.025825. (page 5, 6, 8)

[183] C. Maumet, P. Maurel, J.-C. Ferré, and C. Barillot. Robust estimation of the cerebral blood flow in arterial spin labelling. *Magnetic resonance imaging*, 32(5):497–504, jun 2014, doi: 10.1016/j.mri.2014.01.016. (page 56)

[184] E. R. Mcveigh, R. M. Henkelman, and M. J. Bronskill. Noise and filtration in magnetic resonance imaging. *Medical Physics*, 12(5):586–591, sep 1985, doi: 10.1118/1.595679. (page 92)

[185] M. Möller, M. Freund, C. Greiner, W. Schwindt, C. Gaus, and W. Heindel. Real time fMRI: A tool for the routine presurgical localisation of the motor cortex. *European Radiology*, 15(2):292–295, feb 2005, doi: 10.1007/s00330-004-2513-z. (page 138)

[186] M. Murphy, M. Alley, J. Demmel, K. Keutzer, S. Vasanawala, and M. Lustig. Fast l1-SPIRiT compressed sensing parallel imaging MRI: scalable parallel implementation and clinically feasible runtime. *IEEE transactions on medical imaging*, 31(6):1250–62, jun 2012, doi: 10.1109/TMI.2012.2188039. (page 151)

[187] H. J. Mutsaerts, J. Petr, D. L. Thomas, E. De Vita, D. M. Cash, M. J. van Osch, X. Golay, P. F. Groot, S. Ourselin, J. van Swieten, R. Laforce, F. Tagliavini, B. Borroni, D. Galimberti, J. B. Rowe, C. Graff, F. B. Pizzini, E. Finger, S. Sorbi, M. Castelo Branco, J. D. Rohrer, M. Masellis, B. J. MacIntosh, and G. Investigators. Comparison of arterial spin labeling registration strategies in the multi-center GENetic frontotemporal dementia initiative (GENFI). *Journal of Magnetic Resonance Imaging*, 47(1):131–140, jan 2018, doi: 10.1002/jmri.25751. (page 126, 154)

[188] E. M. Nemoto, H. Yonas, and Y. Chang. Stages and thresholds of hemodynamic failure. *Stroke*, 34(1):2–3, jan 2003, doi: 10.1161/01.str.0000041048.33908.18. (page xvii, 6, 7)

[189] D. G. Norris and C. Schwarzbauer. Velocity Selective Radiofrequency Pulse Trains. *Journal of Magnetic Resonance*, 137(1):231–236, 1999, doi: 10.1006/jmre.1998.1690. (page 9, 40)

[190] H. Nyquist. Thermal agitation of electric charge in conductors. *Physical Review*, 32(1):110–113, 1928, doi: 10.1103/PhysRev.32.110. (page 92)

[191] S. Ogawa, T. M. Lee, A. R. Kay, and D. W. Tank. Brain magnetic resonance imaging with contrast dependent on blood oxygenation. *Proceedings of the National Academy of Sciences*, 87(24):9868–9872, dec 1990, doi: 10.1073/pnas.87.24.9868. (page 115)

[192] K. K. Oguz, X. Golay, F. B. Pizzini, C. A. Freer, N. Winrow, R. Ichord, J. F. Casella, P. C. Van Zijl, and E. R. Melhem. Sickle cell disease: Continuous arterial spin-labeling perfusion MR imaging in children. *Radiology*, 227(2):567–574, may 2003, doi: 10.1148/radiol.2272020903. (page 8)

[193] N. D. Orlov, V. Giampietro, O. O'Daly, S. L. Lam, G. J. Barker, K. Rubia, P. McGuire, S. S. Shergill, and P. Allen. Real-time fMRI neurofeedback to downregulate superior temporal gyrus activity in patients with schizophrenia and auditory hallucinations: A proof-of-concept study. *Translational Psychiatry*, 8(1):1–10, dec 2018, doi: 10.1038/s41398-017-0067-5. (page 138)

[194] K. Oshio and D. A. Feinberg. GRASE (Gradient- and Spin- Echo) imaging: A novel fast MRI technique. *Magnetic Resonance in Medicine*, 20(2):344–349, aug 1991, doi: 10.1002/mrm.1910200219. (page 29)

[195] D. Owen, A. Melbourne, Z. Eaton-Rosen, D. L. Thomas, N. Marlow, J. Rohrer, and S. Ourselin. Deep convolutional filtering for spatio-temporal denoising and artifact removal in arterial spin labelling MRI. In *Medical Image Computing and Computer Assisted Intervention - MICCAI*, volume 11070 LNCS, pages 21–29. Springer Verlag, sep 2018, doi: 10.1007/978-3-030-00928-1_3. (page 175)

[196] L. M. Parkes. Quantification of cerebral perfusion using arterial spin labeling: Two-compartment models. *Journal of Magnetic Resonance Imaging*, 22(6):732–736, dec 2005, doi: 10.1002/jmri.20456. (page 39, 40)

[197] L. M. Parkes, W. Rashid, D. T. Chard, and P. S. Tofts. Normal Cerebral Perfusion Measurements Using Arterial Spin Labeling: Reproducibility, Stability, and Age and Gender Effects. *Magnetic Resonance in Medicine*, 51(4):736–743, apr 2004, doi: 10.1002/mrm.20023. (page 88)

[198] L. M. Parkes and P. S. Tofts. Improved accuracy of human cerebral blood perfusion measurements using arterial spin labeling: Accounting for capillary water permeability. *Magnetic Resonance in Medicine*, 48(1):27–41, jul 2002, doi: 10.1002/mrm.10180. (page 39)

[199] B. Pasley and R. Freeman. Neurovascular coupling. *Scholarpedia*, 3(3):5340, 2008, doi: 10.4249/scholarpedia.5340. (page 115)

[200] E. T. Petersen, T. Lim, and X. Golay. Model-free arterial spin labeling quantification approach for perfusion MRI. *Magnetic Resonance in Medicine*, 55(2):219–232, feb 2006, doi: 10.1002/mrm.20784. (page 15)

[201] E. T. Petersen, K. Mouridsen, and X. Golay. The QUASAR reproducibility study, Part II: Results from a multi-center Arterial Spin Labeling test-retest study. *NeuroImage*, 49(1):104–113, jan 2010, doi: 10.1016/j.neuroimage.2009.07.068. (page 95, 125)

[202] J. Petr, J.-C. Ferre, J.-Y. Gauvrit, and C. Barillot. Improving arterial spin labeling data by temporal filtering. In B. M. Dawant and D. R. Haynor, editors, *SPIE Medical Imaging*, page 76233B. International Society for Optics and Photonics, mar 2010, doi: 10.1117/12.843960. (page 47, 56, 71)

[203] J. Petr, H. J. Mutsaerts, E. De Vita, R. M. Steketee, M. Smits, A. J. Nederveen, F. Hofheinz, J. van den Hoff, and I. Asllani. Effects of systematic partial volume errors on the estimation of gray matter cerebral blood flow with arterial spin labeling MRI. *Magnetic Resonance Materials in Physics, Biology and Medicine*, 31(6):725–734, dec 2018, doi: 10.1007/s10334-018-0691-y. (page 47)

[204] J. Petr, G. Schramm, F. Hofheinz, J. Langner, and J. van den Hoff. Partial volume correction in arterial spin labeling using a Look-Locker sequence. *Magnetic Resonance in Medicine*, 70(6):1535–1543, dec 2013, doi: 10.1002/mrm.24601. (page 9)

[205] J. Pfeuffer, G. Adriany, A. Shmuel, E. Yacoub, P.-F. Van De Moortele, X. Hu, and K. Ugurbil. Perfusion-based high-resolution functional imaging in the human brain at 7 Tesla. *Magnetic resonance in medicine*, 47(5):903–11, may 2002, doi: 10.1002/mrm.10154. (page 55)

[206] D. L. Phillips. A Technique for the Numerical Solution of Certain Integral Equations of the First Kind. *Journal of the ACM (JACM)*, 9(1):84–97, jan 1962, doi: 10.1145/321105.321114. (page 58)

[207] M. A. F. Pimentel, P. Vilela, I. Sousa, and P. Figueiredo. Localization of the hand motor area by arterial spin labeling and blood oxygen level-dependent functional magnetic resonance imaging. *Human Brain Mapping*, 34(1):96–108, jan 2013, doi: 10.1002/hbm.21418. (page 116, 138)

[208] J. Pinto, M. A. Chappell, T. W. Okell, M. Mezue, A. R. Segerdahl, I. Tracey, P. Vilela, and P. Figueiredo. Calibration of arterial spin labeling data - potential pitfalls in post-processing. *Magnetic Resonance in Medicine*, 83(4):1222–1234, apr 2020, doi: 10.1002/mrm.28000. (page 53)

[209] J. M. Pollock, H. Tan, R. A. Kraft, C. T. Whitlow, J. H. Burdette, and J. A. Maldjian. Arterial Spin-Labeled MR Perfusion Imaging: Clinical Applications, may 2009, doi: 10.1016/j.mric.2009.01.008. (page 51)

[210] W. J. Powers. Cerebral hemodynamics in ischemic cerebrovascular disease. *Annals of Neurology*, 29(3):231–240, 1991, doi: 10.1002/ana.410290302. (page 5)

[211] K. P. Pruessmann, M. Weiger, M. B. Scheidegger, and P. Boesiger. SENSE: Sensitivity encoding for fast MRI. *Magnetic Resonance in Medicine*, 42(5):952–962, 1999, doi: 10.1002/(SICI)1522-2594(199911)42:5⟨952::AID-MRM16⟩3.0.CO;2-S. (page 92)

[212] D. Raj, A. W. Anderson, and J. C. Gore. Respiratory effects in human functional magnetic resonance imaging due to bulk susceptibility changes. *Physics in Medicine and Biology*, 46(12):3331–3340, 2001, doi: 10.1088/0031-9155/46/12/318. (page 92)

[213] D. Raj, D. P. Paey, A. W. Anderson, R. P. Kennan, and J. C. Gore. A model for susceptibility artefacts from respiration in functional echo-planar magnetic resonance imaging. *Physics in Medicine and Biology*, 45(12):3809–3820, 2000, doi: 10.1088/0031-9155/45/12/321. (page 92)

[214] J. Rajan, J. Van Audekerke, A. Van Der Linden, M. Verhoye, and J. Sijbers. An adaptive non local maximum likelihood estimation method for denoising magnetic resonance images. In *Proceedings - International Symposium on Biomedical Imaging*, pages 1136–1139, 2012, doi: 10.1109/ISBI.2012.6235760. (page 57)

[215] R. Ranftl, K. Bredies, and T. Pock. Non-local total generalized variation for optical flow estimation. In *Medical Image Computing and Computer Assisted Intervention - MICCAI*, volume 8689 LNCS, pages 439–454. Springer Verlag, 2014, doi: 10.1007/978-3-319-10590-1_29. (page 175)

[216] H. Raoult, J. Petr, E. Bannier, A. Stamm, J.-Y. Gauvrit, C. Barillot, and J.-C. Ferré. Arterial spin labeling for motor activation mapping at 3T with a 32-channel coil: Reproducibility and spatial accuracy in comparison with BOLD fMRI. *NeuroImage*, 58(1):157–167, 2011, doi: 10.1016/j.neuroimage.2011.06.011. (page 116, 138)

[217] K. Restom, Y. Behzadi, and T. T. Liu. Physiological noise reduction for arterial spin labeling functional MRI. *NeuroImage*, 31(3):1104–1115, jul 2006, doi: 10.1016/j.neuroimage.2006.01.026. (page 92)

[218] L. I. Rudin, S. Osher, and E. Fatemi. Nonlinear total variation based noise removal algorithms. *Physica D: Nonlinear Phenomena*, 60(1-4):259–268, nov 1992, doi: 10.1016/0167-2789(92)90242-F. (page 59, 151)

[219] S. Ruiz, S. Lee, S. R. Soekadar, A. Caria, R. Veit, T. Kircher, N. Birbaumer, and R. Sitaram. Acquired self-control of insula cortex modulates emotion recognition and brain network connectivity in schizophrenia. *Human Brain Mapping*, 34(1):200–212, jan 2013, doi: 10.1002/hbm.21427. (page 138)

[220] M. Salari, S. H. Aboutalebi, K. Konstantinov, and H. K. Liu. A highly ordered titania nanotube array as a supercapacitor electrode. *Physical Chemistry Chemical Physics*, 13(11):5038–5041, 2011, doi: 10.1039/c0cp02054k. (page 5)

[221] M. Schloegl, M. Holler, A. Schwarzl, K. Bredies, and R. Stollberger. Infimal convolution of total generalized variation functionals for dynamic MRI. *Magnetic Resonance in Medicine*, 78(1):142–155, jul 2017, doi: 10.1002/mrm.26352. (page 112)

[222] M. Schloegl, S. M. Spann, C. S. Aigner, M. Holler, K. Bredies, and R. Stollberger. Improved Denoising of Dynamic Arterial Spin Labeling with Infimal Convolution of Total Generalized Variation. In *Proceedings of the 25th Annual Meeting of ISMRM*, Honolulu, 2017. (page 63, 70, 114, 151, 152)

[223] S. Schmid. Arterial spin labeling in space and time : new MRI sequences to probe cerebral hemodynamics. 2017. (page xx, 44)

[224] S. Schmid, E. Ghariq, W. M. Teeuwisse, A. Webb, and M. J. P. van Osch. Acceleration-selective arterial spin labeling. *Magnetic Resonance in Medicine*, 71(1):191–199, jan 2014, doi: 10.1002/mrm.24650. (page xix, 9, 42)

[225] M. A. Schwarzbach, S. M. Spann, C. S. Aigner, K. Hammernik, T. Pock, and R. Stollberger. Combining Variational Optimization and Deep Learning for efficient ASL image quality enhancement. In *Magnetic Resonance Materials in Physics, Biology and Medicine*, Rotterdam, 2019. (page 175, 179)

[226] C. Schwarzbauer and W. Heinke. BASE imaging: A new spin labeling technique for measuring absolute perfusion changes. *Magnetic Resonance in Medicine*, 39(5):717–722, may 1998, doi: 10.1002/mrm.1910390508. (page 15)

[227] X. Shao, S. M. Spann, K. Wang, L. Yan, R. Stollberger, and D. J. Wang. High-resolution whole brain ASL perfusion imaging at 7T with 12-fold acceleration and spatial-temporal regularized reconstruction. In *Proceedings of the 28th Annual Meeting of ISMRM*, 2020. (page 181)

[228] X. Shao and D. J. Wang. Single shot high resolution 3D arterial spin labeling using 2D CAIPI and ESPIRiT reconstruction. In *Proceedings of the 25th Annual Meeting of ISMRM*, page 3629, 2017. (page 49, 54, 148, 171)

[229] X. Shao, K. Wang, and D. J. Wang. 7T high - resolution arterial spin labeling reveals layer dependent cerebral blood flow. In *In Proceedings of the 27th Annual Meeting of ISMRM*, page 849, 2019. (page 177)

[230] X. Shao, Y. Wang, S. Moeller, and D. J. Wang. A constrained slice-dependent background suppression scheme for simultaneous multislice pseudo-continuous arterial spin labeling. *Magnetic Resonance in Medicine*, 79(1):394–400, jan 2018, doi: 10.1002/mrm.26643. (page 49, 149)

[231] K. Shimizu, N. Kosaka, T. Yamamoto, H. Shioura, T. Kodera, K.-i. Kikuta, and H. Kimura. Arterial spin labeling perfusion-weighted MRI for long-term follow-up of a cerebral arteriovenous malformation after stereotactic radiosurgery. *Acta Radiologica Short Reports*, 3(1):204798161351016, jan 2014, doi: 10.1177/2047981613510160. (page 8)

[232] D. D. Shin, H. L. Liu, E. C. Wong, and T. T. Liu. Effect of background suppression on CBF quantitation in pseudo continuous arterial spin labeling. *International Society for Magnetic Resonance in Medicine*, 268(1991):2101, 2011. (page 48)

[233] D. D. Shin, T. T. Liu, E. C. Wong, A. Shankaranarayanan, and Y. Jung. Pseudocontinuous arterial spin labeling with optimized tagging efficiency. *Magnetic Resonance in Medicine*, 68(4):1135–1144, oct 2012, doi: 10.1002/mrm.24113. (page 51)

[234] Z. Shirzadi, D. E. Crane, A. D. Robertson, P. J. Maralani, R. I. Aviv, M. A. Chappell, B. I. Goldstein, S. E. Black, and B. J. MacIntosh. Automated removal of spurious intermediate cerebral blood flow volumes improves image quality among older patients: A clinical arterial spin labeling investigation. *Journal of Magnetic Resonance Imaging*, 42(5):1377–1385, nov 2015, doi: 10.1002/jmri.24918. (page 56)

[235] K. Shmueli, P. van Gelderen, J. A. de Zwart, S. G. Horovitz, M. Fukunaga, J. M. Jansma, and J. H. Duyn. Low-frequency fluctuations in the cardiac rate as a source of variance in the resting-state fMRI BOLD signal. *NeuroImage*, 38(2):306–320, nov 2007, doi: 10.1016/j.neuroimage.2007.07.037. (page 116)

[236] A. C. Silva, W. Zhang, D. S. Williams, and A. P. Koretsky. Multi- Slice MRI of Rat Brain Perfusion During Amphetamine Stimulation Using Arterial Spin Labeling. *Magnetic Resonance in Medicine*, 33(2):209–214, feb 1995, doi: 10.1002/mrm.1910330210. (page 14)

[237] A. M. Smith, B. K. Lewis, U. E. Ruttimann, F. Q. Ye, T. M. Sinnwell, Y. Yang, J. H. Duyn, and J. A. Frank. Investigation of low frequency drift in fMRI signal. *NeuroImage*, 9(5):526–533, 1999, doi: 10.1006/nimg.1999.0435. (page 116)

[238] D. K. Sodickson and W. J. Manning. Simultaneous acquisition of spatial harmonics (SMASH): Fast imaging with radiofrequency coil arrays. *Magnetic Resonance in Medicine*, 38(4):591–603, oct 1997, doi: 10.1002/mrm.1910380414. (page 92)

[239] M. Sokolska, A. Bainbridge, A. Rojas-Villabona, X. Golay, and D. L. Thomas. Effect of labelling plane angulation and position on labelling efficiency and cerebral blood flow quantification in pseudo-continuous arterial spin labelling. *Magnetic Resonance Imaging*, 59:61–67, jun 2019, doi: 10.1016/j.mri.2019.02.007. (page 51)

[240] S. M. Spann. Spatio-Temporal TGV denoising for ASL perfusion imaging. In *INGE ST Forschungspreisverleihung*, Graz, Austria, 2018. (page)

[241] S. M. Spann. New Horizons for Arterial Spin Labeling - MRI Encoding Meets Information Technology. In *4th Human- and Biotechnology FoE Day*, Graz, Austria, 2019. (page)

[242] S. M. Spann. Robust 3D Brain Perfusion Imaging using Arterial Spin Labeling. In *INGE ST Netzwerktreffen*, Graz, Austria, 2019. (page)

[243] S. M. Spann. New Horizons for Arterial Spin Labeling. *TU Graz research*, pages 27–29, 2020. (page)

[244] S. M. Spann, C. S. Aigner, K. S. Kazimierski, M. Kraiger, and R. Stollberger. Total generalized variation (TGV) for spatio-temporal denoising of high resolution ASL perfusion data. In *Magnetic Resonance Materials in Physics, Biology and Medicine*, Vienna, 2016. (page)

[245] S. M. Spann, C. S. Aigner, M. Schloegl, A. Lesch, K. Bredies, S. Ropele, D. Pinter, L. Pirpamer, and R. Stollberger. Acceleration of ASL data acquisition using spatio-temporal TGV Reconstruction. In *Proceedings of the 26th Annual Meeting of ISMRM*, Paris, 2018. (page 149)

[246] S. M. Spann, D. Grössinger, C. S. Aigner, J. Pfeuffer, G. Wood, and R. Stollberger. Self-Regulation of Brain Functions using Real-Time Neurofeedback Functional Arterial Spin Labeling. In *Proceedings of the 28th Annual Meeting of ISMRM*, 2020. (page)

[247] S. M. Spann, K. S. Kazimierski, C. S. Aigner, M. Kraiger, K. Bredies, and R. Stollberger. Spatio-temporal TGV denoising for ASL perfusion imaging. *NeuroImage*, 157:81–96, aug 2017, doi: 10.1016/j.neuroimage.2017.05.054. (page 152, 154)

[248] S. M. Spann, K. S. Kazimierski, C. S. Aigner, M. Kraiger, and R. Stollberger. Influence of denoising techniques on the absolute CBF quantification of ASL perfusion data. In *BMT 2016 "Dreilaendertagung" Swiss, Austrian and German Societies of Biomedical Engineerin*, Basel, 2016. (page)

[249] S. M. Spann, K. S. Kazimierski, C. S. Aigner, M. Kraiger, and R. Stollberger. Total generalized variation (TGV) for spatio-temporal denoising of high resolution ASL perfusion data. In *Imaging with Modulated/Incomplete Data 2016*, Graz, 2016. (page)

[250] S. M. Spann, K. S. Kazimierski, C. S. Aigner, and R. Stollberger. Variational Denoising for Arterial Spin Labeling. In *SFB Statusseminar*, Admont, Austria, 2016. (page)

[251] S. M. Spann, K. S. Kazimierski, C. S. Aigner, and R. Stollberger. A denoising method for arterial spin labeling data based on total generalized variation (TGV) with a spatial varying regularization parameter. In *Proceedings of the 25th Annual Meeting of ISMRM*, Honolulu, 2017. (page)

[252] S. M. Spann, M. Schloegl, C. S. Aigner, K. Koschutnig, M. Holler, K. Bredies, and R. Stollberger. Improved functional Arterial Spin Labeling by spatio-temporal ICTGV denoising. In *Proceedings of the 26th Annual Meeting of ISMRM*, Paris, 2018. (page)

[253] S. M. Spann, X. Shao, D. J. Wang, C. S. Aigner, M. Schloegl, K. Bredies, and R. Stollberger. Improving temporal resolution of 3D Arterial Spin Labeling perfusion imaging by combining CAIPIRINHA encoding and spatio-temporal TGV reconstruction. In *Proceedings of the 27th Annual Meeting of ISMRM*, Montreal, 2019. (page 124)

[254] S. M. Spann, X. Shao, D. J. Wang, C. S. Aigner, M. Schloegl, K. Bredies, and R. Stollberger. Robust single-shot acquisition of high resolution whole brain ASL images by combining time-dependent 2D CAPIRINHA sampling with spatio-temporal TGV reconstruction. *NeuroImage*, page 116337, nov 2019, doi: 10.1016/J.NEUROIMAGE.2019.116337. (page)

[255] B. E. Studer, S. M. Jaeggi, M. Buschkuehl, Y.-F. Su, J. Jonides, and W. J. Perring. Improving Fluid Intelligence - Single N-back Is As Effective As Dual N-back. In *In Proceedings of the 50th Annual Meeting of the Psychonomic Society*, Boston, 2009. (page 116)

[256] L. Subramanian, J. V. Hindle, S. Johnston, M. V. Roberts, M. Husain, R. Goebe, and D. Linden. Real-time functional magnetic resonance imaging neurofeedback for treatment of Parkinson's disease. *Journal of Neuroscience*, 31(45):16309–16317, nov 2011, doi: 10.1523/JNEUROSCI.3498-11.2011. (page 138)

[257] M. S. Sussman, J. A. Stainsby, N. Robert, N. Merchant, and G. A. Wright. Variable-density adaptive imaging for high-resolution coronary artery MRI. In *Magnetic Resonance in Medicine*, volume 48, pages 753–764. John Wiley & Sons, Ltd, nov 2002, doi: 10.1002/mrm.10275. (page 32)

[258] Y. Suzuki, T. W. Okell, M. A. Chappell, and M. J. van Osch. A framework for motion correction of background suppressed arterial spin labeling perfusion images acquired with simultaneous multi-slice EPI. *Magnetic Resonance in Medicine*, 81(3):1553–1565, mar 2019, doi: 10.1002/mrm.27499. (page 49, 180)

[259] S. L. Talagala, F. Q. Ye, P. J. Ledden, and S. Chesnick. Whole-brain 3D perfusion MRI at 3.0 T using CASL with a separate labeling coil. *Magnetic Resonance in Medicine*, 52(1):131–140, jul 2004, doi: 10.1002/mrm.20124. (page 14)

[260] H. Tan, W. S. Hoge, C. A. Hamilton, M. Günther, and R. A. Kraft. 3D GRASE PROPELLER: Improved image acquisition technique for arterial spin labeling perfusion imaging. *Magnetic Resonance in Medicine*, 66(1):168–173, jul 2011, doi: 10.1002/mrm.22768. (page 49)

[261] H. Tan, J. A. Maldjian, J. M. Pollock, J. H. Burdette, L. Y. Yang, A. R. Deibler, and R. A. Kraft. A fast, effective filtering method for improving clinical pulsed arterial spin labeling MRI. *Journal of Magnetic Resonance Imaging*, 29(5):1134–1139, may 2009, doi: 10.1002/jmri.21721. (page 56, 70, 96)

[262] W. M. Teeuwisse, S. Schmid, E. Ghariq, I. M. Veer, and M. J. Van Osch. Time-encoded pseudocontinuous arterial spin labeling: Basic properties and timing strategies for human applications. *Magnetic Resonance in Medicine*, 72(6):1712–1722, dec 2014, doi: 10.1002/mrm.25083. (page 45, 51)

[263] W. M. Teeuwisse, A. G. Webb, and M. J. Van Osch. Arterial spin labeling at ultra-high field: All that glitters is not gold. *International Journal of Imaging Systems and Technology*, 20(1):62–70, feb 2010, doi: 10.1002/ima.20218. (page 47, 55, 56)

[264] M. E. Thomason, B. E. Burrows, J. D. Gabrieli, and G. H. Glover. Breath holding reveals differences in fMRI BOLD signal in children and adults. *NeuroImage*, 25(3):824–837, apr 2005, doi: 10.1016/j.neuroimage.2004.12.026. (page 116)

[265] K. R. Thulborn, J. C. Waterton, P. M. Matthews, and G. K. Radda. Oxygenation dependence of the transverse relaxation time of water protons in whole blood at high

field. *BBA - General Subjects*, 714(2):265–270, feb 1982, doi: 10.1016/0304-4165(82) 90333-6. (page 115)

[266] A. N. Tikhonov and V. Y. Arsenin. Solutions of Ill-Posed Problems (A. N. Tikhonov and V. Y. Arsenin). *SIAM Review*, 21(2):266–267, 1979, doi: 10.1137/1021044. (page 58)

[267] T. Tjandra, J. C. Brooks, P. Figueiredo, R. Wise, P. M. Matthews, and I. Tracey. Quantitative assessment of the reproducibility of functional activation measured with BOLD and MR perfusion imaging: Implications for clinical trial design. *NeuroImage*, 27(2):393–401, aug 2005, doi: 10.1016/j.neuroimage.2005.04.021. (page 116, 138)

[268] N. J. Tolentino, C. E. Wierenga, S. Hall, S. F. Tapert, M. P. Paulus, T. T. Liu, T. L. Smith, and M. A. Schuckit. Alcohol effects on cerebral blood flow in subjects with low and high responses to alcohol. *Alcoholism: Clinical and Experimental Research*, 35(6):1034–1040, jun 2011, doi: 10.1111/j.1530-0277.2011.01435.x. (page 6)

[269] M. Uecker, P. Lai, M. J. Murphy, P. Virtue, M. Elad, J. M. Pauly, S. S. Vasanawala, and M. Lustig. ESPIRiT-an eigenvalue approach to autocalibrating parallel MRI: Where SENSE meets GRAPPA. *Magnetic Resonance in Medicine*, 71(3):990–1001, mar 2014, doi: 10.1002/mrm.24751. (page 156)

[270] M. Uecker, F. Ong, J. I. Tamir, D. Bahri, P. Virtue, J. Y. Cheng, T. Zhang, and M. Lustig. Berkeley Advanced Reconstruction Toolbox. In *Proceedings of the 23th Annual Meeting of ISMRM*, page 2486, Toronto, 2015. (page 156)

[271] J. F. Utting, D. L. Thomas, D. G. Gadian, R. W. Helliar, M. F. Lythgoe, and R. J. Ordidge. Understanding and optimizing the amplitude modulated control for multiple-slice continuous arterial spin labeling. *Magnetic Resonance in Medicine*, 54(3):594–604, sep 2005, doi: 10.1002/mrm.20604. (page 13, 14)

[272] L. Vaclavu, V. Van Der Land, D. F. Heijtel, M. J. Van Osch, M. H. Cnossen, C. B. Majoie, A. Bush, J. C. Wood, K. J. Fijnvandraat, H. J. Mutsaerts, and A. J. Nederveen. In vivo T1 of blood measurements in children with sickle cell disease improve cerebral blood flow quantification from arterial spin-labeling MRI. In *American Journal of Neuroradiology*, volume 37, pages 1727–1732. American Society of Neuroradiology, sep 2016, doi: 10.3174/ajnr.A4793. (page 54)

[273] L. Vaclavu, M. Sokolska, A. J. Nederveen, and D. L. Thomas. Accounting for pCASL labelling efficiency variation in patients with low and high arterial blood flow velocities. In *In Proceedings of the 26th Annual Meeting of ISMRM*, page 5530, 2018. (page 50)

[274] T. Valkonen, K. Bredies, and F. Knoll. Total generalized variation in diffusion tensor imaging. *SIAM Journal on Imaging Sciences*, 6(1):487–525, feb 2013, doi: 10.1137/120867172. (page 61)

[275] A. H. Van Beek, J. A. Claassen, M. G. Rikkert, and R. W. Jansen. Cerebral autoregulation: An overview of current concepts and methodology with special focus on the elderly, jun 2008, doi: 10.1038/jcbfm.2008.13. (page 6)

[276] P. van Gelderen, J. de Zwart, and J. Duyn. Pittfalls of MRI measurement of white matter perfusion based on arterial spin labeling. *Magnetic Resonance in Medicine*, 59(4):788–795, apr 2008, doi: 10.1002/mrm.21515. (page 47)

[277] P. van Gelderen, J. de Zwart, P. Starewicz, R. Hinks, and J. Duyn. Real-time shimming to compensate for respiration-inducedB0 fluctuations. *Magnetic Resonance in Medicine*, 57(2):362–368, feb 2007, doi: 10.1002/mrm.21136. (page 92, 107)

[278] P. Van Gelderen, C. W. Wu, J. A. De Zwart, L. Cohen, M. Hallett, and J. H. Duyn. Resolution and reproducibility of BOLD and perfusion functional MRI at 3.0 tesla. *Magnetic Resonance in Medicine*, 54(3):569–576, sep 2005, doi: 10.1002/mrm.20577. (page 116)

[279] M. J. van Osch, W. M. Teeuwisse, Z. Chen, Y. Suzuki, M. Helle, and S. Schmid. Advances in arterial spin labelling MRI methods for measuring perfusion and collateral flow, sep 2018, doi: 10.1177/0271678X17713434. (page xx, 40, 41, 42, 43, 45, 46, 51, 54)

[280] J. Verbree and M. J. P. van Osch. Influence of the cardiac cycle on pCASL: cardiac triggering of the end-of-labeling. *Magnetic Resonance Materials in Physics, Biology and Medicine*, 31(1):223–233, feb 2018, doi: 10.1007/s10334-017-0611-6. (page 50, 170)

[281] M. Vidorreta, E. Balteau, Z. Wang, E. De Vita, M. A. Pastor, D. L. Thomas, J. A. Detre, and M. A. Fernández-Seara. Evaluation of segmented 3D acquisition schemes for whole-brain high-resolution arterial spin labeling at 3T. *NMR in Biomedicine*, 27(11):1387–1396, nov 2014, doi: 10.1002/nbm.3201. (page 31, 32)

[282] M. Vidorreta, Z. Wang, Y. V. Chang, D. A. Wolk, M. A. Fernández-Seara, and J. A. Detre. Whole-brain background-suppressed pCASL MRI with 1D-accelerated 3D RARE Stack-Of-Spirals readout. *PLOS ONE*, 12(8):e0183762, aug 2017, doi: 10.1371/journal.pone.0183762. (page 51, 95, 125, 148, 154, 181)

[283] M. Vidorreta, Z. Wang, I. Rodríguez, M. A. Pastor, J. A. Detre, and M. A. Fernández-Seara. Comparison of 2D and 3D single-shot ASL perfusion fMRI sequences. *NeuroImage*, 66:662–71, feb 2013, doi: 10.1016/j.neuroimage.2012.10.087. (page 31, 34, 47, 55, 95, 124, 126, 139, 148)

[284] R. Vidyasagar, A. Greyling, R. Draijer, D. R. Corfield, and L. M. Parkes. The effect of black tea and caffeine on regional cerebral blood flow measured with arterial spin labeling. *Journal of cerebral blood flow and metabolism : official journal of the International Society of Cerebral Blood Flow and Metabolism*, 33(6):963–8, jul 2013, doi: 10.1038/jcbfm.2013.40. (page 67)

[285] F. von Samson-Himmelstjerna, M. A. Chappell, J. Sobesky, and M. Günther. Subtraction free arterial spin labeling: a new Bayesian-inference based approach for gaining perfusion data from time encoded data. In *Proceedings of the 23th Annual Meeting of ISMRM*, page 275, 2015. (page 45)

[286] F. von Samson-Himmelstjerna, V. I. Madai, J. Sobesky, and M. Guenther. Walsh-ordered hadamard time-encoded pseudocontinuous ASL (WH pCASL). *Magnetic Resonance in Medicine*, 76(6):1814–1824, dec 2016, doi: 10.1002/mrm.26078. (page xx, 43, 44, 45, 46)

[287] J. T. Voyvodic. Real-time fMRI paradigm control, physiology, and behavior combined with near real-time statistical analysis. *NeuroImage*, 10(2):91–106, 1999, doi: 10.1006/nimg.1999.0457. (page 138)

[288] J. Vymazal, A. Righini, R. A. Brooks, M. Canesi, C. Mariani, M. Leonardi, and G. Pezzoli. T1 and T2 in the brain of healthy subjects, patients with Parkinson disease, and patients with multiple system atrophy: Relation to iron content. *Radiology*, 211(2):489–495, 1999, doi: 10.1148/radiology.211.2.r99ma53489. (page 54)

[289] D. J. Wang, Y. Chen, M. A. Fernández-Seara, and J. A. Detre. Potentials and challenges for arterial spin labeling in pharmacological magnetic resonance imaging. *Journal of Pharmacology and Experimental Therapeutics*, 337(2):359–366, may 2011, doi: 10.1124/jpet.110.172577. (page 6)

[290] J. Wang, G. K. Aguirre, D. Y. Kimberg, A. C. Roc, L. Li, and J. A. Detre. Arterial spin labeling perfusion fMRI with very low task frequency. *Magnetic Resonance in Medicine*, 49(5):796–802, may 2003, doi: 10.1002/mrm.10437. (page 168)

[291] J. Wang, D. C. Alsop, L. Li, J. Listerud, J. B. Gonzalez-At, M. D. Schnall, and J. A. Detre. Comparison of quantitative perfusion imaging using arterial spin labeling at 1.5 and 4.0 Tesla. *Magnetic resonance in medicine*, 48(2):242–54, aug 2002, doi: 10.1002/mrm.10211. (page 55)

[292] Z. Wang, A. Bovik, H. Sheikh, and E. Simoncelli. Image Quality Assessment: From Error Visibility to Structural Similarity. *IEEE Transactions on Image Processing*, 13(4):600–612, apr 2004, doi: 10.1109/TIP.2003.819861. (page 70, 71, 74, 98, 156)

[293] Z. Wang. Improving cerebral blood flow quantification for arterial spin labeled perfusion MRI by removing residual motion artifacts and global signal fluctuations.

Magnetic resonance imaging, 30(10):1409–15, dec 2012, doi: 10.1016/j.mri.2012.05.004. (page 47, 49, 56, 70, 96, 118, 155)

[294] Z. Wang, G. K. Aguirre, H. Rao, J. Wang, M. A. Fernández-Seara, A. R. Childress, and J. A. Detre. Empirical optimization of ASL data analysis using an ASL data processing toolbox: ASLtbx. *Magnetic resonance imaging*, 26(2):261–9, mar 2008, doi: 10.1016/j.mri.2007.07.003. (page 47, 49, 56, 70, 96, 118, 126, 155)

[295] Z. Wang, S. R. Das, S. X. Xie, S. E. Arnold, J. A. Detre, and D. A. Wolk. Arterial spin labeled MRI in prodromal Alzheimer's disease: A multi-site study. *NeuroImage: Clinical*, 2:630–636, 2013, doi: 10.1016/j.nicl.2013.04.014. (page 70, 96, 126, 148)

[296] C. Warmuth, M. Günther, and C. Zimmer. Quantification of blood flow in brain tumors: Comparison of arterial spin labeling and dynamic susceptibility-weighted contrast-enhanced MR imaging. *Radiology*, 228(2):523–532, aug 2003, doi: 10.1148/radiol.2282020409. (page 8)

[297] N. Weiskopf, R. Veit, M. Erb, K. Mathiak, W. Grodd, R. Goebel, and N. Birbaumer. Physiological self-regulation of regional brain activity using real-time functional magnetic resonance imaging (fMRI): Methodology and exemplary data. *NeuroImage*, 19(3):577–586, jul 2003, doi: 10.1016/S1053-8119(03)00145-9. (page 138)

[298] R. Weisskoff and R. Rzedzian. Optimal Sampling And Reconstruction Of Mri Signals Resulting From Sinusoidal Gradients. *IEEE Transactions on Signal Processing*, 39(9):2056–2065, 1991, doi: 10.1109/78.134437. (page 27)

[299] J. A. Wells, D. L. Thomas, M. D. King, A. Connelly, M. F. Lythgoe, and F. Calamante. Reduction of errors in ASL cerebral perfusion and arterial transit time maps using image de-noising. *Magnetic resonance in medicine*, 64(3):715–24, sep 2010, doi: 10.1002/mrm.22319. (page 47, 56, 61, 71, 72, 73, 84, 88)

[300] D. S. Williams, J. A. Detre, J. S. Leigh, and A. P. Koretsky. Magnetic resonance imaging of perfusion using spin inversion of arterial water. *Proceedings of the National Academy of Sciences of the United States of America*, 89(1):212–216, 1992, doi: 10.1073/pnas.89.1.212. (page 9, 10, 12, 13, 14)

[301] M. Wintermark, M. Sesay, E. Barbier, K. Borbély, W. P. Dillon, J. D. Eastwood, T. C. Glenn, C. B. Grandin, S. Pedraza, J.-F. Soustiel, T. Nariai, G. Zaharchuk, J.-M. Caillé, V. Dousset, and H. Yonas. Comparative overview of brain perfusion imaging techniques. *Stroke*, 36(9):e83–99, sep 2005, doi: 10.1161/01.STR.0000177884.72657.8b. (page 1, 8)

[302] R. L. Wolf, D. C. Alsop, M. L. McGarvey, J. A. Maldjian, J. Wang, and J. A. Detre. Susceptibility Contrast and Arterial Spin Labeled Perfusion MRI in Cerebrovascular

Disease. *Journal of Neuroimaging*, 13(1):17–27, jan 2003, doi: 10.1111/j.1552-6569.2003.tb00152.x. (page 8)

[303] D. A. Wolk and J. A. Detre. Arterial spin labeling MRI: An emerging biomarker for Alzheimer's disease and other neurodegenerative conditions, aug 2012, doi: 10.1097/WCO.0b013e328354ff0a. (page 2, 8)

[304] E. C. Wong, R. B. Buxton, and L. R. Frank. Implementation of quantitative perfusion imaging techniques for functional brain mapping using pulsed arterial spin labeling. *NMR in biomedicine*, 10(4-5):237–49, jan 1997. (page 15, 18, 67)

[305] E. C. Wong. Vessel-encoded arterial spin-labeling using pseudocontinuous tagging. *Magnetic Resonance in Medicine*, 58(6):1086–1091, dec 2007, doi: 10.1002/mrm.21293. (page 20, 43)

[306] E. C. Wong. An introduction to ASL labeling techniques, 2014, doi: 10.1002/jmri.24565. (page 12, 51)

[307] E. C. Wong, R. B. Buxton, and L. R. Frank. Implementation of quantitative perfusion imaging techniques for functional brain mapping using pulsed arterial spin labeling. *NMR in Biomedicine*, 10(4-5):237–249, 1997, doi: 10.1002/(SICI)1099-1492(199706/08)10:4/5⟨237::AID-NBM475⟩3.0.CO;2-X. (page 118, 139)

[308] E. C. Wong, R. B. Buxton, and L. R. Frank. Quantitative imaging of perfusion using a single subtraction (QUIPSS and QUIPSS II). *Magnetic Resonance in Medicine*, 39(5):702–708, may 1998, doi: 10.1002/mrm.1910390506. (page 15, 22, 23, 52, 69, 98)

[309] E. C. Wong, M. Cronin, W. C. Wu, B. Inglis, L. R. Frank, and T. T. Liu. Velocity-selective arterial spin labeling. *Magnetic Resonance in Medicine*, 55(6):1334–1341, jun 2006, doi: 10.1002/mrm.20906. (page xix, 9, 40, 41)

[310] J. G. Woods, M. A. Chappell, and T. W. Okell. A novel hybrid of time-encoded and sequential multi-PLD PCASL for improved cerebral blood flow estimation. In *Proceedings 26th Scientific Meeting, ISMRM*, page 2161, 2018. (page 45)

[311] J. G. Woods, M. A. Chappell, and T. W. Okell. A general framework for optimizing arterial spin labeling MRI experiments. *Magnetic Resonance in Medicine*, 81(4):2474–2488, apr 2019, doi: 10.1002/mrm.27580. (page 26, 170)

[312] W.-C. Wu, M. Fernández-Seara, J. A. Detre, F. W. Wehrli, and J. Wang. A theoretical and experimental investigation of the tagging efficiency of pseudocontinuous arterial spin labeling. *Magnetic Resonance in Medicine*, 58(5):1020–1027, nov 2007, doi: 10.1002/mrm.21403. (page 19, 20, 22, 50, 149)

[313] W. C. Wu, Y. Mazaheri, and E. C. Wong. The effects of flow dispersion and cardiac pulsation in arterial spin labeling. *IEEE Transactions on Medical Imaging*, 26(1):84–92, jan 2007, doi: 10.1109/TMI.2006.886807. (page 50)

[314] D. Xie, Y. Li, H. Yang, L. Bai, T. Wang, F. Zhou, L. Zhang, and Z. Wang. Denoising arterial spin labeling perfusion MRI with deep machine learning. *Magnetic Resonance Imaging*, 68:95–105, may 2020, doi: 10.1016/j.mri.2020.01.005. (page 175)

[315] G. Xu, H. A. Rowley, G. Wu, D. C. Alsop, A. Shankaranarayanan, M. Dowling, B. T. Christian, T. R. Oakes, and S. C. Johnson. Reliability and precision of pseudo-continuous arterial spin labeling perfusion MRI on 3.0T and comparison with 15O-water PET in elderly subjects at risk for Alzheimer's disease. *NMR in Biomedicine*, 23(3):286–293, apr 2009, doi: 10.1002/nbm.1462. (page 170)

[316] Y. Yang. Perfusion MR imaging with pulsed arterial spin-labeling: Basic principles and applications in functional brain imaging. *Concepts in Magnetic Resonance Part A: Bridging Education and Research*, 14(5):347–357, sep 2002, doi: 10.1002/cmr.10033. (page 116)

[317] Y. Yang, W. Engelien, S. Xu, H. Gu, D. A. Silbersweig, and E. Stern. Transit time, trailing time, and cerebral blood flow during brain activation: Measurement using multislice, pulsed spin-labeling perfusion imaging. *Magnetic Resonance in Medicine*, 44(5):680–685, 2000, doi: 10.1002/1522-2594(200011)44:5⟨680::AID-MRM4⟩3.0.CO;2-Q. (page 145)

[318] F. Q. Ye, J. A. Frank, D. R. Weinberger, and A. C. McLaughlin. Noise reduction in 3D perfusion imaging by attenuating the static signal in arterial spin tagging (ASSIST). *Magnetic resonance in medicine*, 44(1):92–100, jul 2000. (page 34, 47, 49, 148)

[319] K. D. Young, V. Zotev, R. Phillips, M. Misaki, H. Yuan, W. C. Drevets, and J. Bodurka. Real-time fMRI neurofeedback training of amygdala activity in patients with major depressive disorder. *PLoS ONE*, 9(2), feb 2014, doi: 10.1371/journal.pone.0088785. (page 138)

[320] G. Zaharchuk. Arterial Spin Labeling for Acute Stroke: Practical Considerations. *Translational Stroke Research*, 3(2):228–235, jun 2012, doi: 10.1007/s12975-012-0159-8. (page 24, 25, 26, 41)

[321] G. Zaharchuk. Arterial spin-labeled perfusion imaging in acute ischemic stroke, 2014, doi: 10.1161/STROKEAHA.113.003612. (page 8)

[322] H. Zeng and R. T. Constable. Image distortion correction in EPI: Comparison of field mapping with point spread function mapping. *Magnetic Resonance in Medicine*, 48(1):137–146, jul 2002, doi: 10.1002/mrm.10200. (page 27)

[323] H. Zhang, L. Tang, Z. Fang, C. Xiang, and C. Li. Nonconvex and nonsmooth total generalized variation model for image restoration. *Signal Processing*, 143:69–85, feb 2018, doi: 10.1016/j.sigpro.2017.08.021. (page 60)

[324] J. Zhang. How far is arterial spin labeling MRI from a clinical reality? Insights from arterial spin labeling comparative studies in Alzheimer's disease and other neurological disorders. *Journal of Magnetic Resonance Imaging*, 43(5):1020–1045, may 2016, doi: 10.1002/jmri.25022. (page 8, 52)

[325] K. Zhang, H. Herzog, J. Mauler, C. Filss, T. W. Okell, E. R. Kops, L. Tellmann, T. Fischer, B. Brocke, W. Sturm, H. H. Coenen, and N. J. Shah. Comparison of cerebral blood flow acquired by simultaneous [15O]water positron emission tomography and arterial spin labeling magnetic resonance imaging. *Journal of cerebral blood flow and metabolism : official journal of the International Society of Cerebral Blood Flow and Metabolism*, 34(8):1373–80, aug 2014, doi: 10.1038/jcbfm.2014.92. (page 6, 68, 95, 125, 154)

[326] W. Zhang, A. C. Silva, D. S. Williams, and A. P. Koretsky. NMR Measurement of Perfusion Using Arterial Spin Labeling Without Saturation of Macromolecular Spins. *Magnetic Resonance in Medicine*, 33(3):370–376, 1995, doi: 10.1002/mrm.1910330310. (page 14)

[327] L. Zhao and D. Alsop. Optimization of Flip Angle Design for Reduced T2 Blurring of 3D Arterial Spin Labeling. In *Proceedings of the 25th Annual Meeting of ISMRM*, page 3632, 2017. (page 50)

[328] L. Zhao, C.-D. Chang, and D. C. Alsop. Controlling T2 blurring in 3D RARE arterial spin labeling acquisition through optimal combination of variable flip angles and k-space filtering. *Magnetic Resonance in Medicine*, 80(4):1391–1401, oct 2018, doi: 10.1002/mrm.27118. (page 148, 180)

[329] L. Zhao, M. Vidorreta, S. Soman, J. A. Detre, and D. C. Alsop. Improving the robustness of pseudo-continuous arterial spin labeling to off-resonance and pulsatile flow velocity. *Magnetic Resonance in Medicine*, 78(4):1342–1351, oct 2017, doi: 10.1002/mrm.26513. (page 51)

[330] M. Y. Zhao, M. Mezue, A. R. Segerdahl, T. W. Okell, I. Tracey, Y. Xiao, and M. A. Chappell. A systematic study of the sensitivity of partial volume correction methods for the quantification of perfusion from pseudo-continuous arterial spin labeling MRI. *NeuroImage*, 162:384–397, nov 2017, doi: 10.1016/j.neuroimage.2017.08.072. (page 47)

[331] J. Zhou, S. Mori, and P. C. Van Zijl. FAIR excluding radiation damping (FAIRER). *Magnetic Resonance in Medicine*, 40(5):712–719, nov 1998, doi: 10.1002/mrm.1910400511. (page 15)

[332] Z. Zhou, F. Han, S. Yu, D. Yu, S. Rapacchi, H. K. Song, D. J. Wang, P. Hu, and L. Yan. Accelerated noncontrast-enhanced 4-dimensional intracranial MR angiography using golden-angle stack-of-stars trajectory and compressed sensing with magnitude subtraction. *Magnetic Resonance in Medicine*, 79(2):867–878, feb 2018, doi: 10.1002/mrm.26747. (page 152)

[333] B. V. Zlokovic. The Blood-Brain Barrier in Health and Chronic Neurodegenerative Disorders, jan 2008, doi: 10.1016/j.neuron.2008.01.003. (page 8)

[334] Z. Zun, A. Shankaranarayanan, and G. Zaharchuk. Pseudocontinuous arterial spin labeling with prospective motion correction (PCASL-PROMO). *Magnetic Resonance in Medicine*, 72(4):1049–1056, oct 2014, doi: 10.1002/mrm.25024. (page 49, 148)